Uniwersytet im Adama Mickiewicza w Poznaniu
Wydział Fizyki, Zakład Fizyki Mezoskopowej

Current-induced dynamics in magnetic nanopillars

(Indukowana prądem dynamika spinowa w zaworach spinowych)

Pavel Baláž

Rozprawa doktorska

Promotor: prof. dr hab. Józef Barnaś

Abstract

Since a decade, research in spintronics and related areas has been attracting much attention. The main reason for the wide scientific interest is the expectation of remarkable improvement in electronics and computer design offered by spin-dependent phenomena. The magnetization dynamics induced by current flowing through a metallic multilayer with magnetic components is one example of the wide family of spintronics phenomena. The theoretical understanding of this effect is based on the transfer of spin angular momentum between two magnetic layers with noncollinear magnetizations by the conduction electrons. When the density of flowing current is large enough, the current-induced spin torque can cause reorientation of relative magnetic configuration in the multilayer and consequently can change its resistance. After the discovery of these phenomena it was generally believed that current-controlled spin valve devices would replace soon the memory cells operated by external magnetic field. Such a technological progress, if realized, would certainly offer higher data storage density and faster manipulation with the information stored on a hard drive memory. However, it became clear soon that some important issues must be solved before devices based on spin torque could be used in practice. The most important is the reduction of current density required for magnetization switching, as well as enhancement of switching efficiency and thermal stability.

In this thesis the above mentioned issues are systematically examined in various metallic multilayer structures. The coresponding spin transfer torque has been calculated in the framework of a diffusive transport approach. The effect of current-induced torques on the spin dynamics has been examined using computer simulations. The research presented in this thesis ranges from single spin valves with standard and nonstandard torque angular dependence, through dual spin valves with in-plane and/or perpendicular polarizers and spin valves with composite free layer, up to magnetic nanowires with inhomogeneous magnetization. In the case of spin valve structures, tha main focus is the current-induced switching and the possibility of current-induced steady magnetization precessions without external magnetic field. Nonlinear effects in magnetoresistance of a dual spin valve and current-induced spin transfer torque acting on a wide Neel domain wall have also been studied.

Contents

Acknowledgement

First of all I would like to express my thanks to my supervisor, Prof. Józef Barnaś, for his kindness, support and professional guidance during my PhD study, and helpful advices and comments during the writing of my PhD thesis.
I also would like to thank Denis Horváth and Martin Gmitra for introducing me to physics and giving me the right direction.
For many useful discussions and advices I would like to thank my collegues from the SPINSWITCH network, mainly Jacques Miltat, Luis López Díaz and Elżbieta Jaromirska.
Last but not least I would like to thank my colleagues from the Division of Mesoscopic Physics, especially Wojciech Rudziński and Ireneusz Weymann for help when writing the abstract in Polish.

The research presented in this thesis has been supported by European Union through the Marie Curie Research Training Network SPINSWITCH (MRTN-CT-2006-035327) and Polish Ministry of Science and Higher Education as a research project entitled '*Indukowana prądem dynamika spinowa w metalicznych zaworach spinowych*' (*grant promotorski* N N202 489539) in years 2010-2011. Finally, I would like to thank Adam Mickiewicz University Foundation for the support in the form of a scientific scholarship in the year 2011.

1 Introduction

Spintronics is a modern branch of physics, which was developed mainly in the last decade. Its great progress is primarily connected with potential applications promising remarkable improvement in electronics and computer design. The main idea of spintronics is to utilize the well known property of electron – spin.

In present electronic devices electrons are considered just as charge and/or energy carriers. However, when employing magnetic elements in electronic devices, one can utilize dominant character of one spin direction, and polarize the charge current. Such a spin polarized current is not only a carrier of charge and energy but bears also an additional information about spin angular momentum. As already shown theoretically as well as experimentally, spin polarized current flowing from a non-magnetic to a magnetic material might interact with localized electrons' spins and consequently can induce magnetization dynamics. This phenomenon appearing on an interface between nonmagnetic and magnetic materials is called spin transfer torque and becomes an important part of novel concepts for electronic devices based on magnetic elements.

In this thesis multilayered metallic structures are studied theoretically. Namely, the structures consisting of several magnetic and nonmagnetic layers with typical size of several nanometers are examined. As shall be explained further, the resistance of such devices markedly depends on its relative magnetic configuration. Hence such devices are called *magnetic spin valves*[1]. Because of the pillar-like shape of the studied devices they are often referred to as *magnetic (nano)pillars*. Such devices are already used as elementary cells of magnetic memories since they can code elementary logic information in magnetic configuration, which can be read from their resistance; for instance, logical 'zero' as high resistive state and logical 'one' as low resistive state. The magnetic configuration of the spin valve is changed using external magnetic field. However, a magnetic field might influence also magnetization in neighboring cells. Therefore, the cells have to be separated from each other, what makes a limit for density of information in the device. A practical improvement coming with current-induced magnetization dynamics is that the current might be addressed to a specific spin valve without changing the magnetic states of spin valves in its neighborhood. This can increase the density information. Moreover, the current-induced dynamics has been shown to be faster than the field induced one, because when using an electric pulse the magnetization can be switched to the opposite direction after one half precession instead of slow precessional relaxation in external magnetic field. Another promising application of spin valves is connected with a possibility of current-induced steady-state magnetization dynamics emitting microwaves, which might be important for the future wireless communication systems.

However, there are several drawbacks and issues related to spin transfer and metallic spin valve devices. Firstly, the current density needed to the onset of magnetization dynamics is rather large ($10^8\,\mathrm{Acm}^{-2}$). This is mainly a question of used materials and applied switching scheme. Secondly, with the miniaturization of spin valve devices the magnetizations of small magnetic elements become more vulnerable to thermal fluctuations. Hence the thermal stability of the devices is required. Finally, the issue of microwave signal emitted from self-sustained magnetization dynamics is the weakness of the signal. In order to enhance the microwave signal the possibility of synchronization of several current-induced precessions is extensively studied. Therefore, the aim

[1] The term *spin valve* has more general meaning. However in this thesis the term primarily refers to magnetic multilayered structures.

of this thesis is to understand the magnetization dynamics induced by spin polarized current in metallic spin valves in order to deal with the addressed drawbacks.

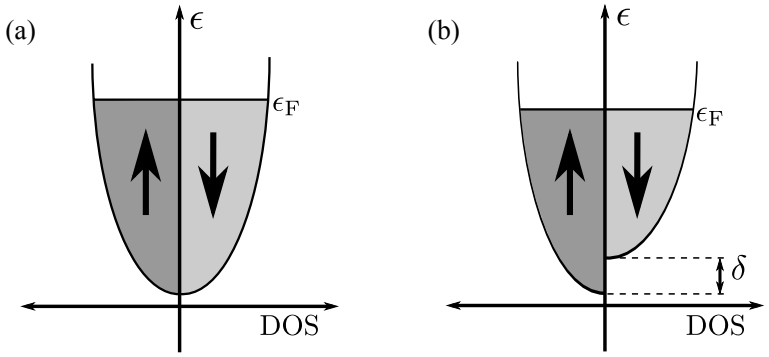

Figure 1: Illustration of Stoner splitting: parabolic energy band (a) in nonmagnetic metal, (b) in magnetic metal. ϵ_{F} stands for the Fermi level, while *delta* is the band splitting.

2 Overview

A new insight into electron and its basic properties was given in 1922 by an experiment conducted by O. Stern and W. Gerlach [1]. They have shown that a beam of silver atoms passing through an inhomogeneous magnetic field is splitted into two parts. According to the interpretation of Uhlenbeck and Goudsmit from 1925 [2], the Stern-Gerlach experiment reveals that particle posses an intrinsic angular momentum, which, in contrast to classical observations, takes only certain discrete values. Electron's magnetic momentum has been found to be close to Bohr magneton $\mu_{\mathrm{B}} = 57\mu\mathrm{eV/T}$, which corresponds to a classical rotation of a charge $e = 1.602 \times 10^{-19}\mathrm{C}$ with orbital angular momentum $\pm\hbar/2$, where $\hbar = h/2\pi = 6.6 \times 10^{-16}\mathrm{eVs}$ is reduced Planck constant.

2.1 Spin-dependent transport in metals

The discovery of spin became soon an important part of solid state physics since it is responsible for magnetic properties of transition metals, like Fe, Co, Ni. It has been shown by Stoner that in some materials the Fermi energy for minority and majority electrons splits due to their relative exchange coupling as

$$\epsilon_{\uparrow}(k) = \epsilon_0(k) - U\,\frac{n_{\uparrow}}{n}\,, \tag{2.1}$$

$$\epsilon_{\downarrow}(k) = \epsilon_0(k) - U\,\frac{n_{\downarrow}}{n}\,, \tag{2.2}$$

where $n_{\uparrow}$ ($n_{\downarrow}$) and $\epsilon_{\uparrow}$ ($\epsilon_{\downarrow}$) are number of electrons and energy for majority (minority) spins, respectively. The energy without considering any splitting is ϵ_0. The strength of Coulomb interaction between two electrons is given by parameter U. Because of the splitting, the densities of states for minority and majority electrons are different, which consequently leads to spontaneous magnetization. When the latter formulas (2.2) are summed over the whole k-space we get the Stoner criterion for ferromagnetism in the form

$$\nu(\epsilon_{\mathrm{F}})U > 1\,, \tag{2.3}$$

where $\nu(\epsilon_{\mathrm{F}})$ is the density of states on the Fermi level. Stoner criterion has been verified for valence bands of transition metals Fe, Co, Ni.

The main concept of spintronics already appears in the mid-thirties when N. F. Mott [3, 4] came up with an idea that some anomalies in the behavior of metallic ferromagnets arise from a

separation of majority and minority spin electrons into two independent transport channels. What the Mott's assumption is saying, in essence, is that the scattering processes leading to electron spin flip are very rare and hence we do not need to consider any transitions between the two spin channels. The rareness of the spin-flip processes in ferromagnetic metals is the main condition for validity of the *Mott's model*. Moreover, from the *Stoner's model* arises that in magnetic metals the transport properties in the majority and minority spin channels are different since they depend on the Fermi energy.

In the late 60s and 70s two channel model has been studied by many researchers who confirmed different scattering, and hence different resistivities, in majority and minority channels. Particularly, Fert and Campbell [5] studied nickel and iron based alloys and determined impurity resistivities for the majority and minority electrons. In their study they, firstly, measured residual resistivities of two different binary alloys, $Ni_{1-x}A_x$ and $Ni_{1-x}B_x$. In case of two independent conduction channels their resistivities can be written as

$$\rho_{\mathrm{A}} = C_{\mathrm{A}} \frac{\rho_{\mathrm{A}\uparrow}\rho_{\mathrm{A}\downarrow}}{\rho_{\mathrm{A}\uparrow} + \rho_{\mathrm{A}\downarrow}}, \qquad \rho_{\mathrm{B}} = C_{\mathrm{B}} \frac{\rho_{\mathrm{B}\uparrow}\rho_{\mathrm{B}\downarrow}}{\rho_{\mathrm{B}\uparrow} + \rho_{\mathrm{B}\downarrow}}, \tag{2.4}$$

where $C_{\mathrm{A}}\rho_{\mathrm{A}\uparrow}$ and $C_{\mathrm{B}}\rho_{\mathrm{B}\uparrow}$ are residual resistivities for the majority spin channels, while $C_{\mathrm{A}}\rho_{\mathrm{A}\downarrow}$ and $C_{\mathrm{B}}\rho_{\mathrm{B}\downarrow}$ are residual resistivities for the minority spin channels. Secondly, they measured residual resistivities in ternary alloys, $Ni_{1-x-y}A_xB_y$. Considering that impurities A and B in a ternary alloy add their resistivities ($\rho_\uparrow = C_{\mathrm{A}}\rho_{\mathrm{A}\uparrow} + C_{\mathrm{B}}\rho_{\mathrm{B}\uparrow}$, and $\rho_\downarrow = C_{\mathrm{B}}\rho_{\mathrm{A}\downarrow} + C_{\mathrm{B}}\rho_{\mathrm{B}\downarrow}$) one can calculate residual resistivity of the ternary alloy, ρ_{AB}. The *Mathiessen's rule* tells us that in case of two or more sources of scattering (in our case two different impurities) one can calculate the overall resistivity of the material by simple adding of partial resistivities coming from single sources ($\rho_{\mathrm{A}} + \rho_{\mathrm{B}}$). Then one obtains a deviation of the ternary alloy resistivity from the Mathiessen's rule in the form

$$\Delta\rho = \rho_{\mathrm{AB}} - (\rho_{\mathrm{A}} + \rho_{\mathrm{B}}) = \frac{(\alpha_{\mathrm{A}} - \alpha_{\mathrm{B}})^2 \rho_{\mathrm{A}}\rho_{\mathrm{B}}}{(1+\alpha_{\mathrm{A}})^2\alpha_{\mathrm{B}}\rho_{\mathrm{A}} + (1+\alpha_{\mathrm{B}})^2\alpha_{\mathrm{A}}\rho_{\mathrm{B}}} \tag{2.5}$$

where $\alpha_{\mathrm{A}} = \rho_{\mathrm{A}\downarrow}/\rho_{\mathrm{A}\uparrow}$, and $\alpha_{\mathrm{B}} = \rho_{\mathrm{B}\downarrow}/\rho_{\mathrm{B}\uparrow}$ describe the asymmetry of the resistivity in single spin channel. If both the transport properties in binary alloys are the same in both spin channels ($\alpha_{\mathrm{A}} = \alpha_{\mathrm{B}} = 1$), $\Delta\rho$ is zero. Otherwise, as also observed in the experiment, $\Delta\rho$ deviates from zero. Fert and Campbell used the analysis of $\Delta\rho$ to determine α_{A} and α_{B} for different materials; A, B = Co, Fe, Mn, Cr, V, Ti. In this way they have confirmed that the transport properties in each spin channel are different.

2.2 Spin-dependent tunneling

Expect of electron transport in ternary alloys the distinct properties of two spin channels in magnetic metals have been demonstrated in 1975 by M. Jullière [6], who studied electric transport through Fe/GeO/Co junction at temperature as low as 4.2 K. Jullière found that when the relative configuration of Fe and Co magnetization is parallel, the resistance of the stack is lower than in the case of antiparallel magnetic ordering. The quantitative measure of given effect is called *Tunneling Magnetoresistance* (TMR), which is defined as

$$\mathrm{TMR} = \frac{R_{\mathrm{AP}} - R_{\mathrm{P}}}{R_{\mathrm{P}}}, \tag{2.6}$$

where R_{P} and R_{AP} is resistance of the stack measured in case of parallel and antiparallel magnetic configuration, respectively. In accord with Stonner's results, Jullière assumed that electrons tunneling from a magnetic electrode are spin polarized with polarization defined as

$$P = \frac{\nu_{\uparrow}(\epsilon_{\mathrm{F}}) - \nu_{\downarrow}(\epsilon_{\mathrm{F}})}{\nu_{\uparrow}(\epsilon_{\mathrm{F}}) + \nu_{\downarrow}(\epsilon_{\mathrm{F}})}\,, \tag{2.7}$$

where $\nu_{\uparrow}(\epsilon_{\mathrm{F}})$ and $\nu_{\downarrow}(\epsilon_{\mathrm{F}})$ are density of states on the Fermi level for majority and minority spin electrons, respectively. Furthermore, Jullière assumed that electrons' polarization does not change during the tunneling. If P_1 denotes the spin polarization of Fe layer and P_2 polarization of Co layer, the expression for TMR reads

$$\mathrm{TMR} = \frac{2P_1P_2}{1 - P_1P_2}\,, \tag{2.8}$$

which is known as *Jullière formula*.

2.3 Giant magnetoresistance

In 1989 it has been shown independently by the groups of A. Fert [7] and P. Grünberg [8] that the resistance of a metallic multilayer, in which ferromagnetic layers alter with non-magnetic ones, depends on the magnitude of external magnetic field applied in the layers' plane. The dependence of the resistance on magnetic fields stems from the magnetic ordering in the multilayer.

It has been show by S. Parkin [9, 10] that the relative orientation of the adjacent magnetization depends on the thickness of the nonmagnetic spacer between them. More precisely, Parkin found that the sign of the exchange coupling between two magnetic layer alters with their distance while the amplitude of the exchange constant decreases. The origin of the observed oscillatory exchange coupling is the Ruderman-Kittel-Kasuya-Yosida (RKKY) interaction mediated by a spin polarized cloud of electrons. The oscillations of exchange constant with the spacer thickness is a manifestation of quantum interference in metals [11]. In consequence, if we assume that the coupling between adjacent magnetic layers is antiferromagnetic, the magnetic configuration of the stack at low applied field is antiparallel. When we apply external magnetic field in a certain direction, the magnetic configuration departs from antiparallel and for enough large field ($H = H_{\mathrm{sat}}$) all the magnetizations become aligned in the same direction. If we denote resistance in the antiparallel configuration ($H = 0$) by R_{AP} and resistance in the parallel configuration ($H = H_{\mathrm{sat}}$) by R_{P}, we can define a quantity similar to TMR, called *Giant Magnetoresistance* (GMR)

$$\mathrm{GMR} = \frac{R_{\mathrm{AP}} - R_{\mathrm{P}}}{R_{\mathrm{P}}}\,. \tag{2.9}$$

The physical interpretation of the observed effect is rather straightforward. Because of the Stonner band splitting, the density of states at the Fermi level for the majority spin electrons is say smaller than for the spin minority. In other words, there are less quantum states available for scattering of majority spins. On the other hand, the minority spins are strongly scattered. Therefore, the resistivity of the majority spin channel is smaller than for the spin minority.

Now let us consider the parallel configuration ($H = H_{\mathrm{sat}}$) in a magnetic multilayer. In magnetic metals or alloys, the majority electrons have spin aligned opposite to the layers magnetization.

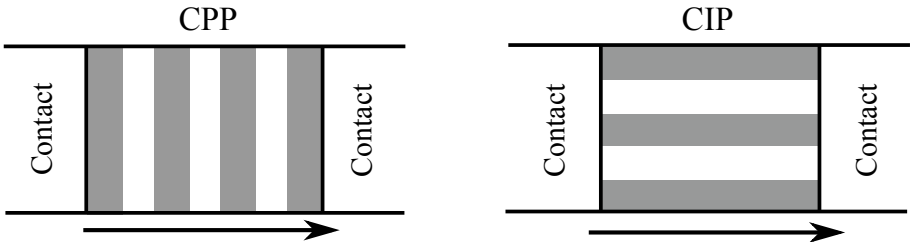

Figure 2: Comparison of current-perpendicular-to-plane (CPP) and current-in-plane (CIP) geometries.

Then, when an electron with ↑ or ↓ spin moves between different layers, it always remains in the same transport channel. The ↑ spins can pass the whole structure without any significant scattering. In contrary, in case of antiparallel magnetic configuration, when an electron with a certain spin direction belongs to the majority channel in one layer, in the adjacent layers it comes to the spin minority channel. Hence, it is strongly scattered in every second magnetic layer. The same applies to the electrons with the spins of the opposite direction. In summary, we can say that in case of parallel magnetic ordering only a part of the electrons is scattered, however, in case of antiparallel configuration all the electrons are strongly scattered. Hence the resistance of the whole stack is higher in the latter case: $R_{\mathrm{AP}} > R_{\mathrm{P}}$.

In the mentioned experiments [7, 8] they used so called current-in-plane (CIP) geometry, what means that the the current flew in the direction parallel to the layers' planes. An alternative geometry is current-perpendicular-to-plane (CPP) [12] where current flows in a direction which is perpendicular to the layers' planes; see Fig. 2. The theoretical interpretation of the effect is similar in both cases. However, in CPP geometry the absolute resistance of the multilayer decreases with increasing lateral size of the devices. Hence, for technological application CIP geometry is preferred [13]. On the other hand, the CPP geometry is more popular with modern spin torque experiments as shall be mentioned later.

More clearly, the effect of GMR might be described using the *resistor model* [11]. In the resistor model, the spin ↑ and spin ↓ transport channels in the multilayer are represented as two parallel branches of an electric circuit. Each magnetic layer is represented by two resistors of different resistances; one in the ↑ branch and the second one in the ↓ branch. Depending on the direction of layer's magnetization, the smaller resistor, R_+, is connected to the spin majority branch, while the bigger one, R_-, is connected to the spin minority branch. This is in agreement with the assumption that the majority spin electrons are less scattered than the minority spins. The nonmagnetic layers are represented by conductors (of the same resistances) connecting the resistors in the circuit. Figs. 3(c) and (d) shows an application of the described model in case of a magnetic trilayer, $\mathrm{F_1/N/F_2}$, where $\mathrm{F_1}$ and $\mathrm{F_2}$ are magnetic layers, which are separated by nonmagnetic spacer N. In the given example, the current direction is considered to be perpendicular to the layers' planes. For simplicity, we assume that $\mathrm{F_1}$ and $\mathrm{F_2}$ are done of the same material. When the magnetizations in the magnetic layers are parallel (Fig. 3(a)), ↑ spins are weakly scattered while the ↓ spins are strongly scattered in both magnetic layers. Hence, both small resistors are in one branch (say ↑), while both big resistors are in the other one (↓). Neglecting the resistance of the interfaces, resistance of the trilayer in the parallel magnetic configuration is

$$R_{\mathrm{P}} = \frac{2R_+R_-}{R_+ + R_-}\,. \tag{2.10}$$

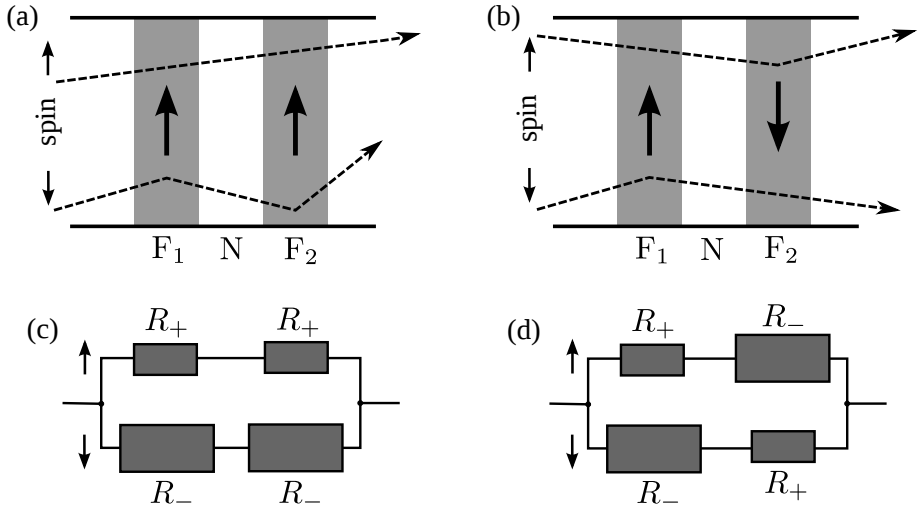

Figure 3: Giant magnetoresistace in a metallic trilayer $F_1/N/F_2$: Figs. (a) and (b) depict spin-dependent electron scattering in two transport channels in case of (a) parallel and (b) antiparallel magnetic configurations. Figs. (c) and (d) show the application of the resistor model in case of (c) parallel and (d) antiparallel magnetic configuration.

In the case of antiparallel configuration of magnetizations, the $\uparrow$ spin electrons are weakly scattered in F_1, but strongly scattered in F_2 layer. On the other hand, $\downarrow$ spin electrons are weakly scattered in F_2 but strongly scattered in F_1. This is modeled by altering small and big resistors in each branch (Fig. 3(b)). For the resistivity of the trilayer in the antiparallel configuration we can write

$$R_{\mathrm{AP}} = \frac{1}{2}(R_+ + R_-)\,. \tag{2.11}$$

Finally, inserting expressions (2.10) and (2.11) into the definition of GMR (2.9) we obtain

$$\mathrm{GMR} = \frac{1}{4}\,\frac{(R_+ - R_-)^2}{R_+ R_-}\,, \tag{2.12}$$

which is obviously a positive value confirming our previous physical conclusion that $R_{\mathrm{AP}} > R_{\mathrm{P}}$.

The latter example depicts qualitatively the way of the GMR calculation. However, in order to obtain a quantitative description one needs to identify the most important scattering processes and material parameters leading to the GMR effect. The first formal theories of GMR in metallic multilayers based on spin-dependent Boltzmann equation appeared soon [14, 15, 16]. Because a generalized form of the diffusive Boltzmann approach is a part of the research presented in this thesis, these theories shall be discussed later in more details (see chapter 3). Later on, microscopic theories employing the quantum Kubo formula [17, 18] were studied. The results of Boltzmann and Kubo descriptions have been found to be equivalent since in both approaches the band structure of the magnetic layers has been approximated by simple parabolic shape. The more realistic band structure has been incorporated into numerical models based on Boltzmann equation and *ab initio* calculations based on the Kubo formula [19, 20, 21].

2.4 Spin injection

Since in a ferromagnetic material the electron mobilities in the two transfer channels are different, there is an imbalance between $\uparrow$ and $\downarrow$ spins. Hence one can say that the current in a ferromagnet is

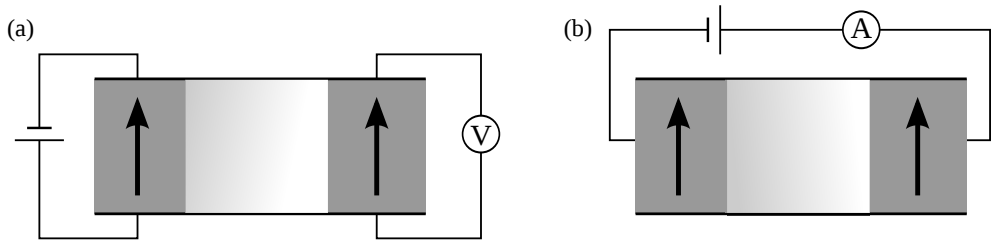

Figure 4: Nonlocal (a) *vs.* local (b) configuration of a spin valve .

spin polarized [2]. In 1976 Aronov [22] proposed that spin polarized current might be injected from a ferromagnetic material to a normal metal attached to the ferromagnet. This has been first carried out in 1985 by Johnson and Silsbee [23, 24] who studied electric transport through a four-terminal device made of two Permalloy (Py) layers separated by nonmagnetic aluminum. The device is depicted in Fig. 4(a). Spin polarized current is injected from the left electrode (injector) to the aluminium. The spin current creates a spin imbalance in the nonmagnet called *spin accumulation*, which is defined as the difference between electrochemical potentials for majority and minority spin electrons. However, because of spin relaxation processes in the nonmagnetic metal the spin accumulation decays with a scale called spin diffusion length, λ_{sf}. The right Py layer stands for the detector, which detects spin accumulation when its distance from the left electrode is $L \ll \lambda_{\mathrm{sf}}$. [3] In the experiment a spin-induced signal of several pV was measured by SQUID at the temperatures of liquid nitrogen.

The configuration shown in Fig. 4(a) is called *nonlocal* since there is no direct potential gradient between the Py electrodes. In the nonlocal geometry the spin accumulation appears just due to the spin diffusion in the nonmagnetic metal. We say that a pure spin current without any charge current is observed. In contrast, in the above mentioned CPP GMR experiments the charge current flowing along the device is also associated with the spin current. Such a configuration, is called *local* (see Fig. 4(b)) and is mostly used in spin-torque switching devices described below.

2.5 Current-induced switching

In 1996 Slonczewski [25] and Berger [26] independently proposed that a spin angular momentum transfered between two ferromagnets separated by a nonmagnetic spacer might be large enough to induce magnetic excitations in one of the layers resulting in the switching of the direction of its magnetization. The experimental evidence of the proposed effect came in 1998 by Tsoi et al. [27] and later on by Katine et al. [28]. The device used in the experiment consisted of two ferromagnetic cobalt layers separated by 6 nm of copper. One of the cobalt layers was thicker (10 nm) while the second one was thinner (2.5 nm). Such a geometry is typical for most of the devices switchable by current. The thick magnetic layer is often called *fixed* or *reference layer* since its magnetization is usually considered to be fixed and uninfluenced by the spin current. Another name for the fixed layer is polarizer because it polarizes the electrons which are transmitted to the second magnetic layer. The thin magnetic layer is called *free* or *sensing layer* because its magnetization is assumed to be free to rotate.

The main contribution to the magnetization dynamics of the free layer comes from the torque

[2] In short we talk about *spin current*.

[3] In nonmagnetic metals $\lambda_{\mathrm{sf}} \sim 100\,\mathrm{nm}$.

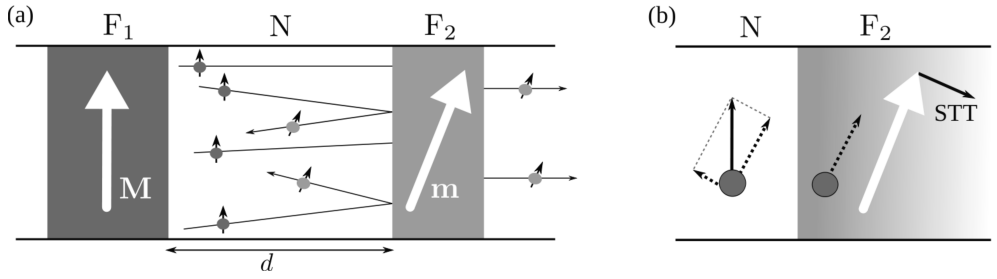

Figure 5: Mechanism of spin transfer torque. (a) Transport of majority spin electrons through a metallic trilayer with fixed layer F_1, nonmagnetic spacer N, and free layer F_2. (b) N/F_2 interface: spin transfer torque as a result of the absorption of transversal spin components in F_2 layer.

induced by the current polarized in the fixed layer. The mechanism of the spin momentum transfer is shown in Fig. 5. Let's assume the electrons are passing through the fixed layer. The majority of electron spins align in the direction parallel to the fixed magnetization, **M**, and the electric current becomes spin polarized. The spin current passes the nonmagnetic spacer and electrons hit the free layer where they become polarized by the free layer's magnetization, **m**. When **m** is collinear with with **M** the electron spins remain unchanged and no magnetization dynamics is observed. However, when the two magnetizations are not collinear the spins in the second layer change their direction since they align to **m** The spin component parallel to **m** (longitudinal spin component) remains unchanged, however the component transversal to **m** disappears at the N/F_2 interface; see Fig. 5(b). Because of the angular moment conservation the transversal spin component is transfered to the free layer and appears as a *spin-transfer torque* (STT) acting on the layers magnetization. When the current density and spin current polarization is large enough one observes magnetic excitations in the free layer, which might lead to the switching of **m** direction. This effect is called *current-induced switching* and has been an important point of research in the field of spintronics because of its promising benefit for the nanotechnologies and magnetic random access memories (MRAM).

In his paper Slonczewski [25] employed the Wentzel–Kramers–Brillouin (WKB) approximation to find the relevant wave functions and to calculate the charge and spin fluxes in a metallic three-layer system assuming additionally parabolic bands. The key assumption of his calculations was that λ_{sf} is far more larger than the thickness of the spacer layer, d, which is well satisfied up to temperatures of 80 K when the in-plane dimension of multilayer is $\sim 100\,\mathrm{nm}$. Under such condition the electron transport is *ballistic*, i.e. electrons pass the nonmagnetic layer without any scattering. This is, however, far from the conditions in experiments conducted at room temperature where $\lambda_{\mathrm{sf}} \lesssim d$ and we have to take into account diffusive features of the electron transport. The differences between these two transport limits will be discussed later. Analyzing the spin fluxes, Slonczewski calculated the spin current and, consequently, the torque acting on the net spin moments. This additional torque, $\boldsymbol{\tau}_{\mathrm{Sloncz}}$, can have quite significant impact on magnetization behavior (when current density is sufficiently large) and can be included in the Landau-Lifshitz-Gilbert equation in a form

$$\boldsymbol{\tau}_{\mathrm{Sloncz}} = \frac{Ig(\theta)}{\mathrm{e}}\, \hat{\boldsymbol{s}} \times (\hat{\boldsymbol{s}} \times \hat{\boldsymbol{S}})\,, \tag{2.13}$$

where $\hat{\boldsymbol{s}} = -\mathbf{m}/M_{\mathrm{s}}$ is a unit vector along the free layer's net spin moment, $\hat{\boldsymbol{S}} = -\mathbf{M}/M_{\mathrm{s}}$ is the unit vector along the fixed layer's (polarizer) spin moment; M_{s} is the saturated magnetization

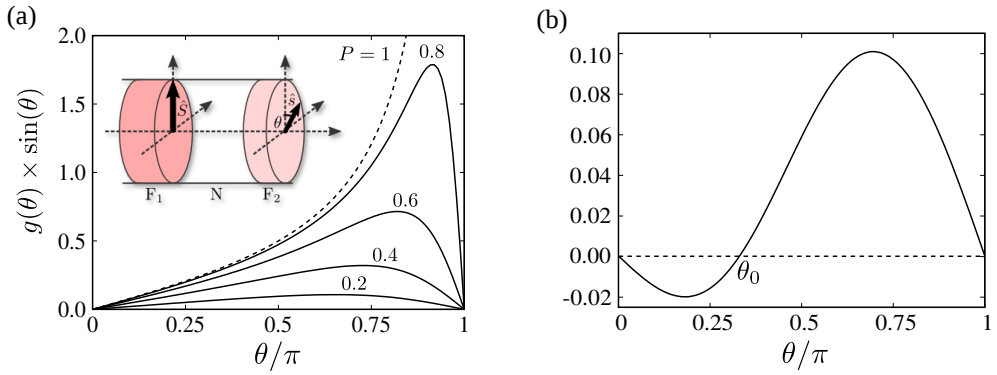

Figure 6: (a) angular dependence of STT derived by Slonczewski calculated for different values of current polarization, P. The inset shows a single spin valve with fixed layer F_1 and free layer F_2; θ is an angle measured between net spin moments' vectors $\hat{\boldsymbol{S}}$ and $\hat{\boldsymbol{s}}$. (b) an example of a wavy-like angular dependence of STT with a compensation point θ_0.

of the fixed (free) layer, I is the charge current density and e is the absolute value of electron charge. Here, $g(\theta)$ is the torque efficiency function depending on the angle θ measured between spin moments of the magnetic layers

$$g(\theta) = \left[-4 + (1+P)^3 \frac{3+\cos\theta}{4P^{3/2}}\right]^{-1}, \tag{2.14}$$

where P is the polarization of incident current. The θ-dependence of g modifies the dependence of STT on the relative angle θ between spin moments of the layers. When the variation of g with θ is negligible, the STT depends on the angle θ just as $\boldsymbol{\tau}_{\mathrm{Sloncz}} \propto \sin\theta$, which is simply given by the vector products in Eq. (2.13). The modification of the angular dependence of the Slonczewski torque with the polarization, P, is shown in Fig. 6(a). With higher polarization, the amplitude of STT becomes larger and the dependence of g on θ becomes more pronounced. Generally, for $P < 1$ the torques disappear in collinear configurations, $\theta = 0$ and π, what is in agreement with our previous physical conclusions. However, In case of $P = 1$, g increases to infinity for $\theta = \pi$, but the polarizations obtained in experiments usually range from $P = 0.3$ to 0.5.

2.6 Current state-of-the-art

After the effect of STT in thin magnetic multilayers had been predicted and then experimentally proven, it was strongly believed that current-controlled spin valve devices would replace soon the magnetoresistive memory cells operated by an external magnetic field. Such a technological progress, if realized, would certainly offer higher data storage density and faster manipulation with the information stored on a hard drive memory. However, it became clear soon that some important issues must be solved before devices based on STT could be used in practice. The most important is the reduction of current density needed for magnetic excitation and magnetization switching in thin films. Moreover, enhancement of switching efficiency and thermal stability is not less important.

2.6.1 Switching schemes

Some progress has been made by using subtle switching schemes based on optimized current and field pulses [29, 30, 31, 32]. The idea of switching scheme is to minimize the Joule heating which is induced in the spin valve during the current pulse and maximize the switching probability and switching rate. For both magnetic tunnel junction as well as for metallic spin valves, a short pulse precessional switching with perpendicularly polarized current seems to be more efficient than collinear in-plane polarization switching [30]. Moreover, it was demonstrated that higher switching probability and faster switching one can obtain with properly set sequence of sub-nanosecond pulses [29]

2.6.2 Non-standard spin valve geometry

An important potential application of spin-torque based devices is current-induced microwave generation. The main intention is to create a self-sustained (steady-state) magnetization precession with electric current and without need of external magnetic field. This problem might be tackled by so called non-standard spin valve structures. Here, the term *non-standard* is related to a spin valve with an unusual wavy-like angular torque dependence, known as *wavy-torque*. It means that STT does not disappear only in the collinear magnetic configuration of the spin valve but also in a certain non-collinear one in which STT alters its sign; Fig. 6(b). The appearance of the wavy-torque is a manifestation of diffusive spin-dependent transport [33, 34] and is observed in spin valves with fixed and free layers constructed of different materials with distinct spin asymmetries. In the last years STT in non-standard spin valves has been extensively studied theoretically [35, 36, 37, 32, 38, 39] as well as experimentally [40, 41]. The wavy-like STT angular dependence has a crucial impact on the resulting current-induced dynamics. In standard spin valves, current flowing in one direction destabilizes certain collinear magnetic configuration and stabilizes the opposite one. In the case of non-standard spin valves, whilst current flowing in one direction destabilizes both collinear configurations, current flowing in the opposite direction stabilizes both of them. In practice, such a dynamic behaviour supports current-induced precession for one current direction and stabilizes the collinear spin configuration for opposite current flow, which might be useful for many future devices. A technological disadvantage of non-standard spin valves is that the STT angular dependence is quite sensitive to layers' thicknesses as well as to material parameters and, therefore, it is difficult to prepare a spin valve with marked wavy-like angular dependence.

2.6.3 Out-of-plane polarizer

An improvement of current-induced switching has been noticed in spin valves with a polarizer with magnetization tilted out of the layer's plane. A spin valve with a perpendicularly magnetized polarizer (see Fig. 7) has been proposed by Kent et al [42] in 2004. The authors have shown that the perpendicular polarizer might fasten the magnetization switching of a free layer with in-plane uniaxial anisotropy. Basically, the enhancement of switching arises from the fact that in a static state the fixed and free magnetizations are perpendicular and hence the initial torque acting on the free layer's magnetization is much higher than in a standard spin valve with in-plane magnetized fixed layer. Therefore, the free magnetization starts to precesses around the x-axis almost immediately after the current onset. Because of the lack of so called *incubation time*, i.e. the initial in-plane precession (around the z-axis) of the magnetization vector before the switching,

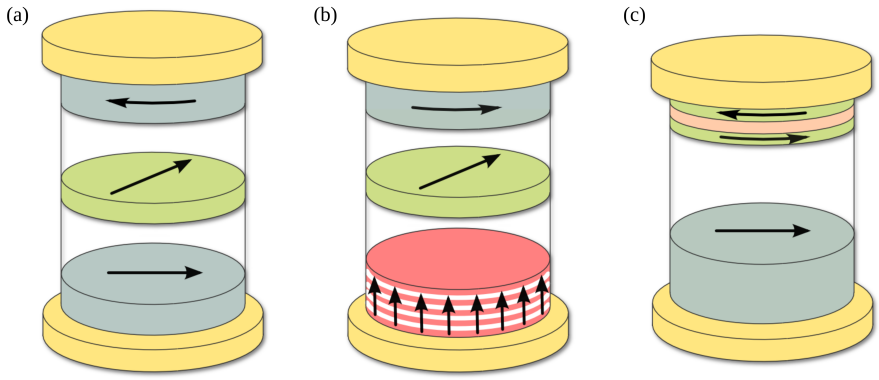

Figure 7: Complex spin valve structures: (a) dual spin valve with two in-plane polarizers, (b) spin valve with a perpendicular out-of-plane polarizer and an in-plane polarized reference layer, (c) spin valve with an composite antiferromagnetically coupled free layer.

it is possible to switch the free layer's magnetization with a subnanosecond pulse of electric current [42, 43]. Because the relative configuration of the fixed and free layers' magnetizations in the static states is unchanged, one needs an additional in-plane magnetized fixed layer to indicate the free layer's magnetization switching via the GMR effect. It has been shown, that one can construct the spin valve in a way that the in-plane fixed layer does not markedly influence the spin dynamics of the free layer [42] but the change of resistance is still observable. On the other hand, it has been found that the STT induced by the in-plane polarizer together with the out-of-plane one might markedly enhance the switching probability, which might became almost 100% even at room temperature [43]. Because in the latter case the STT from the in-plane as well as from the out-of-plane polarizer acts on the free layer, the structure is a special case of a dual spin valve (see 2.6.4).

Recently, the perpendicular polarizer has been used as a part of spin-torque oscillators (STO), because in the presence of a constant current it might induce steady-state out-of-plane precessions (around the x-axis), which are associated with relatively high variation of the magnetoresistance and the output signal. Nowadays, this concept of STO devices is extensively studied experimentally [44] as well as theoretically [45, 46]. In addition, it has been shown in the macrospin approach that different kind of dynamic modes in the free layer might be induced by varying the angle of the out-of-plane polarizer's magnetization [47].

2.6.4 Dual spin valve

One of the possibilities to decrease the critical current density in metallic structures is a geometry proposed by L. Berger [48] in 2003 called *dual spin valve* (DSV). A DSV consists of three magnetic layers separated by nonmagnetic spacers. Usually, it is constructed in a way that both outer magnetic layers have fixed magnetic moments while the central one is considered as a free layer. It has been shown by Berger [48] that in such a geometry a step in spin accumulation appears on both interfaces of the central layer and therefore both interfaces are used to produce STT acting on the central magnetization. This is a difference from standard single spin valves where only one interface produces STT. Because there are two torques that arise at the interfaces of a DSV free layer, the overall torque acting on the central magnetization depends on the relative configuration

of the outer magnetizations. As a consequence, when the magnetizations of the outer layers are antiparallel, the STT acting on the free layer's magnetization is several times higher than in standard single spin valves [48], since the steps in spin accumulation on both interfaces have the same sign. On the other hand, when the DSV is symmetric and the outermost magnetizations are parallel, the steps in spin accumulation on the free layer's interfaces have the same amplitude, but opposite sign, and the central layer's magnetization is uninfluenced by STT.

Recently, dual metallic structures are mainly connected with a novel phenomena called *nonlinear magnetoresistance* observed in DSV with permalloy (Py) central layer and CoFe outer layers with fixed antiparallel magnetizations. It has been shown experimentally [49, 50] that high spin accumulation in the central layer causes dependence of GMR on the applied current density. Moreover, the sign of GMR depends on the current direction. Namely, when the Py magnetization is switched from one collinear configuration to the opposite one, the resistance of a DSV increases for current flowing in one direction, and decreases for the current flowing in opposite direction. Such a behaviour is very different from the results obtained from standard GMR models (e.g. Valet-Fert model [16]) which do not include any dependence of the magnetoresistance on the current. The theoretical description of this phenomenon is still an open problem.

2.6.5 Composite free layer

Another way of spin torque enhancement is the modification of the free layer's structure. A free layer consisting of two or more magnetic layers separated by nonmagnetic layers is generally called *composite free layer* (CFL) or *synthetic free layer*. Usually, the neighboring magnetic layers are strongly coupled via RKKY interaction [9], which might be tuned by the spacer's thickness. When the RKKY coupling is ferromagnetic one refers to the CFL as to synthetic ferromagnet. When the interlayer exchange coupling is negative and the magnetic layers are identical, we call the structure *synthetic antiferromagnet* (SyAF) since its total magnetic moment is zero. However, when the layers of antiferromagnetically coupled CFL are different, the structure has an uncompensated nonzero magnetic moment and we call it *synthetic ferrimagnet* (SyF). To enhance the interlayer exchange coupling in a CFL the magnetic layers are often made of cobalt, CoFe, or CoFeB, while the nonmagnetic spacer is usually ruthenium. Typical thickness for the ruthenium layer is several angstroms, while thicknesses of the magnetic layers are usually several nanometers. In such a geometry the effective coupling field between the magnetic layers is of the order of several kilo-Oersted. The main advantage of a composite free layer is its high thermal stability (see section 11).

2.7 This thesis

This thesis describes a systematic study of the current-induced dynamics in metallic spin valves within the spin-dependent diffusive electronic transport in metals. Employing an theory based on the diffusive equation [33, 34], we modeled current-induced spin dynamics in different types of metallic spin valves. An advantage of the used approach is that current induced dynamics is modeled in consistence with the dynamics of spin accumulation, which depends on the actual magnetic configuration of the spin valve. The spin dynamics has been modeled in a single domain (macrospin) approximation. Particularly, we focused on spin valves recently studied in various STT and GMR experiments.

In section 3 the theoretical approach to the diffusive spin-dependent transport is described. The method of calculation of spin current and spin accumulation in metallic multilayers is introduced. Consequently, STT components are defined in a general non-collinear magnetic configuration of a spin valve. Section 5 introduces the magnetization dynamics in the macrospin model. Landau-Lifshitz-Gilbert equation (LLG) is there introduced and analyzed. The effective magnetic field acting on a magnetic layer is described and the spin dynamics at nonzero temperature is discussed. Section 6 describes the problem of magnetization stability by means of linearized LLG and spin torque ferromagnetic resonance (STT-FMR).

Sections 7 – 13 introduce my contribution to the studied area. Firstly, in section 7 switching induced by a rectangular current pulse in standard and non-standard spin valves is described [32, 51]. The dynamics induced by a wavy-torque shall be in short discussed in the light of more detailed micromagnetic simulations [39, 38]. Secondly, chapter 8 introduces a model of a dual spin valve (DSV) [52], which is intended to have an ability to manipulate with the STT profile and enhance the current-induced switching. The current-induced dynamics of a modified DSV with one perpendicular (out-of-plane) and one in-plane polarizer is analyzed in sections 9 and 10. Thirdly, in section 11 we describe the current-induced dynamics of a SyAF and SyF [53]. A novel feature observed recently in DSV structure, nonlinear effects in GMR, are studied in chapter 12, which presents a simple phenomenological model [54] that qualitatively reproduces the experimentally observed effects. Finally, in section 13 we present a calculation of spin accumulation and spin transfer torque acting on a domain wall. In addition, the appendices describe some additional information and methods used to obtain the results presented in this thesis.

3 Spin-dependent diffusive transport of electrons

Most of recent spin-torque experiment have been conducted at room temperature. This is mainly related to the intention of employing spin-torque devices in novel spintronic devices. Under such conditions spin diffusion is more likely to dominate the electronic transport. Moreover, most of experiments on CPP-GMR at room temperature have been successfully explained within Valet-Fert model [16], which describes electronic transport in frame of Boltzmann equation. Therefore, the theory of STT based on the same assumptions seems to be most relevant. In this chapter a recent model of STT [33, 34], which unifies STT and CPP-GMR description in frame of diffusive transport limit, shall be introduced.

3.1 Valet-Fert model

Valet-Fert model [16] describes the spin-dependent transport properties of metallic multilayers for current perpendicular to the layers' planes. The model is based on the Boltzmann equation and takes into account both bulk as well as interface spin-dependent scattering. The authors have shown that the diffusive model fits well with experimental data when the thicknesses of individual layers are shorter than the spin diffusion length in the given material.

Valet and Fert assumed a model of alternating magnetic and nonmagnetic layers with single parabolic bands with an electron effective mass m and Fermi velocity v_{F} in both types of layers. The current of density J flows along the x axis, which is perpendicular to the layers' planes. The magnetizations of the magnetic layers were considered to be aligned along the z-axis, which lies in the layers' planes[4]. Because the Valet-Fert model considers only collinear magnetic configurations, one can introduce the *distribution function*, $f_s(x, \boldsymbol{v})$, where $s = \uparrow, \downarrow$ denotes the majority and minority electron spins, respectively[5]. In the limit of zero temperature the Boltzmann equation reads [16]

$$\begin{aligned} v_x \frac{\partial f_s}{\partial x}(x, \boldsymbol{v}) - |e| E(x) v_x \frac{\partial f_0}{\partial \epsilon}(v) = & \int \mathrm{d}^3 v' \delta[\epsilon(v') - \epsilon(v)] P_s[x, \epsilon(v)] [f_s(x, \boldsymbol{v}') - f_s(x, \boldsymbol{v})] + \\ & \int \mathrm{d}^3 v' \delta[\epsilon(v') - \epsilon(v)] P_{\mathrm{sf}}[x, \epsilon(v)] [f_{-s}(x, \boldsymbol{v}') - f_s(x, \boldsymbol{v})] \,, \end{aligned} \tag{3.1}$$

where $-|e|$ is the electron charge, $\epsilon(v) = mv^2/2$ the electron kinetic energy, $E(x) = -\partial V(x)/\partial x$ is the local electric field. $P_s(x, \epsilon)$ is the probability of spin-conserving electron transition, while $P_{\mathrm{sf}}(x, \epsilon)$ is the probability of spin-flip electron transitions where $s \to -s$. $f_0(v)$ is the Fermi-Dirac distribution function while $f_s(x, \boldsymbol{v})$ is perturbed Fermi-Dirac distribution, which can be written as [16]

$$f_s(x, \boldsymbol{v}) = f_0(v) + \frac{\partial f_0}{\partial \epsilon} \left([\mu_0 - \mu_s(x)] + h_s(x, \boldsymbol{v}) \right) \,, \tag{3.2}$$

where μ_0 is the equilibrium chemical potential. Apart from the anisotropic perturbation $\propto h_s(x, \boldsymbol{v})$, which appears also in the CIP geometry, authors introduced an isotropic term expressing the local

[4] Note, that we changed the names of the axes used in the original work by Valet and Fert in order to make the notation consistent with the further equations.

[5] In the original paper the spin majority and minority is marked by $+$ and $-$ signs while $\uparrow$ and $\downarrow$ stand for the absolute spin direction $s_z = \pm 1/2$.

variation of the chemical potential in order to account for the spin accumulation, which arises only in the CPP geometry.

Introducing Eq. (3.2) into (3.1) and keeping only linear perturbation terms one obtains [16]

$$v_x \frac{\partial h_s}{\partial x}(x, \boldsymbol{v}) + \left(\frac{1}{\tau_s} + \frac{1}{\tau_{\mathrm{sf}}} \right) h_s(x, \boldsymbol{v}) = v_x \frac{\partial \bar{\mu}_s}{\partial x}(x) + \frac{\bar{\mu}_s - \bar{\mu}_{-s}}{\tau_{\mathrm{sf}}} , \tag{3.3}$$

where $\bar{\mu}_s = \mu_s - |e|V(x)$ is the *electrochemical potential* for spin s. The relaxation time τ_s is related to spin conserving transition processes in the s-spin channel while τ_{sf} is the relaxation time connected to spin-flip processes, respectively. Therefore, the term on the right-hand side which is proportional to τ_{sf}^{-1} expresses the relaxation of the spin accumulation by the spin-flip scattering.

An important feature of the CPP geometry is the cylindrical symmetry of the problem around the x-axis. Thus, $h_s(x, \boldsymbol{v})$ can be written as a series of Legendre polynomials, $P_n(\cos\vartheta)$, where ϑ is an angle between the velocity vector and the x-axis.

$$h_s(x, \boldsymbol{v}) = \sum_{n=1}^{\infty} h_s^{(n)}(x) P_n(\cos\vartheta) . \tag{3.4}$$

This means that the CPP geometry allow us to separate x and $\boldsymbol{v}$ variables.

Furthermore, Valet and Fert have shown that in the limit of small layer thicknesses, d, in comparison to the spin diffusion length, l_{sf}, the Boltzmann approach leads to the following transport equations [16]:

$$\frac{|e|}{\sigma_s} \frac{\partial j_s}{\partial x} = \frac{\bar{\mu}_s - \bar{\mu}_{-s}}{l_s^2} , \tag{3.5a}$$

$$j_s = \frac{\sigma_s}{|e|} \frac{\partial \bar{\mu}_s}{\partial x} , \tag{3.5b}$$

with σ_s and j_s being the conductivity and the current density for the s spin channel, respectively. The first equation, (3.5a), expresses the fact that in the steady-state regime the divergence of spin current is balanced by the spin flip processes. Equation (3.5b) is just the Ohm's law.

Inserting Eq. (3.5b) into Eq. (3.5a) one obtains two second order differential equations for the electrochemical potentials [16]

$$\frac{\partial^2 \bar{\mu}_\uparrow}{\partial x^2} = \frac{1}{l_\uparrow^2} (\bar{\mu}_\uparrow - \bar{\mu}_\downarrow) , \tag{3.6a}$$

$$\frac{\partial^2 \bar{\mu}_\downarrow}{\partial x^2} = \frac{1}{l_\downarrow^2} (\bar{\mu}_\downarrow - \bar{\mu}_\uparrow) , \tag{3.6b}$$

where $l_\uparrow^2 = D_\uparrow \tau_{\mathrm{sf}}$ and $l_\downarrow^2 = D_\downarrow \tau_{\mathrm{sf}}$. Equations (3.6) finally lead to [16]

$$\frac{\partial^2}{\partial x^2} (\bar{\mu}_\uparrow - \bar{\mu}_\downarrow) = \frac{1}{l_{\mathrm{sf}}^2} (\bar{\mu}_\uparrow - \bar{\mu}_\downarrow) , \tag{3.7}$$

where $(1/l_{\mathrm{sf}})^2 = (1/l_\uparrow)^2 + (1/l_\downarrow)^2$. Equations (3.6) also lead to

$$\frac{\partial^2}{\partial x^2} (\sigma_\uparrow \bar{\mu}_\uparrow + \sigma_\downarrow \bar{\mu}_\downarrow) = 0 . \tag{3.8}$$

Equations (3.7) and (3.8) have general solutions which read

$$(\bar{\mu}_\uparrow - \bar{\mu}_\downarrow) = A\exp(x/l_{\mathrm{sf}}) + B\exp(-x/l_{\mathrm{sf}})\,, \tag{3.9a}$$

$$(\sigma_\uparrow\bar{\mu}_\uparrow + \sigma_\downarrow\bar{\mu}_\downarrow) = Cx + D\,. \tag{3.9b}$$

Making use of solutions (3.9) in connection with appropriate conditions which have to be satisfied on an interface between non-magnet/ferromagnet (N/F) interfaces, one might obtain the profiles of the spin-dependent electrochemical potentials in any metallic multilayer. Consequently, one might determine the resistance in any collinear magnetic configuration of the multilayer and calculate the GMR of the studied device.

The Valet-Fert model is limited to collinear magnetic configurations. Hence, it is impossible to use it for the STT calculation. Recently, a more general approach based on the spin diffusion equation was developed in the references [33, 34], which allows to calculate transport properties also in the non-collinear magnetic configurations and hence gives a possibility to calculate the STT acting on the magnetizations. Therefore, in the following we will focus on the generalized diffusive transport approach, and shall also describe the method of calculation of electrochemical potentials and spin currents in a metallic multilayer.

3.2 Diffusive transport model in noncollinear geometry

The generalized diffusive transport approach [33, 34] bases on the 2×2 matrix formalism in which the electron distribution function in a metallic film is given by the distribution function matrix, $\check{f}$. Its variation is given by the diffusion equation. We assume the variation of $\check{f}$ only along the x-axis, hence the diffusion equation reads [55]

$$\check{D}\frac{\partial^2\check{f}}{\partial x^2} = \frac{1}{\tau_{\mathrm{sf}}}\left[\check{f} - \check{1}\frac{\mathrm{Tr}\check{f}}{2}\right], \tag{3.10}$$

where $\check{D}$ is the 2×2 diffusion matrix, and $\check{1}$ is a 2×2 unit matrix.

Making use of this general formalism we shall describe the transport properties of a magnetic and non-magnetic film, separately.

3.2.1 Magnetic layer

In the macrospin approximation, we assume that in a magnetic film the internal exchange field is strong enough to suppress the component of the distribution function which are transversal to the magnetization. Thus, when the quantization axis is chosen along the magnetization, the electron distribution function is diagonal $\check{f} = \begin{pmatrix} f_\uparrow & 0 \\ 0 & f_\downarrow \end{pmatrix}$.

Hence, equation (3.10) lead to the pair of second order differential equations [33]

$$D_\uparrow\frac{\partial^2 f_\uparrow}{\partial x^2} = \frac{1}{\tau_{\mathrm{sf}}}(f_\uparrow - f_\downarrow)\,, \tag{3.11a}$$

$$D_\downarrow\frac{\partial^2 f_\downarrow}{\partial x^2} = \frac{1}{\tau_{\mathrm{sf}}}(f_\downarrow - f_\uparrow)\,, \tag{3.11b}$$

which might be rewritten for the spin-dependent electrochemical potentials leading to equations (3.6) already introduced in the Valet-Fert model. Consequently, they can be rewritten as

$$\frac{\partial^2}{\partial x^2}(\bar{\mu}_\uparrow - \bar{\mu}_\downarrow) = \frac{1}{l_{\mathrm{sf}}^2}\,(\bar{\mu}_\uparrow - \bar{\mu}_\downarrow)\,, \tag{3.12a}$$

$$\frac{\partial^2}{\partial x^2}(\bar{\mu}_\uparrow + \bar{\mu}_\downarrow) = \eta\,\frac{\partial^2(\bar{\mu}_\uparrow - \bar{\mu}_\downarrow)}{\partial x^2}\,, \tag{3.12b}$$

where η is the polarization factor given by

$$\eta = -\frac{D_\uparrow - D_\downarrow}{D_\uparrow + D_\downarrow}\,. \tag{3.13}$$

Equations (3.12) are equivalent to equations (3.7) and (3.8) obtained in the Valet-Fert model from the Boltzmann equation. The general solution of equations (3.12) might be written as [33]

$$\bar{\mu}_\uparrow = (1+\eta)\,[A\exp(x/l_{\mathrm{sf}}) + B\exp(-x/l_{\mathrm{sf}})] + Cx + G\,, \tag{3.14a}$$

$$\bar{\mu}_\downarrow = (\eta-1)\,[A\exp(x/l_{\mathrm{sf}}) + E\exp(-x/l_{\mathrm{sf}})] + Cx + G\,. \tag{3.14b}$$

The parameters A, B, C, and G shall be determined from appropriate boundary condition later.

The electro-chemical potentials can be written as

$$\check{\bar{\mu}} = \bar{\mu}_0\check{1} + g\check{\sigma}_z\,, \tag{3.15}$$

where $\bar{\mu}_0 = (\bar{\mu}_\uparrow + \bar{\mu}_\downarrow)/2$ is the equilibrium electrochemical potential, and $g = (\bar{\mu}_\uparrow - \bar{\mu}_\downarrow)/2$ is the spin accumulation describing spin-dependent splitting of electrochemical potential. Following the latter definitions and (3.14) we can write

$$\bar{\mu}_0 = \eta\,[A\exp(x/l_{\mathrm{sf}}) + B\exp(-x/l_{\mathrm{sf}})] + Cx + G\,, \tag{3.16a}$$

$$g = A\exp(x/l_{\mathrm{sf}}) + B\exp(-x/l_{\mathrm{sf}})\,, \tag{3.16b}$$

In the used matrix notation, the Ohm's law, obtained also from the Valet-Fert model (see Eq 3.5b) reads

$$\check{\jmath} = -\rho(\epsilon_{\mathrm{F}})\check{D}\,\frac{\partial\check{\bar{\mu}}}{\partial x}\,, \tag{3.17}$$

where $\rho(\epsilon_{\mathrm{F}})$ is the density of states at the Fermi level per spin. When the quantization axis is parallel to the local spin polarization one can write $\check{\jmath}$ in the form

$$\check{\jmath} = \frac{1}{2}\,(j_0\check{1} + j_z\check{\sigma}_z) \tag{3.18}$$

where $j_0 = j_\uparrow + j_\downarrow$ and $j_z = j_\uparrow - j_\downarrow$ are charge and z-component of spin current, respectively. One simply finds that

$$\frac{1}{\rho(\epsilon_{\mathrm{F}})}\,j_0 = -C(D_\uparrow + D_\downarrow)\,, \tag{3.19}$$

and

$$\frac{1}{\rho(\epsilon_{\mathrm{F}})}\,j_z = -C(D_\uparrow - D_\downarrow) - \frac{2\tilde{D}}{l_{\mathrm{sf}}}\,[A\exp(x/l_{\mathrm{sf}}) - B\exp(-x/l_{\mathrm{sf}})]\,, \tag{3.20}$$

where

$$\tilde{D} = 2\frac{D_\uparrow D_\downarrow}{D_\uparrow + D_\downarrow}\,. \tag{3.21}$$

3.2.2 Nonmagnetic layer

In a non-magnetic layer, electrons' spins are not aligned along one direction. Hence, spin accumulation and spin currents have to be considered as general three-dimensional vectors in the spin space. Consequently, the electrochemical potentials are written as

$$\check{\bar{\mu}} = \bar{\mu}_0 \check{1} + \boldsymbol{g} \cdot \check{\boldsymbol{\sigma}} \,, \tag{3.22}$$

where $\boldsymbol{g} = (g_x, g_y, g_z)$ and $\check{\boldsymbol{\sigma}} = (\check{\sigma}_x, \check{\sigma}_y, \check{\sigma}_z)$ is vector of Pauli matrices. For the latter equation we can write

$$\bar{\mu}_0 = Cx + G \,, \tag{3.23a}$$
$$\boldsymbol{g} = \boldsymbol{A} \exp(x/l_{\mathrm{sf}}) + \boldsymbol{B} \exp(-x/l_{\mathrm{sf}}) \tag{3.23b}$$

with $\boldsymbol{A} = (A_x, A_y, A_z)$, and $\boldsymbol{B} = (B_x, B_y, B_z)$ Analogically, for the current we can write

$$\check{\jmath} = \frac{1}{2}(j_0 \check{1} + \boldsymbol{j} \cdot \check{\boldsymbol{\sigma}}) \,, \tag{3.24}$$

where

$$\frac{1}{\rho(\epsilon_{\mathrm{F}})} j_0 = -2CD \,, \tag{3.25}$$

and

$$\frac{1}{\rho(\epsilon_{\mathrm{F}})} \boldsymbol{j} = -\frac{2D}{l_{\mathrm{sf}}} \left[\boldsymbol{A} \exp(x/l_{\mathrm{sf}}) - \boldsymbol{B} \exp(-x/l_{\mathrm{sf}})\right] \,, \tag{3.26}$$

where, for a nonmagnetic material $D_\uparrow = D_\downarrow \equiv D$.

3.3 Transport though an interface

The general solutions of the spin diffusion equation in a magnetic and nonmagnetic layers depend on the parameters A ($\boldsymbol{A}$), B ($\boldsymbol{B}$), C, and G, which have to be determined from the appropriate boundary conditions. In a metallic multilayer the boundary conditions are given by the transport properties of the non-magnet/magnet (N/F) interfaces together with the asymptotic behaviour in the the semi-infinite nonmagnetic electrodes. In general, the parameters are different in each layer, however, parameters in each layer depend on both interfaces. Hence, all the parameters have to be determined together from a consistent set of equations which shall be introduced here. But first, we shall describe in short the spin dependent transport through a N/F interface following the study by Brataas et al [55].

In case of collinear magnetic configuration the spin-dependent transport through an interface is simply described by spin-dependent conductivities, $G_\uparrow$, and $G_\downarrow$. However, when the incident spin current is not collinear with the magnetization, an additional parameter, so called *mixing conductance* ($G_{\uparrow\downarrow}$), has to be introduced to completely describe the transport [55]. To define all the interfacial conductances we consider a N/F interface.

The spin current in a normal metal, defined by (3.24), explicitly reads

$$\check{\jmath} = \frac{1}{2} \begin{pmatrix} j_0 + j_z & j_x - ij_y \\ j_x + ij_y & j_0 - j_z \end{pmatrix} = \frac{1}{2} \begin{pmatrix} j_\uparrow & j_x - ij_y \\ j_x + ij_y & j_\downarrow \end{pmatrix} \,. \tag{3.27}$$

When the spins in N are collinear with the magnetization in F, the spin current is diagonal, $\check{j} = \begin{pmatrix} j_\uparrow & 0 \\ 0 & j_\downarrow \end{pmatrix}$, and the spin-dependent conductivities might be expressed by the Landauer formula as[6]

$$G_\uparrow = \frac{e^2}{h}\mathcal{T}_\uparrow\,, \qquad G_\downarrow = \frac{e^2}{h}\mathcal{T}_\downarrow\,, \tag{3.28}$$

where $\mathcal{T}_\uparrow$ and $\mathcal{T}_\downarrow$ are the transmission probabilities given by[7]

$$\mathcal{T}_\uparrow = 1 - \mathcal{R}_\uparrow = 1 - r_\uparrow (r_\uparrow)^*\,, \tag{3.29a}$$
$$\mathcal{T}_\downarrow = 1 - \mathcal{R}_\downarrow = 1 - r_\downarrow (r_\downarrow)^*\,, \tag{3.29b}$$

where $\mathcal{R}_\uparrow$ and $\mathcal{R}_\downarrow$ are the reflection probabilities given by spin-dependent reflection coefficients $r_\uparrow$ and $r_\downarrow$, which are complex numbers in general. From the Ohm's law one obtains

$$\frac{e^2}{2}\, j_\uparrow = G_\uparrow \left(\bar{\mu}_\uparrow^{\mathrm{F}} - \bar{\mu}_\uparrow^{\mathrm{N}}\right)\,, \tag{3.30a}$$
$$\frac{e^2}{2}\, j_\downarrow = G_\downarrow \left(\bar{\mu}_\downarrow^{\mathrm{F}} - \bar{\mu}_\downarrow^{\mathrm{N}}\right)\,. \tag{3.30b}$$

where $\bar{\mu}_\uparrow^{\mathrm{F}}$ ($\bar{\mu}_\uparrow^{\mathrm{N}}$) and $\bar{\mu}_\downarrow^{\mathrm{F}}$ ($\bar{\mu}_\downarrow^{\mathrm{N}}$) are the electrochemical potentials for the spin majority and spin minority, respectively, at the interface on the ferromagnet (normal metal) side. Recalling the definitions stated above the latter expressions might be rewritten as

$$e^2 j_0 = (G_\uparrow + G_\downarrow)(\bar{\mu}_0^{\mathrm{F}} - \bar{\mu}_0^{\mathrm{N}}) + (G_\uparrow - G_\downarrow)(g_z^{\mathrm{F}} - g_z^{\mathrm{N}})\,, \tag{3.31a}$$
$$e^2 j_z = (G_\uparrow - G_\downarrow)(\bar{\mu}_0^{\mathrm{F}} - \bar{\mu}_0^{\mathrm{N}}) + (G_\uparrow + G_\downarrow)(g_z^{\mathrm{F}} - g_z^{\mathrm{N}})\,, \tag{3.31b}$$

where $\bar{\mu}_0^{\mathrm{F}}$ ($\bar{\mu}_0^{\mathrm{N}}$) and g_z^{F} (g_z^{N}) are electrochemical potential and spin accumulation on the ferromagnet (normal metal) side, respectively.

However, when the spins in N are not parallel to magnetization in F, the transversal spin current components are non-zero. Therefore, we shall write equations analogical to Ohm's law for $j_\uparrow$ and $j_\downarrow$ components (3.30). Since in the magnetic layer no transversal spin accumulation is present, the Ohm's law for j_x and j_y reads

$$\frac{e^2}{2}\,(j_x - i j_y) = -G_{\uparrow\downarrow}\,(g_x - i g_y)\,, \tag{3.32a}$$
$$\frac{e^2}{2}\,(j_x + i j_y) = -G_{\downarrow\uparrow}\,(g_x + i g_y)\,, \tag{3.32b}$$

where $G_{\uparrow\downarrow}$ and $G_{\downarrow\uparrow}$ are the mixing conductances. It has been shown by Brataas et al. [55] that the mixing conductances are complex numbers given by

$$G_{\uparrow\downarrow} = \frac{e^2}{h}\,(1 - r_\uparrow (r_\downarrow)^*)\,, \tag{3.33}$$

[6] In the standard Landauer formula the prefactor is twice of that one used here. This is because in this case we consider two independent spin channels.

[7] In the original paper by Brataas et al. [55] the expressions for $\mathcal{T}_\uparrow$ and $\mathcal{T}_\downarrow$ are slightly different since they assumed M transversal modes in each spin channel. However, for our purposes we need just one mode in each channel ($M = 1$), which simplify the expressions.

and hence $G_{\downarrow\uparrow} = (G_{\uparrow\downarrow})^*$. Consequently, the equations (3.32) lead to

$$e^2 j_x = -2\mathrm{Re}\left\{G_{\uparrow\downarrow}\right\} g_x^{\mathrm{N}} + 2\mathrm{Im}\left\{G_{\uparrow\downarrow}\right\} g_y^{\mathrm{N}}\,, \tag{3.34a}$$

$$e^2 j_y = -2\mathrm{Re}\left\{G_{\uparrow\downarrow}\right\} g_y^{\mathrm{N}} - 2\mathrm{Im}\left\{G_{\uparrow\downarrow}\right\} g_x^{\mathrm{N}}\,. \tag{3.34b}$$

The latter result shows that the mixing conductance affects the transversal spin current components only. Xia et al. [56] shown that in metallic spin valves $\mathrm{Im}\left\{G_{\uparrow\downarrow}\right\}$ is about 10% or less of $\mathrm{Re}\left\{G_{\uparrow\downarrow}\right\}$.

Equations (3.31) together with (3.34) are the boundary conditions required to determine the unknown constants in the expressions for spin currents, spin accumulation and electrochemical potentials. While equations (3.31) describe the transport of the charge and longitudinal (z) component of spin, equations (3.34) are related to transversal spin components. Therefore, the latter equations does not make sense in the collinear magnetic configuration since they reduce to trivial identities.

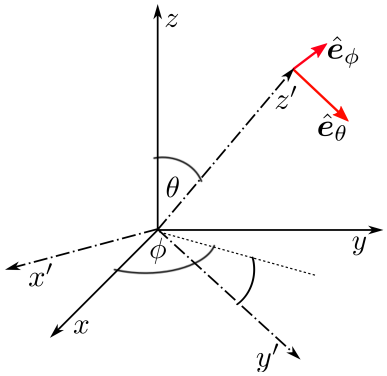

Figure 8: Initial, $O(xyz)$, and rotated, $O(x'y'z')$, coordinate systems. $O(x'y'z')$ is obtained from $O(xyz)$ using rotation transformations given by equations (3.35).

In a magnetic layer there is a natural quantization axis, which is parallel to the magnetization vector. Hence, the spin accumulation and spin currents can be written in a coordinate system with z-axis aligned to the local magnetization. However, in a nonmagnetic layer one has to choose the quantization axis. For simplicity, in a non-magnetic layer we shall choose the local quantization along the magnetization vector of one of the adjacent magnetic layers. For instance, if we consider $\mathrm{F}_1/\mathrm{N}/\mathrm{F}_2$ trilayer, one can consider magnetization of F_1 as a quantization axis in N. Then the spin accumulation and the spin current in N is expressed in the same coordinates as in F_1. However, in general, the net spin moments of F_1 and F_2 are not collinear. Therefore, when writing the boundary conditions for N/F_2 interface, one has to transform spin accumulation and spin current vectors in the N layer from their local coordination system (connected with F_1 spin moment) to the system with z-axis parallel to F_2 magnetization. To do this transformation, one has to know spherical coordinates (θ, ϕ) of net spin moment $\hat{\boldsymbol{s}}$ of F_2 in the F_1 local frame. Then one can do substitution in Eqs. (3.31) and (3.34) as follows [34]:

$$\boldsymbol{g}^{\mathrm{N}} \to \check{\mathrm{R}}_x\left(-\theta\right)\check{\mathrm{R}}_z\left(\phi - \pi/2\right)\boldsymbol{g}^{\mathrm{N}}\,, \tag{3.35a}$$

$$\boldsymbol{j}^{\mathrm{N}} \to \check{\mathrm{R}}_x\left(-\theta\right)\check{\mathrm{R}}_z\left(\phi - \pi/2\right)\boldsymbol{j}^{\mathrm{N}}\,, \tag{3.35b}$$

where $\check{\mathrm{R}}_x\left(\alpha\right)/\check{\mathrm{R}}_z\left(\alpha\right)$ is matrix of rotation by an angle α around the x/z-axis in the counterclockwise direction when looking towards origin of the coordinate system (see appendix B). Explicitly

we can write the transformed spin accumulation as [34]

$$g'_x = g_x^{\mathrm{N}} \sin\phi - g_y^{\mathrm{N}} \cos\phi \,, \tag{3.36a}$$
$$g'_y = \left(g_x^{\mathrm{N}} \cos\phi + g_y^{\mathrm{N}} \sin\phi\right) \cos\theta - g_z^{\mathrm{N}} \sin\theta \,, \tag{3.36b}$$
$$g'_z = \left(g_x^{\mathrm{N}} \cos\phi + g_y^{\mathrm{N}} \sin\phi\right) \sin\theta + g_z^{\mathrm{N}} \cos\theta \,. \tag{3.36c}$$

Analogically, one can write transformation for $\boldsymbol{j}^{\mathrm{N}}$ vector.

Solving required number of the boundary conditions (3.31) and (3.34) with appropriately transformed $\boldsymbol{j}$ and $\boldsymbol{g}$ vectors one can obtain the spatial variation of spin current, spin accumulation as well as electrochemical potential of any metallic spin valve with noncollinear magnetizations. These variations completely determine the spin-transfer torques acting on the magnetizations in the magnetic layer as well as the spin valve resistance. In further we shall describe how to properly calculate these quantities. The used formalism shall be illustrated on an example of simple trilayer structure.

3.4 Material parameters

The intention of the diffusive transport model was to describe the STT phenomenon in terms of the experimentally measured quantities used also for the theoretical description of the GMR effect in the Valet-Fert model. Therefore, we define the spin-dependent bulk resistivities, $\rho_{\uparrow(\downarrow)}$, and interfacial resistances, $R_{\uparrow(\downarrow)}$, which might be expressed as follows [16, 33]

$$\rho_{\uparrow(\downarrow)} = 2\rho^*(1 \mp \beta) \,, \tag{3.37a}$$
$$R_{\uparrow(\downarrow)} = 2R^*(1 \mp \gamma) \,, \tag{3.37b}$$

where $\rho_{\uparrow(\downarrow)}$ are bulk resistivities for spin-majority (spin-minority) electrons, $R_{\uparrow(\downarrow)}$ are interfacial resistances per unit square for spin-majority (spin-minority), and β and γ are bulk and interfacial spin asymmetry coefficients, respectively. Note, that in a nonmagnet the spin $\uparrow$ and spin $\downarrow$ channels are identical what means that in the given notation $\beta = 0$ and hence $\rho_\uparrow = \rho_\downarrow \equiv \rho = 2\rho^*$. The spin-dependent conductances, used in Eqs. (3.31) and (3.34), might be expressed as $G_\uparrow = 1/R_\uparrow$ and $G_\downarrow = 1/R_\downarrow$. Parameters for different materials and interfaces are collected in the appendix A.

To express all the physical quantities used in the model in terms of the material parameters we describe the conduction electrons with free electron model. Then, the spin diffusion parameters read [57]

$$D_{\uparrow(\downarrow)} = \frac{1}{3} v_{\mathrm{F}} \lambda_{\uparrow(\downarrow)} \,, \tag{3.38}$$

where $\lambda_{\uparrow(\downarrow)}$ is the electron mean free in the majority (minority) spin channel. They are given by

$$\lambda_{\uparrow(\downarrow)} = \frac{m_{\mathrm{e}} v_{\mathrm{F}}}{n_0 e^2 \rho_{\uparrow(\downarrow)}} \,, \tag{3.39}$$

where n_0 is the electron density per spin given by

$$n_0 = \frac{1}{6\pi^2} \left(\frac{2m_{\mathrm{e}}\epsilon_{\mathrm{F}}}{\hbar^2}\right)^{3/2} \,, \tag{3.40}$$

where ϵ_{F} is the Fermi energy. The latter expressions lead to the following relation between the diffusion constants and the resistivities

$$D_{\uparrow(\downarrow)} = \frac{\sqrt{2}\pi^2\hbar^3}{e^2 m_{\mathrm{e}}^{3/2}\epsilon_{\mathrm{F}}^{1/2}} \frac{1}{\rho_{\uparrow(\downarrow)}} \,. \tag{3.41}$$

Consequently, the polarization parameter, η, introduced in Eq. (3.12b) and appearing in the solution for spin-dependent electrochemical potentials (3.14) might be rewritten as

$$\eta = -\frac{D_\uparrow - D_\downarrow}{D_\uparrow + D_\downarrow} = -\frac{\rho_\uparrow - \rho_\downarrow}{\rho_\uparrow + \rho_\downarrow} = -\beta \,. \tag{3.42}$$

Apart from this the Fermi level density of states per spin, $\rho(\epsilon_{\mathrm{F}})$, which appears in the expression of particle and spin currents, is in the free electron model given by

$$\rho(\epsilon_{\mathrm{F}}) = \frac{1}{4\pi^2}\left(\frac{2m}{\hbar^2}\right)^{3/2} \epsilon_{\mathrm{F}}^{1/2} \,. \tag{3.43}$$

This allow us directly evaluate the parameters C in a ferromagnetic as well as in a nonmagnetic layer, respectively:

$$C = -\frac{j_0}{\rho(\epsilon_{\mathrm{F}})\,(D_\uparrow + D_\downarrow)} = -e^2 \frac{\rho_\uparrow \rho_\downarrow}{\rho_\uparrow + \rho_\downarrow} j_0 = -e^2 \rho^* (1-\beta^2) j_0 \,, \tag{3.44a}$$

$$C = -\frac{j_0}{2\rho(\epsilon_{\mathrm{F}}) D} = -e^2 \rho^* j_0 \,. \tag{3.44b}$$

3.5 Spin-transfer torque

Knowledge of spin currents allows us to define spin transfer torque acting on the magnetizations in a metallic multilayer. As explained in the introduction, the spin transfer torque acting in a magnetic layer is proportional to the transversal components of the spin current, $\boldsymbol{j}_\perp$, which are absorbed in the ferromagnetic layer. Hence, we define the spin transfer torque as a difference between the transversal components of the spin current on the left ($\boldsymbol{j}_{\perp\mathrm{L}}$) and right ($\boldsymbol{j}_{\perp\mathrm{R}}$) N/F interface taken on their nonmagnetic sides [33]:

$$\boldsymbol{\tau} = \frac{\hbar}{2}\left(\boldsymbol{j}_{\perp\mathrm{L}} - \boldsymbol{j}_{\perp\mathrm{R}}\right) . \tag{3.45}$$

To have a non-zero transversal spin current one needs at least two magnetic layers with non-collinear magnetization separated by a nonmagnet. Therefore, let us consider a trilayer $\mathrm{F_1/N/F_2}$ with the net spin moment $\hat{\boldsymbol{S}}$ in $\mathrm{F_1}$ (fixed layer) and $\hat{\boldsymbol{s}}$ in $\mathrm{F_2}$ (free layer). In general, the torque acting on $\hat{\boldsymbol{s}}$ in the plane defined by both spin moment vectors can be written as [33]

$$\boldsymbol{\tau}_\parallel = aI\, \hat{\boldsymbol{s}} \times (\hat{\boldsymbol{s}} \times \hat{\boldsymbol{S}}) \,, \tag{3.46}$$

where $I = ej_0$ is applied current density and a is a parameter, which generally depends on the angle between $\hat{\boldsymbol{s}}$ and $\hat{\boldsymbol{S}}$ and modifies STT amplitude. As shall be shown, parameter a can be evaluated from the spin current. Note, that transformations (3.35) are tailored so that y-axis of the rotated coordinate system lies in the plane defined by magnetization vectors of $\mathrm{F_1}$ and $\mathrm{F_2}$,

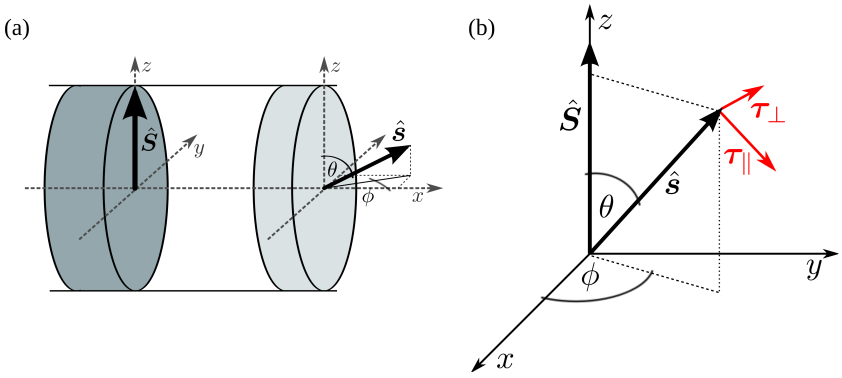

Figure 9: (a) Spin valves with spherical coordinates of $\hat{\boldsymbol{s}}$. (b) Spherical coordinates of $\hat{\boldsymbol{s}}$ and STT components $\boldsymbol{\tau}_{\parallel}$ and $\boldsymbol{\tau}_{\perp}$.

and x-axis is perpendicular to that plane. In other words, y-axis of rotated coordinate system is parallel to $\hat{\boldsymbol{s}} \times (\hat{\boldsymbol{s}} \times \hat{\boldsymbol{S}})$ vector while x-axis is aligned with $\hat{\boldsymbol{s}} \times \hat{\boldsymbol{S}}$ vector. Then, one can obtain amplitude of the in-plane component of STT acting on $\hat{\boldsymbol{s}}$ from the y component of the transformed spin current vector [34]

$$\tau_{\parallel} = \frac{\hbar}{2} j'_y \mid_{\mathrm{N/F_2}} = \frac{\hbar}{2} \left(j_x \cos\phi \sin\theta + j_y \sin\phi \cos\theta + j_z \sin\theta\right) \mid_{\mathrm{N/F_2}} , \tag{3.47}$$

where j_x, j_y, and j_z are taken on the non-magnetic side of $\mathrm{N/F_2}$ interface. By comparison of Equations (3.46) and (3.47) one can easily obtain the expression for $a = (\hbar/2) j'_y \mid_{\mathrm{N/F_2}} / (I \sin\theta)$. In addition, the in-plane torque amplitude can be expressed also as a function of spin accumulation

$$\tau_{\parallel} = \frac{\hbar}{\mathrm{e}^2} \left[\mathrm{Re}\left\{G_{\uparrow\downarrow}\right\} g'_y + \mathrm{Im}\left\{G_{\uparrow\downarrow}\right\} g'_x\right] \mid_{\mathrm{N/F_2}} . \tag{3.48}$$

Similarly, one can define the torque component normal to the plane given by $\hat{\boldsymbol{S}}$ and $\hat{\boldsymbol{s}}$ as [33]

$$\boldsymbol{\tau}_{\perp} = bI\, \hat{\boldsymbol{s}} \times \hat{\boldsymbol{S}} . \tag{3.49}$$

Then one can calculate its amplitude as [34]

$$\tau_{\perp} = \frac{\hbar}{2} j'_x \mid_{\mathrm{N/F_2}} = \frac{\hbar}{2} \left(j_x \sin\phi - j_y \cos\phi\right) \mid_{\mathrm{N/F_2}} , \tag{3.50}$$

which implies that $b = (\hbar/2) j'_x \mid_{\mathrm{N/F_2}} / (I \sin\theta)$. Using spin accumulation, $\tau_{\perp}$ could be expressed as

$$\tau_{\perp} = -\frac{\hbar}{\mathrm{e}^2} \left[\mathrm{Re}\left\{G_{\uparrow\downarrow}\right\} g'_x - \mathrm{Im}\left\{G_{\uparrow\downarrow}\right\} g'_y\right] \mid_{\mathrm{N/F_2}} . \tag{3.51}$$

The total STT acting on $\hat{\boldsymbol{s}}$ is the sum of both components $\boldsymbol{\tau} = \boldsymbol{\tau}_{\parallel} + \boldsymbol{\tau}_{\perp}$. In metallic spin valves the amplitude of $\boldsymbol{\tau}_{\perp}$ is usually of about two order smaller than the one of $\boldsymbol{\tau}_{\parallel}$.

Generally, in a magnetic trilayer STT acts not only on the free layer ($\mathrm{F_2}$) but also on the polarizer ($\mathrm{F_1}$). Recently, it has been shown, that dynamics of the polarizer might be of considerable importance for current induced spin dynamics and/or switching [58, 59, 60]. The STT acting in $\mathrm{F_1}$ might be simply determined in frame of presented model. As noticed above, current in N-layer is written in coordinate system with z-axes aligned along $\hat{\boldsymbol{S}}$. However, the y-axis is rotated from the plane defined by both net spin moments by an angle $\phi - \pi/2$. In order to define STT components

analogically to the previous case of $\hat{\boldsymbol{s}}$ spin, we have to write spin current vector in a coordinate system with z-axis aligned along $\hat{\boldsymbol{S}}$ vector, but rotated so that the y-axis lies in the plane defined by $\hat{\boldsymbol{S}}$ and $\hat{\boldsymbol{s}}$. This might be done as $\boldsymbol{j}'' = \check{\mathrm{R}}_z\left(\phi - \pi/2\right)\boldsymbol{j}^{\mathrm{N}}$. Then, the torque acting on $\hat{\boldsymbol{S}}$ can be written as

$$\boldsymbol{\tau}'_{\parallel} = a' I\, \hat{\boldsymbol{S}} \times \left(\hat{\boldsymbol{S}} \times \hat{\boldsymbol{s}}\right), \tag{3.52}$$

the amplitude of which can be calculated as

$$\tau'_{\parallel} = \frac{\hbar}{2}\, j''_y \mid_{\mathrm{F_1/N}} = \frac{\hbar}{2}\, \left(j_x \sin\phi\cos\theta + j_y \sin\phi\cos\theta - j_z \sin\theta\right) \mid_{\mathrm{F_1/N}} . \tag{3.53}$$

Comparing equations (3.52) and (3.53) we can write: $a' = (\hbar/2) j''_y \mid_{\mathrm{F_1/N}} / \sin\theta$. In the same way one can define the out-of-plane torque components, which reads

$$\boldsymbol{\tau}'_{\perp} = b' I\, \hat{\boldsymbol{S}} \times \hat{\boldsymbol{s}}\,. \tag{3.54}$$

Its amplitude reads

$$\tau'_{\perp} = \frac{\hbar}{2}\, j''_x \mid_{\mathrm{F_1/N}} = \frac{\hbar}{2}\, \left(j_x \sin\phi - j_y \cos\phi\right) \mid_{\mathrm{F1/N}}, \tag{3.55}$$

which implies $b' = (\hbar/2) j''_x \mid_{F1/N} / \sin\theta$.

The presented model completely defines STT components acting on the net spin moments in a single metallic spin valve structure, $\mathrm{F_1/N/F_2}$. Analogically, one can define STT acting on the magnetic layers of any metallic spin valve structure.

3.6 CPP magnetoresistance

As mentioned before, in frame of the Valet-Fert model one can calculate the magnetoresistance only in the collinear configuration. An advantage of the present approach is that one can determine magnetoresistance of a spin valve also in a general noncollinear magnetic configuration. This advantage allow us to study the variation of the magnetoresistance in the presence of magnetization precession, which is an important characteristics of spin-torque oscillators [45, 53]. The method of calculation of the CPP magnetoresistance was introduced in the reference [61].

The resistance of i-th layer consists of two part

$$R_i = R_i^{\mathrm{Spl}} + R_i^{\mathrm{SI}}, \tag{3.56}$$

where R_i^{Spl} is the equilibrium two channel resistance of the i-the layer while $R_i^{\mathrm{SI}} = \Delta V_i^{\mathrm{SI}}/I$ is the resistance in the i-the layer related to the spin accumulation. For a nonmagnetic layer ($\beta = 0$), $\Delta V_i^{\mathrm{Spl}} = 2\rho_i^* d_i$, where ρ_i^* is the bulk resistance of i-th layer, and d_i is its thickness. When index i is related to a magnetic layer ($\beta \neq 0$), from the two channel model we have $R_i^{\mathrm{Spl}} = [(1/R_{i\uparrow}) + (1/R_{i\downarrow})]^{-1}$, where $R_{i\sigma} = R_{i\sigma}^{\mathrm{L}} + \rho_{i\sigma} d_i + R_{i\sigma}^{\mathrm{R}}$ (for $\sigma = \uparrow, \downarrow$). Apart from the bulk resistance, $R_{i\sigma}$ includes also the interface resistances of the left ($R_{i\sigma}^{\mathrm{L}}$) and right ($R_{i\sigma}^{\mathrm{L}}$) interface of the magnetic layers.

When the electric voltage is applied along a spin valve, the driving electric field might be expressed as $E(x) = (1/e)(\partial\bar{\mu}_0/\partial x)$. Then $R_i^{\mathrm{SI}} = \Delta V_i^{\mathrm{SI}}/I$ where the voltage drop in the i-th layer is given by [61]

$$\Delta V_i^{\mathrm{SI}} = \int_{i\in d_i} \left[E(x) - E_0\right] \mathrm{d}x\,, \tag{3.57}$$

where E_0 is a constant value taken far from the interface. According to the expressions (3.16a) and (3.23a), the electrochemical potential of any layer might be expressed as, $\bar{\mu}_0 = -\beta g(x) + Cx + G$ since $\beta = 0$ in a nonmagnetic layer. Then the driving field for a layer reads

$$E(x) = -\frac{\beta}{e\, l_{\mathrm{sf}}} \left[A \exp(x/l_{\mathrm{sf}}) - B \exp(-x/l_{\mathrm{sf}})\right] + C\,. \tag{3.58}$$

Evidently, for a nonmagnetic layer $E(x) = C$ is constant. From equation (3.25) C in a nonmagnetic layer can be directly evaluated

$$C = -\frac{j_0}{2\rho(\epsilon_{\mathrm{F}})D}\,, \tag{3.59}$$

which is just related to the constant material parameters and does not vary with the spin accumulation. Hence, one can set $E_0 = -C$, which implies that $\Delta V_i^{\mathrm{SI}} = 0$ in a nonmagnetic layer. Similarly, in a magnetic layer, where

$$C = -\frac{j_0}{\rho(\epsilon_{\mathrm{F}})(D_\uparrow + D_\downarrow)}\,, \tag{3.60}$$

one can set $E_0 = -C$ which leads to

$$E(x) - E_0 = -\frac{\beta}{e\, l_{\mathrm{sf}}} \left[A \exp(x/l_{\mathrm{sf}}) - B \exp(-x/l_{\mathrm{sf}})\right]\,. \tag{3.61}$$

Finally, the voltage drop in a magnetic layer reads [61]

$$\begin{aligned} \Delta V_i^{\mathrm{SI}} = -\frac{\beta}{e} \Big[& A\big(\exp(x_{i\,\mathrm{R}}/l_{\mathrm{sf}}) - \exp(x_{i\,\mathrm{L}}/l_{\mathrm{sf}})\big) + \\ & B\big(\exp(-x_{i\,\mathrm{R}}/l_{\mathrm{sf}}) - \exp(-x_{i\,\mathrm{L}}/l_{\mathrm{sf}})\big) \Big]\,, \end{aligned} \tag{3.62}$$

where $x_{i\,\mathrm{L}}$ and $x_{i\,\mathrm{R}}$ are the positions of left and right interface of the i-th layer, respectively.

The total resistance of a magnetic multilayer is $R = \sum_i R_i$. In a magnetic trilayer with in-plane magnetizations, the angular dependence of the magnetoresistance is expressed as $\Delta R(\theta) = R(\theta) - R(0)$. To calculate the magnetoresistance one needs to calculate ΔV_i^{SI} contributions only. Finally, it is convenient to define the reduced magnetoresistance as

$$r(\theta) = \frac{R(\theta) - R_{\mathrm{P}}}{R_{\mathrm{AP}} - R_{\mathrm{P}}}\,, \tag{3.63}$$

where $R_{\mathrm{P}} = R(\theta = 0)$ and $R_{\mathrm{AP}} = R(\theta = \pi)$.

3.7 Applications

In this subsection the described theory shall be illustrated on several simple metallic systems. First, an elementary problem of an interface between semi-infinite non-magnetic (N) and ferromagnetic (F) layers shall be studied. It shall be shown that the conduction channel in a nonmagnet is splitted close to an N/F interface and spin current appears also in the nonmagnet (spin injection). Secondly, the most simple functional device, an F/N/F metallic trilayer, shall be considered. It shall be shown how layer thicknesses and different materials might change the spin accumulation in the system resulting in different angular dependence of the STT acting on the free layer's magnetization.

3.7.1 Nonmagnet/Ferromagnet interface

Let us first analyze a N/F interface which is located at $x = 0$. Let the nonmagnetic layer spreads on the left hand side of the interface, $x < 0$, while the magnetic layer is on its right hand side, $x > 0$.

Following the solutions of the spin diffusion equation for a nonmagnetic layer we shall write the expressions for electrochemical potential, spin accumulation, and spin and particle currents, respectively:

$$\bar{\mu}_0^{\mathrm{N}} = C_{\mathrm{N}}\, x + G_{\mathrm{N}}\,, \tag{3.64a}$$

$$g_z^{\mathrm{N}} = A_{\mathrm{N}} \exp(x/l_{\mathrm{sf}}^{\mathrm{N}}) + B_{\mathrm{N}} \exp(-x/l_{\mathrm{sf}}^{\mathrm{N}})\,, \tag{3.64b}$$

$$\frac{1}{\rho(\epsilon_{\mathrm{F}})}\, j_z^{\mathrm{N}} = -\frac{2D}{l_{\mathrm{sf}}^{\mathrm{N}}} \left[A_{\mathrm{N}} \exp(x/l_{\mathrm{sf}}^{\mathrm{N}}) - B_{\mathrm{N}} \exp(-x/l_{\mathrm{sf}}^{\mathrm{N}})\right]\,, \tag{3.64c}$$

$$\frac{1}{\rho(\epsilon_{\mathrm{F}})}\, j_0 = -2C_{\mathrm{N}} D\,. \tag{3.64d}$$

Here, A_{N}, B_{N}, C_{N}, and G_{N} are unknown parameters which are to be evaluated. Because in this system we have only one magnetic layer the transversal components of spin accumulation and spin current are zero: $g_x = g_y = 0$, $j_x = j_y = 0$. As shown before (see Eq. 3.44), from the latter equation in the set we can directly evaluate parameter $C_{\mathrm{N}} = -e^2\rho_{\mathrm{N}}^* j_0$. Furthermore, because the nonmagnetic layer is semi-infinite we require to have finite values of spin accumulation and spin current for $x \to \infty$ and hence $B_{\mathrm{N}} = 0$. Additionally, we can set the zero point of the electrochemical potential at the interface what means that $G_{\mathrm{N}} = 0$ as well. Consequently, calling equations (3.41) and (3.43) we obtain

$$\bar{\mu}_0^{\mathrm{N}} = -e^2\rho_{\mathrm{N}}^*\, j_0\, x\,, \tag{3.65a}$$

$$g_z^{\mathrm{N}} = A_{\mathrm{N}} \exp(x/l_{\mathrm{sf}}^{\mathrm{N}})\,, \tag{3.65b}$$

$$j_z^{\mathrm{N}} = -\frac{1}{e^2\rho_{\mathrm{N}}^*\, l_{\mathrm{sf}}^{\mathrm{N}}}\, A_{\mathrm{N}} \exp(x/l_{\mathrm{sf}}^{\mathrm{N}})\,. \tag{3.65c}$$

Analogically, for the ferromagnetic part we can write

$$\bar{\mu}_0^{\mathrm{F}} = -\beta \left[A_{\mathrm{F}} \exp(x/l_{\mathrm{sf}}^{\mathrm{F}}) + B_{\mathrm{F}} \exp(-x/l_{\mathrm{sf}}^{\mathrm{F}})\right] + C_{\mathrm{F}}\, x + G_{\mathrm{F}}\,, \tag{3.66a}$$

$$g_z = A_{\mathrm{F}} \exp(x/l_{\mathrm{sf}}^{\mathrm{F}}) + B_{\mathrm{F}} \exp(-x/l_{\mathrm{sf}}^{\mathrm{F}})\,, \tag{3.66b}$$

$$\frac{1}{\rho(\epsilon_{\mathrm{F}})}\, j_z^{\mathrm{F}} = -C_{\mathrm{F}}(D_\uparrow - D_\downarrow) - \frac{2\tilde{D}}{l_{\mathrm{sf}}^{\mathrm{F}}} \left[A_{\mathrm{F}} \exp(x/l_{\mathrm{sf}}^{\mathrm{F}}) - B_{\mathrm{F}} \exp(-x/l_{\mathrm{sf}}^{\mathrm{F}})\right]\,, \tag{3.66c}$$

$$\frac{1}{\rho(\epsilon_{\mathrm{F}})}\, j_0 = -C_{\mathrm{F}}\,(D_\uparrow + D_\downarrow)\,. \tag{3.66d}$$

According to the latter equation $C_{\mathrm{F}} = -e^2\rho_{\mathrm{F}}^*(1-\beta^2) j_0$ (see Eq. 3.44). Moreover, the requirement of converge of g_z^{F} and j_z^{F} for $x \to \infty$ implies that $A_{\mathrm{F}} = 0$, and therefore

$$\bar{\mu}_0^{\mathrm{F}} = -\beta B_{\mathrm{F}} \exp(-x/l_{\mathrm{sf}}) - e^2\rho_{\mathrm{F}}^*(1-\beta^2) j_0\, x + G_{\mathrm{F}} \tag{3.67}$$

Making use of the free electron model we obtain

$$g_z^{\mathrm{F}} = B_{\mathrm{F}} \exp(-x/l_{\mathrm{sf}}^{\mathrm{F}})\,, \tag{3.68a}$$

$$j_z^{\mathrm{F}} = \beta j_0 + \frac{1}{e^2\rho_{\mathrm{F}}^*\, l_{\mathrm{sf}}^{\mathrm{F}}}\, B_{\mathrm{F}} \exp(-x/l_{\mathrm{sf}}^{\mathrm{F}})\,. \tag{3.68b}$$

Finally, just three unknown parameters appear in the previous equations: A_N, B_F, and G_F. To evaluate them we use the first pair of the boundary conditions (3.31) at the interface ($x = 0$). Additionally, to reduce the number of the unknown parameters to the number of the boundary equations we use the fact that the longitudinal component of the spin current passes the interface without any change, i.e. $j_z^\mathrm{N}(x = 0) = j_z^\mathrm{F}(x = 0)$, which leads to

$$A_\mathrm{N} = -\beta e^2 \rho_\mathrm{N}^* \, l_\mathrm{sf}^\mathrm{N} j_0 - \frac{\rho_\mathrm{N}^* \, l_\mathrm{sf}^\mathrm{N}}{\rho_\mathrm{F}^* \, l_\mathrm{sf}^\mathrm{F}} B_\mathrm{F} \, . \tag{3.69}$$

Hence, from equations (3.31) we obtain

$$\begin{aligned} &e^2 \left[1 - \beta \left(G_\uparrow - G_\downarrow\right) \rho_\mathrm{N}^* \, l_\mathrm{sf}^\mathrm{N}\right] j_0 = \\ &\quad \left[\left(\frac{\rho_\mathrm{N}^* \, l_\mathrm{sf}^\mathrm{N}}{\rho_\mathrm{F}^* \, l_\mathrm{sf}^\mathrm{F}} + 1 - \beta\right) G_\uparrow - \left(\frac{\rho_\mathrm{N}^* \, l_\mathrm{sf}^\mathrm{N}}{\rho_\mathrm{F}^* \, l_\mathrm{sf}^\mathrm{F}} + 1 + \beta\right) G_\downarrow\right] B_\mathrm{F} \, + \left(G_\uparrow + G_\downarrow\right) G_\mathrm{F} \, , \end{aligned} \tag{3.70a}$$

$$\begin{aligned} &e^2 \beta \left[1 - \left(G_\uparrow + G_\downarrow\right) \rho_\mathrm{N}^* \, l_\mathrm{sf}^\mathrm{N}\right] j_0 = \\ &\quad \left[-\beta \left(G_\uparrow - G_\downarrow\right) - \frac{1}{\rho_\mathrm{F}^* \, l_\mathrm{sf}^\mathrm{F}}\right] B_\mathrm{F} \, + \left(G_\uparrow - G_\downarrow\right) G_\mathrm{F} \, , \end{aligned} \tag{3.70b}$$

Solving these two equation we can obtain the unknown parameters in the form

$$B_\mathrm{F} = \frac{e^2 j_0}{F} \left\{ R_\mathrm{F} \left(1 - \gamma^2\right) \left[R^* \left(\gamma - \beta\right) + \beta R_\mathrm{N}\right] \right\} , \tag{3.71a}$$

$$\begin{aligned} G_\mathrm{F} = \frac{e^2 j_0}{F} \Big\{ &\left[R^* \left(1 - \gamma^2\right)\right]^2 - R^* R_\mathrm{F} \beta \left(\beta + 2\gamma\right) \left(1 - \gamma^2\right) \\ &- \beta R_\mathrm{N} \left[\gamma \left(R_\mathrm{N} + R_\mathrm{F}\right) - R_\mathrm{F} \beta \left(1 - \gamma^2\right)\right] \Big\} , \end{aligned} \tag{3.71b}$$

where we already substituted $G_\uparrow$ and $G_\downarrow$ by R^* and γ as given in (3.37). Moreover, we used $R_\mathrm{N} = \rho_\mathrm{N}^* \, l_\mathrm{sf}^\mathrm{N}$ and $R_\mathrm{F} = \rho_\mathrm{F}^* \, l_\mathrm{sf}^\mathrm{F}$. The denominator in both expression is

$$F = R^* \left(1 - \gamma^2\right) + \gamma^2 \left(R_\mathrm{F} + R_\mathrm{N}\right) \, . \tag{3.72}$$

Consequently, from equation (3.69) we obtain

$$A_\mathrm{N} = -\frac{e^2 j_0}{F} \left\{ R_\mathrm{N} \left[R^* \gamma \left(1 - \gamma^2\right) + \beta \left(\gamma^2 R_\mathrm{F} + R_\mathrm{N}\right)\right] \right\} . \tag{3.73}$$

Knowing the three parameters, the spin-dependent transport through the N/F interface is completely described.

Let us now, making use of the obtained results, inspect the Cu/Co interface. The used material parameters are given in the appendix A. The spin flip length of Cu has been chosen as $l_\mathrm{sf}^\mathrm{N} = 300\,\mathrm{nm}$ while in the Co layer it is $l_\mathrm{sf}^\mathrm{F} = 60\,\mathrm{nm}$. Figure 10(a) shows the quantities defined by equations (3.64) and (3.66) in both nonmagnetic and magnetic layer close to their interface. In the plots of electrochemical potential ($\bar{\mu}_0$) and spin accumulation (g_z) we set $j_0 = 1$. The quantities are depicted in the global frame with z axis parallel to the magnetization of the F layer. As the pictures show, when the electrons flow from N to F layer, the spin accumulation builds up in the interface vicinity: because the $R_\uparrow < R_\downarrow$ and $\rho_\uparrow < \rho_\downarrow$ the spin $\uparrow$ electrons passes the interface and enter the F layer easier than spin $\downarrow$ electrons. Hence the $\downarrow$ spins are accumulated in the

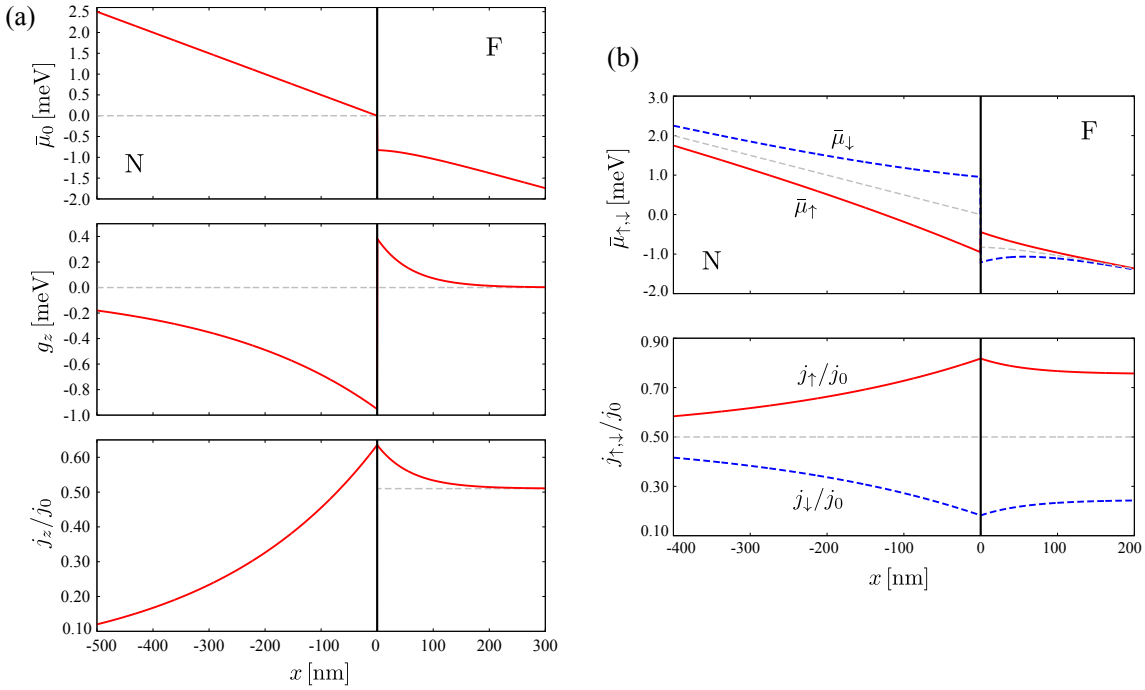

Figure 10: Spin-dependent transport through a Cu/Co interface. (a) Spatial dependence of the electrochemical potential ($\bar{\mu}_0$), spin accumulation (g_z), and spin current (j_z) normalized to the total particle current (j_0) in the connected Cu and Co layers close to their interface. (b) Spatial dependence of electrochemical potentials and normalized currents for the spin majority ($\uparrow$) and spin minority ($\downarrow$) in the Cu and Co layers close to their interface.

left hand side of the N/F while on its right hand side a depopulation of $\uparrow$ spins occurs. As the electrons departs from the interface, the spin accumulation decays in the N as well as in the F layer. However, because the spin-flip length in the Cu layer is longer than in the Co layer, the spin accumulation decreases slower on the left-hand side of the interface. As a consequence of spin accumulation, a spin-polarized current appears in the N layer, which decreases to zero with the distance from the interface. Oppositely, in the F layer the current polarization decreases to βj_0. Fig. 10(b) shows the spin-dependent electrochemical potentials defined as $\bar{\mu}_{\uparrow(\downarrow)} = \bar{\mu}_0 \pm g$. In agreement with the spatial dependence of spin accumulation, the potential splitting is maximal at the interface and decreases with the distance, $|x|$. In addition, the electron current in $\uparrow$ and $\downarrow$ spin channels is shown there. In the nonmagnet, $j_\uparrow$ and $j_\downarrow$ with the distance from the interface approaches their common equilibrium value $j_\uparrow = j_\downarrow = j_0/2$ with zero spin current, $j_z = 0$. In the magnetic layer, the currents in the spin channel remain different also far from the interface.

3.7.2 Magnetic trilayers

Let us now analyze spin-dependent transport in magnetic trilayers E_1–F_1/N/F_2–E_2, where F_1 and F_2 are magnetic layers separated by a nonmagnetic spacer, N. The trilayer structure is sandwiched between semi-infinite nonmagnetic electrodes, E_1 and E_2. As it was shown on the previous example, to describe the transport through a N/F interface we need to adjust 3 parameters which might be easily obtained analytically. Similarly, a magnetic layer between nonmagnetic electrodes can be described using 6 parameters which have to be found. However, the calculations become more complicated since in the central N layer spin accumulation and spin current are generally three-

component vectors described by 7 parameters (see. Eqs. (3.23b) and (3.24)), which are non-zero in general. As in the previous example, for electrodes E_1 (E_2) spin current and spin accumulation are aligned along F_1 (F_2) net spin moments, therefore $A_y = A_y = B_x = B_y = 0$. To have the electrochemical potential convergent when $x \to -\infty$ in E_1 and $x \to \infty$ in E_2, we set $B_z = 0$ in E_1 and $A_z = 0$ in E_2 as well. Moreover, the parameter G expresses just a constant shift of electrochemical potential and could be set to zero in E_1 electrode. Finally, we end up with 16 unknown parameters, which are to be evaluated from the boundary conditions (3.31) and (3.34). Note, if the spin accumulation and spin current in the N layer are written in the local coordinate system of F_1, one has to transform $\boldsymbol{g}^{\mathrm{N}}$ and $\boldsymbol{j}^{\mathrm{N}}$ to the local frame of F_2 as expressed by (3.35), when writing the boundary condition for the N/F_2 interface. Because of the relatively big number of equations to be solved it is more convenient to solve them numerically.

First, we shall study a symmetric trilayer structure with identical F_1 and F_2 layer. In practice, no current-induced dynamics is observed in such device, however, it can give us an insight into the properties of spin-dependent transport through a trilayer. Fig. 11 shows the spacial dependence of

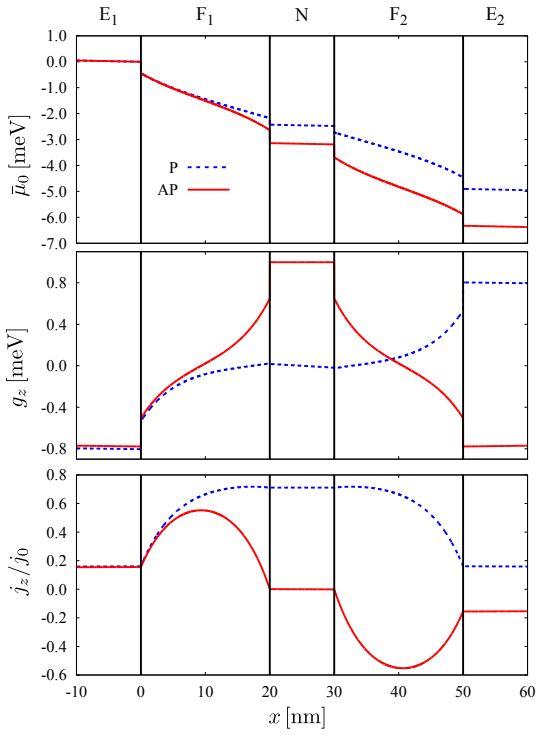

Figure 11: Spin dependent transport through Py(20)/Cu(10)/Py(20) spin valve in collinear magnetic configurations: parallel (dashed line) and anti-parallel (solid line). Spin accumulation, g_z, and spin current, j_z, is shown in the local frame of F_1.

electrochemical potential, spin accumulation and spin current in Py(20)/Cu(10)/Py(20) spin valve in the collinear magnetic configurations, parallel (P) and antiparallel (AP), which is sandwiched between semi-infinite Cu electrodes. Here, Py = $Ni_{20}Fe_{20}$ is Permalloy. The numbers in the brackets express the layer thicknesses in nanometers. The bulk and interfacial parameters used in the calculations are given in the appendix A. The spin-flip length in Cu was considered as large as $l_{\mathrm{sf}}(\mathrm{Cu}) = 1\,\mu m$. In case of parallel configuration, the spin accumulation profile is antisymmetric with respect to the central symmetry axes of the device. The spin $\uparrow$ electrons easily pass both magnetic layers and hence the spin accumulation in the central N layer is almost zero. Oppositely,

in case of AP configuration, the spin accumulation profile is symmetric. It increases in the F_1, which is more transparent for spin $\uparrow$ electrons, however decreases in F_2, in which spin $\downarrow$ electrons have higher mobility than spin $\uparrow$ ones. As a consequence, high spin accumulation is induced in the N layer. This is also in agreement with the fact that the drop in electrochemical potential, $\bar{\mu}_0$, between E_1/F_1 and F_2/E_2 interfaces is bigger in the AP configuration than in the P one provided that current density is the same in both cases ($I = ej_0 = \text{const.}$). In opposite to g_z, the profile of spin current, j_z, is symmetric in the P configuration, but antisymmetric in the AP one. This is related with the fact that the current flowing through a magnetic material is polarized in agreement with the local net spin moment direction.

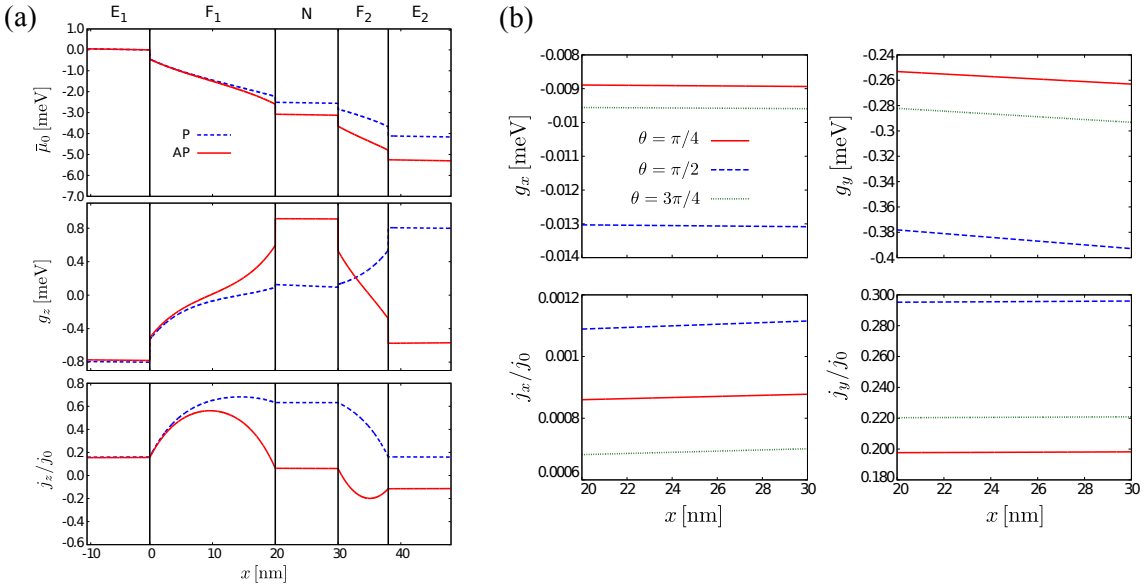

Figure 12: Spin dependent transport through Py(20)/Cu(10)/Py(8) spin valve. (a) electrochemical potential, spin accumulation and spin current in the collinear magnetic configurations, (b) spin accumulation and spin current in the N layer calculated at noncollinear configurations, where θ is the relative angle between F_1 and F_2 net spin moments.

In practice, devices used for spin-torque experiments are constructed in a way that magnetization dynamics of one layer can be neglected while the second one is free to rotate in any direction. This effect might be simply achieved when the thicknesses of the magnetic layers are different. Therefore, we shall consider an asymmetric spin valve with F_1 and F_2 made of the same material, but having different thicknesses. Namely, we shall inspect a Py(20)/Cu(10)/Py(8) trilayer sandwiched between Cu electrodes, as in the previous case. In such a device, F_1 might be considered as fixed layer while F_2 as the free one. Fig. 12(a) depicts the spatial dependence of electrochemical potential, spin accumulation and spin current in collinear, P and AP, configurations. The spatial dependence of all three quantities are similar to the previous case, however, because of different layer thicknesses their profiles became asymmetric. Additionally, we depicted the spacial variation of transversal spin accumulation and spin current components (see Fig. 12(b)), which are non-zero when the magnetizations in F_1 and F_2 are noncollinear. Here we considered the relative angle between their net spin moments to be $\theta = \pi/4, \pi/2$, and $3\pi/4$. The amplitudes of the transversal components of spin accumulation and spin currents are important since they determine the STT amplitude (see Eq. 3.45). Therefore, one should notice that $|g_y| \gg |g_x|$ as well as $|j_y| \gg |j_x|$, what implies that $|\boldsymbol{\tau}_{\parallel}| \gg |\boldsymbol{\tau}_{\perp}|$. Moreover, the figures show that all quantities are far more higher when

the two magnetizations are perpendicular than at $\theta = \pi/4$ or $3\pi/4$. Figure 13(a) shows the STT

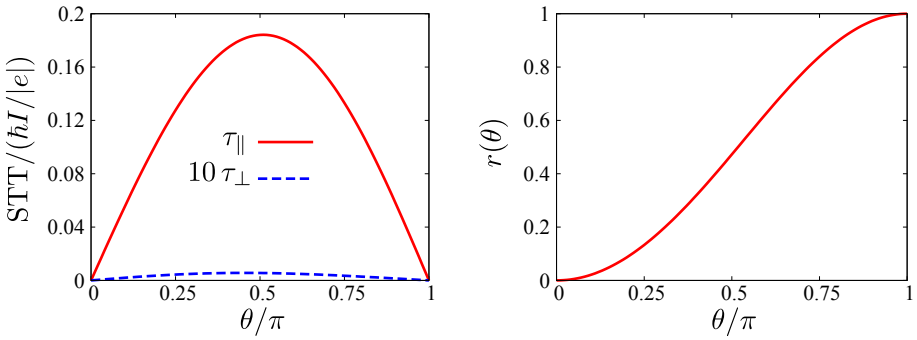

Figure 13: Angular dependence of spin transfer torque (a) and reduced magnetoresistance (b) as a function of relative angle between F_1 and F_2 net spin moments.

as a function of relative angle between the net spin moments of F_1 and F_2. The amplitude of the in-plane STT component is of about two orders higher than of the out-of-plane one. The angular dependence of $\tau_{\|}$ is rather symmetric with maximum at $\theta = \pi/2$ and zero in the collinear configurations, $\theta = 0$, and π. In addition, following the method described above, one might inspect the angular dependence of the magnetoresistance. The reduced magnetoresistance defined by (3.63) of the studied spin valve is shown in Fig. 13(b). It shows that the magnetoresistance monotonously increases with the angle θ.

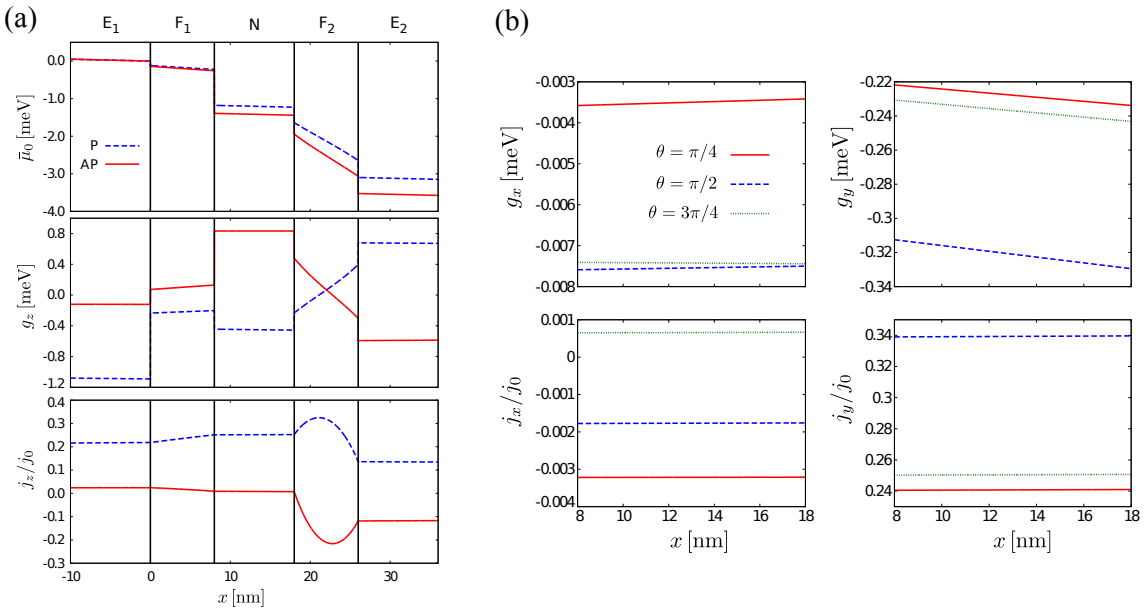

Figure 14: Spin dependent transport through Co(8)/Cu(10)/Py(8) spin valve. (a) electrochemical potential, spin accumulation and spin current in the collinear magnetic configurations, (b) spin accumulation and spin current in the N layer calculated at noncollinear configurations, where θ is the relative angle between F_1 and F_2 net spin moments.

Another way of construction of spin-torque-switchable devices is to use magnetic layers of different materials. If the magnetocrystalline anisotropy of one of them is stronger than that of the second one, it can be considered as the fixed layer even if the thicknesses of both layers are comparable. This condition is fulfilled in Co(8)/Cu(10)/Py(8), where the uniaxial anisotropy in

Co layer is of an order of magnitude higher than that in the Py one. Fig. 14(a) shows the quantities characteristic for the spin-dependent transport in this device. On one hand side, one can see the the variation of spin accumulation in F_1 (Co) layer is rather mild in comparison to the F_2 (Py) layer. Similarly, the spin current reaches higher values in F_2 than in F_1. This appears because the spin asymmetry, β, in cobalt is smaller than in permalloy (see appendix A). On the other hand, the decay of spin accumulation and spin current in the Py layer is faster than in the Co one, because the spin diffusion length in cobalt is of an order larger than in permalloy. These differences of F_1 and F_2 lead to a non-standard angular dependence of STT and magnetoresistance shown in Fig. 15. Oppositely to the Py/Cu/Py spin valve, the STT angular dependence has the zero

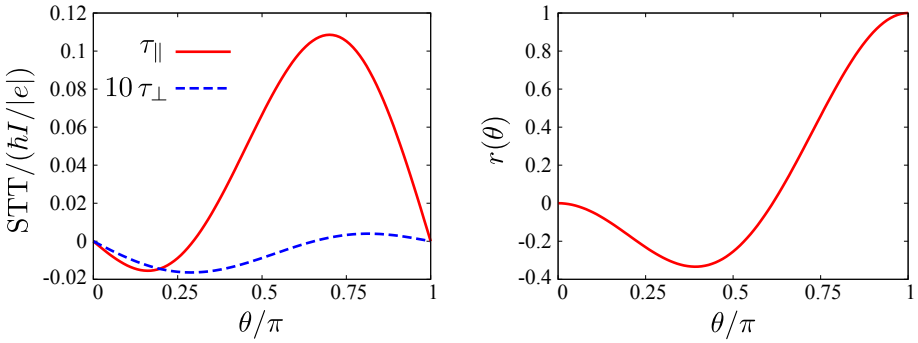

Figure 15: Angular dependence of spin transfer torque (a) and reduced magnetoresistance (b) as a function of relative angle between F_1 and F_2 net spin moments.

points not only in the collinear configuration (for $\theta = 0$ and π) but also in a certain non-collinear configurations, in which the STT vector changes its direction. As shall be shown in section 7 this difference has an important impact on the current induced dynamics of the Py magnetization. Similarly to the Py/Cu/Py trilayer, the out-of-plane STT component, $\tau_\perp$ is of about two orders smaller than the in-plane one, $\tau_\parallel$. Furthermore, the normalized magnetoresistance, $r(\theta)$ becomes negative, what implies that the minimum of magnetoresistance is not in the parallel magnetic configuration, as before, but in a certain noncollinear magnetization ordering. However, as in the standard spin valves, the relation $R_P < R_{AP}$ is still fulfilled.

Later on, making use of the results obtained in this part we shall study the current induced dynamics in both Py(20)/Cu(10)/Py(8) and Co(8)/Cu(10)/Py(8) spin valves. The differences between standard STT and wavy-like angular dependence shall be pointed out and their possible technological applications shall be discussed.

In summary, described procedure of calculation of electrochemical potential, spin accumulation and spin currents can be applied for an arbitrary number of layers. However, the number of unknown parameters, and hence the computational requirements, increase with the number of layers. Generally, a multilayer with n magnetic layers has $n-1$ nonmagnetic spacers and 2 electrodes. Each magnetic layer contributes with 3 and each nonmagnetic spacer with 7 unknown parameters. Additionally, left electrode has 1 and right electrode 2 constants to be found. Together there are $N = 10n - 4$ parameters which have to be evaluated. For the studied trilayer $n = 2$ and hence $N = 16$. For a dual spin valve structure, which shall be discussed latter on, $n = 3$ and therefore $N = 26$ parameters have to be determined.

4 Energy of a monodomain magnetic particle

The novel fabrication and experimental techniques allow us to study magnetic properties of solid state on nanometer scale. As the particle size is reduced the exchange interaction becomes more important and usually the uniform mode is preferred. Hence, it is reasonable to consider that such a nanoparticle is uniformly magnetized and its magnetic state might be expressed by a magnetization vector, $\mathbf{M}$.

In case of uniform magnetization the exchange energy remains constant with respect to $\mathbf{M}$ direction and does not contribute to the overall effective field. The most important factors which contribute to the energy of a ferromagnetic particle are the external magnetic field (Zeeman energy), magnetocrystalline anisotropy, and magnetostatic field. When more magnetic particles are considered, one has to take into account also interparticle interactions. Depending on the distance between the particles, one can take into account magnetostatic interparticle interaction (long-range but weak coupling), which can be described in terms of demagnetizing tensor, and exchange interparticle interaction (short-range but strong coupling), which can be described in terms of RKKY coupling.

In this section we shall discuss all these types of energy and their impact on magnetization. In the end of this section we write down a typical energy functional and derive effective magnetic field, which is an important part of magnetization dynamics description.

4.1 Zeeman energy

It can be easily experimentally observed that when a magnetized particle with magnetization $\mathbf{M}$ is located in an external magnetic field, $\mathbf{H}_{\text{ext}}$, the magnetization vector aligns with $\mathbf{H}_{\text{ext}}$ in order to minimize the energy. The energy density of such a uniformly magnetized particle might be written as [62]

$$\varepsilon_Z = -\mu_0 \, \mathbf{M} \cdot \mathbf{H}_{\text{ext}} \, . \tag{4.1}$$

This contribution to the energy is usually called *Zeeman energy*. It is minimal when $\mathbf{M}$ is parallel to $\mathbf{H}_{\text{ext}}$ and maximal when $\mathbf{M}$ is antiparallel to $\mathbf{H}_{\text{ext}}$.

4.2 Magnetocrystalline anisotropy

In magnetism, anisotropy is a dependence of energy of a ferromagnet on the direction of its magnetization. In other words, one can experimentally observe that some directions of magnetization are preferred even if there is no applied external magnetic field. These preferred directions, which are connected with local energy minima, are called *easy axes*. Oppositely, one can observe also directions with energy maxima, which are called *hard axes*.

The most important factors leading to anisotropic behavior in ferromagnet is the crystalline structure. Therefore, we talk about *magnetocrystalline anisotropy*. The primary reason for the magnetocrystalline anisotropy is the spin-orbit interaction [63], which couples electronic spins with the orbital moments. At the surfaces this might lead to an additional term, called surface anisotropy, which dominates in very thin films.

Depending on the symmetry of the lattice cell one can discuss more complex anisotropies (eg. cubic, tetragonal, hexagonal, rhombohedral, etc.). However, in the pillar structures studied

in this thesis we take into account only the *uniaxial anisotropy*. In this case, there is only one preferred direction for magnetization, i.e. one easy axis. Thus, the anisotropic energy is constant with respect to magnetization rotation around the easy axis and depends only on the relative angle between magnetization, $\mathbf{M} = (M_x, M_y, M_z)$, and the easy axis.

To express the anisotropic energy, it is convenient to introduce spherical coordinates where the magnetization direction vector, $\boldsymbol{m} = \mathbf{M}/M_\mathrm{s}$, is given by angles θ and ϕ as follows

$$\begin{aligned} m_x &= M_x/M_\mathrm{s} = \sin\theta\cos\phi\,, \\ m_y &= M_y/M_\mathrm{s} = \sin\theta\sin\phi\,, \\ m_z &= M_z/M_\mathrm{s} = \cos\theta\,. \end{aligned} \tag{4.2}$$

Moreover, without lost of generality, we can assume that the easy axis coincides with the z-axis of the Cartesian coordinate system. Then, we can express the energy density in the case of uniaxial anisotropy as a function of m_z only. In addition, we know that the anisotropic energy is symmetric with respect to the direction. Hence, the energy density is an even function of m_z, which can be expressed as a series with even powers of $\cos\theta$, or, alternatively, $\sin\theta$. Therefore, the energy density in the presence of uniaxial anisotropy reads

$$\varepsilon_\mathrm{ani}(\boldsymbol{m}) = K_0 + K_1\sin^2\theta + K_2\sin^4\theta + K_3\sin^6\theta + \dots\,, \tag{4.3}$$

where $K_0, K_1, \dots$ are anisotropy constants having units of energy density (Jm^{-3}). In further we shall consider that $K_2, K_3, \dots$ are negligible with respect to K_0 and K_1, and we have

$$\varepsilon_\mathrm{ani}(\boldsymbol{m}) = K_0 + K_1\sin^2\theta\,. \tag{4.4}$$

Clearly, when $K_1 > 0$ the energy minima are located on the easy axis for $\theta = 0, \pi$. In this case we talk about *easy axis anisotropy*. Conversely, when $K_1 < 0$ the minima of the energy are reached for $\theta = \pi/2$, when $\mathbf{M}$ lies in the $x - y$ plane. Thus, this case is called *easy plane anisotropy*.

When discussing the problems of magnetization dynamics, it is convenient to include the anisotropy in an indirect way. Namely, we take into account the fact that when magnetization is tilted from the easy axis, magnetic anisotropy acts as a magnetic field trying to align the magnetization again with the easy axis. When magnetization is tilted from the easy axis, the anisotropy field exerts the same torque on $\mathbf{M}$ as the anisotropy itself. On one hand side, this torque is as large as $\mu_0|\mathbf{H}_\mathrm{ani}|M_\mathrm{s}\sin\theta$, where $\mathbf{H}_\mathrm{ani}$ is a magnetic field due to uniaxial anisotropy. On the other hand, the torque can be obtained by differentiating the expression for ε_ani [64],

$$\frac{\mathrm{d}\varepsilon_\mathrm{ani}}{\mathrm{d}\theta} = 2K_1\sin\theta\cos\theta\,. \tag{4.5}$$

Comparing these two torques we obtain that

$$H_\mathrm{ani} = \frac{2K_1}{\mu_0 M_\mathrm{s}}\cos\theta\,, \tag{4.6}$$

where $\cos\theta = \boldsymbol{m}\cdot\hat{\boldsymbol{e}}_\mathrm{ani}$, where $\hat{\boldsymbol{e}}_\mathrm{ani}$ is a unit vector along the easy axis. Thus, the anisotropy field might be written as

$$\mathbf{H}_\mathrm{ani} = H_\mathrm{ani}\,(\boldsymbol{m}\cdot\hat{\boldsymbol{e}}_\mathrm{ani})\;\hat{\boldsymbol{e}}_\mathrm{ani}\,, \tag{4.7}$$

where $H_\mathrm{ani} = (2K_1)/(\mu_0 M_\mathrm{s})$.

4.3 Magnetostatic energy

Consider a spherical ferromagnetic particle with no magnetocrystalline anisotropy. Clearly, there is no preferred direction for magnetization. However, in case of an ellipsoidal particle, magnetization aligns along the longest axis. This effect is called *shape anisotropy*. On the other side, two magnetic particles placed close to each other tend to organize their magnetic moment in order to minimize the overall magnetic energy. Both these effects are caused by *magnetostatic interaction*.

The magnetostatic interaction might be treated in terms of *magnetostatic* or *demagnetization field*, $\mathbf{H}_\mathrm{m}$, which may be described in terms of magnetic potential, Φ_M. It is a nonlocal potential determined by magnetization, which generally depends on the position $\boldsymbol{r}$ as [62]

$$\Phi_M(\boldsymbol{r}) = \frac{1}{4\pi} \int_V \mathbf{M}(\boldsymbol{r}') \cdot \nabla' \left(\frac{1}{|\boldsymbol{r} - \boldsymbol{r}'|} \right) \mathrm{d}\boldsymbol{r}' \tag{4.8}$$

where the integration is performed through the whole volume, V, of the magnetic body; ∇' is derivation with respect to $\boldsymbol{r}'$. If the magnetization of the particle is uniform, $\mathbf{M}(\boldsymbol{r}) = \mathbf{M}$,

$$\Phi_M(\boldsymbol{r}) = \frac{1}{4\pi} \mathbf{M} \cdot \int_V \nabla' \left(\frac{1}{|\boldsymbol{r} - \boldsymbol{r}'|} \right) \mathrm{d}\boldsymbol{r}' \,. \tag{4.9}$$

The magnetostatic field at $\boldsymbol{r}$ is then defined as

$$\mathbf{H}_\mathrm{m} = -\nabla \Phi_M \,. \tag{4.10}$$

To evaluate the magnetostatic field we shall use maxwell equations

$$\nabla \times \mathbf{H}_\mathrm{m} = 0 \,, \tag{4.11a}$$

$$\nabla \cdot \mathbf{B}_\mathrm{m} = 0 \,, \tag{4.11b}$$

where, $\mathbf{B}_\mathrm{m}$ is the magnetic induction generally expressed as $\mathbf{B}_\mathrm{m} = \mu_0(\mathbf{H}_\mathrm{m} + \mathbf{M})$. Hence, from (4.11b) we obtain, that inside a magnetic body ($\mathbf{M} \neq \mathbf{0}$)

$$\nabla \cdot \mathbf{H}_\mathrm{m} = -\nabla \cdot \mathbf{M} \,, \tag{4.12}$$

while outside the body ($\mathbf{M} = \mathbf{0}$) we have

$$\nabla \cdot \mathbf{H}_\mathrm{m} = 0 \,. \tag{4.13}$$

Alternatively, we can rewrite equations (4.12) and (4.13) in terms of Φ_M using (4.10)

$$\Delta \Phi_M = \begin{cases} \nabla \cdot \mathbf{M} & \text{inside magnetic body,} \\ 0 & \text{outside magnetic body,} \end{cases} \tag{4.14}$$

where $\Delta = \nabla^2$. On the boundary of the magnetic particle, the boundary conditions

$$\Phi_M \,|_\mathrm{in} = \Phi_M \,|_\mathrm{out} \,, \tag{4.15a}$$

$$\frac{\partial \Phi_M}{\partial n} \,|_\mathrm{in} = \frac{\partial \Phi_M}{\partial n} \,|_\mathrm{out} + \mathbf{M} \cdot \boldsymbol{n} \tag{4.15b}$$

have to be obeyed. In (4.15), $\boldsymbol{n}$ stands for a unit vector normal to the particle's surface, and $\partial/\partial n$ is derivative with respect to the distance from the surface.

Knowing the magnetostatic field, the magnetostatic energy density is simply given by

$$\varepsilon_\mathrm{m} = -\frac{\mu_0}{2} \mathbf{M} \cdot \mathbf{H}_\mathrm{m} \,. \tag{4.16}$$

4.3.1 General tensor formulation

For a uniformly magnetized body the internal magnetostatic field can be expressed using so called *demagnetization tensor*, $\bar{\boldsymbol{N}}$. When the demagnetization field inside the body is uniform, as in the case of ellipsoidal particle, one can simply write

$$\mathbf{H}_\mathrm{m} = -\bar{\boldsymbol{N}} \cdot \mathbf{M}\,, \tag{4.17}$$

where $\bar{\boldsymbol{N}}$ depends only on principal axes of the ellipsoid. But generally, uniformly magnetized body does not necessarily have a uniform demagnetization tensor. However, it can be shown that even when $\mathbf{H}_\mathrm{m}$ is not uniform one can still write expression (4.17) with $\mathbf{H}_\mathrm{m}$ replaced by a uniform averaged field, $\langle \mathbf{H}_\mathrm{m} \rangle$ [65].

Conversely, when magnetization is not uniform, equation (4.17) fails. Hence, Newell, Williams, and Dunlop [66] generalized the concept of demagnetization tensor and proposed a method for its calculation. Generally, their concept might be applied for both internal and external magnetostatic field. To illustrate their idea, let us consider a volume V', generally different from volume of the magnetized particle, V. The averaged magnetostatic field due to magnetization $\mathbf{M}$ in this volume is

$$\langle \mathbf{H}'_\mathrm{m} \rangle = \frac{1}{V'} \int_{V'} [-\nabla \Phi_M(\boldsymbol{r}'')]\, \mathrm{d}\boldsymbol{r}''\,, \tag{4.18}$$

and one can write equation similar to (4.17),

$$\langle \mathbf{H}'_\mathrm{m} \rangle = -\mathbf{M} \cdot \bar{\boldsymbol{N}}\,. \tag{4.19}$$

where

$$N_{ij} = -\frac{1}{4\pi V'} \int_{V'} \mathrm{d}\boldsymbol{r}'' \int_V \mathrm{d}\boldsymbol{r}' \frac{\partial}{\partial r'_i} \frac{\partial}{\partial r'_j} \left(\frac{1}{|\boldsymbol{r}'' - \boldsymbol{r}'|} \right)\,, \tag{4.20}$$

where we used $\nabla''(1/|\boldsymbol{r}'' - \boldsymbol{r}'|) = -\nabla'(1/|\boldsymbol{r} - \boldsymbol{r}'|)$; r'_i is i-th component of $\boldsymbol{r}'$ vector. If volume V' is also a uniformly magnetized body with magnetization $\mathbf{M}'$, the energy density in the volume V' is

$$\varepsilon_\mathrm{m} = -\frac{\mu_0}{2}\, \mathbf{M} \cdot \bar{\boldsymbol{N}} \cdot \mathbf{M}'\,. \tag{4.21}$$

Tensor $\bar{\boldsymbol{N}}$ is dimensionless and symmetric. Trace of the tensor reads

$$\mathrm{Tr}\bar{\boldsymbol{N}} = -\frac{1}{4\pi V'} \int_{V'} \mathrm{d}\boldsymbol{r}'' \int_V \mathrm{d}\boldsymbol{r}'\, \nabla'^2 \left(\frac{1}{|\boldsymbol{r}'' - \boldsymbol{r}'|} \right)\,. \tag{4.22}$$

Because $\nabla'^2(1/|\boldsymbol{r}'' - \boldsymbol{r}'|) = -4\pi\delta(\boldsymbol{r}'' - \boldsymbol{r})$ [67] the latter double integral expresses the fraction of the volume V', which overlaps the volume of the magnetic particle, V. If the two volumes are identical, $\bar{\boldsymbol{N}}$ is the ordinary demagnetization tensor given by (4.17) with $\mathrm{Tr}\bar{\boldsymbol{N}} = 1$. Usually, in this case $\bar{\boldsymbol{N}}$ is called as *self-demagnetization tensor*. Then the contribution to the energy density of the magnetized particle with volume V is

$$\varepsilon_\mathrm{m} = -\frac{\mu_0}{2}\, \mathbf{M} \cdot \bar{\boldsymbol{N}} \cdot \mathbf{M}\,. \tag{4.23}$$

On the other hand, when V and V' do not overlap, the trace vanishes ($\mathrm{Tr}\bar{\boldsymbol{N}} = 0$) and the tensor can be used to describe the magnetostatic interaction between two separated magnetized particles. Hence, we shall call $\bar{\boldsymbol{N}}$ as *mutual demagnetization tensor* [66].

In addition, the volume integrals in equation (4.20) might be rewritten using Gauss's theorem as

$$\begin{aligned}\bar{\boldsymbol{N}} &= \frac{1}{4\pi V'}\int_{V'} \mathrm{d}\boldsymbol{r}''\,\nabla''\int_{V}\mathrm{d}\boldsymbol{r}'\,\nabla'\left(\frac{1}{|\boldsymbol{r}''-\boldsymbol{r}'|}\right)\\ &= \frac{1}{4\pi V'}\int_{\boldsymbol{S}'}\mathrm{d}\boldsymbol{S}'\int_{\boldsymbol{S}}\frac{\mathrm{d}\boldsymbol{S}}{|\boldsymbol{r}''-\boldsymbol{r}'|}\,,\end{aligned} \tag{4.24}$$

where $\mathrm{d}\boldsymbol{S} = \hat{\boldsymbol{n}}\,\mathrm{d}S$ with $\hat{\boldsymbol{n}}$ being the normal to the surface.

The approach of generalized demagnetization tensor appeared to be very effective method for calculation of the magnetostatic field in case of non-uniformly magnetized bodies since they can be discretized to a set of blocks with uniform magnetization. Then each block can be considered as a separate contribution to the overall magnetostatic field. Since the analytical expression for the demagnetization field is known only for few geometries, the mentioned scheme is also useful for calculating demagnetization tensors for uniformly magnetized bodies of various shapes. The description of the block scheme is given in appendix C.

4.4 Interlayer exchange coupling

In *1986* Grünberg et al. [68] observed for the first time an antiferromagnetic coupling between Fe layers' magnetic moments separated by Cr spacers. Later on, Parking et al. [9, 10] shown that this phenomena occurs with almost any transition metal being the spacer layer. Moreover, they showed that the strength of the coupling constant strongly depends on the spacer's thickness. Namely, it oscillates and changes its sign, i.e. the interaction changes its character from ferromagnetic to antiferromagnetic and vice versa. The amplitude of coupling constant decreases with increasing spacer's width (see Figure 16).

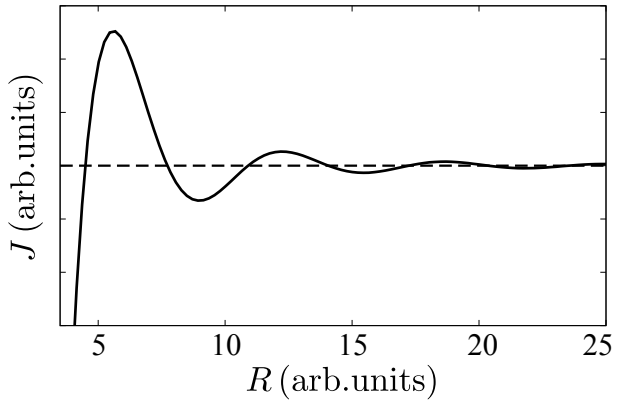

Figure 16: Example of variation of interlayer exchange coupling parameter with spacer width, R.

There are several theories which explain the mechanism of interlayer exchange coupling. One of the most effective theories describes the effect in frame of Ruderman-Kittel-Kasuya-Yosida (RKKY) model [69]. The RKKY model was originally proposed by Ruderman and Kittel [70] to explain the indirect coupling between nuclear spins by means of interaction through conduction

electrons. Later the theory was extended to the case of electronic magnetic moments by Kasuya [71] and Yosida [72]. In this theory, the interaction between conduction electron of spin $\boldsymbol{s}$ and a localized spin $\boldsymbol{S}$ is described by a contact exchange potential [69]

$$V(\boldsymbol{s},\boldsymbol{r}) \equiv A\delta(\boldsymbol{r}-\boldsymbol{R})\,\boldsymbol{s}\cdot\boldsymbol{S}\,, \tag{4.25}$$

where $\boldsymbol{r}$ and $\boldsymbol{R}$ are positions of conduction and localized spins, respectively. Using second-order perturbation theory, one obtains effective interaction between localized spins, $\boldsymbol{S}_i$ and $\boldsymbol{S}_j$,

$$V_{ij} = J(\boldsymbol{R}_{ij})\,\boldsymbol{S}_i\cdot\boldsymbol{S}_j\,, \tag{4.26}$$

where $\boldsymbol{R}_{ij}$ is relative distance between i-th and j-th localized spins. In the free electrons approximation one obtains that $J(\boldsymbol{R}) \propto K(2k_{\mathrm{F}}R)$ [69], where

$$\begin{aligned} K(x) &= \frac{x\cos x - \sin x}{x^4} \\ &\approx \frac{\cos x}{x^3} \text{ for } x\to\infty\,. \end{aligned} \tag{4.27}$$

To account for the interlayer exchange coupling, Yafet [73] considered two dimensional layers with uniform spin distribution. In frame of free electron model he found $J \propto Y(2k_{\mathrm{F}}D)$, where D is the spacer thickness, and

$$\begin{aligned} Y(x) &= \frac{x\cos x - \sin x}{2x^2} - \int_x^\infty \frac{\sin x'}{x'}\mathrm{d}x' \\ &\approx -\frac{\sin x}{x} \text{ for } x\to\infty\,. \end{aligned} \tag{4.28}$$

Later on, Bruno and Chappert studied the RKKY coupling in case of arbitrary Fermi surface [74].

Consider a trilayer structure with two magnetic layers, F_i, with magnetizations $\mathbf{M}_i$ and thicknesses d_i; where $i = 1, 2$. The layers are separated by a thin nonmagnetic spacer. Then, the energy density due to the RKKY coupling in the i-th layer is given by

$$\varepsilon_{\mathrm{RKKY}\,i} = -\frac{J}{d_i\,M_{\mathrm{s}1}M_{\mathrm{s}2}}\,\mathbf{M}_1\cdot\mathbf{M}_2 = -\frac{J}{d_i}\,\boldsymbol{m}_1\cdot\boldsymbol{m}_2\,, \tag{4.29}$$

where J is given in the units of J/m^2. Then the exchange field acting on the i-th layer is given by

$$\mathbf{H}_{\mathrm{RKKY}\,i} = \frac{J}{\mu_0 d_i M_{\mathrm{s}j}}\,\mathbf{M}_j = \frac{J}{\mu_0 d_i}\,\boldsymbol{m}_j\,, \tag{4.30}$$

where $j = 1, 2$ and $j \neq i$. From the latter expression we can see that the coupling is ferromagnetic for $J > 0$ ($\boldsymbol{m}_1$ is parallel with $\boldsymbol{m}_2$) and antiferromagnetic for $J < 0$ ($\boldsymbol{m}_1$ is antiparallel with $\boldsymbol{m}_2$).

4.5 Exchange bias anisotropy

In *1956* Meiklejohn an Bean [75] reported an observation of a *new type of magnetic anisotropy* resulting from an interfacial exchange interaction between ferromagnetic and antiferromagnetic materials. The essentials of exchange bias anisotropy might be described as follows. Consider an interface between ferro- (F) and antiferromagnetic (AF) materials. Usually, on the interface there are AF grains with parallel spin planes, which gives rise to localized magnetic moments [76].

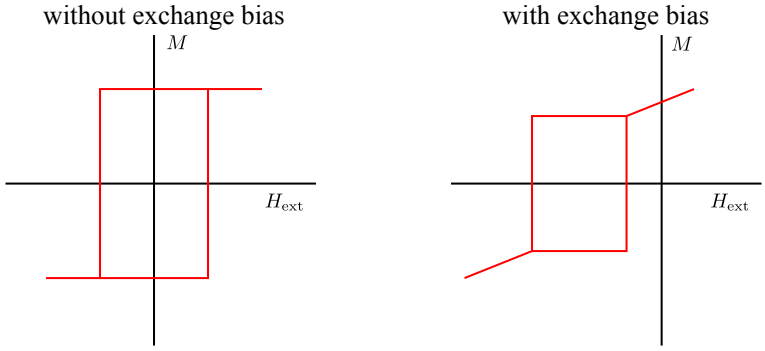

Figure 17: Comparison of hysteresis loop of a magnetic layer adjacent to an antiferromagnet with and without exchange bias coupling.

Obviously, magnetic structure in F is ordered below the Currie temperature, T_C, of a given ferromagnetic material. Similarly, AF is magnetically ordered below its Neel temperature, T_N, which is usually smaller than T_C. If one applies a magnetic field at temperature T, $T_N < T < T_C$, the F magnetization aligns along the field, while AF structure remains paramagnetic. Then, if one cools the F/AF system down below T_N, the ordered localized AFM spins will couple to the aligned FM spins at the same direction. Consequently, localized uncompensated AF spins exert a torque on F spins and keep them aligned in the direction of the cooling field. As a consequence, when switching the F magnetization back and forth using an external magnetic field (at $T < T_N$), the hysteresis loop shall be not symmetric but shifted along the field-axis; see Fig. 17.

Exchange bias is an important effect which is often used to fix the reference layer magnetization in a given direction. Since this interaction is usually not connected with the free layer, we do not consider it in the energy functional for the free layer.

4.6 Energy functional

Finally, we can write the energy functional, which includes all the important energy terms

$$E[\mathbf{M}] = \int_V \left\{ \varepsilon_Z(\mathbf{M}, \mathbf{H}_{ext}) + \varepsilon_{ani}(\mathbf{M}) + \varepsilon_m(\mathbf{M}) + \varepsilon_{RKKY}(\mathbf{M}, \mathbf{M}') \right\} \mathrm{d}V \,, \tag{4.31}$$

where we integrate through the volume, V, of the magnetic particle/layer. Then, the effective field acting on the magnetization, $\mathbf{M}$, is defined as

$$\mathbf{H}_{eff}(\boldsymbol{m}) = -\frac{1}{\mu_0 V} \frac{\delta E[\mathbf{M}]}{\delta \mathbf{M}} = -\frac{1}{\mu_0 V M_s} \frac{\delta E[\boldsymbol{m}]}{\delta \boldsymbol{m}} \,. \tag{4.32}$$

This definition leads to the effective field expression in the form

$$\mathbf{H}_{eff}(\boldsymbol{m}) = \mathbf{H}_{ext} + H_{ani}(\boldsymbol{m} \cdot \hat{\boldsymbol{e}}_{ani})\, \hat{\boldsymbol{e}}_{ani} - M_s \bar{\boldsymbol{N}} \cdot \boldsymbol{m} + \frac{J}{\mu_0 d} \boldsymbol{m}' \,. \tag{4.33}$$

Generally, the energy functional might be extended in case of more relevant magnetic interactions in the system. In micromagnetism, energy functional includes also exchange interaction.

5 Magnetization dynamics

The energy of a magnetic moment of a solid body is a complicated function including contributions of the crystalline structure, shape and external factors like fields and temperature. In a local equilibrium, variation in any of these contributions changes the energy of the magnetic moment and results in magnetization dynamics. In this section the theoretical framework of magnetization dynamics shall be described.

First, consider a single spin operator, $\hat{\mathcal{S}} = (\hat{\mathcal{S}}_x, \hat{\mathcal{S}}_y, \hat{\mathcal{S}}_z)$. In the Heisenberg picture, the spin dynamics is described by Heisenberg equation of motion (see eg. [77])

$$\frac{\mathrm{d}\hat{\mathcal{S}}_\xi}{\mathrm{d}t} = \frac{i}{\hbar}\left[\hat{H}, \hat{\mathcal{S}}_\xi\right], \tag{5.1}$$

where $\xi = x, y, z$; $\hat{\mathcal{S}}_\xi$ is the operator of a spin component and $\hat{H}$ is the Hamiltonian of the system. The brackets $\left[\hat{A}, \hat{B}\right]$ stand for the commutator of the operators $\hat{A}$ and $\hat{B}$, which is defined as

$$\left[\hat{A}, \hat{B}\right] = \hat{A}\hat{B} - \hat{B}\hat{A}\,. \tag{5.2}$$

The well known commutation relations of the angular momenta might be written as

$$\left[\hat{\mathcal{S}}_\zeta, \hat{\mathcal{S}}_\xi\right] = -i\hbar \sum_\eta \epsilon_{\xi\zeta\eta}\hat{\mathcal{S}}_\eta\,, \tag{5.3}$$

where $\xi, \zeta, \eta \in \{x, y, z\}$, and $\epsilon_{\xi\zeta\eta}$ stands for Levi-Civita symbol, which is defined as

$$\epsilon_{\xi\zeta\eta} = \begin{cases} 1 & \text{if } (\xi,\zeta,\eta) \text{ is an even even permutation of } (x,y,z) \\ -1 & \text{if } (\xi,\zeta,\eta) \text{ is an odd permutation of } (x,y,z) \\ 0 & \text{if } \xi = \zeta \text{ or } \xi = \eta \text{ or } \zeta = \eta\,. \end{cases} \tag{5.4}$$

To the first order of $\hbar$ one can write the equation of motion (5.1) [78] in the form

$$\frac{\mathrm{d}\hat{\mathcal{S}}_\xi}{\mathrm{d}t} = \frac{i}{\hbar}\left(\sum_\zeta \frac{\mathrm{d}\hat{H}}{\mathrm{d}\hat{\mathcal{S}}_\zeta}\left[\hat{\mathcal{S}}_\zeta, \hat{\mathcal{S}}_\xi\right] + \mathcal{O}(\hbar^2)\right). \tag{5.5}$$

Using the commutation relation (5.3) one obtains

$$\frac{\mathrm{d}\hat{\mathcal{S}}_\xi}{\mathrm{d}t} = \sum_\zeta \sum_\eta \frac{\mathrm{d}\hat{H}}{\mathrm{d}\hat{\mathcal{S}}_\zeta}\epsilon_{\xi\zeta\eta}\hat{\mathcal{S}}_\eta + \mathcal{O}(\hbar^2) \tag{5.6}$$

which can be written as a complex equation for all spin components as

$$\frac{\mathrm{d}\hat{\mathcal{S}}}{\mathrm{d}t} = -\hat{\mathcal{S}} \times \frac{\mathrm{d}\hat{H}}{\mathrm{d}\hat{\mathcal{S}}} + \mathcal{O}(\hbar^2)\,, \tag{5.7}$$

where we used the cross-product definition in the form

$$[\boldsymbol{A} \times \boldsymbol{B}]_\xi = \sum_\zeta \sum_\eta \epsilon_{\xi\zeta\eta} A_\zeta B_\eta\,. \tag{5.8}$$

In the semi-classical limit we consider $\hbar \to 0$ and the equation of motion reads

$$\frac{\mathrm{d}}{\mathrm{d}t}\langle\hat{\mathcal{S}}\rangle = -\langle\hat{\mathcal{S}}\rangle \times \mathbf{H}_{\mathrm{eff}}\,. \tag{5.9}$$

where

$$\mathbf{H}_{\mathrm{eff}} = \frac{1}{\gamma}\left\langle \frac{\mathrm{d}\hat{H}}{\mathrm{d}\hat{\mathcal{S}}} \right\rangle\,, \tag{5.10}$$

where $\gamma = \gamma_{\mathrm{g}}\mu_0 = g\mu_0\mu_{\mathrm{B}}/\hbar$ [8] with g being the Landeé factor[9], and μ_{B} is the Bohr magneton. In the semiclassical approximation the effective field is expressed as

$$\mathbf{H}_{\mathrm{eff}} = \frac{1}{\mu_0}\frac{\mathrm{d}E}{\mathrm{d}\mathbf{S}}\,, \tag{5.11}$$

where E is the energy of classical net spin moment $\mathbf{S}$. Comparing (5.10) and (5.11) one obtains $\mathbf{S} = g\mu_{\mathrm{B}}\langle\hat{\mathcal{S}}\rangle/\hbar$. Consequently, Eq. (5.9) leads to the equation of motion of a classical net spin moment in a magnetic field, $\mathbf{H}_{\mathrm{eff}}$,

$$\frac{\mathrm{d}\mathbf{S}}{\mathrm{d}t} = -\gamma\,\mathbf{S} \times \mathbf{H}_{\mathrm{eff}}\,. \tag{5.12}$$

Usually, for the net spin moment, $\mathbf{S}$, in the latter equation is replaced by magnetization,

$$\frac{\mathrm{d}\mathbf{M}}{\mathrm{d}t} = -\gamma\,\mathbf{M} \times \mathbf{H}_{\mathrm{eff}}\,, \tag{5.13}$$

where the effective field is usually defined as

$$\mathbf{H}_{\mathrm{eff}} = -\frac{1}{\mu_0}\frac{\mathrm{d}E}{\mathrm{d}\mathbf{M}}\,. \tag{5.14}$$

5.1 Landau-Lifshitz-Gilbert equation

From Eq. (5.13) one can see that the time change of the net spin moment, $\mathrm{d}\mathbf{M}/\mathrm{d}t$ is perpendicular to the vector $\mathbf{M}$. Hence, equation (5.13) describes precession of $\mathbf{M}$, around the effective magnetic field $\mathbf{H}_{\mathrm{eff}}$. Additionally, $\mathrm{d}\mathbf{M}/\mathrm{d}t$ is perpendicular also to the effective field and hence the energy, E, of the system, which depends on the angle between $\mathbf{M}$ and $\mathbf{H}_{\mathrm{eff}}$, remains unchanged. However, when $\mathbf{M}$ stands for a macrospin related to a solid body, the net spin moment is coupled to additional degrees of freedom which provide energy dissipation. As a result, the net spin moment losses its energy and the angle between $\mathbf{M}$ and $\mathbf{H}_{\mathrm{eff}}$ gradually decreases until $\mathbf{M}$ reaches the energy minimum ($\mathbf{M} \parallel \mathbf{H}_{\mathrm{eff}}$). This process is called as (magnetization) damping and was for the first time theoretically studied by Landau and Lifshitz in *1935* [79]. In their formalism, they introduced the damping effect in the form of a phenomenological term

$$-\frac{\lambda}{M_{\mathrm{s}}}\,\mathbf{M} \times (\mathbf{M} \times \mathbf{H}_{\mathrm{eff}})\,, \tag{5.15}$$

[8] In SI units $\gamma = 2.21 \times 10^5\,(\mathrm{A/m})^{-1}\mathrm{s}^{-1}$ and $\gamma_{\mathrm{g}} = 1.76 \times 10^{11}\,\mathrm{T}^{-1}\mathrm{s}^{-1}$.

[9] For electron $g \simeq 2$.

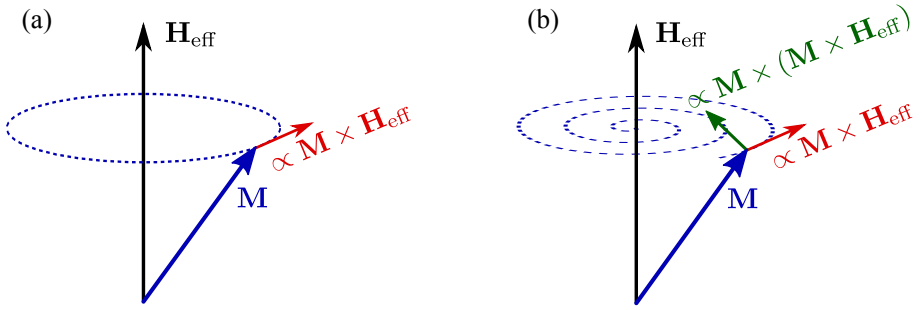

Figure 18: Comparison of the undamped gyromagnetic precessions (a) and damped precessions (b) of magnetization $\mathbf{M}$ in an effective magnetic field $\mathbf{H}_{\text{eff}}$. Figures show direction of both torques acting on magnetization; precessional $[\propto \mathbf{M} \times \mathbf{H}_{\text{eff}}]$ and damping $[\propto \mathbf{M} \times (\mathbf{M} \times \mathbf{H}_{\text{eff}})]$.

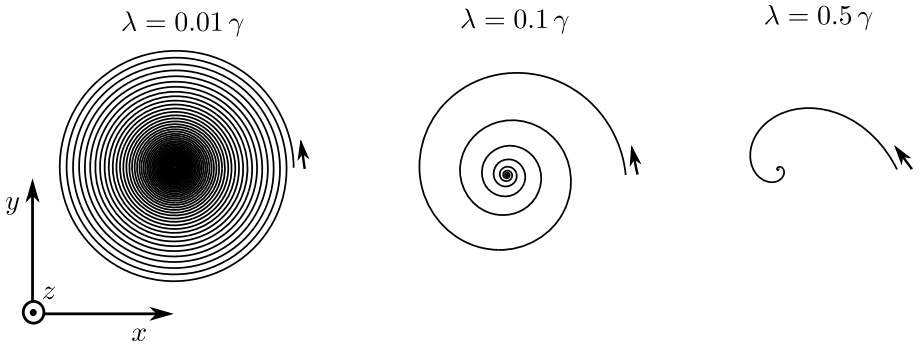

Figure 19: Influence of damping on the magnetization trajectories. Trajectories were obtained by numerical integration of Landau-Lifshitz equation (5.16) for different values of damping parameter, λ. Here, the only considered field was external field $\mathbf{H}_{\text{ext}} = H_{\text{ext}}\hat{\mathbf{e}}_z$, where $H_{\text{ext}} = 10^3\,\text{A/m}$. Each simulation started with magnetization tilted by 10° from the external field direction. The time integration step was as large as $\Delta t = 1\,\text{ps}$.

where $M_{\text{s}} = |\mathbf{M}|$ is the saturation magnetization of the solid body, and λ is a phenomenological *damping parameter*. Adding the phenomenological expression to (5.13) one obtains the *Landau-Lifshitz equation* which reads

$$\frac{\mathrm{d}\mathbf{M}}{\mathrm{d}t} = -\gamma\,\mathbf{M} \times \mathbf{H}_{\text{eff}} - \frac{\lambda}{M_{\text{s}}}\,\mathbf{M} \times (\mathbf{M} \times \mathbf{H}_{\text{eff}})\ , \tag{5.16}$$

The latter expression might be alternatively written as

$$\frac{\mathrm{d}\mathbf{M}}{\mathrm{d}t} = -\gamma\,\mathbf{M} \times \left(\mathbf{H}_{\text{eff}} + \frac{\lambda}{\gamma M_{\text{s}}}\,\mathbf{M} \times \mathbf{H}_{\text{eff}}\right)\ . \tag{5.17}$$

From the latter expression it is obvious that the damping term acts as an additional magnetic field perpendicular to $\mathbf{H}_{\text{eff}}$ pushing $\mathbf{M}$ towards $\mathbf{H}_{\text{eff}}$. The action of the damping term and comparison with undamped precessions is shown in Figure 18. The damping parameter in the magnetic materials is usually small in comparison to the precessional term, but its microscopic origin is still an object of extensive studies. The action of the damping term on the magnetization trajectories is shown in Fig. 19. One can see that larger λ reduces the precessional motion and shortens the magnetization trajectory towards the static point.

In order to analyze the basic properties of the Landau-Lifshitz equation (5.16) let us calculate

the dot product $\mathbf{M} \cdot \mathrm{d}\mathbf{M}/\mathrm{d}t$

$$\mathbf{M} \cdot \frac{\mathrm{d}\mathbf{M}}{\mathrm{d}t} = -\gamma\, \mathbf{M} \cdot (\mathbf{M} \times \mathbf{H}_{\mathrm{eff}}) - \frac{\lambda}{M_{\mathrm{s}}}\, \mathbf{M} \cdot [\mathbf{M} \times (\mathbf{M} \times \mathbf{H}_{\mathrm{eff}})] \,. \tag{5.18}$$

Since the right-hand side of the latter expression is zero, we obtained

$$\mathbf{M} \cdot \frac{\mathrm{d}\mathbf{M}}{\mathrm{d}t} = 0 \,. \tag{5.19}$$

Then, for time variation of $M_{\mathrm{s}}^2 = \mathbf{M} \cdot \mathbf{M}$ one can write

$$\frac{\mathrm{d}M_{\mathrm{s}}^2}{\mathrm{d}t} = \frac{\mathrm{d}}{\mathrm{d}t}\,(\mathbf{M} \cdot \mathbf{M}) = 2\,\mathbf{M} \cdot \frac{\mathrm{d}\mathbf{M}}{\mathrm{d}t} = 0 \,, \tag{5.20}$$

what expresses the conservation of magnetization amplitude by the Landau-Lifshitz dynamics. This result allows us to scale the magnetization vector with its length, M_{s}, and use *reduced magnetization*, $\boldsymbol{m} = \mathbf{M}/M_{\mathrm{s}}$. Then the Landau-Lifshitz equation reads

$$\frac{\mathrm{d}\boldsymbol{m}}{\mathrm{d}t} = -\gamma \boldsymbol{m} \times \mathbf{H}_{\mathrm{eff}} - \lambda\, \boldsymbol{m} \times (\boldsymbol{m} \times \mathbf{H}_{\mathrm{eff}}) \,. \tag{5.21}$$

5.1.1 Gilbert damping

Fundamentally different approach to the magnetization damping was proposed by Gilbert in 1955. In his study [80, 81], he reformulated the undamped magnetization equation of motion in Lagrangian form and introduced the damping by means of Rayleigh dissipation function. Namely, he considered the equation of motion for an damped magnetization in Lagrangian form

$$\frac{\mathrm{d}}{\mathrm{d}t} \frac{\delta \mathcal{L}[\mathbf{M}, \dot{\mathbf{M}}]}{\delta \dot{\mathbf{M}}} - \frac{\delta \mathcal{L}[\mathbf{M}, \dot{\mathbf{M}}]}{\delta \mathbf{M}} + \frac{\mathrm{d}\mathcal{R}[\dot{\mathbf{M}}]}{\mathrm{d}\dot{\mathbf{M}}} = 0 \,, \tag{5.22}$$

where $\mathcal{L}[\mathbf{M}, \dot{\mathbf{M}}]$ is the Lagrangian, and $\mathcal{R}[\dot{\mathbf{M}}]$ is the Rayleigh dissipation function, which reads

$$\mathcal{R}[\dot{\mathbf{M}}] = \frac{\eta}{2} \int \dot{\mathbf{M}}(\boldsymbol{r}, t) \cdot \dot{\mathbf{M}}(\boldsymbol{r}, t) \mathrm{d}\boldsymbol{r} \,. \tag{5.23}$$

Variable $\dot{\mathbf{M}}$ is simply $\dot{\mathbf{M}} = \mathrm{d}\mathbf{M}/\mathrm{d}t$ and η is a parameter.

Equation (5.22) leads to Landau-Lifshitz-like equation with and precessional term and a damping term in the form

$$\frac{\alpha}{M_{\mathrm{s}}}\, \mathbf{M} \times \frac{\mathrm{d}\mathbf{M}}{\mathrm{d}t} \,, \tag{5.24}$$

where $\alpha = \eta\gamma M_{\mathrm{s}}$ is so called *Gilbert damping parameter* analogical to parameter λ in Landau's and Lifshitz's phenomenology (5.16). Then the *Landau-Lifshitz-Gilbert equation* of magnetization motion reads

$$\frac{\mathrm{d}\mathbf{M}}{\mathrm{d}t} = -\gamma\, \mathbf{M} \times \mathbf{H}_{\mathrm{eff}} + \frac{\alpha}{M_{\mathrm{s}}}\, \mathbf{M} \times \frac{\mathrm{d}\mathbf{M}}{\mathrm{d}t} \,, \tag{5.25}$$

or alternatively

$$\frac{\mathrm{d}\mathbf{M}}{\mathrm{d}t} = -\gamma\, \mathbf{M} \times \left(\mathbf{H}_{\mathrm{eff}} - \frac{\alpha}{\gamma M_{\mathrm{s}}} \frac{\mathrm{d}\mathbf{M}}{\mathrm{d}t} \right) \,, \tag{5.26}$$

where the second term in the brackets is referred to as *dissipative field*.

5.1.2 Comparison of Landau-Lifshitz and Gilbert damping

Although Landau-Lifshitz and Landau-Lifshitz-Gilbert equations are different, they have similar features. First, multiplying equation (5.17) by $\mathbf{M}$, we obtain expression of the magnetization amplitude conservation as in the case of Landau-Lifshitz equation. Second, it can be shown, that Landau-Lifshitz form of the damping might be derived from the Gilbert one. To demonstrate it, we vector multiply both sides of Eq. (5.25) by $\mathbf{M}$

$$\mathbf{M} \times \frac{\mathrm{d}\mathbf{M}}{\mathrm{d}t} = -\gamma\, \mathbf{M} \times (\mathbf{M} \times \mathbf{H}_{\mathrm{eff}}) + \frac{\alpha}{M_{\mathrm{s}}}\, \mathbf{M} \times \left(\mathbf{M} \times \frac{\mathrm{d}\mathbf{M}}{\mathrm{d}t} \right) . \tag{5.27}$$

Using vector identity $\mathbf{A} \times (\mathbf{B} \times \mathbf{C}) = (\mathbf{A} \cdot \mathbf{C})\, \mathbf{B} - (\mathbf{A} \cdot \mathbf{B})\, \mathbf{C}$ and taking into account what we learned before, $\mathbf{M} \cdot \mathrm{d}/\mathrm{d}t$, we obtain

$$\mathbf{M} \times \frac{\mathrm{d}\mathbf{M}}{\mathrm{d}t} = -\gamma\, \mathbf{M} \times (\mathbf{M} \times \mathbf{H}_{\mathrm{eff}}) - \alpha M_{\mathrm{s}}\, \frac{\mathrm{d}\mathbf{M}}{\mathrm{d}t} . \tag{5.28}$$

The latter expression can be substituted in the right-hand side of equation (5.16) and one obtains

$$\frac{\mathrm{d}\mathbf{M}}{\mathrm{d}t} = -\gamma\, \mathbf{M} \times \mathbf{H}_{\mathrm{eff}} - \frac{\gamma\alpha}{M_{\mathrm{s}}}\, \mathbf{M} \times (\mathbf{M} \times \mathbf{H}_{\mathrm{eff}}) - \alpha^2\, \frac{\mathrm{d}\mathbf{M}}{\mathrm{d}t} . \tag{5.29}$$

Finally, we obtain *Landau-Lifshitz-like* equation

$$\frac{\mathrm{d}\mathbf{M}}{\mathrm{d}t} = -\gamma'\, \mathbf{M} \times \mathbf{H}_{\mathrm{eff}} - \alpha\, \frac{\gamma'}{M_{\mathrm{s}}}\, \mathbf{M} \times (\mathbf{M} \times \mathbf{H}_{\mathrm{eff}}) , \tag{5.30}$$

where $\gamma' = \gamma/(1 + \alpha^2)$. Formally, equations (5.16) and (5.30) are the same after replacing $\gamma \to \gamma'$ and $\lambda \to \gamma'\alpha$.

Both Landau-Lifshitz and Landau-Lifshitz-Gilbert equations belongs to the same family of damped gyromagnetic precession equations [82]. The problem of differences between Landau-Lifshitz and Gilbert damping terms were studied first by Kikuchi [83] and later on by Mallinson [84], who studied problem of magnetization switching in an external magnetic field. They noticed that both damping terms are equivalent only in the case of vanishing damping parameter ($\alpha \to 0$ and $\lambda \to 0$), however, when the damping is large enough the dynamics given by both terms is markedly different. Namely, the Landau-Lifshitz term (5.15) does not change the magnetization precession but the magnitude of $\mathrm{d}\mathbf{M}/\mathrm{d}t$ increases and the switching time decreases. On the other hand, the Gilbert damping term (5.24) results in decrease of magnetization precession rate and magnitude of $\mathrm{d}\mathbf{M}/\mathrm{d}t$. Consequently, the switching time increases as the damping is larger. Intuitively, the behavior of Landau-Lifshitz damping is physically implausible. The highly damped magnetization simply moves following the energy gradient of the system as described by the Gilbert term. Therefore, the Gilbert damping form is preferred in modeling of the the magnetization dynamics since it leads to a plausible physical behavior [78, 83, 84, 81]. In addition, one should bear in mind that the Gilbert formalism is not unique since other types of gyromagnetic damped equations might be constructed.

Recently, the differences between Landau-Lifshitz and Gilbert damping forms were studied by Stiles et al. [85] in the light of current-induced domain wall motion. They showed that with Landau-Lifshitz damping the spin-transfer torque produces uniform translation of the wall and the damping always reduces the domain wall distortion caused by non-adiabatic spin-torque term. Then the

magnetic energy of the domain wall remains close to its energy minimum. Conversely, with the Gilbert damping, the damping term itself distort the domain wall and raises its magnetic energy. The distortion-induced magnetostatic torque stops domain wall motion. Stilles et al summed up that Landau-Lifshitz damping term is preferable to Gilbert's one since this term moves the magnetic energy of the domain wall towards a local minimum. This remains, however, still an open question, which needs further experimental research.

5.1.3 Energy dissipation

Let us now study the variation of energy due to the Gilbert damping term. First, multiply both side of equation (5.17) by $\mathbf{H}_{\text{eff}} - (\alpha/\gamma M_{\text{s}})(\mathrm{d}\mathbf{M}/\mathrm{d}t)$. One obtains

$$\frac{\mathrm{d}\mathbf{M}}{\mathrm{d}t} \cdot \left(\mathbf{H}_{\text{eff}} - \frac{\alpha}{\gamma M_{\text{s}}} \frac{\mathrm{d}\mathbf{M}}{\mathrm{d}t} \right) = 0 \,, \tag{5.31}$$

which leads to

$$\frac{\mathrm{d}\mathbf{M}}{\mathrm{d}t} \cdot \mathbf{H}_{\text{eff}} = \frac{\alpha}{\gamma M_{\text{s}}} \left| \frac{\mathrm{d}\mathbf{M}}{\mathrm{d}t} \right|^2 \,. \tag{5.32}$$

Now, consider the free energy of a magnetic particle, $\mathcal{F}(\mathbf{M}, \mathbf{H})$, which is a total differential of magnetization, $\mathbf{M}$, and applied magnetic field, $\mathbf{H}$. By integrating through the whole particle's volume, V, one obtains

$$\frac{\mathrm{d}\mathcal{F}}{\mathrm{d}t} = \int_V \mathrm{d}^3\boldsymbol{r} \left[\frac{\delta \mathcal{F}}{\delta \mathbf{M}} \cdot \frac{\partial \mathbf{M}}{\partial t} + \frac{\delta \mathcal{F}}{\delta \mathbf{H}} \cdot \frac{\partial \mathbf{H}}{\partial t} \right] = \int_V \mathrm{d}^3\boldsymbol{r} \left[-\mathbf{H}_{\text{eff}} \cdot \frac{\partial \mathbf{M}}{\partial t} - \mathbf{M} \cdot \frac{\partial \mathbf{H}}{\partial t} \right] \tag{5.33}$$

Making use of (5.32) one obtains

$$\frac{\mathrm{d}\mathcal{F}}{\mathrm{d}t} = - \int_V \mathrm{d}^3\boldsymbol{r} \, \frac{\alpha}{\gamma M_{\text{s}}} \left| \frac{\mathrm{d}\mathbf{M}}{\mathrm{d}t} \right|^2 - \int_V \mathrm{d}^3\boldsymbol{r} \, \mathbf{M} \cdot \frac{\partial \mathbf{H}}{\partial t} \,, \tag{5.34}$$

which is an energy balance equation for the magnetization dynamics. When the applied field is constant, $\mathrm{d}\mathbf{H}/\mathrm{d}t = 0$, one obtain

$$\frac{\mathrm{d}\mathcal{F}}{\mathrm{d}t} = - \int_V \mathrm{d}^3\boldsymbol{r} \, \frac{\alpha}{\gamma M_{\text{s}}} \left| \frac{\mathrm{d}\mathbf{M}}{\mathrm{d}t} \right|^2 \,. \tag{5.35}$$

If $\alpha \geq 0$, one obtains $\partial \mathcal{F}/\partial t \leq 0$. Hence, the latter expression tells us that the Gilbert damping term minimizes the free energy and is responsible for the energy dissipation. Equation (5.35) expresses the so called *Lyapunov structure* of the Landau-Lifshitz-Gilbert equation [82].

5.2 Thermal activation

Semiclassical Landau-Lifshitz-Gilbert equation describes dynamics of a magnetic moment in an isolated system. However, in practice, it is impossible to separate a magnetic moments from the lattice. Hence, there is a continuous energy exchange between magnetic subsystem with the lattice degrees of freedom, such like phonons, magnons, nuclear spins etc., which influences the the magnetization trajectory, [86, 87].

To properly introduce various factors in the dynamic model one has to identify their magnitude and the rate at which they influence the dynamics. Generally, the coupling of macroscopic magnetic moments to the lattice is weak in comparison to the influence of strong magnetic fields, and the processes on the lattice level are far more faster then the magnetization dynamics. Practically, influence of many processes, which are relatively fast in comparison to magnetization dynamics, appear as a random noise which depends on the temperature. Hence, one can use statistical physics to treat these additional degrees of freedom. It allows us to calculate probability distribution of a certain micro state, described by generalized coordinates of a complex system in a given macrostate, identified by macroscopic quantities like energy, temperature, etc.

In this part temperature shall be introduced into the model of magnetization dynamics. Particularly, we shall introduce stochastic effective magnetic field which stands for thermal influence on magnetization. Following the pioneering work of W. F. Brown [88] from *1963* we shall use Fokker-Planck equation to derive the statistical properties of this fluctuating magnetic field.

5.2.1 Stochastic Landau-Lifshitz-Gilbert equation

The main idea of the thermal activation in the Landau-Lifshitz-Gilbert equation is to introduce the thermal noise in the form of a stochastic field $\mathbf{H}_{\mathrm{th}}$, which might be added to the effective field. Provided that the contributions coming from large number of microscopic degrees of freedom might be simply added together, one can, according to the central limit theorem, consider $\mathbf{H}_{\mathrm{th}}$ as a Gaussian random process. [88] Therefore, the components of $\mathbf{H}_{\mathrm{th}} = (H_{\mathrm{th}\,x}, H_{\mathrm{th}\,y}, H_{\mathrm{th}\,z})$ obey

$$\langle H_{\mathrm{th}\,\xi}(t)\rangle = 0, \tag{5.36a}$$

$$\langle H_{\mathrm{th}\,\xi} H_{\mathrm{th}\,\eta}(t')\rangle = 2\mathcal{D}\,\delta_{\xi\eta}\,\delta(t-t')\,, \tag{5.36b}$$

where the $\xi, \eta \in \{x, y, z\}$ and $\langle x\rangle$ stands for the average of a stochastic variable x taken over a set of independent realizations of the stochastic process. The first equation (5.36a) says that the average of the thermal field, $\mathbf{H}_{\mathrm{th}}$, vanishes in each direction. The second relation (5.36b) sets the strength of the fluctuations to be proportional to $\mathcal{D}$. Moreover, we assume that the thermal field components are uncorrelated, as well as the autocorrelation time of the thermal field is much shorter than the response time of the magnetization. Additionally, note that the thermal field is not a real magnetic field, since it is not derived from an energy functional as the effective magnetic field, $\mathbf{H}_{\mathrm{eff}}$. Thermal field might be considered as a mathematical representation of stochastic influence acting on magnetization modeling their statistical properties. If the strength of the stochastic fluctuations depend on temperature, it is evident that $\mathcal{D}$ is dependent on the temperature. The knowledge of this dependence is crucial and shall be evaluated below.

Assuming equations (5.36) we can introduce the *Stochastic Landau-Lifshitz-Gilbert Equation*

$$\frac{\mathrm{d}\mathbf{M}}{\mathrm{d}t} = -\gamma\mathbf{M}\times(\mathbf{H}_{\mathrm{eff}} + \mathbf{H}_{\mathrm{th}}) + \frac{\alpha}{M_{\mathrm{s}}}\,\mathbf{M}\times\frac{\mathrm{d}\mathbf{M}}{\mathrm{d}t}\,, \tag{5.37}$$

which might be transformed to the form

$$\frac{\mathrm{d}\mathbf{M}}{\mathrm{d}t} = -\gamma'\mathbf{M}\times(\mathbf{H}_{\mathrm{eff}} + \mathbf{H}_{\mathrm{th}}) - \frac{\gamma'\alpha}{M_{\mathrm{s}}}\,\mathbf{M}\times[\mathbf{M}\times(\mathbf{H}_{\mathrm{eff}} + \mathbf{H}_{\mathrm{th}})]\,, \tag{5.38}$$

In order to understand the structure of stochastic Landau-Lifshitz-Gilbert equation we rewrite

it as

$$\begin{aligned}\frac{\mathrm{d}\mathbf{M}}{\mathrm{d}t} =& -\gamma'\mathbf{M}\times\mathbf{H}_{\mathrm{eff}} - \frac{\alpha\gamma'}{M_{\mathrm{s}}}\mathbf{M}\times(\mathbf{M}\times\mathbf{H}_{\mathrm{eff}}) \\ & -\gamma'\mathbf{M}\times\mathbf{H}_{\mathrm{th}} - \frac{\alpha\gamma'}{M_{\mathrm{s}}}\mathbf{M}\times(\mathbf{M}\times\mathbf{H}_{\mathrm{th}})\,,\end{aligned} \tag{5.39}$$

where the first two terms include only deterministic part of the magnetic field and the latter two include the stochastic contribution. For convenience we define

$$A_\xi(\mathbf{M},t) = \left[-\gamma'\mathbf{M}\times\mathbf{H}_{\mathrm{eff}} - \frac{\alpha\gamma'}{M_{\mathrm{s}}}\mathbf{M}\times(\mathbf{M}\times\mathbf{H}_{\mathrm{eff}})\right]_\xi \tag{5.40a}$$

$$\begin{aligned}B_{\xi\zeta}(\mathbf{M},t) &= -\gamma'\epsilon_{\xi\eta\zeta}M_\eta - \frac{\alpha\gamma'}{M_{\mathrm{s}}}\epsilon_{\xi\eta\alpha}M_\eta\epsilon_{\alpha\beta\zeta}M_\beta \\ &= -\gamma'\epsilon_{\xi\eta\zeta}M_\eta - \frac{\alpha\gamma'}{M_{\mathrm{s}}}(\delta_{\xi\beta}\delta_{\xi\zeta}-\delta_{\xi\zeta}\delta_{\eta\beta})M_\eta M_\beta \\ &= -\gamma'\epsilon_{\xi\eta\zeta}M_\eta - \frac{\alpha\gamma'}{M_{\mathrm{s}}}(M_\xi M_\zeta - \delta_{\xi\zeta}M^2)\,,\end{aligned} \tag{5.40b}$$

where we used Einstein summation rule, and we took into account that where $M^2 = M_{\eta\eta} = M_{\mathrm{s}}^2$. Levi-Civita symbol, $\epsilon_{\xi\eta\zeta}$, is defined by (5.4). On that account, we can simplify equation (5.38) as

$$\frac{\mathrm{d}M_\xi}{\mathrm{d}t} = A_\xi(\mathbf{M},t) + B_{\xi\zeta}(\mathbf{M},t)H_\zeta^{\mathrm{th}}(t)\,. \tag{5.41}$$

The latter equation is a general form of Langevin equation with multiplicative noise [86, 87], where the multiplicative factor $B_{\xi\zeta}(\mathbf{M},t)$ is a function of magnetization $\mathbf{M}$. This knowledge allow us to establish important properties of the stochastic Landau-Lifshitz-Gilbert equation, mainly the dependence of $\mathcal{D}$ on temperature T. Hence, we shall write and solve the Fokker-Planck equation, which describes the evolution of the probability density function of stochastic processes expressed by the Langevin equation (5.41).

5.2.2 Fokker-Planck equation

The Fokker-Planck equation describes the time evolution of the Probability Density Function, $W(\mathbf{M},t)$, of the magnetization. Pratically, $W(\mathbf{M},t)$ gives the relative probability that under given conditions magnetization occurs in a certian direction ($\mathbf{M}$). The Fokker-Planck equation for Langevin equation with multiplicative noise (5.41) reads [88, 89]

$$\frac{\partial W}{\partial t} = -\frac{\partial}{\partial M_\xi}\left[\left(A_\xi + \mathcal{D}B_{\eta\zeta}\frac{\partial B_{\xi\zeta}}{\partial M_\eta}\right)W\right] + \frac{\partial^2}{\partial M_\xi \partial M_\eta}[(\mathcal{D}B_{\xi\zeta}B_{\eta\zeta})W]\,. \tag{5.42}$$

By taking the M_j derivatives of the second term on the right-hand side we obtain

$$\frac{\partial W}{\partial t} = \frac{\partial}{\partial M_\xi}\left[\left(A_\xi - \mathcal{D}B_{\xi\zeta}\frac{\partial B_{\eta\zeta}}{\partial M_\eta} - \mathcal{D}B_{\xi\zeta}B_{\eta\zeta}\frac{\partial}{\partial M_\eta}\right)W\right]\,. \tag{5.43}$$

Now, we will evaluate the individual terms of Eq. (5.43). Taking into account the definitions (5.40) we find

$$\frac{\partial B_{\xi\zeta}}{\partial M_\eta} = -\gamma'\epsilon_{\xi\eta\zeta} - \frac{\alpha\gamma'}{M_{\mathrm{s}}}(\delta_{\xi\eta}m_\zeta + \delta_{\eta\zeta}m_\xi - 2\delta_{\xi\zeta}m_\eta)\,. \tag{5.44}$$

After contraction of the index ξ one obtain

$$\frac{\partial B_{\eta\zeta}}{\partial M_\eta} = -2\frac{\alpha\gamma'}{M_\mathrm{s}} M_\zeta \,, \tag{5.45}$$

because of the sums $\epsilon_{\eta\eta\zeta} = 0$ and $\delta_{\eta\eta} = 3$. Then

$$B_{\xi\zeta}\frac{\partial B_{\eta\zeta}}{\partial M_\eta} = 2\frac{\alpha^2\gamma'^2}{M_\mathrm{s}^2}\left(M_\xi M^2 - M_\xi M^2\right) = 0 \,, \tag{5.46}$$

where we have used that $\epsilon_{\xi\eta\zeta} M_\eta M_\zeta = 0$.
Thus, we find, that the second term on the right hand side of (5.42) vanishes identically.
Finally, the third term can be written as

$$B_{\xi\zeta}B_{\eta\zeta}\frac{\partial W}{\partial M_\eta} = -\gamma'^2(\alpha^2+1)\left[\mathbf{M}\times\left(\mathbf{M}\times\frac{\partial W}{\partial M_\eta}\right)\right]_\xi \tag{5.47}$$

Then, the Fokker-Planck equation (5.43) might be written as [88, 86]

$$\begin{aligned}\frac{\partial W}{\partial t} = -\frac{\partial}{\partial \mathbf{M}}\Bigg\{\Bigg[&-\gamma'\mathbf{M}\times\mathbf{H}_\mathrm{eff} - \frac{\alpha\gamma'}{M_\mathrm{s}}\mathbf{M}\times(\mathbf{M}\times\mathbf{H}_\mathrm{eff}) \\ &+ \frac{1}{2t_\mathrm{N}}\mathbf{M}\times\left(\mathbf{M}\times\frac{\partial}{\partial\mathbf{M}}\right)\Bigg]W\Bigg\} \,,\end{aligned} \tag{5.48}$$

where $\dfrac{\partial}{\partial\mathbf{M}}$ stands for divergence operator

$$\frac{\partial}{\partial\mathbf{M}}\mathbf{A} = \frac{\partial A_\xi}{\partial M_\xi} \,.$$

and

$$\frac{1}{t_\mathrm{N}} = 2\mathcal{D}\gamma'^2(1+\alpha^2) \,, \tag{5.49}$$

where t_N is so-called free-diffusion *Neél time*.

One can easily see that the stationary solution of the Fokker-Planck equation W_0, for which

$$\frac{\mathrm{d}W_0}{\mathrm{d}t} = 0 \,, \tag{5.50}$$

is forced to be the Boltzmann distribution [88]

$$W_0(\mathbf{M}) \propto \exp\left(-\beta\, E(\mathbf{M})\right) \,, \tag{5.51}$$

where $\beta = (k_\mathrm{B}T)^{-1}$ and

$$E(\mathbf{M}) = -\mu_0 v \mathbf{H}_\mathrm{eff}\cdot\mathbf{M} \tag{5.52}$$

is the energy of magnetic particle or micromagnetic computational cell of volume v. From equation (5.52) we obtain

$$\mu_0 v\mathbf{H}_\mathrm{eff} = -\frac{\partial E}{\partial\mathbf{M}} \,. \tag{5.53}$$

We find

$$\frac{\partial W_0}{\partial \mathbf{M}} = \beta\mu_0 v \mathbf{H}_{\text{eff}} W_0 \,. \tag{5.54}$$

Hence,

$$\left[\frac{\partial}{\partial \mathbf{M}} . \left(\mathbf{M} \times \frac{\partial W_0}{\partial \mathbf{M}}\right)\right]_\xi = \partial_{M_\xi}(\epsilon_{\xi\eta\zeta} M_\zeta \partial_{M_\zeta} W_0) = 0 \tag{5.55}$$

and the first term on the right hand side of the Fokker-Planck equation (5.42) vanishes. Thus, the Fokker-Planck equation with the stationary solution W_0 reads

$$0 = \left[-\frac{\alpha\gamma'}{M_\text{s}} \mathbf{M} \times (\mathbf{M} \times \mathbf{H}_{\text{eff}})\, W_0 + \frac{1}{2t_\text{N}} \mathbf{M} \times (\mathbf{M} \times \beta\mu_0 v \mathbf{H}_{\text{eff}}\, W_0)\right] \tag{5.56}$$

from which we find another expression for the Neél time

$$t_\text{N} = \frac{1}{\alpha} \frac{\mu_0 v M_\text{s}}{2\gamma' k_\text{B} T} \,. \tag{5.57}$$

By comparison of (5.49) and (5.57) we obtain desired relation of the strength of thermal field fluctuations and temperature

$$\mathcal{D} = \frac{\alpha}{1+\alpha^2} \frac{k_\text{B} T}{\mu_0 V \gamma' M_\text{s}} \,. \tag{5.58}$$

Equations (5.36), (5.38) and (5.58) provide full description of the magnetization dynamics in an effective field at a non-zero temperature.

Practically, in numerical simulation is the thermal fluctuating field calculated as

$$\mathbf{H}_\text{th} = \sqrt{2 \frac{\alpha}{1+\alpha^2} \frac{k_\text{B} T}{\mu_0 V \gamma' M_\text{s}} \frac{1}{\Delta t}}\, \boldsymbol{\eta} \,, \tag{5.59}$$

where Δt is dicrete time integration step and $\boldsymbol{\eta}$ is vector with components being random numbers with Gaussian distribution having with zero mean and unit distribution; $\eta_i \in \mathcal{G}(0,1)$ for $i = x, y, z$. For computer generation of random numbers see Appendix F.

The effect of temperature on the magnetization trajectory is illustrated in Figure 20.

5.3 Generalized Landau-Lifshitz-Gilbert equation

In the last decade the physics of nanomagnetism has been markedly extended. New experiments and theories have shown that magnetic field is not the only factor which can influence the magnetization dynamics in a nanomagnet. It has been shown that spin-polarized current or heating might markedly influence the spin dynamics and cannot be treated on the level of stochastic thermal noise. Therefore, in order to include additional torques acting on the magnetization, an extension of the Landau-Lifshitz-Gilbert equation is required. Generally, we can write Landau-Lifshitz-Gilbert equation (without the stochastic field) in the form

$$\frac{\mathrm{d}\mathbf{M}}{\mathrm{d}t} - \frac{\alpha}{M_\text{s}} \mathbf{M} \times \frac{\mathrm{d}\mathbf{M}}{\mathrm{d}t} = \boldsymbol{\Gamma} \,, \tag{5.60}$$

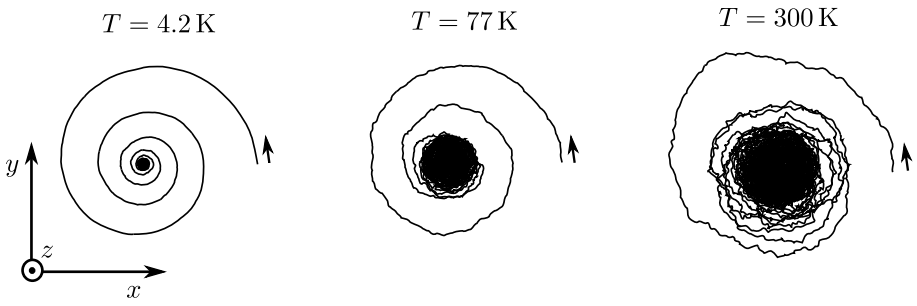

Figure 20: Effect of thermal fluctuations on the magnetization trajectories. Trajectories were obtained by numerical integration of Stochastic Landau-Lifshitz-Gilbert equation (5.37) for different values of temperature, T. Here, the only considered field was the external field $\mathbf{H}_{\text{ext}} = H_{\text{ext}}\hat{\mathbf{e}}_z$, where $H_{\text{ext}} = 10^3\text{A/m}$. The Gilbert damping parameter was set to $\alpha = 0.1$. In expression (5.58), the volume, V, of the particle was taken as a volume of a sphere with radius $r = 100\,\text{nm}$. Saturated magnetization of the particle was chosen as large as $M_{\text{s}} = 10^6\,\text{A/m}$. Each simulation started with magnetization tilted 10° from the external field direction. The time integration step was $\Delta t = 1\,\text{ps}$.

where $\mathbf{\Gamma}$ is the overall torque acting on the magnetization given by

$$\mathbf{\Gamma} = -\gamma\,\mathbf{M} \times \mathbf{H}_{\text{eff}} + \mathbf{T}\,. \tag{5.61}$$

The first term of latter expression stands for torque due to the effective magnetic field. The second term stands for additional factors which influence the spin dynamics.

In this thesis we focus on the influence of current-induced spin transfer torque in magnetic multilayers on the free layer(s) spin dynamics. In the Section 3 we already introduced the formula for the spin transfer torque, which can be calculated under various assumptions. In the presence of spin polarized current in the case of simple trilayer we have

$$\mathbf{T} = \frac{\gamma I}{\mu_0 M_{\text{s}} d}\,\boldsymbol{\tau}\,, \tag{5.62}$$

where $\boldsymbol{\tau} = \boldsymbol{\tau}_{\parallel} + \boldsymbol{\tau}_{\perp}$ with

$$\boldsymbol{\tau}_{\parallel} = \frac{\tilde{a}}{M_{\text{s}}^3}\,\mathbf{M} \times (\mathbf{M} \times \mathbf{M}_{\text{fix}})\,, \tag{5.63a}$$

$$\boldsymbol{\tau}_{\perp} = \frac{\tilde{b}}{M_{\text{s}}^2}\,\mathbf{M} \times \mathbf{M}_{\text{fix}}\,, \tag{5.63b}$$

where $\mathbf{M}_{\text{fix}}$ is the fixed layer's magnetization, and $\tilde{a}$ and $\tilde{b}$ are model dependent parameters or functions proportional to $\hbar/(2e)$. The torque components, $\boldsymbol{\tau}_{\parallel}$ and $\boldsymbol{\tau}_{\perp}$ are perpendicular. While $\boldsymbol{\tau}_{\parallel}$ acts in the plane defined by $\mathbf{M}_1$ and $\mathbf{M}_2$ vectors, $\boldsymbol{\tau}_{\perp}$ is normal to this plane. Similarly, one can introduce the spin transfer torque also in case of magnetic tunnel junctions [90, 91].

Similarly, as in the case without spin-torque terms, one can find that the length of the magnetization vector is constant. Moreover, taking the vector product $\mathbf{M}$ with both side of (5.60) and substituting it back to the original equation one can find

$$\frac{\mathrm{d}\mathbf{M}}{\mathrm{d}t} = -\gamma'\,\mathbf{M} \times \mathbf{H}_{\text{eff}} - \frac{\gamma'\alpha}{M_{\text{s}}}\,\mathbf{M} \times (\mathbf{M} \times \mathbf{H}_{\text{eff}}) + \frac{\gamma' I}{\mu_0 M_{\text{s}} d}\,\boldsymbol{\tau}'\,, \tag{5.64}$$

where $\boldsymbol{\tau}' = \boldsymbol{\tau}'_{\parallel} + \boldsymbol{\tau}'_{\perp}$ are given by

$$\boldsymbol{\tau}'_{\parallel} = \frac{\tilde{a} + \alpha\tilde{b}}{M_{\mathrm{s}}^3}\,\mathbf{M} \times (\mathbf{M} \times \mathbf{M}_{\mathrm{fix}})\,, \tag{5.65a}$$

$$\boldsymbol{\tau}'_{\perp} = \frac{\tilde{b} - \alpha\tilde{a}}{M_{\mathrm{s}}^2}\,\mathbf{M} \times \mathbf{M}_{\mathrm{fix}}\,, \tag{5.65b}$$

Equation (5.64) is the generalized Landau-Lifshitz-Gilbert equation in the Landau-Lifshitz form.

5.3.1 Thermal activation in the presence of spin transfer torque

Following papers [92, 93, 94] we consider thermal activation in the generalized Landau-Lifshitz-Gilbert (5.60) equation in the form

$$\frac{\mathrm{d}\mathbf{M}}{\mathrm{d}t} - \frac{\alpha}{M_{\mathrm{s}}}\,\mathbf{M} \times \frac{\mathrm{d}\mathbf{M}}{\mathrm{d}t} = -\gamma\,\mathbf{M} \times (\mathbf{H}_{\mathrm{eff}} + \mathbf{H}_{\mathrm{th}}) + \frac{\gamma}{\mu_0 M_{\mathrm{s}} d}\,\tau\,. \tag{5.66}$$

The critical assumption of this model of thermal activation is that the spin torque does not contain a fluctuating field. The justification for this choice is that the spin torque comes form the conduction electrons whose transport properties are less affected by thermal fluctuations since the Fermi level is much higher than the thermal energy [94]. Similarly as in the section 5.2.2 we can write down the Fokker-Planck equation related to (5.66). In case of $I = 0$ spin transfer torque term vanishes and the Fokker-Planck equation will be the same as (5.42). Then, the Boltzmann distribution is the solution of the Fokker-Planck equation and one can use it to find the relation between $\mathcal{D}$ and temperature. However, when $I \neq 0$, the Fokker-Planck equation reads

$$\frac{\partial W}{\partial t} = \frac{\partial}{\partial M_\xi}\left[\left(A_\xi + \frac{\gamma'}{\mu_0 M_{\mathrm{s}} d}\,\tau_\xi - \mathcal{D}B_{\xi\zeta}\frac{\partial B_{\eta\zeta}}{\partial M_\eta} - \mathcal{D}B_{\xi\zeta}B_{\eta\zeta}\frac{\partial}{\partial M_\eta}\right) W\right]\,, \tag{5.67}$$

where $\mathbf{A}$ and $\mathbf{B}$ components are given by (5.40). One can easily find that Boltzmann distribution is no more solution of the Fokker- Planck equation when current acts on magnetization. The reason of this is that the studied system is out of equilibrium due to applied current.

However, it is still meaningful to obtain a stationary solution, W_0, i.e. $\partial W_0/\partial t = 0$. Hence, we solve the equation

$$\begin{aligned} 0 = \frac{\partial}{\partial \mathbf{M}}\Bigg\{\Bigg[&-\gamma'\mathbf{M} \times \mathbf{H}_{\mathrm{eff}} + \frac{\gamma' I}{\mu_0 M_{\mathrm{s}} d}\,\boldsymbol{\tau} - \frac{\alpha\gamma'}{M_{\mathrm{s}}}\mathbf{M} \times (\mathbf{M} \times \mathbf{H}_{\mathrm{eff}}) \\ &+ \gamma'\mathcal{D}\,(1+\alpha^2)\,\mathbf{M} \times \left(\mathbf{M} \times \frac{\partial}{\partial \mathbf{M}}\right)\Bigg] W_0\Bigg\}\,, \end{aligned} \tag{5.68}$$

where $\mathcal{D}$ depends on temperature T as given by (5.58). Following Li and Zhang [94] we assume it in the form

$$W_0 \propto \exp(-E/k_{\mathrm{B}}T^*)\,, \tag{5.69}$$

where T^* is an effective temperature different form T. It holds that

$$\frac{\partial W_0}{\partial \mathbf{M}} = -\frac{1}{k_{\mathrm{B}}T^*}\,\frac{\partial E}{\partial \mathbf{M}}\,W_0 \equiv \frac{1}{k_{\mathrm{B}}T^*}\,\mathbf{H}_{\mathrm{eff}}\,W_0\,. \tag{5.70}$$

Hence, the first term of (5.68) disappears and we obtain

$$\frac{\partial}{\partial \mathbf{M}}\left\{\left[\frac{\gamma' I}{\mu_0 M_\mathrm{s} d}\boldsymbol{\tau} + \frac{\gamma'\alpha}{M_\mathrm{s}}\left(\frac{T}{T^*}-1\right)\mathbf{M}\times(\mathbf{M}\times\mathbf{H}_\mathrm{eff})\right]W_0\right\} = 0\,. \tag{5.71}$$

The latter equation does not have necessarily solution for arbitrary choice of $\mathbf{H}_\mathrm{eff}$. Li and Zhang [94] solved equation (5.71) for an simplified effective field considering only external magnetic field, uniaxial anisotropy, and the largest component of demagnetization field (perpendicular to the layer's plane and to anisotropy axis). In such a case, the expression for the effective temperature can be written as

$$T^* = T\left(1-\frac{I}{I_\mathrm{c}}\right)^{-1} \tag{5.72}$$

where I_c is the critical current density (see next section). According to Li and Zhang [94] the concept of effective temperature should be understood in terms of a stationary solution of the probability density. The thermally averaged dynamical variable, for example, the magnetization vector, $\langle\mathbf{M}\rangle = \int W_0\mathbf{M}\sin\theta\,\mathrm{d}\theta\mathrm{d}\phi$, would behave as if the temperature of the system was T^*. However, the magnetic temperature, which is defined through the thermal fluctuations, remains to be T.

A disadvantage of this approach is, that it is applicable only when $I < I_\mathrm{c}$ because otherwise T^* would become negative. It means that it cannot be used to explain the thermal assisted current-induced switching, which requires $I > I_\mathrm{c}$.

5.4 Scaling of Landau-Lifshitz-Gilbert equation

For convenience, one can use in Landau-Lifshitz-Gilbert the reduced magnetization $\boldsymbol{m} = \mathbf{M}/M_\mathrm{s}$ instead of $\mathbf{M}$. However, when discussing spin torque effect, more appropriate physical quantity is the net spin moment or a unit vector along the net spin moment defined as $\hat{\boldsymbol{s}} = -\mathbf{M}/M_\mathrm{s} = -\boldsymbol{m}$. Then, generalized Landau-Lifshitz-Gilbert equation (5.60) can be written as

$$\begin{aligned}&\frac{\mathrm{d}\hat{\boldsymbol{s}}}{\mathrm{d}t} + \alpha\,\hat{\boldsymbol{s}}\times\frac{\mathrm{d}\hat{\boldsymbol{s}}}{\mathrm{d}t} = \boldsymbol{\Gamma}\,,\ \text{where}\\ &\boldsymbol{\Gamma} = -\gamma_\mathrm{g}\mu_0\,\hat{\boldsymbol{s}}\times\mathbf{H}_\mathrm{eff} + \frac{\gamma_\mathrm{g} I}{M_\mathrm{s} d}\boldsymbol{\tau}\,,\end{aligned} \tag{5.73}$$

where we substituted $\gamma = \gamma_\mathrm{g}\mu_0$. Note, that using $\hat{\boldsymbol{s}}$ instead of $\mathbf{M}$ one has to appropriately redefine the effective field, because it becomes a function of $\hat{\boldsymbol{s}}$ as well. The torque components in (5.73) are defined

$$\boldsymbol{\tau}_\parallel = a\,\hat{\boldsymbol{s}}\times\left(\hat{\boldsymbol{s}}\times\hat{\boldsymbol{S}}\right)\,, \tag{5.74a}$$

$$\boldsymbol{\tau}_\perp = b\,\hat{\boldsymbol{s}}\times\hat{\boldsymbol{S}}\,, \tag{5.74b}$$

where the capital $\hat{\boldsymbol{S}} = -\mathbf{M}_\mathrm{fix}/M_\mathrm{s}$ is the unit vector along the net spin moment of the fixed layer. In the analysis of spin dynamics we shall use Landau-Lifshitz-Gilbert equation in the form given by (5.30). The stochastic thermal field can be analogically introduced to (5.73) obeying equations (5.36) together with (5.58).

6 Magnetization stability

Before studying the dynamics of any system it is useful to have some knowledge on static equilibrium properties of a given system. This holds also for magnetization and spin dynamics. Therefore, in this section we shall study the static properties of the Landau-Lifshitz-Gilbert equation (LLG) with spin torque terms. Our goal is to identify stationary solutions of LLG and conditions under which these points are stable or unstable. In practice, this provides us with an important information on critical current and/or critical magnetic applied field which are necessary for observation of dynamic behavior.

In a magnetic nanoparticle the static points in case of zero applied field are mainly given by the type of anisotropy. The simplest model for static properties of a spherical particle with uniaxial anisotropy was proposed by Stoner and Wohlfarth in 1948 [95]. This model is useful to examine equilibrium magnetic configurations when a monodomain particle is in an external magnetic field. However, Stoner-Wohlfarth model does not describe magnetization dynamics and, as shall be explained below, cannot be extended to current-induced dynamics. Therefore, we shall study Landau-Lifshitz-Gilbert equation by means of linear stability theory. We will see that this theory provides us with useful tools to study the static properties of magnetization. Finally, the theory of spin torque ferromagnetic resonance shall be described.

6.1 Linear stability of an equilibrium solution

Let us first generally introduce the theory of linear stability [96]. Consider a general autonomous differential equation

$$\frac{\mathrm{d}\boldsymbol{x}}{\mathrm{d}t} = f(\boldsymbol{x})\,, \quad x \in \mathbb{R}^n \tag{6.1}$$

with a *stationary solution* or an equilibrium we mean a point $\boldsymbol{x}_0$ which is constant in time, i.e. $f(\boldsymbol{x}_0) = 0$. Then $\boldsymbol{x}_0$ is said to be *stable* if any solution of (6.1) starting *close* to $\boldsymbol{x}_0$ remains in its vicinity for all later times.

Now let us linearize this equation in the close vicinity of $\boldsymbol{x}_0$ given by points

$$\boldsymbol{x} = \boldsymbol{x}_0 + \boldsymbol{y}\,, \tag{6.2}$$

where $\boldsymbol{y}$ is a small deviation from the equilibrium. Then we can expand equation (6.1) using the Taylor series as

$$\frac{\mathrm{d}\boldsymbol{x}}{\mathrm{d}t} = \frac{\mathrm{d}\boldsymbol{x}_0}{\mathrm{d}t} + \frac{\mathrm{d}\boldsymbol{y}}{\mathrm{d}t} = f(\boldsymbol{x}_0) + \bar{\mathbf{D}}\boldsymbol{y} + \mathcal{O}(|\boldsymbol{y}|^2)\,, \tag{6.3}$$

where

$$\bar{\mathbf{D}} = \begin{pmatrix} \partial f_1(\boldsymbol{x})/\partial x_1 & \partial f_1(\boldsymbol{x})/\partial x_2 & \cdots & \partial f_1(\boldsymbol{x})/\partial x_n \\ \partial f_2(\boldsymbol{x})/\partial x_1 & \partial f_2(\boldsymbol{x})/\partial x_2 & \cdots & \partial f_2(\boldsymbol{x})/\partial x_n \\ \vdots & \vdots & & \vdots \\ \partial f_n(\boldsymbol{x})/\partial x_1 & \partial f_n(\boldsymbol{x})/\partial x_2 & \ldots & \partial f_n(\boldsymbol{x})/\partial x_n \end{pmatrix}_{\boldsymbol{x}=\boldsymbol{x}_0} \tag{6.4}$$

is a matrix of derivatives taken at $\boldsymbol{x} = \boldsymbol{x}_0$.

Taking into account equation (6.1) and omitting higher order terms in $\boldsymbol{y}$ one obtains

$$\frac{\mathrm{d}\boldsymbol{y}}{\mathrm{d}t} = \bar{\mathbf{D}}\,\boldsymbol{y}\,. \tag{6.5}$$

Since $\boldsymbol{x}_0$ is equilibrium, $\bar{\mathbf{D}}$ is a matrix with constant elements and the solution of (6.5) is given by

$$\boldsymbol{y}(t) = e^{\bar{\mathbf{D}}t}\,\boldsymbol{y}_0\,, \tag{6.6}$$

where $\boldsymbol{y}_0$ is the initial condition for $\boldsymbol{y}(t)$ in $t = 0$. If the eigenvalues of $\bar{\mathbf{D}}$ are positive the solution, $\boldsymbol{y}(t)$ departs from $\boldsymbol{y}_0$ with passing time. Conversely, if the eigenvalues of $\bar{\mathbf{D}}$ are negative $\boldsymbol{y}(t)$ remains in the vicinity of $\boldsymbol{y}_0$. Thus, solution $\boldsymbol{y}(t)$ is stable when the eigenvalues of $\bar{\mathbf{D}}$ have all negative real parts. Furthermore, when all the eigenvalues of $\bar{\mathbf{D}}$ have negative real parts, the equilibrium solution of (6.1), $\boldsymbol{x} = \boldsymbol{x}_0$, is stable as well [96].

The latter theorem offers us an useful tool to study the stability conditions taking into account also the dynamical features of the studied system. Let us now apply this theory to the Landau-Lifshitz-Gilbert equation (LLG), which is a first order differential equation for time-dependent vector $\hat{\boldsymbol{s}} = (s_x, s_y, s_z)$. Because the LLG dynamics does not affect the vector length, there are only two independent variables of $\hat{\boldsymbol{s}}$ which vary in time. Therefore, it is more convenient to rewrite LLG in spherical coordinates using the angles θ and ϕ (see appendix D)

$$\frac{\mathrm{d}}{\mathrm{d}t}\begin{pmatrix}\theta\\ \phi\end{pmatrix} = \frac{1}{1+\alpha^2}\begin{pmatrix}1 & \alpha\\ -\alpha\sin^{-1}\theta & \sin^{-1}\theta\end{pmatrix}\begin{pmatrix}v_\theta\\ v_\phi\end{pmatrix}\,, \tag{6.7}$$

where where $v_\theta = \boldsymbol{\Gamma}\cdot\hat{\mathbf{e}}_\theta$ and $v_\phi = \boldsymbol{\Gamma}\cdot\hat{\mathbf{e}}_\phi$ stand for overall torques exerted by both effective magnetic field and spin current (see Eq. 5.73). Suppose that point $\hat{\boldsymbol{s}}_0 = (\theta_0, \phi_0)$ is a stationary solution of (6.7). Then it has to obey

$$v_\theta(\theta_0, \phi_0) = 0\,, \tag{6.8a}$$
$$v_\phi(\theta_0, \phi_0) = 0\,. \tag{6.8b}$$

Then we can linearize equation (6.7) around this equilibrium, i.e. for $\theta = \theta_0 + \delta s_\theta$ and $\phi = \phi_0 + \delta s_\phi$:

$$\frac{\mathrm{d}}{\mathrm{d}t}\begin{pmatrix}\delta s_\theta\\ \delta s_\phi\end{pmatrix} = \bar{\mathcal{D}}\begin{pmatrix}\delta s_\theta\\ \delta s_\phi\end{pmatrix}\,, \tag{6.9}$$

where

$$\bar{\mathcal{D}} = \frac{1}{1+\alpha^2}\begin{pmatrix}1 & \alpha\\ -\alpha\sin^{-1}\theta_0 & \sin^{-1}\theta_0\end{pmatrix}\begin{pmatrix}\mathrm{d}v_\theta/\mathrm{d}\theta & \mathrm{d}v_\theta/\mathrm{d}\phi\\ \mathrm{d}v_\phi/\mathrm{d}\theta & \mathrm{d}v_\phi/\mathrm{d}\phi\end{pmatrix}_{(\theta_0,\phi_0)} \tag{6.10}$$

is a 2×2 matrix, which is also called *dynamic matrix* [97]. Equation (6.9) is analogical to (6.5) and therefore eigenvalues of the dynamic matrix give us desired information about the stability of stationary points.

Additionally, we shall show that the inspection of stability might be expressed in terms of two conditions for trace and determinant of the dynamic matrix. Consider an arbitrary 2×2 dynamic matrix with real elements

$$\bar{\mathcal{D}} = \begin{pmatrix}a & b\\ c & d\end{pmatrix} \tag{6.11}$$

with eigenvalues λ. Then the relation is obeyed

$$\det\left(\bar{\mathcal{D}} - \lambda\bar{\mathcal{I}}\right) = 0\,, \tag{6.12}$$

where $\bar{\mathcal{I}}$ is 2×2 identity matrix. The latter equation can be rewritten as

$$(a - \lambda)(d - \lambda) - bc = 0\,, \tag{6.13}$$

or alternatively

$$\lambda^2 - \lambda\,\mathrm{Tr}\bar{\mathcal{D}} + \det\bar{\mathcal{D}} = 0\,. \tag{6.14}$$

This equation has a solutions given by [98]

$$\lambda_{1,2} = \frac{\mathrm{Tr}\bar{\mathcal{D}}}{2} \pm \sqrt{A}\,, \qquad \text{where} \qquad A = \left(\frac{\mathrm{Tr}\bar{\mathcal{D}}}{2}\right)^2 - \det\bar{\mathcal{D}}\,. \tag{6.15}$$

Let us analyze the latter result in the light of the stability condition, i.e. $\mathrm{Re}\{\lambda_{1,2}\} < 0$. Because of the square root term in (6.15) we have to consider two cases. First, if the term A in (6.15) is negative, the real part of the eigenvalues is simply given by the trace. Then the stability condition reads

$$\mathrm{Tr}\bar{\mathcal{D}} < 0\,. \tag{6.16}$$

Moreover, from the condition $A < 0$ follows that $(\mathrm{Tr}\bar{\mathcal{D}}/2)^2 < \det\bar{\mathcal{D}}$ what implies that $\det\bar{\mathcal{D}} > 0$ is obeyed as well. Second, if A is positive, $\sqrt{A}$ is real and the stability conditions lead to

$$\frac{\mathrm{Tr}\bar{\mathcal{D}}}{2} < -\sqrt{A} \quad \text{and} \quad \frac{\mathrm{Tr}\bar{\mathcal{D}}}{2} < \sqrt{A}\,. \tag{6.17}$$

Obviously, because $\sqrt{A}$ is positive, the second inequality of (6.17) is automatically fulfilled when the first one is obeyed. Hence, we shall analyze only the first relation of (6.17). From there one can see that $\mathrm{Tr}\bar{\mathcal{D}} < 0$. Solving the first inequality in (6.17) on can easily find that

$$\det\bar{\mathcal{D}} > 0\,. \tag{6.18}$$

From the analysis above we learn that in both cases ($A > 0$ and $A < 0$) there are two conditions, which are simultaneously obeyed in a stable equilibrium

$$\mathrm{Tr}\bar{\mathcal{D}} < 0 \quad \text{and} \quad \det\bar{\mathcal{D}} > 0\,. \tag{6.19}$$

Depending on the sign of A one of these conditions is fulfilled automatically and the second one gives us the desired information about the critical current. In standard spin valves one often observes steady-state precessional states close to the stationary points. This means that usually the eigenvalues of the dynamic matrix have also non-zero imaginary part (coming from the square root term, A), which gives rise to the precessional motion [34]. Therefore, in most of the studied cases (6.16) is sufficient to determine the critical current given by

$$\mathrm{Tr}\bar{\mathcal{D}} = 0\,. \tag{6.20}$$

6.2 Spin-torque ferromagnetic resonance

A method analogical to the previous one with better physical background is based on the theory of ferromagnetic resonance in the presence of electric current. The method was introduced and applied to a macrospin model of spin valve with perpendicularly polarized fixed layer [45]. Here, this approach shall be described.

As before, we consider Landau-Lifshitz-Gilbert equation in the form given by (5.73) with a stationary point $\boldsymbol{s}_0 = (\theta_0, \phi_0)$. Then we can linearize any point in its vicinity as

$$\boldsymbol{s} = \boldsymbol{s}_0 + \delta\boldsymbol{s} = \begin{pmatrix} 1 \\ 0 \\ 0 \end{pmatrix} + \begin{pmatrix} 0 \\ \delta s_\theta \\ \delta s_\phi \end{pmatrix} . \tag{6.21}$$

Similarly, one can expand the effective field around this point

$$\mathbf{H}_{\text{eff}} = \mathbf{H}_{\text{eff}}(\boldsymbol{s}_0) + \frac{1}{M_\text{s}} \frac{\partial \mathbf{H}_{\text{eff}}}{\partial \boldsymbol{s}}(\boldsymbol{s}_0)\delta\boldsymbol{s} = \boldsymbol{H}_0 + \boldsymbol{h} = \begin{pmatrix} 0 \\ H_{0,\theta} \\ H_{0.\phi} \end{pmatrix} + \begin{pmatrix} 0 \\ h_\theta \\ h_\phi \end{pmatrix} . \tag{6.22}$$

where

$$\boldsymbol{H}_0 = \mathbf{H}_{\text{eff}}(\boldsymbol{s}_0) = \frac{1}{M_\text{s}} \frac{\partial E}{\partial \boldsymbol{s}}(\boldsymbol{s}_0) = \frac{1}{Ms} \left(E_\theta \hat{\mathbf{e}}_\theta + \frac{1}{\sin\theta} E_\phi \hat{\mathbf{e}}_\phi \right)_{\boldsymbol{s}_0} , \tag{6.23}$$

$$\begin{aligned} \boldsymbol{h} = \frac{1}{M_\text{s}} \frac{\partial \mathbf{H}_{\text{eff}}}{\partial \boldsymbol{s}}(\boldsymbol{s}_0)\delta\boldsymbol{s} = \\ \frac{1}{M_\text{s}^2} \left[\left(E_{\theta\theta}\delta s_\theta + \frac{1}{\sin\theta} E_{\theta\phi}\delta s_\phi \right) \hat{\mathbf{e}}_\theta + \frac{1}{\sin\theta} \left(E_{\theta\phi}\delta s_\theta + \frac{1}{\sin\theta} E_{\phi\phi}\delta s_\phi \right) \hat{\mathbf{e}}_\phi \right]_{\boldsymbol{s}_0} , \end{aligned} \tag{6.24}$$

and hence

$$H_{0,\theta} = -\frac{E_\theta}{M_\text{s}} , \qquad H_{0,\phi} = -\frac{E_\phi}{M_\text{s}\sin\theta} ,$$

$$h_\theta = \frac{E_{\theta\theta}}{M_\text{s}}\delta s_\theta + \frac{E_{\theta\phi}}{M_\text{s}\sin\theta}\delta s_\phi , \qquad h_\phi = \frac{E_{\theta\phi}}{M_\text{s}\sin\theta}\delta s_\theta + \frac{E_{\phi\phi}}{M_\text{s}\sin^2\theta}\delta s_\phi ,$$

where

$$E_\theta = \frac{\partial E}{\partial \theta} , \qquad E_\phi = \frac{\partial E}{\partial \phi} ,$$

$$E_{\theta\theta} = \frac{\partial^2 E}{\partial \theta^2} , \qquad E_{\phi\phi} = \frac{\partial^2 E}{\partial \phi^2} , \qquad E_{\theta\phi} = \frac{\partial^2 E}{\partial\theta\,\partial\phi} .$$

In the local frame we linearize LLG neglecting second order contribution of the small dynamic parts. The linearized equation can be then solved considering solutions $\delta s_\theta = A\exp(-\mathrm{i}\omega t)$ and $\delta s_\phi = B\exp(-\mathrm{i}\omega t)$. Solving linearized equation one can obtain the expression for the generalized frequency

$$\begin{aligned} (1+\alpha^2)\,\omega = -\frac{\mathrm{i}}{2} \left[\Delta\omega - 2\left(a_j - \alpha b_j\right) S_r\right] \\ \pm \sqrt{-\frac{1}{4}\left[\Delta\omega - 2\left(a_j - \alpha b_j\right) S_r\right]^2 + (1+\alpha^2)\left[b_j \frac{\Delta\omega}{\alpha} S_r + \left(a_j^2 + b_j^2\right) S_r^2 + \omega_0^2\right]} , \end{aligned} \tag{6.25}$$

where $a_j = (\gamma_\mathrm{g}/dM_\mathrm{s})aI$, $b_j = (\gamma_\mathrm{g}/dM_\mathrm{s})bI$, are the spin torque parameters and

$$\left(\frac{\omega_0}{\gamma}\right)^2 = \frac{E_{\theta\theta}E_{\phi\phi} - E_{\theta\phi}^2}{M_\mathrm{s}^2 \sin^2\theta}\,, \tag{6.26a}$$

$$\frac{\Delta\omega}{\gamma} = \alpha\left(\frac{E_{\theta\theta}}{M_\mathrm{s}} + \frac{E_{\phi\phi}}{M_\mathrm{s}\sin^2\theta}\right)\,, \tag{6.26b}$$

are resonance frequency and linewidth, respectively [99]. S_r is the first component of the fixed layer net spin moment, $\hat{\boldsymbol{S}} = (S_x, S_y, S_z)$, in the local coordinate systems, which reads

$$S_r = S_x \sin\theta_0 \cos\phi_0 + S_y \sin\theta_0 \sin\phi_0 + S_z \cos\theta_0\,. \tag{6.27}$$

For the most common case, when $\hat{\boldsymbol{S}} = (0, 0, 1)$, we have $S_r = \cos\theta_0$.

When we consider $b_j \ll a_j$, the generalized frequency reads

$$\begin{aligned}(1+\alpha^2)\,\omega = &-\frac{\mathrm{i}}{2}\,(\Delta\omega - 2a_j S_r) \\ &\pm\sqrt{-\frac{1}{4}\,(\Delta\omega - 2a_j S_r)^2 + (1+\alpha^2)\left(a_j^2 S_r^2 + \omega_0^2\right)}\,,\end{aligned} \tag{6.28}$$

what corresponds to result obtained in [45]. Note, that equation (6.28) strongly resembles the structure of eigenvalues (6.15). Both these methods are analogical from the mathematical point of view.

Simply, we can write $\omega = \omega' + i\omega''$, where ω' is the square-root term in equation (6.28) and $\omega'' = (\Delta\omega - 2a_j S_r)/2$. Then, to determine the stability of a given equilibrium point one needs to consider several possibilities. First, if $\omega'' < 0$, perturbation decays in time and (θ_0, ϕ_0) is stable. Moreover, if ω' is real, we obtain small amplitude damped oscillations around the considered static position whose frequency is given by ω' and linewidth is given by ω''. Second, if $\omega'' > 0$, the perturbation diverges and (θ_0, ϕ_0) is unstable. As a result, if ω' is real, $\omega'' = 0$ is a condition which provides a critical line for the stability/instability of (θ_0, ϕ_0). However, if ω has no real part, the critical current is given by condition $\omega = 0$. Additionally, if $S_r = 0$, the critical current can be obtained from the condition $\omega_0 = 0$.

6.3 Critical currents for a standard trilayer

Finally, let us apply the above discussed methods to adjust critical current for a most common trilayer spin valve structure with one fixed and one free layer. Our goal is to determine the current density which is needed to destabilize equilibrium positions of the free layer magnetization provided that the fixed layer's magnetization remains unchanged. Hence, we shall make use of the equation of motion (6.7) in spherical coordinate system (θ, ϕ) with an effective field defined as (see Section 4.6)

$$\mathbf{H}_\mathrm{eff}(\hat{\boldsymbol{s}}) = -H_\mathrm{ext}\hat{\mathbf{e}}_z - H_\mathrm{ani}(\hat{\boldsymbol{s}}\cdot\hat{\mathbf{e}}_z)\,\hat{\mathbf{e}}_z + \mathbf{H}_\mathrm{dem}\,, \tag{6.29}$$

where $\mathbf{H}_\mathrm{dem}$ is approximated by the expression for flat ellipsoid, which is close to the effective field of a thin layer of elliptical cross-section,

$$\mathbf{H}_\mathrm{dem} = (H_{\mathrm{d}x}s_x, H_{\mathrm{d}y}s_y, H_{\mathrm{d}z}s_z)\,, \tag{6.30}$$

where $H_{\mathrm{d}x} = N_x M_\mathrm{s}$, $H_{\mathrm{d}y} = N_y M_\mathrm{s}$, and $H_{\mathrm{d}z} = N_z M_\mathrm{s}$. From equation (6.29) one can see that the easy axis as well as the external magnetic field are aligned with $\hat{\mathbf{e}}_z$. From the definition of $\boldsymbol{\Gamma}$ (Eq. 5.73), and unit vectors $\hat{\mathbf{e}}_\theta$ and $\hat{\mathbf{e}}_\phi$ (Eq. D.2) one can easily find that

$$v_\theta = \boldsymbol{\Gamma}\cdot\hat{\mathbf{e}}_\theta = \frac{|\gamma_\mathrm{g}|}{M_\mathrm{s} d}\,\tau_\theta - |\gamma_\mathrm{g}|\mu_0\,(H_{\mathrm{d}x} - H_{\mathrm{d}y})\cos\phi\sin\phi\sin\theta\,, \tag{6.31a}$$

$$\begin{aligned} v_\phi = \boldsymbol{\Gamma}\cdot\hat{\mathbf{e}}_\phi &= \frac{|\gamma_\mathrm{g}|}{M_\mathrm{s} d}\,\tau_\phi \\ &- |\gamma_\mathrm{g}|\mu_0\,\left[H_\mathrm{ext} + \left(H_\mathrm{ani} + H_{\mathrm{d}x}\cos^2\phi + H_{\mathrm{d}y}\sin^2\phi - H_{\mathrm{d}z}\right)\cos\theta\right]\sin\theta\,, \end{aligned} \tag{6.31b}$$

where

$$\tau_\theta = a\,I\sin\theta\,, \tag{6.32a}$$

$$\tau_\phi = -b\,I\sin\theta \tag{6.32b}$$

stand for the current-induced torque parts defined by equations (5.74) where we assumed that the fixed layer's net spin moment, $\hat{\boldsymbol{S}} = \hat{\mathbf{e}}_z$, is aligned along the anisotropy field axis. One can easily find that the above mention conditions for a stationary point (6.8) are satisfied for $\theta = 0$ and π. The point $\theta = 0$ stands for parallel configuration of fixed and free layer's net spin moments (P) while the point $\theta = \pi$ corresponds to antiparallel configuration of $\hat{\boldsymbol{S}}$ and $\hat{\boldsymbol{s}}$. In these points the condition of vanishing trace (6.20) leads to critical currents given by [34][10]

$$I_\mathrm{c}^\mathrm{P} = \frac{\alpha\mu_0 M_\mathrm{s} d}{a(0) - \alpha b(0)}\left(H_\mathrm{ani} + H_\mathrm{ext} - H_{\mathrm{d}z} + \frac{H_{\mathrm{d}x} + H_{\mathrm{d}y}}{2}\right) \tag{6.33}$$

for $\theta = 0$ and

$$I_\mathrm{c}^\mathrm{AP} = -\frac{\alpha\mu_0 M_\mathrm{s} d}{a(\pi) - \alpha b(\pi)}\left(H_\mathrm{ani} - H_\mathrm{ext} - H_{\mathrm{d}z} + \frac{H_{\mathrm{d}x} + H_{\mathrm{d}y}}{2}\right), \tag{6.34}$$

for $\theta = \pi$, where parameters $a(\theta)$ and $b(\theta)$ are calculated in respective magnetic configurations. Note, that the critical currents in P and AP configurations are not symmetric in general, i.e. $I_\mathrm{c}^\mathrm{P} \neq -I_\mathrm{c}^\mathrm{AP}$, which stems from the dependence of the critical current on the external magnetic field H_ext and on the fact that generally $a(\theta = 0) \neq a(\theta = \pi)$ and $b(\theta = 0) \neq b(\theta = \pi)$.

Described method is applied in Section 9 to study critical current in dual spin valves with one perpendicular and one in-plane polarizer.

6.4 Critical current in case of thermal activation

The critical current in the presence of thermal fluctuations was experimentally and theoretically studied by Koch et al [100]. In their study they measured rate of current-induced magnetization reversal in a standard Co/Cu/Co spin valve. They explained their results in frame of a simplified macrospin model. They included the spin transfer torque in the form of effective magnetic field

$$\frac{1}{\gamma}\frac{\mathrm{d}\mathbf{M}}{\mathrm{d}t} = \mathbf{M}\times\left[\mathbf{H} - \frac{\alpha}{M_\mathrm{s}}\,\mathbf{M}\times(\mathbf{H} + \mathbf{H}_\mathrm{s})\right], \tag{6.35}$$

[10] Note, because the studied equilibria are coincident with the poles of the spherical coordinate system we had to rotate the studied structure in order to study the stability of these equilibria.

where $\mathbf{H}$ is the effective field, and $\mathbf{H}_\mathrm{s} = [(\eta I\hbar)/(2em\alpha)]\boldsymbol{n}_\mathrm{s}$ represents the Slonczewski's torque term [25] with polarization η. In a special case when $\mathbf{H}$ is collinear with $\mathbf{H}_\mathrm{s}$ one can rewrite LLG as

$$\frac{1}{\gamma}\frac{\mathrm{d}\mathbf{M}}{\mathrm{d}t} = \mathbf{M}\times\left[\mathbf{H} - \frac{\tilde{\alpha}}{M_\mathrm{s}}\mathbf{M}\times\mathbf{H}\right], \tag{6.36}$$

where $\tilde{\alpha} = \alpha(1 + H_\mathrm{s}/H)$ is an effective damping parameter including also the spin torque action. Note, if $H_\mathrm{s} < -H$ than $\tilde{\alpha} < 0$ turns to repulsion due to energy pumping rather than damping. Then, the thermal effective field can be added to the LLG analogically as described in Section 5.2.1, but with an effective temperature $\tilde{T}$ which obeys $\tilde{\alpha}\tilde{T} = \alpha T$. Then one can use a picture for thermally activation magnetization reversal without spin current but with an effective damping $\tilde{\alpha}$ and effective temperature $\tilde{T}$. Then the thermal-activation life-time, τ, is given simply by

$$\tau = \tau_0 \exp\left(E/k_\mathrm{B}\tilde{T}\right), \tag{6.37}$$

where τ_0 is inverse of the attempt frequency and E is the energy barrier which has to be overcame during the reversal process. Then the switching rate, which is proportional to τ^{-1}, is controlled by the current density via the parameter $\tilde{T}$, which explicitly reads

$$\tilde{T} = \frac{T}{1 + I\,(\eta\hbar/2em\alpha H)}\,. \tag{6.38}$$

This relation leads to critical current [100, 101]

$$I_\mathrm{c} = I_{\mathrm{c}\,0}\,\left[1 - (k_\mathrm{B}T/E)\ln\left(\tau/\tau_0\right)\right], \tag{6.39}$$

where I_{c0} is critical current calculated at zero temperature, $T = 0$. The switching rate is then given by

$$\tau^{-1} = \tau_0^{-1}\,\exp\left[-\Delta_0\,(1 - I/I_{\mathrm{c}0})\right], \tag{6.40}$$

where $\Delta_0 = E/k_\mathrm{B}T$ and $\Delta = \Delta_0(1 - I/I_{\mathrm{c}0})$ defines the thermal stability in the presence of current-induced torque. Equations (6.39) and (6.40) can be used when $I \ll I_{\mathrm{c}0}$. For higher currents the spin torque becomes dominant and the thermal fluctuations are suppressed.

Recently, more accurate theories [102] based on the Fokker-Planck equation show that the thermal stability is not linear in $1 - I/I_{\mathrm{c}0}$, as found by Koch et al [100], but $\Delta = \Delta_0(1 - I/I_{\mathrm{c}0})^2$.

7 Current-pulse-induced magnetization switching in standard and nonstandard spin valves

In this section we shall deal with current-induced dynamics of single spin valves, i.e. spin valves with only one polarizer with fixed magnetization (called as *fixed layer* or *reference layer*) and one *free layer* (also known as *sensing layer*). As already mentioned in the introduction, there are two types of single spin valves: *standard* spin valves, with spin transfer torque (STT) vanishing only in collinear configurations of the fixed and free layers' magnetization, and *nonstandard* spin valves with STT vanishing also in a certain noncollinear magnetic configuration. Current-induced dynamics and magnetization switching in standard spin valves have been extensively studied from the late 1990s theoretically [25, 26] as well as experimentally [27, 103, 28, 104]. On the other hand, study of nonstandard spin valves started with theoretical predictions [105, 33, 34], which were further studied theoretically [35, 36, 37, 32, 51] and experimentally confirmed [40, 41]. In addition, experimental results were also analyzed using micromagnetic computer simulations [39, 38].

As already shown in Section 3, a nonstandard angular dependence of STT appears when bulk and interface asymmetries of the fixed layer's material are markedly different from the material parameters of the free layer. Moreover, the spin accumulation in the nonmagnetic spacer must be large enough and, hence, large spin diffusion length in the central nonmagnetic layer is required ($\propto 1\mu$m). Thus, such a nonstandard angular dependence of STT can be observed e.g. in Co(8)/Cu(10)/Py(8) [33] trilayer, sandwiched between nonmagnetic Cu electrodes, with Co(8) being the fixed and Py(8) the free layer. The numbers in the brackets stand for layer thicknesses in nanometers.

The main difference between current-induced magnetization dynamics in standard and nonstandard spin valves consists in the following: In standard spin valves, current (which is large enough) flowing in one direction destabilizes the free layer's magnetization from the parallel (P) configuration (with respect to the fixed layer's magnetization) and stabilizes the antiparallel magnetic configuration (AP). To destabilize the free layer's magnetization from AP configuration one needs to reverse the current direction. Conversely, in nonstandard spin valves, current flowing in one direction destabilizes both P and AP magnetic configurations while current flowing in the opposite direction stabilizes both of them. This special feature leads to a nonstandard magnetization dynamics when the free layer's magnetization might steadily precess without need of external magnetic field [35]. This might be interesting from the application point of view since magnetization precessions generate microwaves, which are used in wireless communication devices.

In this chapter, we shall examine switching properties of a nonstandard spin valve, i.e. ability to change the free layer's magnetization by electric current pulse. This is important from the point of view of employing spin valve as a memory cell. Experimentally, one can distinguish between P and AP magnetic configuration utilizing the effect of current-perpendicular-to-plane giant magnetoresistance (GMR). Fast and effective switching between these two states with electric current pulses might enhance recently used hard memory disks based on magnetic field switching. Here, we shall examine switching in Cu-Co(8)/Cu(10)/Py(8)-Cu spin valve with a short rectangular electric pulse as a function of pulse parameters (pulse length and current density). In order to compare current-pulse-induced switching in a nonstandard spin valve with a standard one, we start the analysis of standard Cu-Py(20)/Cu(10)/Py(8)-Cu spin valve. Note, that both studied spin valves have identical free layers and spacers and differ only in the fixed layer. Then we shall

describe the dynamics of free layer magnetization in the nonstandard spin valve. Finally, we shall discuss the possibility of an enhancement of current-induced switching in nonstandard spin valves employing some specific switching schemes.

7.1 Model

Here, we assume that both magnetic layers of the studied spin valves have no domain structure. Hence, one can employ the macrospin (single domain) model to study the magnetization dynamics. Time evolution of the unit vector $\hat{\boldsymbol{s}} = (s_x, s_y, s_z)$ along the net spin moment of the sensing layer is described by the generalized Landau-Lifshitz-Gilbert equation (for details see Section 5),

$$\frac{\mathrm{d}\hat{\boldsymbol{s}}}{\mathrm{d}t} = -|\gamma_\mathrm{g}|\mu_0\, \hat{\boldsymbol{s}} \times \mathbf{H}_\mathrm{eff} - \alpha\, \hat{\boldsymbol{s}} \times \frac{\mathrm{d}\hat{\boldsymbol{s}}}{\mathrm{d}t} + \frac{|\gamma_\mathrm{g}|}{M_\mathrm{s} d}\, \boldsymbol{\tau}\,, \tag{7.1}$$

where γ_g is the gyromagnetic ratio, μ_0 is the magnetic vacuum permeability, M_s is the saturation magnetization and d is the free layer's thickness. The Gilbert damping parameter α is assumed to be constant, $\alpha = 0.01$. The effective field, $\mathbf{H}_\mathrm{eff}$, includes contributions from the external magnetic field (H_ext), uniaxial magnetic anisotropy (H_ani), demagnetization field ($\mathbf{H}_\mathrm{dem}$) and the thermal field ($\mathbf{H}_\mathrm{th}$) (for details see Section 4):

$$\mathbf{H}_\mathrm{eff} = -H_\mathrm{ext}\hat{\mathbf{e}}_z - H_\mathrm{ani}\,(\hat{\boldsymbol{s}} \cdot \hat{\mathbf{e}}_z)\,\hat{\mathbf{e}}_z + \mathbf{H}_\mathrm{dem} + \mathbf{H}_\mathrm{th}\,, \tag{7.2}$$

where $\hat{\mathbf{e}}_z$ is the unit vector along the axis z which is parallel to the in-plane magnetic easy axis. Note, that by definition, the external field is positive when it is pointing along the negative z axis. The demagnetization field corresponds to the sensing layer of an elliptical shape with the major and minor axis of 130 and 60 nanometers, respectively, and thickness of 8 nanometers. The magnetic easy axis is assumed to be along the longer axis of the ellipse, and $H_\mathrm{ani} = 100.5\,\mathrm{Oe}$. Finally, $\mathbf{H}_\mathrm{th}$ is the stochastic thermal field [88, 86, 106] related to the temperature, T, (for details see Section 5.2.2).

As concerns the STT, we take into account both in-plane and out-of-plane components, $\boldsymbol{\tau} = \boldsymbol{\tau}_\parallel + \boldsymbol{\tau}_\perp$, where

$$\boldsymbol{\tau}_\parallel = aI\, \hat{\boldsymbol{s}} \times (\hat{\boldsymbol{s}} \times \hat{\boldsymbol{S}})\,, \tag{7.3a}$$

$$\boldsymbol{\tau}_\perp = bI\, \hat{\boldsymbol{s}} \times \hat{\boldsymbol{S}}\,, \tag{7.3b}$$

where $\hat{\boldsymbol{S}}$ is a unit vector parallel to the net spin moment of the reference layer, $\hat{\boldsymbol{S}} = \hat{\mathbf{e}}_z$. Current density I is defined as positive when current flows from the reference layer towards the sensing one. Finally, the angular dependence of the parameters a and b has been calculated in the diffusive transport limit (for details see Section 3). The resulting in-plane and out-of-plane torque components of both studied spin valves are shown on Fig. 21, where θ is the angle between the magnetic moments of the reference and sensing layer ($\hat{\boldsymbol{s}} \cdot \hat{\boldsymbol{S}} = \cos\theta$).

7.2 Current-induced dynamics

Now, we shall analyze switching in the both standard and nonstandard spin valves from the P to AP state induced by a current pulse. Numerical solution of the LLG equation has been performed using the Heun Scheme [107, 86] (for details see Appendix E). For the initial configuration we

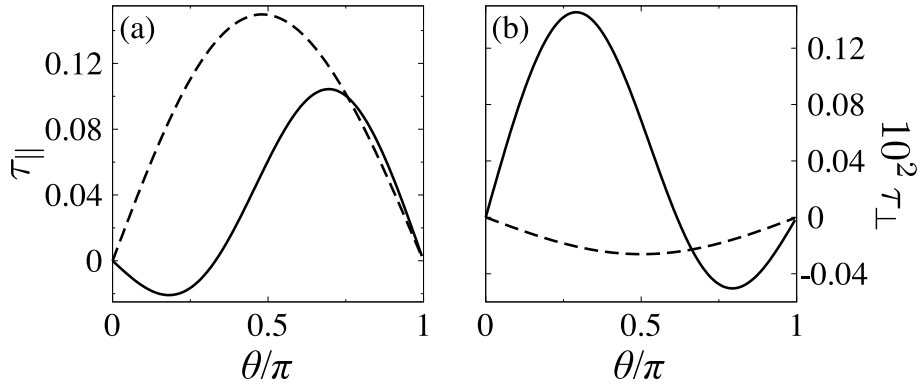

Figure 21: Comparison of spin-transfer torque in standard and nonstandard spin valves. (a) in-plane torque components, (b) out-of-plane torque components. Solid line corresponds to nonstandard, Co(8)/Cu(10)/Py(8), spin valve while dashed line is related to standard, Py(20)/Cu(10)/Py(8), spin valve.

assume a biased state with $\theta(t = 0) = 1°$ and $\phi(t = 0) = \pi/2$, where ϕ is the polar angle describing orientation of the vector $\hat{\boldsymbol{s}}$. The current pulse $i(t)$ of constant current density I and duration t_p is applied at $t = 0$, $i(t) = I[\Theta(t) - \Theta(t - t_p)]$, where $\Theta(x) = 1$ for $x > 0$ and $\Theta(x) = 0$ for $x \leq 0$.

A successful switching with the corresponding switching time t_s is counted when $\overline{s_z}(t_\mathrm{s}) < -0.99$, where $\overline{s_z}(t)$ is the exponentially weighted moving average [108]

$$\overline{s_z}(t) = \eta\, s_z(t) + (1 - \eta)\, \overline{s_z}(t - \Delta t)\,, \tag{7.4}$$

where Δt is the integration step, and the weighting parameter $\eta = 0.1$. The moving average $\overline{s_z}$ is calculated for time $t > t'$ when $s_z(t')$ reaches the value of -0.9; otherwise $\overline{s_z}(t) = s_z(t)$.

From the experimental point of view it is more convenient to reformulate the switching condition in terms of the magnetoresistance. We note that this holds only for the standard spin valves, in which the magnetoresistance is a monotonic function of the θ angle [109, 61]. In asymmetric spin valves the magnetoresistance can be a non-monotonic function of θ [61, 110], and therefore direct calculation of the magnetoresistance is then needed (this issue is discussed in the section 3.6).

7.2.1 Standard spin valve

First we consider a standard spin valve, Py(20)/Cu(10)/Py(8). The in-plane and out-of-plane components of the STT acting on the Py(8) sensing layer show sine-like angular dependences. Switching time as a function of the pulse duration t_p and reduced current density I/I_0 ($I_0 = 10^8\mathrm{Acm}^{-2}$) in zero temperature limit and absence of external magnetic field is shown in Figure 22. Two different regions in the switching diagram can be distinguished. First, the white non-switching region is observed for short current pulses and low current densities. In this region, the energy gain due to STT does not overcome the Gilbert damping and system stays in the initial local magnetic energy minimum. The second region corresponds to successful switching to the AP state. The switching time decreases nonmonotonously with increasing current density. The most bright area corresponds to the ultra-fast switching, in which the spin reaches the AP configuration before the current pulse ends ($t_\mathrm{s} < t_\mathrm{p}$). In such a case the switching is realized in a single ultra-fast step after a half precession around the x axis; see Fig. 22(b) right.

It is interesting to know that the boundary between non-switching and ultra-fast switching regions develops into a ripple structure. In this region, the energy gain due to spin-transfer leads to so called *retarded switching*, where the switching time $t_s > t_p$; see Figure 22(b) left. The switching for $t > t_p$ is associated with a ringing, where the spin relaxes to the AP state due to energy dissipation via the Gilbert damping only. Such dissipation, however, is rather slow and therefore the retarded switching is much more slower than the ultra-fast single-step switching.

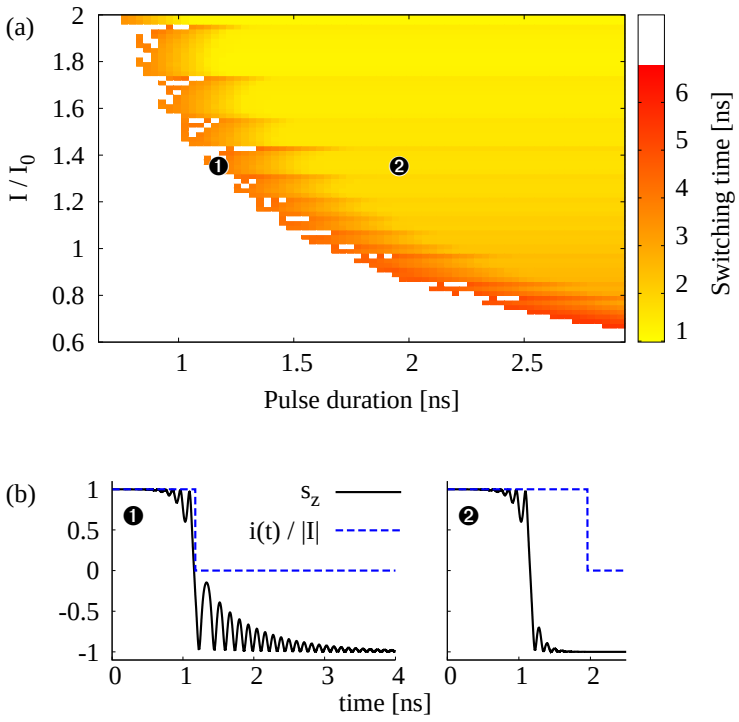

Figure 22: Current-pulse driven switching in the Py(20)/Cu(10)/Py(8) spin valve in the absence of magnetic field. (a) Switching time as a function of the pulse duration t_p and reduced current density I/I_0, $I_0 = 10^8 \mathrm{Acm}^{-2}$. (b) Temporal evolution of the s_z spin component under rectangular current pulse (dashed lines) of amplitude $I/I_0 = 1.4$ and duration $t_p = 1.2\,\mathrm{ns}$ (*retarded switching*, left) and $t_p = 2\,\mathrm{ns}$ (*fast switching*, right), corresponding to the points marked in the switching diagram (a).

In order to speed up switching from P to AP state one may consider a negative external magnetic field. In turn, a positive magnetic field exceeding the anisotropy field leads to commonly observed steady-state out-of-plane precessional (OPP) modes [103, 104, 28], which are the result of the energy balance between Gilbert damping and the energy gain from the spin-transfer.

The analysis shows that for positive external magnetic field, the continuous switching region in the diagram shown in Fig. 22(a) splits into a non-compact current dependent stripe structure. Figure 23(a) shows the switching diagram for $H_{ext} = 200\,\mathrm{Oe}$. The switching regions alternate with the stripes where the spin transfer generates the OPP regime. Since, the current pulse is finite, the final state depends on the actual spin state at $t = t_p$. This is shown in Fig. 23(b), where two switching events under the current pulses of the same amplitude ($I = 2.75\,I_0$) and different pulse duration are driven via the OPP regime. One can notice that in the switching regions the spin dynamics is similar to the zero-field switching discussed above.

To account for the stripe structure in more details, we plot in Fig. 23(c) map of the final spin

states as a function of the initial spin position $\hat{\boldsymbol{s}}_0 = \hat{\boldsymbol{s}}(t=0)$ for constant current amplitude and pulse duration $t_\mathrm{p} \to \infty$. The gray (black) regions correspond to the initial spin position, which results in the final OPP (AP) regime. Comparing the maps calculated for two different current densities ($I = 2.75\, I_0$ and $I = 3.00\, I_0$), one can see that the dynamical phase portrait depends rather strongly on the current density. In other words, current-driven dynamics from the same initial state can lead to different final states. Further increase of external magnetic field leads to shrinking of the P→AP switching regions. For fields much larger than the coercive field the switching stripes disappear and the OPP regime remains only.

The stripe structure is a result of deterministic dynamics and fixed initial condition. When a distribution of initial configurations is taken into account, some smearing of the border between the stripes appears (not shown). The boundaries are also smeared when non-zero temperature is considered. Figure 23(d) shows the switching probability as a function of the current pulse density, calculated for pulse duration $t_\mathrm{p} = 3\,\mathrm{ns}$ at $T = 4.2\,\mathrm{K}$ and $T = 77\,\mathrm{K}$, and for a fixed initial configuration. The statistics has been calculated from 10^4 events for each value of the current density. The switching probability follows the stripe structure corresponding to the zero temperature limit, and decreases with decreasing current amplitude. For $T = 77\,\mathrm{K}$, the probability is reduced by the factor of about 3 and the peaks broaden.

7.2.2 Nonstandard spin valve

The Co(8)/Cu(10)/Py(8) spin valve exhibits non-standard STT acting on the Py(8) layer. Due to the *wavy*-like dependence of the STT, shown by the solid lines in Fig. 21, positive current ($I > 0$) stabilizes both the P and AP configurations, while a negative ($I < 0$) current destabilizes both the collinear configurations. This characteristic property of the *wavy* torque raises a question whether it is possible to switch an asymmetric spin valve between P and AP states with current pulse only.

Figure 24(a) shows the switching diagram from P to AP for a rectangular current pulse. One can distinguish four characteristic switching regions. First region, denoted by (i), corresponds to low current amplitudes and/or short pulses, where switching does not take place. The non-compact region (ii) corresponds to relatively short pulses leading to the fast switching processes. In region (iii) the P/AP bistability of the final states is observed. Finally, in the region (iv) the final state of the dynamics depends on the current density, resulting in the band-like structure. This structure contains regions with final P state, which alternate with the regions of final AP state.

To explain the complex diagram structure, let us study current-pulse-induced dynamics due to the 6 ns pulse of amplitude $I = -3.45\, I_0$ at zero temperature. The time dependence of the spin components is shown in Fig. 24(b). When the current pulse is applied (in zero external magnetic field), it induces initially small-angle in-plane precessions (IPP) of the sensing layer around the z-axis. The precessional angle rapidly increases and spin dynamics turns to the OPP regime. Numerical analysis reveals that the transition to OPP regime depends on the current amplitude, and spin can precess with positive or negative s_x component. Assuming constant initial spin direction, OPP direction depends mainly on the current density. This appears because the spin trajectory is modified due to the current density. Such a situation is shown in Figure 23(c) for the Py/Cu/Py spin valve. Due to the sustained energy pumping to the system via the spin-transfer, the OPP angle decreases and the spin is finally driven into one of the possible static states (SS) close to the $\hat{\mathbf{e}}_x$ (SS_+), or $-\hat{\mathbf{e}}_x$ (SS_-), depending on the sign of the s_x component in the OPP regime. The $\mathrm{SS}_\pm$ states are the static fixed points. The $\mathrm{SS}_\pm$ points are close to the maximum magnetic

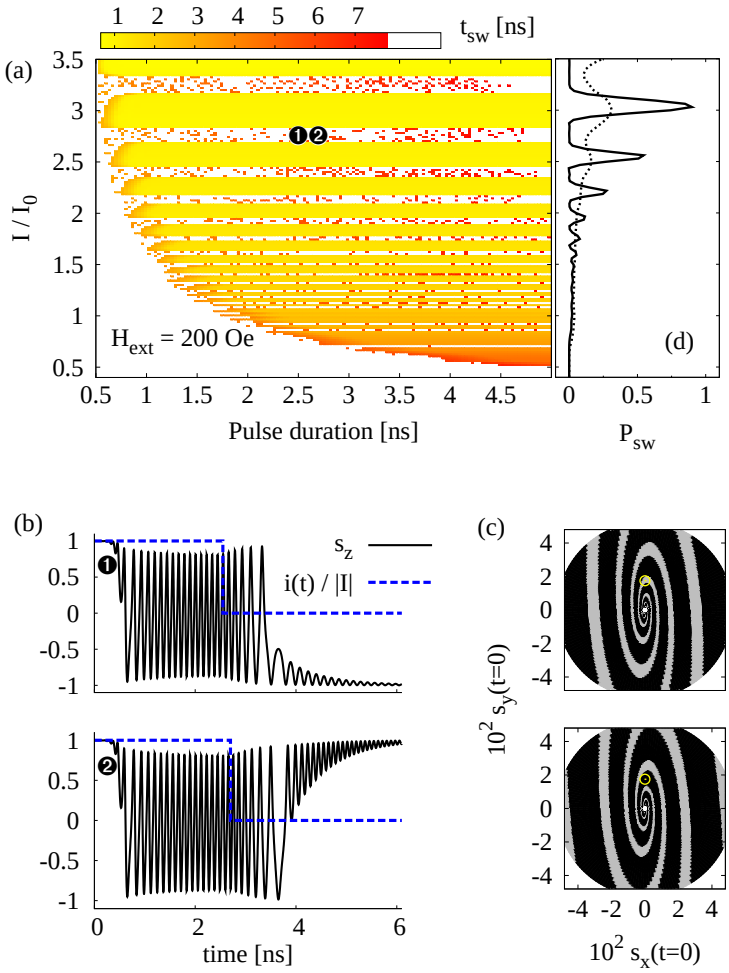

Figure 23: Effect of the external magnetic field $H_{\mathrm{ext}} = 200\,\mathrm{Oe}$ on the current-pulse driven dynamics in the Py(20)/Cu(10)/Py(8) spin valve. (a) Switching time as a function of reduced current density I/I_0 ($I_0 = 10^8 \mathrm{Acm}^{-2}$) and pulse duration t_{p}. (b) Temporal evolution of the s_z spin component under current pulses (dashed lines) marked in the switching diagram (a), corresponding to the amplitude $I = 2.75\,I_0$ and durations $t_{\mathrm{p}} = 2.56\,\mathrm{ns}$ (upper part) and $t_{\mathrm{p}} = 2.7\,\mathrm{ns}$ (lower part). (c) The maps of the final states as a function of initial spin bias for current pulse of $I = 2.75\,I_0$ (upper part) and $I = 3.0\,I_0$ (lower part), and for $t_{\mathrm{p}} \to \infty$. The spin dynamics initialized from the points inside the gray (black) areas leads finally to OPP regime (AP state). Circles denote the initial spin bias used in the simulations. (d) Thermally assisted switching probability, P_{sw}, from P to AP state, driven by a 3 ns rectangular current pulse, calculated as a function of current density at $T = 4.2\,\mathrm{K}$ (solid line) and $T = 77\,\mathrm{K}$ (dotted line).

energy. Therefore, if current is turned off, the spin position becomes unstable and the spin is driven due to Gilbert damping through the OPP regime with decreasing precessional frequency to the IPP regime. In the IPP regime, the spin precesses around $+\hat{\mathbf{e}}_z$ ($-\hat{\mathbf{e}}_z$) direction and is finally damped to the P (AP) state. We can observe that the position of the spin in the SS_- (SS_+) results in the final P (AP) state, see Fig. 24(b). Thus the alternation between P and AP states in the region (iv) in the diagram shown in Fig. 24(a), is predominantly controlled by current.

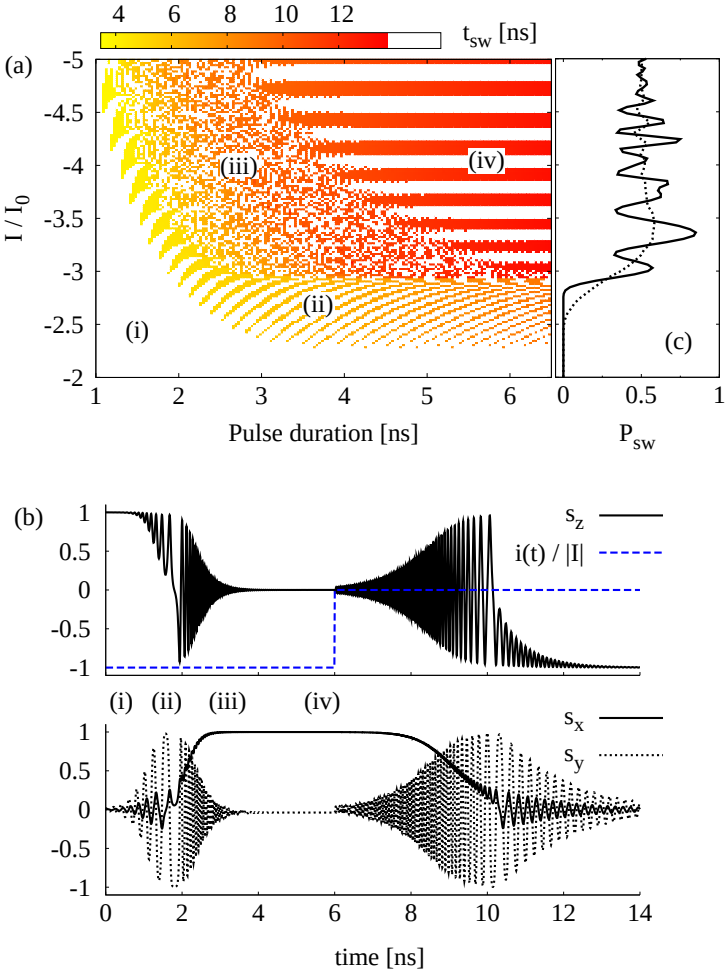

Figure 24: Current-pulse induced switching in the asymmetric Co(8)/Cu(10)/Py(8) spin valve at zero magnetic field. (a) Switching time as a function of the pulse duration t_p and reduced current density I/I_0, $I_0 = 10^8 \mathrm{Acm}^{-2}$. (b) Temporal evolution of $\hat{\boldsymbol{s}}$ under the 6 ns current pulse of the amplitude $I = -3.45\, I_0$. (c) Thermally assisted switching probability, P_sw, from P to AP, driven by 6 ns rectangular current pulse, calculated as a function of current density at $T = 4.2\,\mathrm{K}$ (solid line) and $T = 77\,\mathrm{K}$ (dotted line).

To better understand the regions in the diagram [Fig. 24(a)], one has to consider shorter pulses. According to the diagram, the pulse for successful switching has to exceed a critical current density and duration. In the static limit ($t_\mathrm{p} \to \infty$) the critical density is about $I = -1.0\, I_0$. For a finite pulse duration, higher densities are necessary to drive the spin during the time t_p away from the P state. When the pulse is shorter than a critical one, the relaxation back to the P state appears [region (i)]. For the higher current densities, the spin is driven faster away and a shorter escape time is needed. If the pulse ends just before the onset of the OPP regime, the relaxation via the

Gilbert dissipation drives the system to the AP state [region (ii)]. If the spin is driven further away from the P state, the IPP regime switches fast to the OPP one. In such a case the final state strongly depends on the precession phase at $t = t_{\mathrm{p}}$. This gives rise to the P/AP bistability in the region (iii). The bistable regime appears up to the pulse duration that is not longer than the time necessary for spin stabilization in the $\mathrm{SS}_{\pm}$ state. Note, that this analysis is valid only for current amplitudes $I \gtrsim 3\, I_0$. In case of smaller amplitudes, only the steady-state large-angle IPP regime occurs, and apart from the region (i) only the region (ii) is present. The periodic rib-like structure in the region (ii) appears due to the dependence of the final state on the precession phase at time $t = t_{\mathrm{p}}$.

The final state is affected by the thermal noise for $T > 0$ that modifies the overall spin switching trajectory. Figure 24 shows switching probability as a function of the current density for $t_{\mathrm{p}} = 6\,\mathrm{ns}$, and $T = 4.2\,\mathrm{K}$ (solid line) and $T = 77\,\mathrm{K}$ (dotted line). The switching probability oscillates following the zero-temperature stripe structure, similarly as for the spin valve Py(20)/Cu(10)/Py(8), see Figure 23(b). However, the probability P_{sw} oscillates now around $P_{\mathrm{sw}} = 0.5$, and for increased current densities approaches this value for any temperature. For higher current densities the spin is driven via the OPP-like transient regime much closer to the SS state. This regime is sensitive to the thermal fluctuations mainly due to the component of the thermal field transverse to the spin trajectory. When the spin remains in the transient regime for a longer time, the impact of thermal fluctuations is more pronounced and leads to equilibration of the probabilities for switching to the P and AP states ($P_{\mathrm{sw}} \to 0.5$).

7.3 Enhancement of switching in nonstandard spin valve

From the above follows that the fastest switching processes in the asymmetric spin valves appear in the region (ii) [see Fig. 24(a)]. This region, however, is non-compact and therefore to obtain a successful switching one has to set the current pulse parameters very precisely. In the region (iii) the bistability of the final state makes the switching out of control. Thus, the most suitable for switching is the region (iv). For a proper choice of parameters (pulse duration and current amplitude, thermal effects), corresponding to the maximum of P_{sw}, see Fig. 24(c), it is possible to obtain controllable switching. However, complex spin dynamics, especially the ringing after the end of current pulse, significantly lengthen the switching time. In practice, the longer the switching time is the more sensitive is the spin evolution to the external disturbances and temperature. Therefore, it is required from the applications point of view to shorten the switching time as much as possible. Accordingly, one can consider two switching schemes for a nonstandard spin valve structure. The first one is based on two current pulses of opposite current direction (*double-pulse* switching scheme). The second one makes use of single pulse of current followed by a pulse of magnetic field (hybrid switching scheme)

7.3.1 Double-pulse switching scheme

This scheme includes two rectangular current pulses of certain amplitudes and durations. The first pulse of negative current, referred to as *destabilizing pulse*, drives the spin out of its initial position. The second pulse of positive current, called *stabilizing pulse*, controls the dynamics and drives the spin into the final state. The stabilizing pulse additionally shortens the switching time (suppressing the ringing) via additional energy dissipation.

Figure 25(a) shows time evolution of the s_z component due to single current-pulse and double current-pulse. Here we consider infinitely long stabilizing pulse that in principle has no effect on the spin dynamics for $t \gtrsim 6.5\,\mathrm{ns}$. Due to the first current pulse of density $I = -4.0\,I_0$, the STT drives the spin to the SS state. When the first pulse is not followed by the second (stabilizing) one, the spin returns back via the OPP and IPP regimes to the initial state. In the case of double-pulse, however, the stabilizing pulse of $I = 2.0\,I_0$ drives the spin to the AP state. More systematical study reveals that including the stabilizing current pulse of $I = 2\,I_0$ leads to considerable modification of the switching diagram. First, the region (ii) becomes wider and the switching times under these current pulses falls down from 4 to 1 ns. Second, the bistability in the region (iii) becomes reduced, but still not completely removed. Finally, in the region (iv) the bands related to switching become enlarged, e.g., at $T = 0\,\mathrm{K}$, in the range of amplitudes from $I \simeq -3.5\,I_0$ to $-4.5\,I_0$ one obtains controllable switching for pulses $t_\mathrm{p} \gtrsim 4\,\mathrm{ns}$.

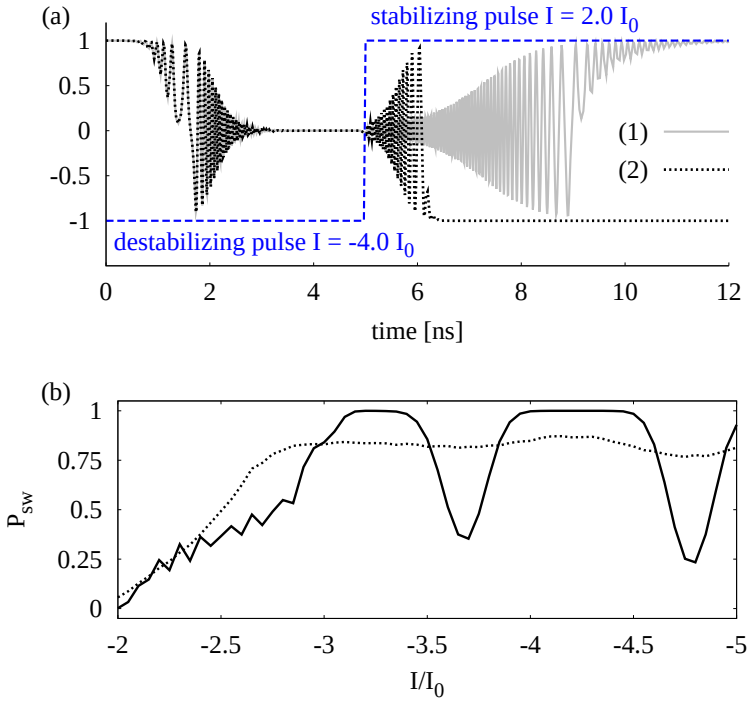

Figure 25: Demonstration of *double-pulse switching scheme* making use of second (stabilizing) pulse. (a) Evolution of s_z spin component. Line (1) corresponds to a single $t_\mathrm{p} = 5\,\mathrm{ns}$ (*destabilizing*) current pulse of amplitude $I = -4.0\,I_0$ in zero magnetic field and zero temperature. Line (2) shows the evolution of s_z in the case when the first pulse is followed by a second (*stabilizing*) pulse of opposite direction and $I = 2.0\,I_0$ (the double current pulse is shown by the blue dashed line). (b) Thermally assisted switching probability P_sw from the P to AP states, driven by a 5 ns (*destabilizing*) current pulse (negative) followed by a *stabilization* current pulse of $I = 2.0\,I_0$ and $t_\mathrm{p} \to \infty$, calculated as a function of the reduced current density I/I_0 of the *destabilizing* pulse, $I_0 = 10^8\,\mathrm{Acm}^{-2}$, for $T = 4.2\,\mathrm{K}$ (solid line) and $T = 77\,\mathrm{K}$ (dotted line).

In addition to the enhanced controllability due to the stabilizing pulse, one can observe enhancement of the switching probability at finite temperatures. Figure 25(b) shows the switching probability as a function of the current density of 5 ns destabilizing pulse, that is followed by a stabilization current pulse of $I = 2.0\,I_0$ and $t_\mathrm{p} \to \infty$. For $T = 4.2\,\mathrm{K}$ and $I < -3\,I_0$, the probability

P_{sw} oscillates with increasing current magnitude, similarly as in the case of a single pulse, see Fig. 24(c). The regions of successful switching are then broadened and the corresponding amplitude is close to unity. In the case of $T = 77\,\mathrm{K}$, the switching probability in this region is roughly constant and approaches $P_{\mathrm{sw}} \simeq 0.8$.

7.3.2 Hybrid switching scheme

Hybrid switching scheme combines both pulse of electric current followed by a pulse of magnetic current. The idea of current-field-pulse scheme is simple. Initially, one applies a pulse of electric current, which pushes the spin out of its initial configuration towards the out-of-plane stationary points. After the current is switched off, a pulse of magnetic field is applied in the direction of desired magnetization state. Then the magnetization is simply damped into the final in-plane stationary point. An example of this scheme is shown on Fig. 26. This scheme is supposed to be

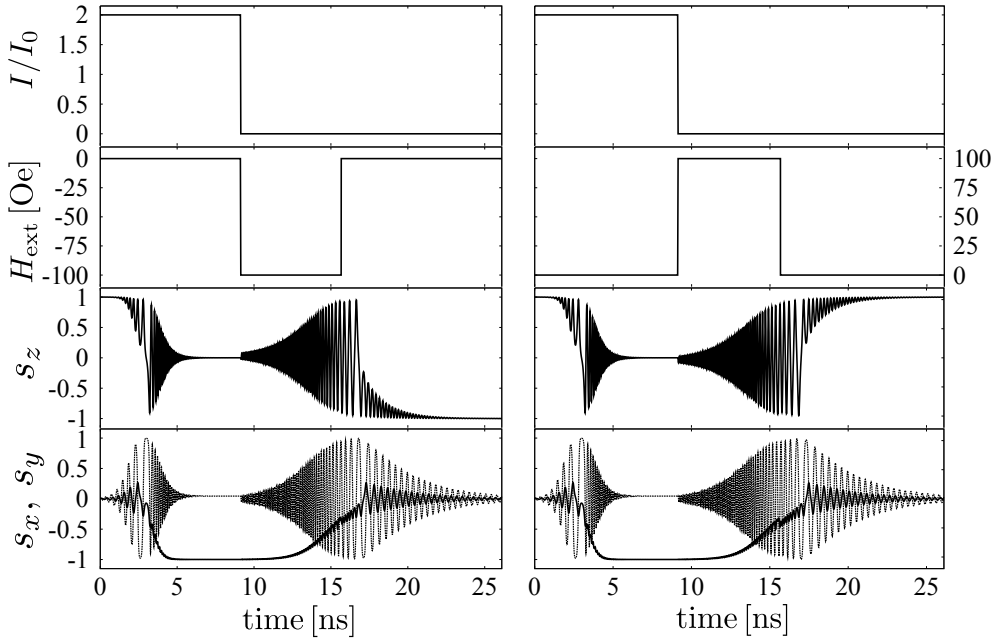

Figure 26: The hybrid switching scheme based on the current and magnetic field pulses. From the top: the current pulse; magnetic field pulse; time evolution of spin component s_z; time evolutions of spin components s_x (solid line) and s_y (dot line). The left part describes switching to the AP state, while spin dynamics in the right part ends in the initial P state.

faster than switching by one or two magnetic field pulses, because energy pumping by current is usually more efficient than energy dissipation in external magnetic field. Moreover, for enough long pulses the scheme might lead to 100% switching probability even for non-zero temperature. A disadvantage of this scheme in comparison to the double-pulse scheme is the limitation of the switching rate caused by slow magnetization dynamics in the field pulse phase.

8 Current-induced dynamics in noncollinear dual spin valves

In the introduction we mentioned that there are several issues which should be solved. First of them is the critical current needed to induce current-induced dynamics in spin valves. In order to efficiently manipulate with magnetization direction and decrease necessary energy costs, the reduction of critical current is required. Consequently, enhancement of spin-transfer torque (STT) is needed also to fasten up the spin dynamics and reduce the switching rate.

Another problem is related to the angular dependence of STT. When we compare STT angular dependences in different standard and non-standard spin valve structures, we can see more or less pronounced differences in their symmetries and amplitudes. All these features might influence the current-induced spin dynamics including the critical currents. On one side, the angular dependence of STT can be controlled by means of used materials with different bulk and interracial parameters. However, this way is technologically inefficient because the choice of materials which can be used for spin valve construction is restricted and we still cannot properly prepare materials with desired properties. On the other hand, STT also depends on the thicknesses of the used layers.

Motivated by the above mentioned issues, in this chapter, so called *dual spin valve* (DSV) is considered. The concept of dual spin valve was introduced by L. Berger [48] who proposed a spin valve structure with two ferromagnetic polarizers (fixed layers) and a sensing (free) layer sandwiched between them and separated from them by nonmagnetic spacers. In his study, Berger has shown that when the magnetizations of the outer layers (polarizers) are antiparallel, the spin transfer torque acting on the central layer is enhanced in comparison to single spin valves (SSV), with only one polarizer. The enhancement of STT results in reduction of critical current and switching rate. The main reason for this effect is the enhancement of the spin accumulation at the free layer's interfaces. While in a single spin valve there is only one interface which can produce spin torque on the magnetization, in DSV both interfaces of the free layer can be used for STT generation.

Berger has studied DSV only in collinear magnetic configurations. Here, DSV structure in non-collinear magnetic configurations is considered. In agreement with Berger [48] we show that the spin accumulation in a dual spin valve might be enhanced in the antiparallel magnetic configuration. In turn, STT can be eliminated in a symmetric DSV structure with parallel orientation of the outer magnetizations. Moreover, it shall be demonstrated that one can manipulate with the angular dependence of STT acting on the central layer varying the angle between outer magnetizations.

8.1 Model

Considered nanopillar structure, $F_L/N_L/F_C/N_R/F_R$, consists of three ferromagnetic (F) layers separated by normal-metal (N) layers; see Fig. 27. Spin moment of the central layer, F_C, is free to rotate, while the right F_R and left F_L ferromagnetic layers are much thicker and their net spin moments are fixed for current densities of interest. Such a fixing can be achieved either by sufficiently strong coercive fields, or by exchange anisotropy at interfaces with antiferromagnetic materials.

In the Landau-Lifshitz-Gilbert phenomenological description, the dynamics of a unit vector

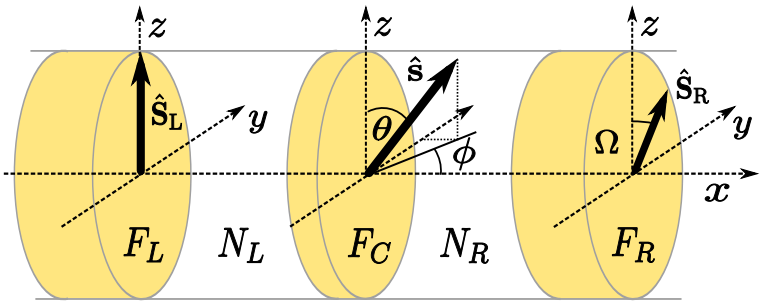

Figure 27: Cartoon of noncollinear dual spin valve with two fixed magnetic moments of the outer magnetic layers, $\mathrm{F_L}$ and $\mathrm{F_R}$, and free central magnetic layer, $\mathrm{F_C}$, separated by normal-metal layers $\mathrm{N_L}$ and $\mathrm{N_R}$. Here, $\hat{\boldsymbol{S}}_{\mathrm{L}}$, $\hat{\boldsymbol{S}}_{\mathrm{R}}$, and $\hat{\boldsymbol{s}}$ are unit vectors along the spin moments of the $\mathrm{F_L}$, $\mathrm{F_R}$, and $\mathrm{F_C}$ layers, respectively.

along the net spin moment $\hat{\boldsymbol{s}}$ of the central (free) magnetic layer is given by (for details see Sec. 5).

$$\frac{\mathrm{d}\hat{\boldsymbol{s}}}{\mathrm{d}t} + \alpha\,\hat{\boldsymbol{s}} \times \frac{\mathrm{d}\hat{\boldsymbol{s}}}{\mathrm{d}t} = \boldsymbol{\Gamma}\,, \qquad \text{where} \qquad \boldsymbol{\Gamma} = -|\gamma_{\mathrm{g}}|\mu_0\,\hat{\boldsymbol{s}} \times \mathbf{H}_{\mathrm{eff}} + \frac{|\gamma_{\mathrm{g}}|}{M_{\mathrm{s}}d}\,\boldsymbol{\tau}\,. \tag{8.1}$$

The standard effective magnetic field, $\mathbf{H}_{\mathrm{eff}}$, is used

$$\mathbf{H}_{\mathrm{eff}} = -H_{\mathrm{ext}}\hat{\mathbf{e}}_z - H_{\mathrm{ani}}\,(\hat{\boldsymbol{s}}\cdot\hat{\mathbf{e}}_z)\,\hat{\mathbf{e}}_z + \mathbf{H}_{\mathrm{dem}}\,. \tag{8.2}$$

Up to now the description of dynamics is identical with single spin valves since we omitted magnetostatic interactions between magnetic layers. However, the term for STT, $\boldsymbol{\tau}$, have to be extended since the free layer in DSV encounters STT acting on both interfaces.

8.1.1 Spin-transfer torque

The STT acting on a magnetic layer is determined by the electron spin angular momentum absorbed from conduction electrons within a few interfacial atomic layers of the ferromagnet [93]. Thus, the STT acting on the central layer $\mathrm{F_C}$ can be calculated as

$$\boldsymbol{\tau} = \frac{\hbar}{2}(\boldsymbol{j}_{\perp}^{\mathrm{L}} - \mathbf{j}_{\perp}^{\mathrm{R}}), \tag{8.3}$$

where $\boldsymbol{j}_{\perp}^{\mathrm{L}}$ and $\boldsymbol{j}_{\perp}^{\mathrm{R}}$ are the spin current components perpendicular to magnetic moment of the free layer and calculated at the corresponding left and right normal-metal/ferromagnet interfaces. The torque consists of in-plane $\boldsymbol{\tau}_{\parallel}$ and out-of-plane $\boldsymbol{\tau}_{\perp}$ part, $\boldsymbol{\tau} = \boldsymbol{\tau}_{\parallel} + \boldsymbol{\tau}_{\perp}$, which read

$$\boldsymbol{\tau}_{\parallel} = I\,\hat{\boldsymbol{s}} \times \left[\hat{\boldsymbol{s}} \times \left(a_{\mathrm{L}}\hat{\boldsymbol{S}}_{\mathrm{L}} - a_{\mathrm{R}}\hat{\boldsymbol{S}}_{\mathrm{R}}\right)\right]\,, \tag{8.4a}$$

$$\boldsymbol{\tau}_{\perp} = I\,\hat{\boldsymbol{s}} \times \left(b_{\mathrm{L}}\hat{\boldsymbol{S}}_{\mathrm{L}} - b_{\mathrm{R}}\hat{\boldsymbol{S}}_{\mathrm{R}}\right)\,, \tag{8.4b}$$

where I is the current density, and $\hat{\boldsymbol{S}}_{\mathrm{L}}$ and $\hat{\boldsymbol{S}}_{\mathrm{R}}$ are the unit vectors pointing along the fixed net-spins of the $\mathrm{F_L}$ and $\mathrm{F_R}$ layers, respectively. The parameters a_{L}, a_{R}, b_{L}, and b_{R} depend, generally, on the magnetic configuration and material composition of the system, and have been calculated in the diffusive transport limit [33], as described in Section 3.

Let us now examine how the STT, given by (8.4), affects spin dynamics of the free magnetic layer. Following Appendix D, we rewrite Eq.(8.1) in spherical coordinates (θ, ϕ), where $\hat{\boldsymbol{s}} = (\cos\phi\sin\theta, \sin\phi\sin\theta, \cos\theta)$; see Fig. 27. Then LLG reads

$$\frac{\mathrm{d}}{\mathrm{d}t}\begin{pmatrix}\theta\\ \phi\end{pmatrix} = \frac{1}{1+\alpha^2}\begin{pmatrix}1 & \alpha\\ -\alpha\sin^{-1}\theta & \sin^{-1}\theta\end{pmatrix}\begin{pmatrix}v_\theta\\ v_\phi\end{pmatrix}, \tag{8.5}$$

where the overall torques v_θ and v_ϕ are given by

$$v_\theta = \boldsymbol{\Gamma}\cdot\hat{\mathbf{e}}_\theta = -|\gamma_\mathrm{g}|\mu_0 H_\theta + \frac{|\gamma_\mathrm{g}|}{M_\mathrm{s}d}\tau_\theta\,, \tag{8.6a}$$

$$v_\phi = \boldsymbol{\Gamma}\cdot\hat{\mathbf{e}}_\phi = -|\gamma_\mathrm{g}|\mu_0 H_\phi + \frac{|\gamma_\mathrm{g}|}{M_\mathrm{s}d}\tau_\phi\,. \tag{8.6b}$$

The terms H_θ and H_ϕ in Eqs. (8.6) describe the torques due to effective magnetic fields. These terms are implicitly given in equations (6.31). More important for our analysis are τ_θ and τ_ϕ, which stand for STT components acting in the $\hat{\mathbf{e}}_\theta$ and $\hat{\mathbf{e}}_\phi$ directions, respectively. Since they include both $\boldsymbol{\tau}_\parallel$ and $\boldsymbol{\tau}_\perp$ one can write: $\tau_\theta = \tau_\theta^\parallel + \tau_\theta^\perp$ and $\tau_\phi = \tau_\phi^\parallel + \tau_\phi^\perp$, where $\tau_\theta^\parallel = \boldsymbol{\tau}_\parallel\cdot\hat{\mathbf{e}}_\theta$, $\tau_\theta^\perp = \boldsymbol{\tau}_\perp\cdot\hat{\mathbf{e}}_\theta$; $\tau_\phi^\parallel = \boldsymbol{\tau}_\parallel\cdot\hat{\mathbf{e}}_\phi$, and $\tau_\phi^\perp = \boldsymbol{\tau}_\perp\cdot\hat{\mathbf{e}}_\phi$.

As we have already mentioned, the main contribution to STT comes from $\boldsymbol{\tau}_\parallel$. Assuming now that magnetic moment of the left magnetic layer is fixed along the z-axis, $\hat{\boldsymbol{S}}_\mathrm{L} = (0,0,1)$, and magnetic moment of the right magnetic layer is rotated by an angle Ω from the z-axis and fixed in the layer's plane, as shown on Fig. 27, $\hat{\boldsymbol{S}}_\mathrm{R} = (0, \sin\Omega, \cos\Omega)$, one finds

$$\tau_\theta^\parallel = (a_\mathrm{L} - a_\mathrm{R}\cos\Omega)I\sin\theta + a_\mathrm{R}I\sin\Omega\sin\phi\cos\theta\,, \tag{8.7a}$$

$$\tau_\phi^\parallel = a_\mathrm{R}I\cos\phi\sin\Omega\,. \tag{8.7b}$$

The component $\tau_\theta^\parallel$ consists of two terms. The first one is analogous to the term which describes STT in a SSV. However, its amplitude is now modulated due to the presence of $\mathrm{F_R}$. In turn, the second term in Eq. (8.7a) is nonzero only in noncollinear magnetic configurations ($\Omega \neq 0, \pi$). From Eq. (8.7b) follows that $\tau_\phi^\parallel$ is also nonzero in noncollinear configurations, and only if the magnetization points out of the layer's plane ($\phi \neq \pi/2$). When magnetic moments of the outer magnetic layers are parallel ($\Omega = 0$), $\tau_\theta^\parallel = (a_\mathrm{L} - a_\mathrm{R})I\sin\theta$. For a symmetric DSV, $a_\mathrm{L}(\theta) = a_\mathrm{R}(\theta)$, and hence STT acting on $\hat{\boldsymbol{s}}$ vanishes. On the other hand, in the antiparallel configuration of $\hat{\boldsymbol{S}}_\mathrm{L}$ and $\hat{\boldsymbol{S}}_\mathrm{R}$ ($\Omega = \pi$), the maximal spin torque enhancement can be achieved, $\tau_\theta^\parallel = (a_\mathrm{L} + a_\mathrm{R})I\sin\theta$.

Similar analysis of $\boldsymbol{\tau}_\perp$ leads to the following formulas for $\tau_\theta^\perp$ and $\tau_\phi^\perp$:

$$\tau_\theta^\perp = b_\mathrm{R}I\cos\phi\sin\Omega\,, \tag{8.8a}$$

$$\tau_\phi^\perp = -(b_\mathrm{L} - b_\mathrm{R}\cos\Omega)I\sin\theta + b_\mathrm{R}\cos\theta\sin\phi\sin\Omega\,. \tag{8.8b}$$

Thus, if the outer magnetic moments are collinear, $\tau_\theta^\perp = 0$, while $\tau_\phi^\perp$ reduces to $\tau_\phi^\perp = -(b_\mathrm{L} - b_\mathrm{R})I\sin\theta$ for $\Omega = 0$, and $\tau_\phi^\perp = -(b_\mathrm{L} + b_\mathrm{R})I\sin\theta$ for $\Omega = \pi$. Hence, in symmetric spin valves, where $b_\mathrm{L} = b_\mathrm{R}$, $\tau_\phi^\perp$ vanishes in the parallel configuration of the outermost magnetic moments and is enhanced in the antiparallel configuration.

8.2 Symmetric dual spin valves

Consider first symmetric DSVs with antiparallel orientation of magnetic moments of the outermost ferromagnetic films: $\hat{\boldsymbol{S}}_\mathrm{L} = (0,0,1)$ and $\hat{\boldsymbol{S}}_\mathrm{R} = (0,0,-1)$. As follows from Eqs. (8.7)

and (8.8), such a configuration may lead to enhancement of STT in comparison to that in SSVs. To show this let us analyze first STT in two types of structures: the double spin valve F(20)/Cu(10)/F(8)/Cu(10)/F(20) in the antiparallel configuration, and the corresponding single spin valve F(20)/Cu(10)/F(8). The numbers in brackets correspond to layer thicknesses in nanometers.

Figure 28 shows the angular dependence of STT for DSVs and SSVs, when the vector $\hat{\boldsymbol{s}}$ changes its orientation (described by angle θ) in the layer plane ($\phi = \pi/2$). The magnetic layers made of Permalloy, $Ni_{80}Fe_{20}$ (Fig. 28a), and of Cobalt (Fig. 28b) are considered. Due to the additional fixed layer (F_R), STT in DSVs is about twice as large as in SSVs, which is consistent with Berger's predictions [26]. Additionally, the angular dependence of STT acting on the free layer in Co/Cu/Co spin valves is more asymmetric than in Py/Cu/Py. This asymmetry, however, disappears in Co/Cu/Co/Cu/Co DSVs due to superposition of the contributions from both fixed magnetic layers to the STT.

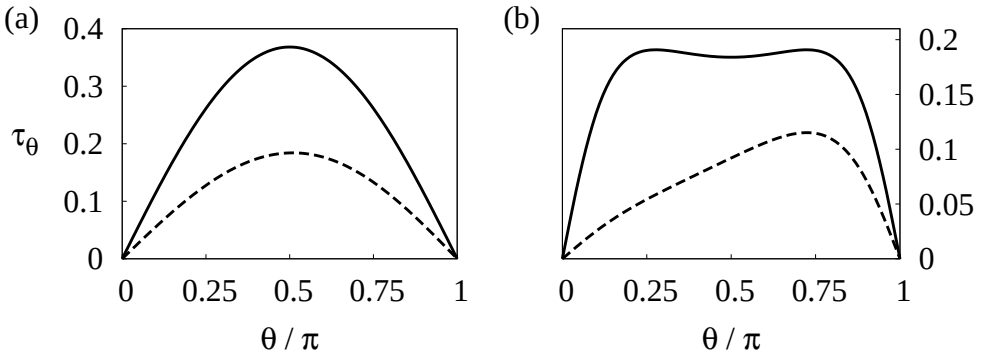

Figure 28: Spin transfer torque τ_θ in symmetric DSVs, F(20)/Cu(10)/F(8)/Cu(10)/F(20), in the antiparallel configuration, $\Omega = \pi$, (solid lines), and STT in SSVs, F(20)/Cu(10)/F(8) (dashed lines), where (a) F = Permalloy, (b) F = Cobalt. STT is shown in the units of $\hbar|I|/|e|$, and calculated for $\phi = \pi/2$.

The enhanced STT in dual spin valves may lead to reduction of the critical current for the spin dynamics, and to a decrease of the switching time. The latter is defined as the time needed to switch the magnetization from one stable position to the opposite one. The fixed points of the dynamics of $\hat{\boldsymbol{s}}$ are given by the equations $v_\theta = 0$ and $v_\phi = 0$. If $\Omega = \pi$, they are satisfied for $\theta = 0$, and $\theta = \pi$. Employing the stability condition of the linearized Landau-Lifshitz-Gilbert equation (described in Section 6.1), one finds the critical current destabilizing the initial ($\theta = 0$) state in the form

$$I^0_{c,\mathrm{DSV}} = \frac{\alpha\mu_0 M_\mathrm{s} d}{a^0_\mathrm{L} + a^0_\mathrm{R}} \left(H_\mathrm{ext} + H_\mathrm{ani} + \frac{H_{\mathrm{d}x} + H_{\mathrm{d}y}}{2} - H_{\mathrm{d}z} \right) , \tag{8.9}$$

where a^0_L and a^0_R are calculated for $\theta \to 0$. The terms resulting from $\boldsymbol{\tau}_\perp$ have been omitted here because of their small contribution to the critical current. Equation (8.9) is analogous to the expression for critical current in SSV; see Section 6.3. The critical current in DSVs with F = Cobalt is 6-times smaller than in SSVs, as reported by Berger [48]. However, if F = Permalloy, the critical current is reduced only by a factor of 2. This difference arises from the dependence of spin accumulation on spin-flip length which is about 10-times longer in Cobalt than in Permalloy [33].

The switching time in DSVs as well as in SSVs was found from numerical integration of equations (8.1), including Eq. (8.2) and Eq. (8.4). In the simulations we assumed a constant current of density I. The positive current ($I > 0$) is defined for electrons flowing from F_R towards F_L (current then flows from F_L towards F_R); opposite current is negative. Apart from this, the demagnetization field of the free layer of elliptical cross-section with the axes' lengths 130 nm and 60 nm has been assumed, while external magnetic field was absent, $H_{ext} = 0$. For each value of the current density, the evolution of $\hat{\boldsymbol{s}}$ was found from Eq. (8.1). In all simulations, the spin was initially slightly tilted in the layer plane from the orientation $\hat{\boldsymbol{s}} = (0, 0, 1)$, assuming $\theta_0 = 1°$ and $\phi_0 = \pi/2$. A successful switching was controlled using moving average [108] (for details see Section 7). Fig. 29 compares the switching times in DSVs and in the corresponding SSVs. In both cases shown in Fig. 29, a considerable reduction of the switching time is observed in DSVs. Similarly as for the critical current, the reduction of current required for switching in DSVs with Cobalt layers is larger from that in DSVs with Permalloy layers.

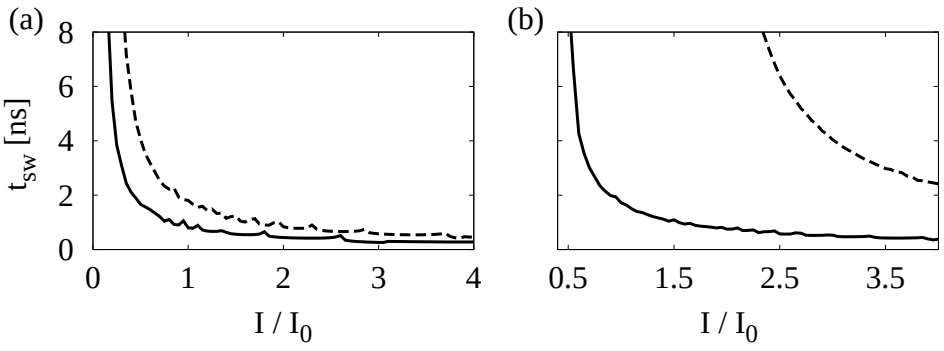

Figure 29: Switching time in DSVs F(20)/Cu(10)/F(8)/Cu(10)/F(20) in the antiparallel magnetic configuration, $\Omega = \pi$, (solid lines), and in SSVs F(20)/Cu(10)/F(8) (dashed lines), where (a) F = Permalloy, (b) F = Cobalt. The switching time is shown as a function of the normalized current density I/I_0, with $I_0 = 10^8 \mathrm{Acm}^{-2}$. The other parameters as in Fig. 28.

8.3 Exchange-biased dual spin valve

Consider now an asymmetric exchange-biased DSV structure with an antiferromagnetic layer IrMn adjacent to the F_R layer in order to pin its magnetic moment in a required orientation, i.e. the structure Co(20)/Cu(10)/Py(4)/Cu(4)/Co(10)/IrMn(8). The left magnetic layer, F_L = Co(20), is assumed to be thick enough so its magnetic moment is fixed, $\hat{\boldsymbol{S}}_L = \hat{\mathbf{e}}_z$. In turn, magnetic moment of the right ferromagnetic layer, F_R = Co(10), is fixed in the layer plane at a certain angle Ω with respect to $\hat{\boldsymbol{S}}_L$ due to the exchange-bias coupling to IrMn.

In a general case, $\Omega \neq 0$, the points $\theta = 0$ and $\theta = \pi$ are no more solutions of the conditions for fixed points, $v_\theta = 0$ and $v_\phi = 0$, because of the additional terms in STT, which appear in non-collinear situations (see eq. 8.7a). These additional terms lead to a nontrivial θ-dependence of STT, and to a shift of the fixed points out of the collinear positions. To analyze this effect in more details, let us consider the STT assuming $\hat{\boldsymbol{s}}$ in the layer plane ($\phi = \pi/2$). According to Eq. (8.7b) and Eq. (8.8b), and to the fact that the parameters b are much smaller than a, the component τ_ϕ is very small. In Fig. 30(a) the second component of the torque, τ_θ, is shown as a function of the angle θ for different values of the angle Ω. The configurations where $\tau_\theta = 0$

are presented by the contour in the base plane of Fig. 30(a). In the whole range of the angle Ω, two 'trivial' zero points are present. Additionally, for small angles close to $\Omega = 0$, two additional zero points occur. The appearance of these additional zero points closely resembles non-standard *wavy*-like STT angular dependence (see the previous chapter). In contrast to SSVs, the *wavy*-like θ-dependence in exchange-biased DSVs is related rather to asymmetric geometry of the multilayer than to bulk and interface spin asymmetries. This trend is depicted in Fig. 30(b), where variation of STT is shown for different thicknesses of F_R at $\Omega = 0$. The *wavy*-like torque angular dependence appears for the thickness of F_R markedly different from that of F_L.

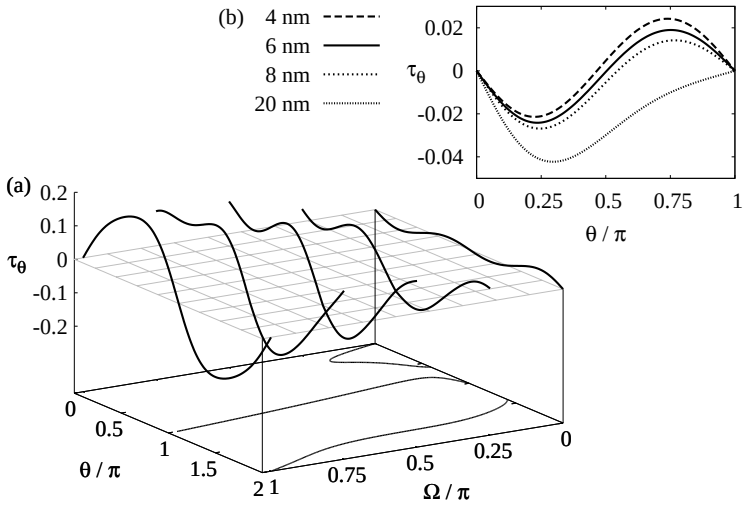

Figure 30: (a) STT acting on the central magnetic layer in Co(20)/Cu(10)/Py(4)/Cu(4)/Co(10)/IrMn(8) exchange-biased DSV as a function of the angle θ, calculated for $\Omega = k\pi/4$, $k = 0, 1, 2, 3, 4$. The contour plot in the base plane corresponds to zeros of τ_θ. (b) Wavy-like STT angular dependence in exchange biased DSV for $\Omega = 0$, calculated for different thicknesses of the F_R layer. STT is shown in the units of $\hbar|I|/|e|$.

The above described STT calculations, extended to arbitrary orientation of $\hat{\boldsymbol{s}}$, allow to performed numerical simulations of spin dynamics induced by a constant current in zero external magnetic field ($H_{\text{ext}} = 0$). As before, the sample cross-section was assumed in the form of an ellipse with the axes' lengths 130 nm and 60 nm. In the simulation we analyzed the long-term current-induced spin dynamics started from the initial state corresponding to $\theta_0 = 1°$, $\phi_0 = \pi/2$.

The current-induced spin dynamics of the free layer depends on the angle Ω, current density I, and current direction. Different regimes of STT-induced spin dynamics can be distinguished in a dynamical phase diagram, which shows the average value $\langle s_z \rangle$ of the z component of the free layer net-spin in a stable dynamical regime [Fig. 31(a)] and its dispersion $D(s_z) = \sqrt{\langle s_z^2 \rangle - \langle s_z \rangle^2}$ [Fig. 31(b)] as a function of current and the angle Ω. The average value $\langle s_z \rangle$ provides an information on the spin orientation, whereas the dispersion distinguishes between static states (for which $D = 0$) and steady precessional regimes (where $D > 0$), in which the z component is involved. For each point in the diagram, a separate run from the initial biased state $\phi_0 = \pi/2$ and $\theta_0 = 1°$ was performed. In the $\langle s_z \rangle$ diagram, Fig. 31(a), one can distinguish three specific regions. Region (i) covers parameters for which a weak dynamics is induced only: $\hat{\boldsymbol{s}}$ finishes in the equilibrium stable point which is very close to $\hat{\boldsymbol{s}} = (0, 0, 1)$. As the angle Ω increases, STT becomes strong enough

to cause switching,see the region (ii). The higher the angle Ω, the smaller is the critical current needed for destabilization of the initial state. For smaller Ω, the current-induced dynamics occurs for currents flowing in the opposite direction, see the region (iii). This behavior is caused by different sign of STT in the initial state. From $\langle s_z \rangle$ one can conclude, that none of the previously mentioned stationary states is reached. The map of $D(s_z)$, Fig. 31(b), reveals three different modes of current-induced dynamics. For small current amplitudes, in-plane precession (IPP) around the initial stable position is observed. The precessional angle rises with increasing current amplitude. Above a certain critical value of I, the precessions turn to out-of-plane precessions (OPPs). In a certain range of Ω, the OPPs collapse to a static state (SS), where the spin $\hat{\boldsymbol{s}}$ remains in an out-of-plane position close to $\pm\hat{\mathbf{e}}_x$.

As $\hat{\boldsymbol{S}}_{\mathrm{R}}$ departs from the collinear orientation, the critical current for destabilization of the initial state increases. This growth is mostly pronounced close to $\Omega = \pi/2$. To describe the critical current analytically, one needs to analyze Eq. (8.5) with respect to the stability of $\hat{\boldsymbol{s}}$ in the upper position. Assuming that even in noncollinear configuration the stable position of $\hat{\boldsymbol{s}}$ is close to $\theta = 0$, we have linearized Eq. (8.5) around this point for arbitrary Ω, one finds the critical current needed for destabilization of the considered stable state (for details see Section 6)

$$I^0_{c,\,\mathrm{EBDSV}} \simeq \frac{\alpha\mu_0 M_{\mathrm{s}} d\left(H_{\mathrm{ani}} + \frac{H_{\mathrm{dx}}+H_{\mathrm{dy}}}{2} - H_{\mathrm{dz}}\right)}{a^0_{\mathrm{L}}(\Omega) - a^0_{\mathrm{R}}(\Omega)\cos\Omega}\,, \tag{8.10}$$

where $a^0_{\mathrm{L}}(\Omega)$ and $a^0_{\mathrm{R}}(\Omega)$ are calculated (for each configuration) assuming $\theta \to 0$. Comparison of Eq. (8.10) with the results of numerical simulations is shown in Fig. 31. When considering the opposite stable point as the initial state, we need to take a_{L} and a_{R} for $\theta \to \pi$. Clearly, to destabilize the $\theta = \pi$ state one needs current of opposite direction.

The current-induced oscillations are usually observed experimentally *via* the magnetoresistance effect [104]. When electric current is constant, then magnetic oscillations cause the corresponding resistance oscillations, which in turn lead to voltage oscillations. The later are measured directly in experiments. In Fig. 31(d) we show oscillations in the system resistance associated with the IPP (left) and OPP (right). As the amplitude of the oscillations corresponding to the OPP mode is sufficiently large to be measured experimentally, the amplitude associated with the IPP mode is relatively small. This is the reason, why IPP mode is usually not seen in experiments.

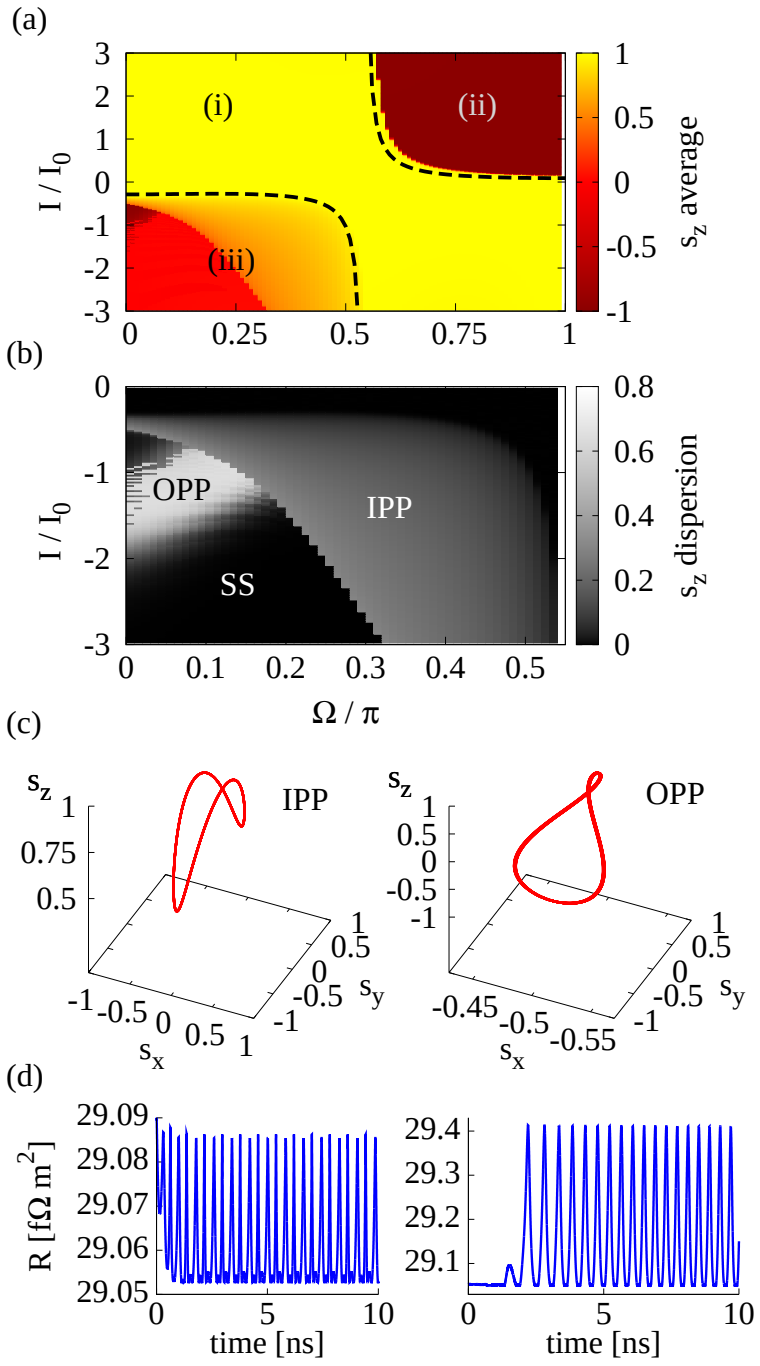

Figure 31: Dynamical phase diagram for Co(20)/Cu(10)/Py(4)/Cu(4)/Co(10)/IrMn(8) exchange-biased double spin valve as a function of the angle Ω and normalized current density I/I_0 (with $I_0 = 10^8 \mathrm{Acm}^{-2}$): (a) average value of the s_z spin component; (b) dispersion of the s_z spin component; (c) typical precessional orbits; (d) resistance oscillations associated with the IPP for $\Omega = 0.4\pi$ and $I = -1.3I_0$ (left part), and with the OPP for $\Omega = 0.1\pi$ and $I = -1.3I_0$ (right part).

9 Current-induced dynamics in out-of-plane polarized dual spin valves

In the previous chapter we discussed a possibility for current-induced switching enhancement using the dual spin valve geometry. Another way of dealing with this problem was suggested by Kent et al [42], who proposed a single spin valve with perpendicularly polarized fixed layer and in-plane magnetized free layer. It has been shown that when a short current pulse passes such a spin valve, the free layer's magnetization might be switched after one half precessional period, similarly to precessional switching by transversal magnetic field [111, 112]. In field-induced as well as current-induced precessional switching, magnetization of the free layer is pushed out of the layer's plane, which creates a strong demagnetizing field. This causes out-of-plane large angle magnetization precessions. The magnetization can end up in the opposite state, if transversal field/current is switched off when magnetization passes its basin of attraction. Obviously, the efficiency of this method strongly depends on the current pulse which has to be optimized for any given system.

If the fixed layer's magnetization is perpendicular to free layer's one in both stationary points, there is no difference in resistance, and therefore it is useful to add another in-plane polarized layer with fixed magnetization, which acts as reference layer. The spin valve is usually constructed in such a way that the in-plane magnetized fixed layer does not influence the current-induced dynamics of the free layer and is used just for measurement of GMR. However, it has been shown by Lee et al. [43] that if the spin valve geometry allows the in-plane fixed layer to influence the magnetization dynamics by spin transfer torque, the probability of switching in the free layer might be markedly enhanced, especially when the current pulse is short enough (about 100 ps). In the light of previous section, the above mentioned device is a dual spin valve with one out-of-plane (perpendicular) and one in-plane fixed layers. Hence we shall employ here the model described in chapter 8 to study the current-induced switching in such a device.

In this chapter, we first extend the calculations by Ebels et al. [45], who studied the critical current in single spin valves with one perpendicular polarizer. Namely, we study how the critical current is influenced by the spin transfer torque (STT) due to the in-plane polarizer. Moreover, here we use the STT obtained in the diffusive transport approach, while in reference [45] the Slonczewski's term obtained in the ballistic regime was used.

9.1 Model

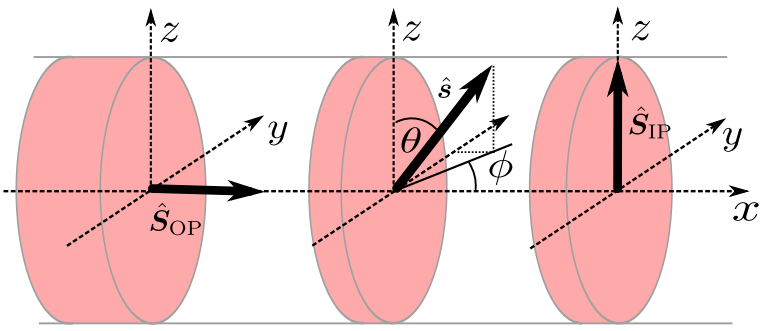

Figure 32: Schematic picture of the studied dual spin valve with one out-of-plane and one in-plane polarizer.

In this section we shall use the same model as in Section 8. Therefore, the spin dynamics shall be described by Landau-Lifshitz-Gilbert equation given by (8.1) together with the effective field (8.2). Then, in the local spherical coordinates, the LLG is given by (8.5) where v_θ and v_ϕ are the same as (8.6).

However, a difference appears in the STT components, which is included in (8.6). Contrary to the previous system with both polarizers being magnetized in the layers' planes, here $\hat{\boldsymbol{S}}_{\rm L}$ is magnetized in the direction $\hat{\mathbf{e}}_x$ perpendicular to the layers plane. Hence we shall call it *out-of-plane* or *perpendicular polarizer* and mark it as $\hat{\boldsymbol{S}}_{\rm OP}$; $\hat{\boldsymbol{S}}_{\rm L} \to \hat{\boldsymbol{S}}_{\rm OP} = \hat{\mathbf{e}}_x$; see Figure 32. The in-plane magnetized fixed layer shall be called *in-plane polarizer* or *reference layer* and we shall mark it as $\hat{\boldsymbol{S}}_{\rm IP}$. In comparison to chapter 8 we can write $\hat{\boldsymbol{S}}_{\rm R} \to \hat{\boldsymbol{S}}_{\rm IP} = \hat{\mathbf{e}}_z$. Hence, one can write the expressions for spin torque components as

$$\boldsymbol{\tau}_{\parallel} = I\,\hat{\boldsymbol{s}} \times \Big[\hat{\boldsymbol{s}} \times \Big(a_{\rm OP}\,\hat{\boldsymbol{S}}_{\rm OP} - a_{\rm IP}\,\hat{\boldsymbol{S}}_{\rm IP}\Big)\Big]\,, \tag{9.1a}$$

$$\boldsymbol{\tau}_{\perp} = I\,\hat{\boldsymbol{s}} \times \Big(b_{\rm OP}\,\hat{\boldsymbol{S}}_{\rm OP} - b_{\rm IP}\,\hat{\boldsymbol{S}}_{\rm IP}\Big)\,, \tag{9.1b}$$

where the parameters $a_{\rm OP}$, $b_{\rm OP}$, $a_{\rm IP}$, and $b_{\rm IP}$ are to be calculated according to the diffusive transport model (see Section 3). In spherical coordinates one can write $\tau_\theta = \tau_\theta^{\parallel} + \tau_\theta^{\perp}$ and $\tau_\phi = \tau_\phi^{\parallel} + \tau_\phi^{\perp}$, with

$$\tau_\theta^{\parallel} = -a_{\rm OP}\,I\,\cos\phi\cos\theta - a_{\rm IP}\,I\,\sin\theta\,, \qquad \tau_\theta^{\perp} = b_{\rm OP}\,I\,\sin\phi\,, \tag{9.2a}$$

$$\tau_\phi^{\parallel} = a_{\rm OP}\,I\,\sin\phi\,, \qquad \tau_\phi^{\perp} = b_{\rm OP}\,I\,\cos\phi\cos\theta + b_{\rm IP}\,I\,\sin\theta\,. \tag{9.2b}$$

9.2 Spin-transfer torque

Before investigating the stationary points of $\hat{\boldsymbol{s}}$, let us calculate numerically the angular dependence of STT. Since, as we learned before, $b_{\rm OP} \ll a_{\rm OP}$ and $b_{\rm IP} \ll a_{\rm IP}$, we shall disregard these torque components ($b_{\rm OP} \to 0$, $b_{\rm IP} \to 0$). Therefore, in further we shall consider only the in-plane torque components. In this chapter we are interested in the influence of the in-plane polarizer on the critical currents and stability of $\hat{\boldsymbol{s}}$. Hence, we shall study both single spin valve with out-of-plane polarizer (i.e $a_{\rm IP} = 0$) and dual spin valve with both in plane and out-of-plane polarizers.

Because the magnetization vectors of the out-of-plane and in-plane polarizers are perpendicular, it is sufficient to check the angular dependence of STT due to out-of-plane polarizer when $\hat{\boldsymbol{s}}$ is rotated in the (y,z)-plane, i.e. when the angle $\theta = \pi/2$ is fixed and ϕ is varied as $\phi \in (0,\pi)$. In other words, we vary just the angle between $\hat{\boldsymbol{s}}$ and $\hat{\boldsymbol{S}}_{\rm OP}$ ($\theta_{\rm OP} \in (0,\pi)$) while the angle between $\hat{\boldsymbol{s}}$ and $\hat{\boldsymbol{S}}_{\rm IP}$ is constant ($\theta_{\rm IP} = \pi/2$). As a result, the toque due to the in-plane polarizer is approximately constant, while the torque due to the out-of-plane polarizer varies with $\theta_{\rm OP}$. Similarly, one can analyze the angular dependence of STT due to the in-plane polarizer when the spin is rotated in the (y,z)-plane, i.e. when $\phi = \pi/2$ is fixed while $\theta \in (0,\pi)$, and hence $\theta_{\rm IP} \in (0,\pi)$ is changed. In a single spin valve with perpendicular polarizer only, one needs to calculate one torque component rotating the spin in the (y,z)-plane.

Figure 33 shows the angular dependence of $a_{\rm OP}(\theta_{\rm OP})$ for a dual spin valve of the structure Cu-Co(2)/Cu(6)/Py(5)/Cu(12)/Py(20)-Cu, where numbers in brackets stand for layers' thicknesses in nanometers. Here, we consider the Co(2) layer as the out-of-plane polarizer, provided that the this layer has a strong out-of-plane magnetocrystalline anisotropy which fixes its magnetization in the perpendicular direction[11]. The layer Py(5) is the sensing layer.

[11] In the next section (10) we shall discuss this issue in more details.

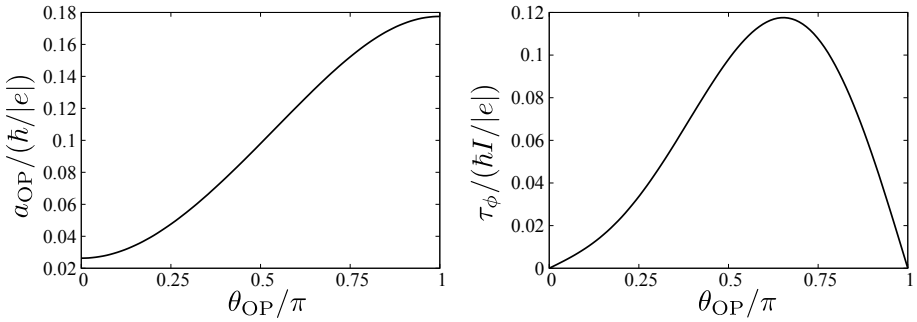

Figure 33: Angular dependence of STT in a single spin valve with perpendicular polarizer: Cu-Co(2)/Cu(6)/Py(5)-Cu, where Co(2) is the perpendicular polarizer, and Py(5) is the free layer.

Figure 34, in turn, depicts the angular dependence of the parameters $a_{\mathrm{OP}}(\theta_{\mathrm{OP}})$ and $a_{\mathrm{IP}}(\theta_{\mathrm{IP}})$ in Cu-Co(2)/Cu(6)/Py(5)/Cu(12)/Py(20)-Cu with Co(2) being the out-of-plane and Py(20) the in-plane polarizer.

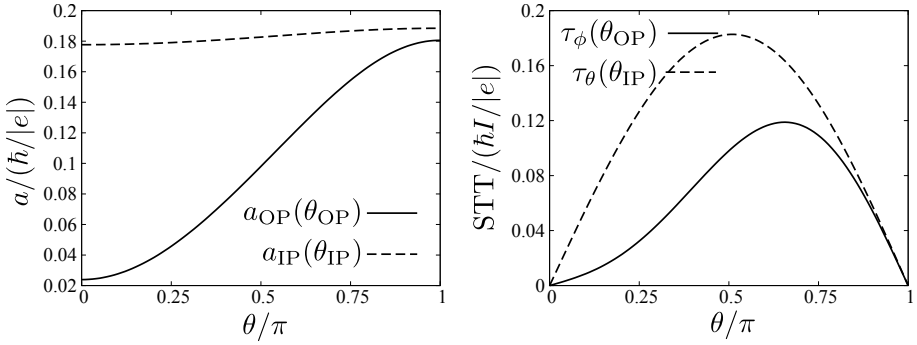

Figure 34: Angular dependence of STT in a dual spin valve with one perpendicular and one in-plane polarizer: Cu-Co(2)/Cu(6)/Py(5)/Cu(12)/Py(20)-Cu, where Co(2) is the out-of-plane polarizer, Py(20) is the in-plane polarizer, and Py(5) is the free layer.

In further we shall examine the stationary points and their stability employing the formalism of spin-torque ferromagnetic resonance [45].

9.3 Stationary states

First, we shall analyze stationary states of spin valves without and with the in-plane polarized reference layer. The static points of the sensing layer's dynamics obey the equations

$$v_\theta = 0\,, \qquad v_\phi = 0\,. \tag{9.3}$$

To simplify the analysis we shall assume that the parameter a_{OP} (a_{IP}) depends only on the angle between $\hat{\boldsymbol{s}}$ and $\hat{\boldsymbol{S}}_{\mathrm{OP}}$ ($\hat{\boldsymbol{S}}_{\mathrm{IP}}$). Hence we write

$$a_{\mathrm{OP}} = \frac{\hbar}{|e|}\sum_{n=0}^{N} a_{\mathrm{OP}\,n}\cos^n\theta_{\mathrm{OP}}\,, \qquad \text{where} \qquad \cos\theta_{\mathrm{OP}} = \hat{\boldsymbol{s}}\cdot\hat{\boldsymbol{S}}_{\mathrm{OP}}\,, \tag{9.4}$$

$$a_{\mathrm{IP}} = \frac{\hbar}{|e|}\sum_{n=0}^{N} a_{\mathrm{IP}\,n}\cos^n\theta_{\mathrm{IP}}\,, \qquad \text{where} \qquad \cos\theta_{\mathrm{IP}} = \hat{\boldsymbol{s}}\cdot\hat{\boldsymbol{S}}_{\mathrm{IP}}\,, \tag{9.5}$$

where $a_{\mathrm{OP}\,n}$ and $a_{\mathrm{IP}\,n}$ are constant parameters obtained by fitting the latter expressions to the numerical results for a_{OP} and a_{IP}, presented in figures 33 and 34. It has been checked that $N = 4$ is sufficient for an accurate fit.

9.3.1 In-plane stationary points

First, we shall study the static states of $\hat{\boldsymbol{s}}$ which are in the layer's plane. To avoid a singularity in the local spherical coordinates (see Appendix D), which appears for $\theta = 0$ and π, we rotate our sample in such a way that the easy axis is oriented along x axis and the current flows along the z-axis. In other words, in former equations we make the substitution $\hat{\mathbf{e}}_x \to \hat{\mathbf{e}}_z$ and $\hat{\mathbf{e}}_z \to -\hat{\mathbf{e}}_x$, and hence

$$\mathbf{H}_{\mathrm{eff}} = H_{\mathrm{ext}}\hat{\mathbf{e}}_x - H_{\mathrm{ani}}\,(\hat{\boldsymbol{s}}\cdot\hat{\mathbf{e}}_x)\,\hat{\mathbf{e}}_x + \mathbf{H}_{\mathrm{dem}}\,, \tag{9.6}$$

where $\mathbf{H}_{\mathrm{dem}} = (H_{\mathrm{d}z}s_x, H_{\mathrm{d}y}s_y, H_{\mathrm{d}x}s_z)$. Moreover, $\hat{\boldsymbol{S}}_{\mathrm{OP}} = (0,0,1)$ and $\hat{\boldsymbol{S}}_{\mathrm{IP}} = (-1,0,0)$. In this rotated coordinate system, all the in-plane points obey $\theta_{\mathrm{OP}} = \theta = \pi/2$ and therefore STT from the out-of-plane polarizer is constant; i.e $a_{\mathrm{OP}} = (\hbar/|e|)\sum_{n=0}^{4} a_{\mathrm{OP}\,n}$ is constant.

In case without reference layer, from Eqs. (9.3) we have one equation for the ϕ coordinate

$$H_{\mathrm{ext}}\sin\phi - (H_{\mathrm{ani}} + H_{\mathrm{d}y} - H_{\mathrm{d}z})\cos\phi\sin\phi = \frac{I}{\mu_0 M_{\mathrm{s}} d}a_{\mathrm{OP}}\,. \tag{9.7}$$

When $I = 0$, Eq. (9.7) has solution for $\phi = 0$ and π, i.e. spin is aligned along the easy axis. When $I \neq 0$, $\phi = 0$ and π are no more static points of the dynamics. We will study this case making use of the stability conditions from FMR theory.

Introducing the in-plane polarizer one ends up with two equations

$$H_{\mathrm{ext}}\sin\phi - (H_{\mathrm{ani}} + H_{\mathrm{d}y} - H_{\mathrm{d}z})\cos\phi\sin\phi = \frac{I}{\mu_0 M_{\mathrm{s}} d}a_{\mathrm{OP}}\,, \tag{9.8a}$$

$$0 = \frac{I}{\mu_0 M_{\mathrm{s}} d}a_{\mathrm{IP}}\sin\phi\,, \tag{9.8b}$$

where $a_{\mathrm{IP}} = (\hbar/|e|)\sum_{n=0}^{4} a_{\mathrm{IP}\,n}(-\cos\phi)^n$. The first equation is the same as (9.7). The second one describes the influence of the in-plane polarizer. Eq. (9.8b) is obeyed when $I = 0$; in this case we have, as before, static states at $\phi = 0$ and π. When $I \neq 0$, Eq. (9.8b) is obeyed only and only for $\phi = 0$ and π,[12] however these points are no more solutions of Eq. (9.8a). From this follows that there are no in-plane static points in system with in-plane polarizer. This means, that the free layer cannot be switched by a continuously applied current and the current must be switched off to stabilize $\hat{\boldsymbol{s}}$ in one of the equilibrium positions along the easy axis.

9.3.2 Out-of-plane stationary points

Out-of-plane static points will be studied in normal (non-rotated) coordination system (the same as introduced in Appendix D).

[12] Note, since the angular dependence of a_{IP} is standard, it is zero only for $\phi = \pi/2$, what is not a solution of Eq. (9.8a)

In case without the reference layer, Eqs. (9.3) lead to the following system of two equations for θ and ϕ

$$-\left(H_{\mathrm{d}x}-H_{\mathrm{d}y}\right)\sin\phi\cos\phi\sin\theta=\frac{I}{\mu_0 M_{\mathrm{s}} d}a_{\mathrm{OP}}(\theta,\phi)\cos\phi\sin\theta\,, \tag{9.9a}$$

$$\begin{aligned}&\left[H_{\mathrm{ext}}+\left(H_{\mathrm{ani}}+H_{\mathrm{d}x}\cos^2\phi+H_{\mathrm{d}y}\sin^2\phi-H_{\mathrm{d}z}\right)\cos\theta\right]\sin\theta \\ &\quad=\frac{I}{\mu_0 M_{\mathrm{s}} d}a_{\mathrm{OP}}(\theta,\phi)\sin\phi\,,\end{aligned} \tag{9.9b}$$

where, $a_{\mathrm{OP}}=(\hbar/|e|)\sum_{n=0}^{4}a_{\mathrm{OP}\,n}(\cos\phi\sin\theta)^n$. Eqs. (9.9) are nonlinear equations, which cannot be directly evaluated since there is angular dependence of $a_{\mathrm{OP}}(\theta,\phi)$. However, the static states can be obtained solving Eqs. (9.9) numerically, what shall be done below.

When the in-plane polarizer is added, we obtain system of equations

$$-\left(H_{\mathrm{d}x}-H_{\mathrm{d}y}\right)\sin\phi\cos\phi\sin\theta=\frac{I}{\mu_0 M_{\mathrm{s}} d}\left(a_{\mathrm{OP}}(\theta,\phi)\cos\phi\sin\theta+a_{\mathrm{IP}}(\theta)\sin(\theta)\right)\,, \tag{9.10a}$$

$$\left[H_{\mathrm{ext}}+\left(H_{\mathrm{ani}}+H_{\mathrm{d}x}\cos^2\phi+H_{\mathrm{d}y}\sin^2\phi-H_{\mathrm{d}z}\right)\cos\theta\right]\sin\theta=\frac{I}{\mu_0 M_{\mathrm{s}} d}a_{\mathrm{OP}}(\theta,\phi)\sin\phi\,, \tag{9.10b}$$

where $a_{\mathrm{IP}}=(\hbar/|e|)\sum_{n=0}^{4}a_{\mathrm{IP}\,n}\cos^n\theta$. Similarly, as in the previous case, Eqs. (9.10) can be solved numerically.

9.4 Stability of the stationary points

Now, let us study stability of the stationary points discussed above. We shall employ here the generalized FMR Theory [45, 99] (For details see Section 6.2).

From Eq. 8.1 with STT terms described by 9.1 we derive the generalized complex frequency, $\omega=\omega'+i\omega''$,

$$(1+\alpha^2)\omega=-\frac{i}{2}(\Delta\omega-2\tilde{S}_r)\pm\sqrt{-\frac{1}{4}(\Delta\omega-2\tilde{S}_r)^2+(1+\alpha^2)(\omega_0^2+\tilde{S}_r)}\,, \tag{9.11}$$

where $\omega''=-(\Delta\omega-2\tilde{S}_r)/2$ while ω' is the square-root term. Moreover, ω_0 and $\Delta\omega$ are resonance frequency and linewidth, respectively, defined by 6.26. Furthermore, $\tilde{S}_r=(|\gamma_{\mathrm{g}}|I/M_{\mathrm{s}}d)\,a_{\mathrm{OP}}\cos\phi\sin\theta$ for single out-of-plane polarized spin valves, and $\tilde{S}_r=(|\gamma_{\mathrm{g}}|I/M_{\mathrm{s}}d)\,(a_{\mathrm{OP}}\cos\phi\sin\theta-a_{\mathrm{IP}}\cos\theta)$ when also in-plane polarizer is present.

9.4.1 In-plane stationary points

Since ω' in (9.11) is positive, the condition for stability of a static point (θ_0,ϕ_0) is $\omega''(\theta_0,\phi_0)<0$ (perturbation decays in time). If $\omega''(\theta_0,\phi_0)>0$, the static point (θ_0,ϕ_0) is unstable. Thus, the condition for critical current is

$$\omega''(\theta_0,\phi_0)=0\,. \tag{9.12}$$

Consider first the case when there is no reference layer. In rotated coordinate system, the condition (9.12) cannot be applied, because $\tilde{S}_r=0$. In such a case, the condition for critical

current is $\omega_0 = 0$, what is here equivalent to $E_{\phi\phi} = 0$ and leads to equation for critical in-plane rotation angle, ϕ_c,

$$\cos\phi_c = \eta \pm \sqrt{\eta^2 + 1/2}\,, \qquad \eta = \frac{1}{4}\frac{H_{\mathrm{ext}}}{H_{\mathrm{ani}} + H_{\mathrm{d}y} - H_{\mathrm{d}z}}\,. \tag{9.13}$$

Then, from Eq. (9.7), we can evaluate the critical current

$$I_c = \frac{\mu_0 M_{\mathrm{s}} d}{a_{\mathrm{OP}}(\theta = \pi/2)}\left[H_{\mathrm{ext}}\sin\phi_c - (H_{\mathrm{ani}} + H_{\mathrm{d}y} - H_{\mathrm{d}z})\cos\phi_c\sin\phi_c\right]\,. \tag{9.14}$$

This current formula has four branches [two different sings of the square root in Eq. (9.13) combined with different signs of angle ϕ_c]. These results are fully consistent with results in [45].

When the spin valve contains both out-of-plane polarizer as well as in-plane reference layer, there are no in-plane static points, as shown before. However, there is a possibility, that there are stationary points slightly tilted from the layer's plane, which might be also stable. This case shall be investigated numerically below.

9.4.2 Out-of-plane stationary points

Applying the condition for critical current (9.12) to the out-of-plane points we obtain the condition for the critical current stabilizing the out-of-plane static point (θ_0, ϕ_0)

$$I_c = \alpha\frac{\mu_0 M_{\mathrm{s}} d\, h(\theta_0,\phi_0)}{a_{\mathrm{OP}}(\theta_0,\phi_0)\cos\phi_0\sin\theta_0}\,, \qquad \text{where} \tag{9.15}$$

$$h(\theta,\phi) = H_{\mathrm{ext}}\cos\theta + \left[H_{\mathrm{ani}} - H_{\mathrm{d}z} + \frac{1}{2}(H_{\mathrm{d}x} + H_{\mathrm{d}y})\right]\cos(2\theta) - \frac{1}{2}(H_{\mathrm{d}x} - H_{\mathrm{d}y})(2 - \cos(2\theta))\cos(2\phi)\,,$$

when only out-of-plane polarizer is present.

When we introduce the in-plane polarized reference layer, we obtain the critical current

$$I_c = \alpha\frac{\mu_0 M_{\mathrm{s}} d\, h(\theta_0,\phi_0)}{a_{\mathrm{OP}}(\theta_0,\phi_0)\cos\phi_0\sin\theta_0 - a_{\mathrm{IP}}(\theta_0)\cos\theta_0}\,, \tag{9.16}$$

where $h(\theta_0, \phi_0)$ remains the same as defined in Eq. (9.15). These equations, however, cannot be used for direct calculation of I_c, because we do not know the stationary point (which also depends on the current) explicitly.

For the calculation of the critical current needed to stabilize the out-of-plane stationary points, we have mapped the imaginary part, ω'', of the generalized complex frequency. Hence, for each value of applied in-plane magnetic field, $\mathbf{H}_{\mathrm{eff}}$, and current density, I, we have found the in plane static point (θ_0, ϕ_0), solving numerically Eqs. (9.9) [or (9.10)]. In this stationary point we evaluate ω'' and monitor the term under the square root in Eq. (9.11). Since the square root term is real, the line of the zero values of ω'' gives us the critical current for stabilization of the out-of-plane point at a given magnetic field.

9.5 Numerical results

9.5.1 Single spin valve

First, let us study the single spin valve structure with a perpendicular polarizer. We have calculated the critical currents destabilizing the in-plane, as well as out-of-plane static points. They are shown in the $H - I$ diagram, Fig. 35. The dashed lines show the critical currents which destabilize the

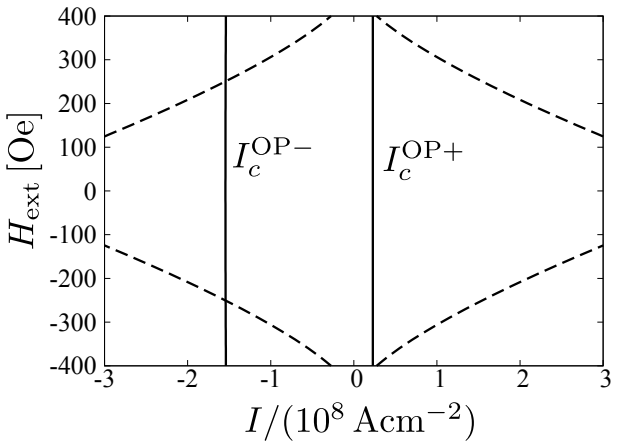

Figure 35: Critical current for in-plane (dashed line) and out-of-plane (solid line) static points for spin valve without in-plane polarized reference layer

in-plane static points. They are symmetric, similarly as in the limit of STT independent on the angle θ_{OP}.

The solid lines show the currents needed for stabilization of the out-of plane points. When a static point is close to $(\theta = \pi/2, \phi = 0)$, $\omega'' < 0$ for $I < I_c^{\mathrm{OP}-}$. When $\omega'' = 0$, square root term is always real in the calculated range of values. On the other hand, when a static point is close to $(\theta = \pi/2, \phi = \pi)$, $\omega'' < 0$ for $I > I_c^{\mathrm{OP}+}$. If $\omega'' = 0$, then the square root term is positive as well. In other words, negative current larger than $|I_c^{\mathrm{OP}-}|$ stabilizes point close to $(\theta = \pi/2, \phi = 0)$, while positive current larger than $|I_c^{\mathrm{OP}+}|$ stabilizes point close to $(\theta = \pi/2, \phi = \pi)$. $I_c^{\mathrm{OP}-}$ as well as $I_c^{\mathrm{OP}+}$ seem to be independent of the applied in-plane magnetic field. The distribution of the out-of-plane points in the calculated range of H_{ext} and I is shown on Fig 36.

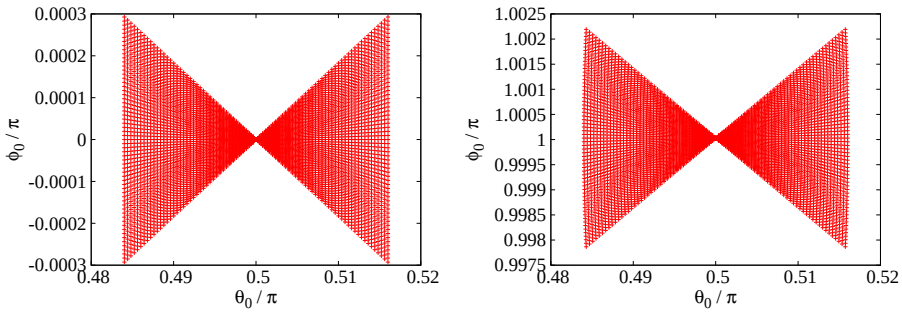

Figure 36: Distribution of out-of-plane static points for spin valve without in-plane polarized reference layer in the range of I and H_{ext} shown in the Figure 35

The origin of the asymmetry in the critical currents for out-of-plane static points, $|I_c^{\mathrm{OP}-}| \neq |I_c^{\mathrm{OP}+}|$ could be understood from Eq. (9.15) [or Eq. (9.16)]. Function $h(\theta = \pi/2, \phi = 0) = h(\theta =$

$\pi/2, \phi = \pi$) does not have any influence on the asymmetry of critical currents. However, a_{OP} in the first point is $a_{\mathrm{OP}}(\theta = \pi/2, \phi = 0) = (\hbar/|e|)(a_{\mathrm{OP}\,0} + a_{\mathrm{OP}\,1} + a_{\mathrm{OP}\,2} + a_{\mathrm{OP}\,3} + a_{\mathrm{OP}\,4})$, while in the opposite point $a_{\mathrm{OP}}(\theta = \pi/2, \phi = 0) = (\hbar/|e|)(a_{\mathrm{OP}\,0} - a_{\mathrm{OP}\,1} + a_{\mathrm{OP}\,2} - a_{\mathrm{OP}\,3} + a_{\mathrm{OP}\,4})$. If we would not consider any angular dependence of STT, both critical currents would be the same. This means, that the angular dependence of STT takes the responsibility for asymmetry in the critical currents needed to stabilize the out-of-plane static points.

The mentioned asymmetry is crucial for the switching, because stability of the out-of-plane static points is important for out-of-plane precessions and for current-induced switching as well. Because of the asymmetry, negative currents might first destabilize the in-plane static state and then stabilize the out-of-plane one (e.g. at $|H_{\mathrm{ext}}| \gtrsim 300\,\mathrm{Oe}$). However, for positive current, the out-of-plane static state is stabilized before in-plane one is destabilized. This may cause huge differences in the spin dynamics induced by positive and negative current, which may be examined by numerical simulations.

9.5.2 Dual spin valve

Let us now study the structure with in-plane polarized reference layer. Similarly as in the previous case, we calculated the critical currents stabilizing the out-of-plane static points; see Fig. 37. This

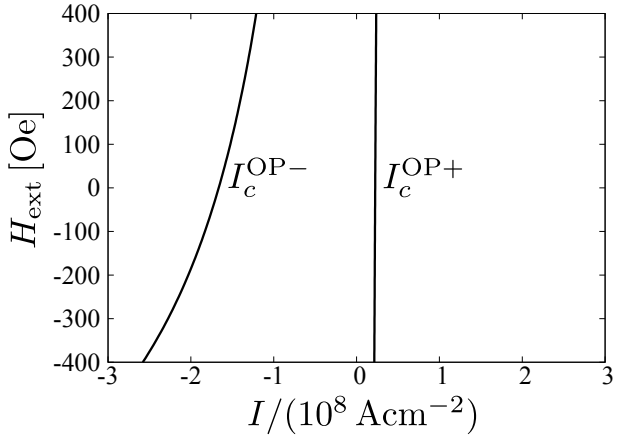

Figure 37: Critical current for the out-of-plane static points for a spin valve with in-plane polarized reference layer

figure shows, that $I_c^{\mathrm{OP}-}$ depends now on the applied magnetic field. This stems from the fact, that the in-plane polarizer breaks the symmetry of the dynamic system with respect to external magnetic field. This can be also shown in the asymmetry of distribution of the out-of-plane static points, which arises when the in-plane polarized reference layer is added; see Fig. 38. The second critical current, $I_c^{\mathrm{OP}-}$, remains, however, independent of the applied magnetic field in the range of our calculations.

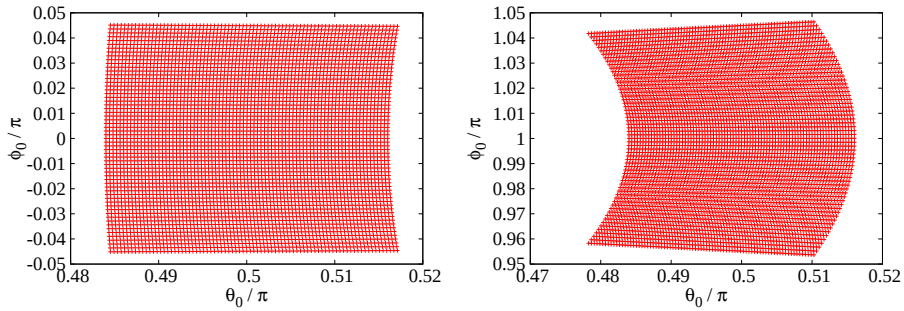

Figure 38: Distribution of out-of-plane static points for spin valve with in-plane polarized reference layer in the range of I and H_{ext} shown in the Figure 37

10 Current-induced switching in out-of-plane polarized dual spin valves

In the previous chapter (9) we investigated a simplified model of a dual spin valve with one out-of-plane (perpendicular) and one in-plane magnetized polarizer; see Figure 32. In this section we shall study more realistic model of such a dual spin valve. Our motivation for this study was an experiment by Lee et al [43], who measured the switching probability in a dual spin valve with out-of-plane and in-plane polarizers by a current pulse at room temperature. They compared the results for various pulse durations with current-induced switching in conventional single spin valves with one in-plane polarizer only and came to the following results. While in conventional spin valves a reliable switching can be obtained by long current pulses, in spin valves with both polarizers a 100% switching probability is achieved for short ($t_{\text{p}} \sim 100\,\text{ps}$) current pulses. For long pulses ($t_{\text{p}} \gtrsim 6\,\text{ns}$), switching in dual spin valves resembles switching in conventional spin valves. Therefore, the authors of reference [43] conclude that the out-of-plane polarizer has just an initiation role and then does not markedly influence the spin dynamics. In addition, they also identify an intermediate current pulse length ($t_{\text{p}} \sim 1\,\text{ns}$) which markedly reduces the switching probability in dual spin valve structure.

In order to study these features we employed the macrospin simulations to study a dual spin valve of similar structure as in [43], Cu-OPP(6.5)/Cu(6)/Py(5)/Cu(12)Py(20)-Cu, where OPP is the out-of-plane polarizer, OPP = $[\text{Co}(0.5)/\text{Cu}(0.7)]_5/\text{Co}(0.5)$. Numbers in the brackets stand for layers thicknesses in nanometers.

10.1 Model

The dynamics of the free layer's spin moment $\hat{\boldsymbol{s}}$ is described by the Landau-Lifshitz-Gilbert equation (5.73)

$$\begin{aligned} \frac{\mathrm{d}\hat{\boldsymbol{s}}}{\mathrm{d}t} + \alpha\,\hat{\boldsymbol{s}} \times \frac{\mathrm{d}\hat{\boldsymbol{s}}}{\mathrm{d}t} &= \boldsymbol{\Gamma}\,, \\ \boldsymbol{\Gamma} = -|\gamma_{\text{g}}|\mu_0 \hat{\boldsymbol{s}} \times \mathbf{H}_{\text{eff}} + \frac{|\gamma_{\text{g}}|}{M_{\text{s}} d}\,\boldsymbol{\tau}\,, \end{aligned} \tag{10.1}$$

where $\boldsymbol{\tau}$ stands for the spin-transfer torque (STT) as described in the previous chapter by equations (9.1). A difference appears in the effective magnetic field, which reads

$$\mathbf{H}_{\text{eff}} = -H_{\text{ext}}\hat{\mathbf{e}}_z - H_{\text{ani}}(\hat{\boldsymbol{s}} \cdot \hat{\mathbf{e}}_z)\hat{\mathbf{e}}_z + \mathbf{H}_{\text{dem}}(\hat{\boldsymbol{s}}) + \mathbf{H}_{\text{int}}(\hat{\boldsymbol{S}}_{\text{OP}}, \hat{\boldsymbol{S}}_{\text{IP}}) + \mathbf{H}_{\text{th}}\,, \tag{10.2}$$

where $\mathbf{H}_{\mathrm{int}}$ was added to include the magnetostatic influence of the polarizers on the free layer. This term, similarly as the self-demagnetizing field ($\mathbf{H}_{\mathrm{dem}}$), is described in the generalized tensor formulation of magnetostatic field (for details see Section 4.3.1). It can be written as

$$\mathbf{H}_{\mathrm{int}} = \left(\bar{\boldsymbol{N}}_{\mathrm{OP}} \cdot \hat{\boldsymbol{S}}_{\mathrm{OP}}\right) M_{\mathrm{s\,OP}} + \left(\bar{\boldsymbol{N}}_{\mathrm{IP}} \cdot \hat{\boldsymbol{S}}_{\mathrm{IP}}\right) M_{\mathrm{s\,IP}}\,, \tag{10.3}$$

where $\bar{\boldsymbol{N}}_{\mathrm{OP}}$ and $\bar{\boldsymbol{N}}_{\mathrm{IP}}$ are mutual demagnetizing tensors describing the magnetostatic field due to the out-of-plane an in-plane polarizer acting on $\hat{\boldsymbol{s}}$, respectively. Moreover, $M_{\mathrm{s\,OP}}$ and $M_{\mathrm{s\,IP}}$ are the saturated magnetization of the out-of-plane and in-plane polarizer, respectively. Generally, $\bar{\boldsymbol{N}}_{\mathrm{OP}}$ and $\bar{\boldsymbol{N}}_{\mathrm{IP}}$ are 3×3 symmetric tensors. However, since for elliptical thin layers, the off-diagonal terms of the demagnetization tensors are of several orders smaller than the diagonal components, the magnetostatic interaction field can be approximately written as

$$\begin{aligned}\mathbf{H}_{\mathrm{int}} = &\left(H_{\mathrm{OP}x}\, S_{\mathrm{OP}x}, H_{\mathrm{OP}y}\, S_{\mathrm{OP}y}, H_{\mathrm{OP}z}\, S_{\mathrm{OP}z}\right) \\ &+ \left(H_{\mathrm{IP}x}\, S_{\mathrm{IP}x}, H_{\mathrm{IP}y}\, S_{\mathrm{IP}y}, H_{\mathrm{IP}z}\, S_{\mathrm{IP}z}\right),\end{aligned} \tag{10.4}$$

where $H_{\mathrm{OP}x} = N_{\mathrm{OP}xx}\, M_{\mathrm{s\,OP}}$, $H_{\mathrm{OP}y} = N_{\mathrm{OP}yy}\, M_{\mathrm{s\,OP}}$, $H_{\mathrm{OP}z} = N_{\mathrm{OP}zz}\, M_{\mathrm{s\,OP}}$; analogically for IP-components. For fixed $\hat{\boldsymbol{S}}_{\mathrm{OP}} = (1, 0, 0)$ and $\hat{\boldsymbol{S}}_{\mathrm{IP}} = (0, 0, 1)$, $\mathbf{H}_{\mathrm{int}}$ reduces to $\mathbf{H}_{\mathrm{int}} = H_{\mathrm{OP}x}\hat{\mathbf{e}}_x + H_{\mathrm{IP}z}\hat{\mathbf{e}}_z$.

In addition, $\mathbf{H}_{\mathrm{th}}$ is thermal stochastic field describing the influence of thermally activated processes and is given by equation (5.59).

10.1.1 Effective bulk parameters

An issue which has to be discussed first is the way in which the out-of-plane polarizer shall be treated. In the previous section we considered the out-of-plane polarizer as a thin single layer, Co(2). For the problem studied there, such an approximation was sufficient since it does not qualitatively change the results. However, in most of recent experiment, the out-of-plane polarizer is not a simple layer but consists of several thin magnetic layers ($\sim 0.1\,\mathrm{nm}$) separated by thin nonmagnetic layers [46, 43, 113, 114]. Such a structure of the fixed layer causes strong out-of-plane surface anisotropy in each layer and hence guarantees the out-of-plane magnetization. Electrons passing such a structure are strongly scattered on the interfaces. Hence we shall consider here the the out-of-plane polarizer as a single layer with some effective bulk parameters, i.e. bulk resistivity, ρ^*_{OP}, bulk spin asymmetry, β_{OP}, and spin-diffusion length $l_{\mathrm{sf\,OP}}$.

The first two of them might be calculated simply from a two channel model (see Section 3). We consider that each layer and internal interface is represented by two resistors: for spin $\uparrow$ and $\downarrow$. Resistors belonging to the same channel are connected in series. Then the resistance of the perpendicular polarizer is given by

$$\frac{1}{R_{\mathrm{OP}}} = \frac{1}{R'_{\uparrow}} + \frac{1}{R'_{\downarrow}}\,, \tag{10.5}$$

where $R'_{\uparrow(\downarrow)}$ is the resistance of the spin $\uparrow$ (spin $\downarrow$) channel. For simplicity we shall consider the polarizer as a periodic stack consisting of M thin ferromagnetic layers with the same thicknesses, d_{F}, separated by nonmagnetic layers $(M-1)$ with thicknesses d_{N}. Then the channel resistances are given by

$$R'_{\uparrow(\downarrow)} = M\,\rho_{\mathrm{F}\uparrow(\downarrow)} d_{\mathrm{F}} + (M-1)\,\rho_{\mathrm{N}\uparrow(\downarrow)} d_{\mathrm{N}} + 2(M-1)\,R_{\uparrow(\downarrow)}\,, \tag{10.6}$$

where $\rho_{\mathrm{F}\uparrow(\downarrow)}$ is the bulk resistivity of the ferromagnetic layers for $\uparrow$ ($\downarrow$) channel, $\rho_{\mathrm{N}\uparrow(\downarrow)}$ is the bulk resistivity for the nonmagnetic layers for $\uparrow$ ($\downarrow$) channel, and $R_{\uparrow(\downarrow)}$ is the interface resistance of the N/F interfaces for $\uparrow$ ($\downarrow$) channel. Using the standard relations for the bulk spin-dependent resistivities and interface resistances (3.37) one can obtain

$$\rho^*_{\mathrm{OP}} = M(d_{\mathrm{F}}/d)\,\rho^*_{\mathrm{F}} + (M-1)(d_{\mathrm{N}}/d)\,\rho^*_{\mathrm{N}} + 2(M-1)\,R^*/d\,, \tag{10.7a}$$

$$\beta_{\mathrm{OP}} = \left[M(d_{\mathrm{F}}/d)\,\beta\,\rho^*_{\mathrm{F}} + 2(M-1)\,\gamma\,R^*/d\right]/\rho^*_{\mathrm{OPP}}\,, \tag{10.7b}$$

where $d = Md_{\mathrm{F}} + (M-1)d_{\mathrm{N}}$ is the thickness of the out-of-plane polarizer layer. Furthermore, ρ^*_{OP} and β_{OPP} obey the relations

$$R'_{\uparrow(\downarrow)}/d = 2\,\rho^*_{\mathrm{OP}}\,(1 \mp \beta_{\mathrm{OP}})\ . \tag{10.8}$$

The spin-flip length in the out-of-plane polarizer can be estimated as

$$\frac{1}{l_{\mathrm{sf\,OP}}} = \left(\frac{d_{\mathrm{F}}}{d}\right)\frac{N}{l_{\mathrm{sf\,F}}} + \left(\frac{d_{\mathrm{N}}}{d}\right)\frac{N-1}{l_{\mathrm{sf\,N}}}\,, \tag{10.9}$$

where $l_{\mathrm{sf\,F}}$ and $l_{\mathrm{sf\,N}}$ is the spin-flip length in the ferromagnet and nonmagnet, respectively.

Figure 39 shows the angular dependence of STT components calculated for the studied spin valve with the out-of-plane polarizer consisting of 6 Cobalt and 5 Copper layers ($M = 6$, $d_{\mathrm{F}} = 0.5\,\mathrm{nm}$ and $d_{\mathrm{N}} = 0.7\,\mathrm{nm}$). The effective bulk parameters for this structure were calculated as $\rho^*_{\mathrm{OP}} \simeq 80\,\mu\Omega\mathrm{cm}$, $\beta_{\mathrm{OP}} = 0.76$, and $l_{\mathrm{sf\,OP}} = 58\,\mathrm{nm}$. Other material parameters used in the calculations can be found in Appendix A. The angular dependence of STT due to the out-of-plane polarizer, $\tau_{\parallel\mathrm{OP}}$ and $\tau_{\perp\mathrm{OP}}$, acting on the left interface of the free layer, were calculated for $\hat{\boldsymbol{s}}$ rotating in the (x,y)-plane, i.e. at constant $\theta = \pi/2$ while $\phi \in (0,\pi)$. Conversely, STT components acting on the right interface of the free layer due to the in-plane polarizer, $\tau_{\parallel\mathrm{IP}}$ and $\tau_{\perp\mathrm{IP}}$, were calculated at $\phi = \pi/2$ and $\hat{\boldsymbol{s}}$ rotating in the (y,z)-plane by angle $\theta \in (0,\pi)$. From the figure 39 one can see that

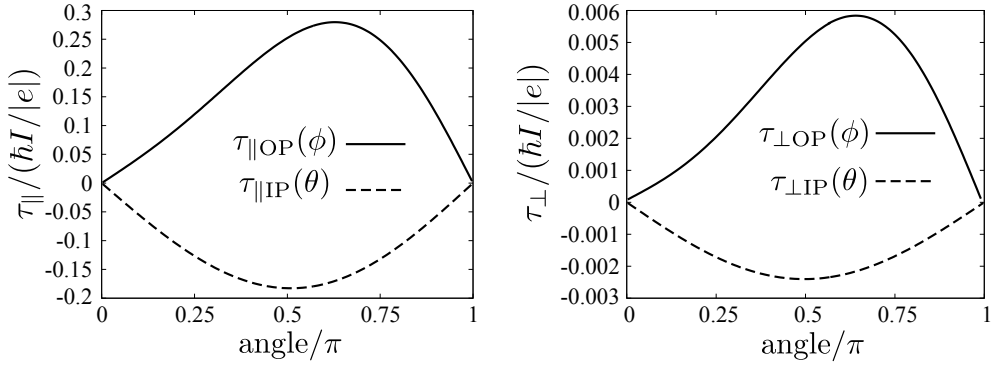

Figure 39: Angular dependences of the in-plane (left) and out-of-plane (right) STT components. $\tau_{\parallel\mathrm{OP}}(\phi) = a_{\mathrm{OP}}\sin\phi$ and $\tau_{\perp\mathrm{OP}}(\phi) = b_{\mathrm{OP}}\sin\phi$ are STT due to the out-of-plane polarizer acting on the left interface of the free layer. $\tau_{\parallel\mathrm{IP}}(\theta) = -a_{\mathrm{IP}}\sin\theta$ and $\tau_{\perp\mathrm{IP}}(\theta) = -b_{\mathrm{IP}}\sin\theta$ are STT due to the in-plane polarizer acting on the right interface of the free layer.

OP-components are markedly higher than IP ones. This is caused by strong electron scattering and spin filtering on the internal interfaces of the out-of-plane polarizer, which enhance its bulk resistivity and spin asymmetry.

10.1.2 Dynamics of the in-plane polarizer

In addition, we shall examine the influence of the dynamics of the in-plane polarizer on the switching probability. The dynamics of the in-plane polarizer is mainly induced by the spin transfer torque due to noncollinear configuration of $\hat{\boldsymbol{s}}$ and $\hat{\boldsymbol{S}}_{\mathrm{IP}}$, as well as by effective magnetic field. Obviously, the dynamics of $\hat{\boldsymbol{S}}_{\mathrm{IP}}$ is less pronounced than that of $\hat{\boldsymbol{s}}$ because of smaller spin accumulation at the Cu(12)/Py(20) interface and relatively large thickness of the in-plane polarizing layer.

The dynamics of $\hat{\boldsymbol{S}}_{\mathrm{IP}}$ is, similarly as for $\hat{\boldsymbol{s}}$, described by LLG, which reads

$$\begin{aligned} \frac{\mathrm{d}\hat{\boldsymbol{S}}_{\mathrm{IP}}}{\mathrm{d}t} + \alpha\, \hat{\boldsymbol{S}}_{\mathrm{IP}} \times \frac{\mathrm{d}\hat{\boldsymbol{S}}_{\mathrm{IP}}}{\mathrm{d}t} &= \boldsymbol{\Gamma}' \,, \\ \boldsymbol{\Gamma}' = -|\gamma_{\mathrm{g}}|\mu_0\, \hat{\boldsymbol{S}}_{\mathrm{IP}} \times \mathbf{H}'_{\mathrm{eff}} + \frac{|\gamma_{\mathrm{g}}|}{M_{\mathrm{s}} d'}\, \boldsymbol{\tau}' \,, \end{aligned} \tag{10.10}$$

where d' is the thickness of the in-plane polarizer; α and M_{s} are considered to be the same as for the sensing layer. Moreover, the effective field $\mathbf{H}'_{\mathrm{eff}}$ of the in-plane polarizer is given by

$$\mathbf{H}'_{\mathrm{eff}} = -H_{\mathrm{ext}}\hat{\mathbf{e}}_z - H_{\mathrm{ani}}(\hat{\boldsymbol{S}}_{\mathrm{IP}} \cdot \hat{\mathbf{e}}_z)\hat{\mathbf{e}}_z + \mathbf{H}'_{\mathrm{dem}}(\hat{\boldsymbol{S}}_{\mathrm{IP}}) + \mathbf{H}'_{\mathrm{int}}(\hat{\boldsymbol{S}}_{\mathrm{OP}}, \hat{\boldsymbol{s}}) + \mathbf{H}'_{\mathrm{th}} \,, \tag{10.11}$$

where $\mathbf{H}'_{\mathrm{dem}}$ is the demagnetizing field calculated for the in-plane polarizer, and $\mathbf{H}'_{\mathrm{int}}$ stands for the magnetostatic influence of the out-of-plane polarizer and free layer on $\hat{\boldsymbol{S}}_{\mathrm{IP}}$, obtained analogically as for the free layer. Thermal stochastic field, $\mathbf{H}'_{\mathrm{th}}$, obeys the same statistics as $\mathbf{H}_{\mathrm{th}}$ but is not correlated with $\mathbf{H}_{\mathrm{th}}$. The spin transfer torque is than given by $\boldsymbol{\tau}' = \boldsymbol{\tau}'_{\parallel} + \boldsymbol{\tau}'_{\perp}$.

$$\boldsymbol{\tau}'_{\parallel} = a' I\, \hat{\boldsymbol{S}}_{\mathrm{IP}} \times \left(\hat{\boldsymbol{S}}_{\mathrm{IP}} \times \hat{\boldsymbol{s}} \right) \,, \tag{10.12a}$$

$$\boldsymbol{\tau}'_{\perp} = b' I\, \hat{\boldsymbol{S}}_{\mathrm{IP}} \times \hat{\boldsymbol{s}} \,, \tag{10.12b}$$

where the parameters a' and b' depend on the magnetic configuration of the spin valve and are to be evaluated from the diffusive transport model.

10.2 Switching probability

Using the above described model we have calculated the switching probability of the free layer as follows. We started from the configuration with $\hat{\boldsymbol{s}}$ parallel to $\hat{\boldsymbol{S}}_{\mathrm{IP}}$. We shall refer to this configuration as to parallel one (P). First, at zero current ($I = 0$) and under constant conditions (i.e. constant temperature T, constant external field $\mathbf{H}_{\mathrm{ext}}$), $\hat{\boldsymbol{s}}$ evolves during certain equilibration period, t_{eq}, until it reaches the closest equilibrium position. From the preliminary numerical simulations we found that it is sufficient when $t_{\mathrm{eq}} = 5\,\mathrm{ns}$. Note, that position of $\hat{\boldsymbol{s}}$ after the equilibration period is slightly smeared around the equilibrium due to the thermal fluctuations. After this period, at time $t = t_{\mathrm{eq}}$, we apply a quasi-rectangular current pulse of a given length t_{p}. The shape of the applied pulse is shown in figure 40. First, the current raises during a raising time, t_{r}, from $I = 0$ up to its maximum value, $I = I_{\mathrm{p}}$. Then it remains constant during a period t_{c}. After this period current decreases down to $I = 0$ in time t_{f}. The pulse length, t_{p}, is measured at the half value of I_{p} (see Fig. 40). Lengths of the raising and falling periods were set as constant (disregarding the current amplitude) according to experimental values given in [43]; $t_{\mathrm{r}} = 65\,\mathrm{ps}$ and $t_{\mathrm{f}} = 105\,\mathrm{ps}$. The period t_{c} is then taken according to desired pulse length, t_{p}. During the pulse and after the pulse

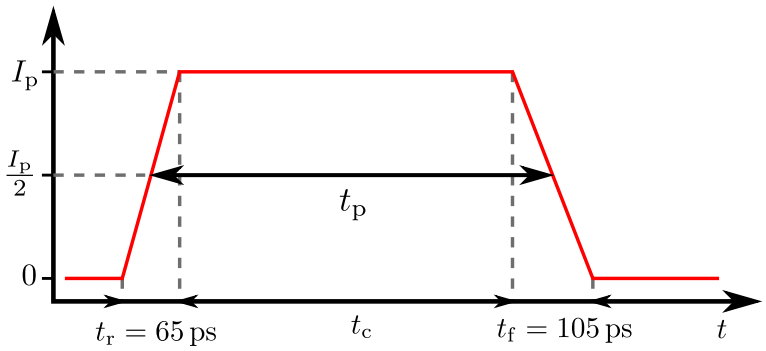

Figure 40: Scheme of the quasi-rectangular pulse with raise time, t_r, and falling time, t_f. The pulse length is measured at the half of current amplitude.

we calculated the moving average [108] of s_z component of the free layer's spin

$$\overline{s_z}(t) = \eta\, s_z(t) + (1-\eta)\,\overline{s_z}(t-\Delta t)\,, \tag{10.13}$$

where Δt is the integration step, and the weighting parameter $\eta = 10^{-3}$. The moving average $\overline{s_z}$ is calculated for time $t > t'$ when $s_z(t')$ reaches the value of -0.95; otherwise $\overline{s_z}(t) = s_z(t)$. A successful switching from P to antiparallel (AP) configuration, where $\hat{\boldsymbol{s}}$ is antiparallel to $\hat{\boldsymbol{S}}_\mathrm{IP}$, is counted when $\overline{s_z}(t_\mathrm{s}) < -0.99$, where t_s is the switching time. If the spin does not switch during next 25 ns after the current pulse the switching was not successful. This algorithm was tested and gave reasonable results at various conditions.

The switching probability might be than calculated from a number of independent simulations with the same parameters (temperature, pulse length, current amplitude, external field, etc). Here convergence of the switching probability, P_sw, was checked after each 1000 of independent simulations. It has been found that number of simulations $N = 10^4$ is sufficient for a reasonable calculations of P_sw. Note, in a similar way one can also calculate the switching probability from AP to P configuration.

Figure 41 shows the switching probability from P to AP in the studied dual spin valve. In the simulations we considered an external magnetic field in the z-direction as large as $H_\mathrm{ext} = 230\,\mathrm{Oe}$, which partly compensates the magnetostatic field from the in-plane polarizer. Moreover, we set the damping parameter to $\alpha = 0.1$. The reason for this high value is that in macrospin simulations α is rather an effective parameter, which should include also effects arising from inhomogeneous magnetization in real systems. In other words, in case of a real system, the free layer's magnetization might be inhomogeneous what results in damping enhancement. During the simulation we assumed constant temperature $T = 300\,\mathrm{K}$. Let us first analyze the left panel of Fig. 41, which depicts the case when only dynamics of the free layer was considered while $\hat{\boldsymbol{S}}_\mathrm{IP}$ was completely fixed. Current induced switching is observed for both current directions. This indicates, that the dynamics is mainly driven by the out-of-plane polarizer, whose action is symmetric with respect to current direction. To achieve current-induced switching one needs first to exceed certain critical value of the current density. These values are different for positive and negative currents. The asymmetry in critical currents is caused by both effective magnetic field and STT exerted by the in-plane polarizer, which depends on the current direction. Moreover, for various pulse lengths, t_p, one can see differences in P_sw as a function of I. For short pulse length, $t_\mathrm{p} = 100\,\mathrm{ps}$, there are distinct oscillations of P_sw with I, which range from $P_\mathrm{sw} = 0$ to 1. For intermediate

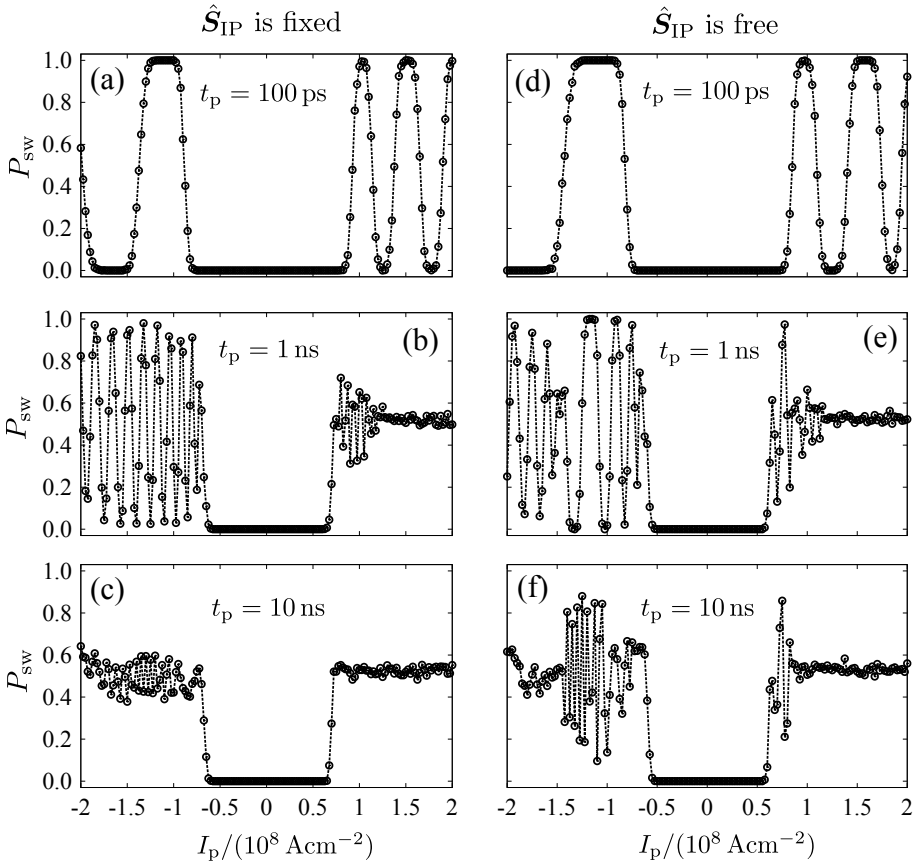

Figure 41: Switching probability from P to AP for current pulses $t_{\mathrm{p}} = 100\,\mathrm{ps}$, 1 ns, and 10 ns, as a function of current density, I_{p}. External magnetic field and temperature are $\mathbf{H}_{\mathrm{ext}} = 230\,\mathrm{Oe}$ and $T = 300\,\mathrm{K}$, respectively.

current lengths, $t_{\mathrm{p}} = 1\,\mathrm{ns}$, one can observe strong differences in P_{sw} for negative and positive currents. While for $I > 0$ the switching probability becomes almost constant, $P_{\mathrm{sw}} \sim 0.5$, for $I < 0$ one can see rapid oscillations of P_{sw} with the current density. Finally, for long current pulses, $t_{\mathrm{p}} = 10\,\mathrm{ns}$, the switching probability for sufficient current densities remains close to $P_{\mathrm{sw}} = 0.5$ for both current directions.

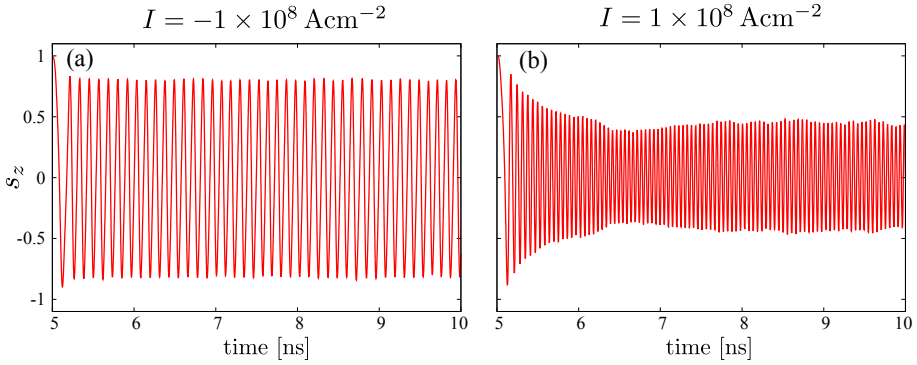

Figure 42: Trajectories of the z-component of $\hat{\boldsymbol{s}}$ under a constant current of amplitude (a) $I = -1 \times 10^8\,\mathrm{Acm}^{-2}$, and (b) $I = 1 \times 10^8\,\mathrm{Acm}^{-2}$, starting after equilibration at $t = 5\,\mathrm{ns}$. Here, $\hat{\boldsymbol{S}}_{\mathrm{IP}}$ was considered to be fixed. Simulation parameters are the same as in Fig. 41.

This behavior of $P_{\mathrm{sw}}(I_{\mathrm{p}})$ might be elucidated when comparing current-induced dynamics at

negative and positive current direction. Figure 42 shows the trajectories of $\hat{\boldsymbol{s}}$ for $I = \pm 1.0 \times 10^8\,\mathrm{Acm}^{-2}$ with both $\hat{\boldsymbol{S}}_{\mathrm{OP}} = \hat{\mathbf{e}}_x$ and $\hat{\boldsymbol{S}}_{\mathrm{IP}} = \hat{\mathbf{e}}_z$ being fixed. In both cases on can observe current-induced quasi-periodic out-of-plane precessions (around the x-axis). However, their frequencies and precessional amplitudes are markedly different. The main reason for the difference comes from a competition between STT and strong magnetostatic field of the perpendicular polarizer. This magnetostatic field pushes $\hat{\boldsymbol{s}}$ out of the layer's plane to the $\hat{\mathbf{e}}_x$ direction. For $I > 0$ the action of STT tries to align spin in the direction of $\hat{\boldsymbol{S}}_{\mathrm{OP}}$ and spin can precess around the direction of the magnetostatic field, which speeds up the precessional frequency. Oppositely, when $I < 0$, STT pushes the spin in the opposite direction and consequently slows down its precessional motion.

Assume now a quasi rectangular current pulse of a certain magnitude I_{p}. When the pulse is applied, the spin starts to precess around the x-axis with large precessional angle and amplitude. If the current is switched off fast enough, and the spin at that moment is close to the opposite direction, it moves directly to the closest equilibrium just due to energy dissipation in external magnetic field. However, because the precession rate depends on the current density, I_{p}, the same pulse length leads to oscillations of P_{sw} shown in Fig. 41(a). This switching mechanism is similar to the precessional switching by external magnetic field [111, 112]. If the current pulse is well optimized, precessional mechanism leads to ultrafast switching at low energy costs. Because the initial precession is similar for both current directions, precessional switching can be achieved for $I_{\mathrm{p}} < 0$ as well as for $I_{\mathrm{p}} > 0$, but at different current densities. When the current pulse is longer ($t_{\mathrm{p}} = 1\,\mathrm{ns}$), $\hat{\boldsymbol{s}}$ comes into steady precessional motion around $\hat{\mathbf{e}}_x$ with a certain frequency and amplitude, both depending on I_{p}. Therefore, a small change in I_{p} might result in different final configuration after the pulse is applied. For negative currents (in the studied range of I_{p}) the precessional amplitudes are large enough and the final state is not strongly influenced by the thermal fluctuations. Moreover, the frequency of the precessions is relatively small and hence the periodicity in P_{sw} is observed. Conversely, for $I_{\mathrm{p}} > 0$, precessional amplitude is smaller and precessions are fast. The net spin moment is pushed closer to the $\hat{\mathbf{e}}_x$ direction, which makes the dynamics of $\hat{\boldsymbol{s}}$ more vulnerable to thermal fluctuations. As a result, when the current disappears the probability that $\hat{\boldsymbol{s}}$ is closer to P or AP basin of attraction is approximately the same, and hence $P_{\mathrm{sw}} \sim 0.5$. Finally, after sufficiently long action of current, the spin $\hat{\boldsymbol{s}}$ is longer influenced by the thermal fluctuations and the effect of probability equalization for P and AP is more pronounced, even in the case of large precessional amplitudes at $I_{\mathrm{p}} < 0$.

Let us now discuss the right column of 41. It shows the dependence of switching probability of $\hat{\boldsymbol{s}}$ on I_{p}, when $\hat{\boldsymbol{S}}_{\mathrm{OP}} = \hat{\mathbf{e}}_x$ is fixed but $\hat{\boldsymbol{S}}_{\mathrm{IP}}$ is free. Then, the dynamics is described by equation (10.10), which is coupled with (10.1). Interestingly, comparing figures 41(a) and 41(d) one can see that in the short-pulse regime, dynamics of $\hat{\boldsymbol{S}}_{\mathrm{IP}}$ leads to an enlargement of the intervals with $P_{\mathrm{sw}} \sim 1$. Similar enhancement of P_{sw} one can notice also for longer pulses. Namely, for $t_{\mathrm{p}} = 1\,\mathrm{ns}$ one observes intervals with $P_{\mathrm{sw}} \sim 1$ for negative currents and a peak with high P_{sw} for positive current density. For $t_{\mathrm{p}} = 10\,\mathrm{ns}$ the enhancement of switching probability is observed mainly for smaller values of positive I. Figure 43 shows the dynamics of $\hat{\boldsymbol{s}}$ and $\hat{\boldsymbol{S}}_{\mathrm{IP}}$ for several values of constant I. For $I = -1 \times 10^8\,\mathrm{Acm}^{-2}$, $\hat{\boldsymbol{S}}_{\mathrm{IP}}$ oscillates around $\hat{\mathbf{e}}_z$ with relatively large amplitude. These precessions influence mainly the frequency of $\hat{\boldsymbol{s}}$, which is smaller than in the case with fixed $\hat{\boldsymbol{S}}_{\mathrm{IP}}$, and leads to the enhancement of P_{sw}. In the studied range of I, the character of coupled precessions of $\hat{\boldsymbol{s}}$ and $\hat{\boldsymbol{S}}_{\mathrm{IP}}$ remains the same for different current amplitudes. For positive current densities, the dynamics of $\hat{\boldsymbol{s}}$ and $\hat{\boldsymbol{S}}_{\mathrm{IP}}$ strongly depends on the current density. While for smaller

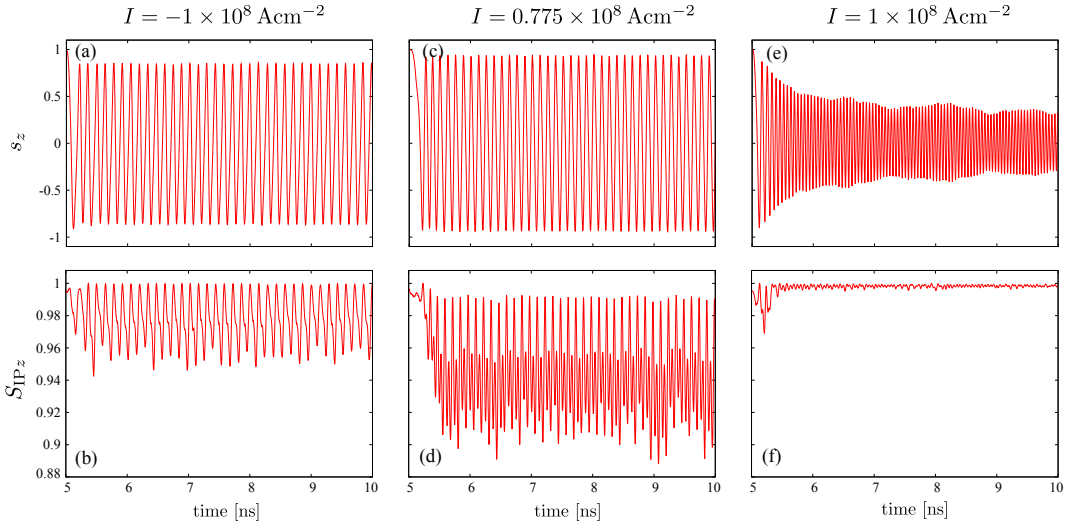

Figure 43: Simultaneous dynamics of $\hat{\boldsymbol{s}}$ and $\hat{\boldsymbol{S}}_{\mathrm{IP}}$. Trajectories of the $\hat{\boldsymbol{s}}$ and $\hat{\boldsymbol{S}}_{\mathrm{IP}}$ z-components under a constant current of amplitude (a-b) $I = -1 \times 10^8\,\mathrm{Acm}^{-2}$, and (c-d) $I = 0.775 \times 10^8\,\mathrm{Acm}^{-2}$, (e-f) $I = 1 \times 10^8\,\mathrm{Acm}^{-2}$ starting after equilibration at $t = 5\,\mathrm{ns}$. Simulation parameters are the same as in Fig. 41.

values of $I \lesssim 0.9 \times 10^8\,\mathrm{Acm}^{-2}$ there are pronounced in-plane precessions of $\hat{\boldsymbol{S}}_{\mathrm{IP}}$ [Fig. 43(d)], for higher current densities $\hat{\boldsymbol{S}}_{\mathrm{IP}}$ is fast damped in the direction of $\hat{\mathbf{e}}_z$ and its dynamics is mainly due to the thermal fluctuations [Fig. 43(f)]. As a result, at small current densities $\hat{\boldsymbol{s}}$ precesses around $\hat{\mathbf{e}}_x$ with large amplitude and its switching probability might reach high values for properly optimized pulse as shown in the case of $I = 0.775 \times 10^8\,\mathrm{Acm}^{-2}$ [Fig. 43(c)], which corresponds to the peak shown in 41(e). On the other side, for higher current density, the dynamics of $\hat{\boldsymbol{s}}$ [Fig. 43(e)] is similar to the case with fixed $\hat{\boldsymbol{S}}_{\mathrm{IP}}$ [Fig. 43(b)] and consequently $P_{\mathrm{sw}} \sim 0.5$.

Similar enhancement of the switching probability can be observed also in the case of switching from AP to P configuration, see Fig. 44.

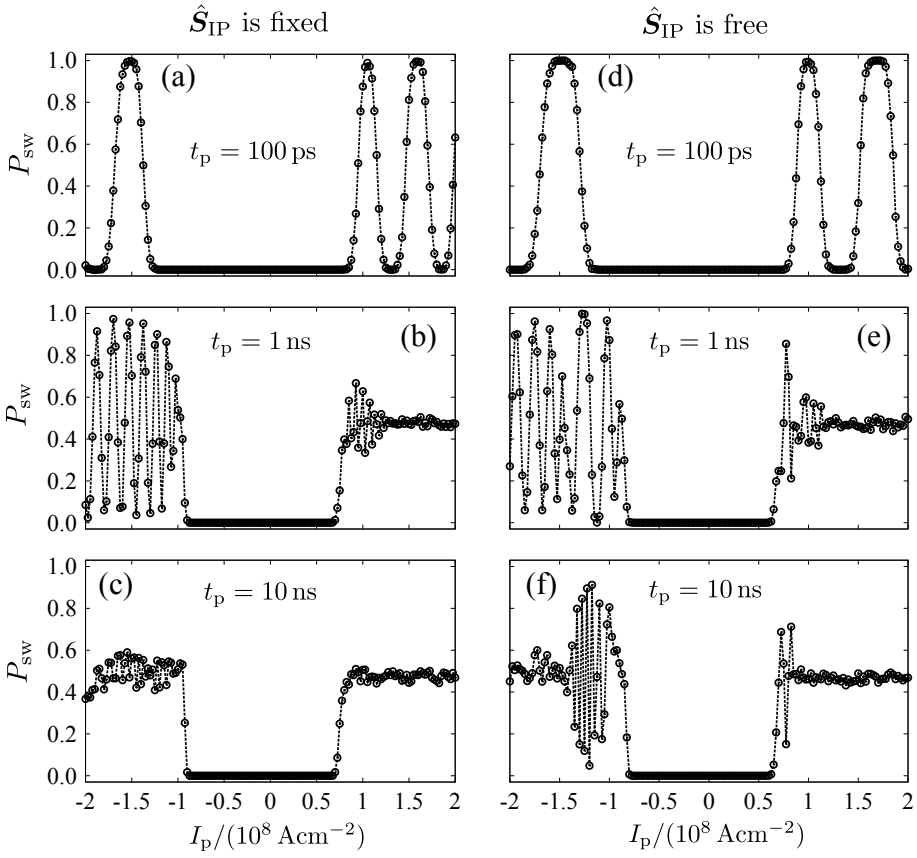

Figure 44: Switching probability from AP to P for current pulses $t_{\mathrm{p}} = 100\,\mathrm{ps}$, 1 ns, and 10 ns as a function of current density, I. Simulation parameters are the same as for Fig. 41.

11 Dynamics of composite free layer with antiferromagnetic interlayer coupling

The term *composite layer* refers to a superlattice consisting of two (or more) magnetic layers separated by nonmagnetic spacer. Usually, the magnetizations of magnetic layers are strongly coupled via the RKKY interaction (see section 4.4), which can be either ferromagnetic or antiferromagnetic (depending on the spacer thickness). In practice, a special importance have composite layers with antiferromagnetic coupling. We distinguish two types of antiferromagnetically coupled composite layers: *synthetic antiferromagnet* (SyAF), which consists of two identical ferromagnetic layers separated by a nonmagnetic spacer (usually ruthenium), and *synthetic ferrimagnet*, where the two magnetic layers differs in thickness or material.

In many spin torque experiments, SyAF is used as a reference layer because its magnetic flux is closed and does not magnetically affect the sensing layer [115]. Recently, it has been shown that in such a geometry, magnetic excitations in the SyAF fixed layer might be induced by STT due to dynamic coupling [58] with the free layer. It has been observed [59, 60] that the dynamics of the SyAF fixed layer might have a remarkable impact on the resistance oscillations measured in experiments, and therefore, they should not be neglected in the interpretation of experimental results.

Moreover, composite layers are also used as free layers because of their high *thermal stability*. Thermal stability is measured by Δ_0 defined as

$$\Delta_0 = \frac{M_\mathrm{s} H_\mathrm{ani} V}{2 k_\mathrm{B} T}\,, \tag{11.1}$$

where M_s, H_ani, and V are the saturated magnetization, uniaxial anisotropy field, and volume of the free layer, respectively. k_B is the Boltzmann constant and T is the temperature. For a reliable memory cell, which should be able to keep the stored information longer than 10 years, $\Delta_0 > 40$ is required [116]. In the recent experiments [117] it has been shown that the thermal stability in an antiferromagnetically coupled composite layers is much higher ($\Delta_0 > 80$) than in a single free layer. Moreover, the thermal stability measured in ferromagnetically coupled composite layer ($\Delta_0 = 248 \pm 60$) [118, 119] seems to exceed even that for the SyAF and SyF.

A Switching scheme for a SyAF free layer by magnetic field pulses has been proposed in 2004 [120]. Later on, a possibility of current-induced switching of SyAF was demonstrated experimentally [121]. In turn, the possibility of critical current reduction has been shown for a CFL with ferromagnetically coupled magnetic layers [122]. However, the reduction of critical current in the case of antiferromagnetically coupled CFLs is still an open problem. Recent numerical study of the switching of a SyAF free layer [123] shows that the corresponding critical current in most cases is higher than the current required for switching of a simple free layer, and only in a narrow range of relevant parameters the critical current is reduced.

In this chapter the current-induced dynamics of a composite free layer (CFL) with antiferromagnetic coupling is studied. We consider a system $AF/\mathrm{F}_0/\mathrm{N}_1/\mathrm{F}_1/\mathrm{N}_2/\mathrm{F}_2$, shown in Fig. 45, where AF is an antiferromagnetic layer (used to bias magnetization of the reference magnetic layer F_0), F_1 and F_2 are two magnetic layers, while N_1 and N_2 are non-magnetic spacers. The part $\mathrm{F}_1/\mathrm{N}_2/\mathrm{F}_2$ is the CFL structure with antiferromagnetic interlayer exchange coupling. We examine current-induced dynamics of both SyAF and SyF free layers. These two structures differ only in the thickness of F_1 layer, while RKKY coupling and other pillar parameters remain the same.

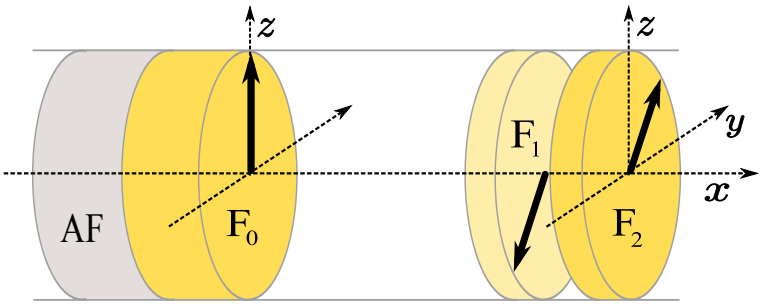

Figure 45: Scheme of the spin valve pillar structure with a composite free layer.

11.1 Model

Because CFL consist of two magnetic layers, which are strongly coupled, the dynamics of CFL in the macrospin approximation is described by two coupled Landau-Lifshitz-Gilbert equations (LLGs),

$$\begin{aligned} \frac{\mathrm{d}\hat{\boldsymbol{S}}_i}{\mathrm{d}t} + \alpha\,\hat{\boldsymbol{S}}_i \times \frac{\mathrm{d}\hat{\boldsymbol{S}}_i}{\mathrm{d}t} &= \boldsymbol{\Gamma}_i\,, \\ \boldsymbol{\Gamma}_i = -|\gamma_\mathrm{g}|\mu_0 \hat{\boldsymbol{S}}_i \times \mathbf{H}_{\mathrm{eff}\,i} + \frac{|\gamma_\mathrm{g}|}{M_\mathrm{s} d_i}\,\boldsymbol{\tau}_i\,, \end{aligned} \tag{11.2}$$

for $i = 1, 2$, where $\hat{\boldsymbol{S}}_i$ stands for a unit vector along the net spin moment of the i-th layer, whereas $\mathbf{H}_{\mathrm{eff}\,i}$ and $\boldsymbol{\tau}_i = \boldsymbol{\tau}_{\parallel_i} + \boldsymbol{\tau}_{\perp i}$ are the effective field and current-induced torque, respectively, both acting on $\hat{\boldsymbol{S}}_i$. The damping parameter α and the saturation magnetization M_s are assumed the same for both magnetic components of the CFL. Furthermore, d_i stands for thickness of the F_i layer.

The effective magnetic field for the F_i layer is

$$\mathbf{H}_{\mathrm{eff}\,i} = -H_\mathrm{ext}\hat{\mathbf{e}}_z - H_{\mathrm{ani}}(\hat{\boldsymbol{S}}_i \cdot \hat{\mathbf{e}}_z)\hat{\mathbf{e}}_z + \mathbf{H}_{\mathrm{dem}\,i}(\hat{\boldsymbol{S}}_i) + \mathbf{H}_{\mathrm{int}\,i}(\hat{\boldsymbol{S}}_0, \hat{\boldsymbol{S}}_j) + H_{\mathrm{RKKY}\,i}\,\hat{\boldsymbol{S}}_j\,, \tag{11.3}$$

where $i, j = 1, 2$ and $i \neq j$. In the latter equation, $\mathbf{H}_{\mathrm{dem}\,i} = (\bar{\mathbf{N}}_i \cdot \hat{\boldsymbol{S}}_i) M_\mathrm{s}$ and $\mathbf{H}_{\mathrm{int}\,i} = (\bar{\mathbf{N}}_{0i} \cdot \hat{\boldsymbol{S}}_0) M_{\mathrm{s}0} + (\bar{\mathbf{N}}_{ji} \cdot \hat{\boldsymbol{S}}_j) M_\mathrm{s}$ are the self-demagnetizing and magnetostatic fields, respectively. Tensors $\bar{\mathbf{N}}_i$ and $\bar{\mathbf{N}}_{ij}$ are calculated in the general tensor formalism (see 4.3.1). The effective field $\mathbf{H}_{\mathrm{eff}\,i}$ also includes stochastic thermal noise $\mathbf{H}_{\mathrm{th}\,i}$, which obeys the statistics given by (5.36a) and (5.36b). Here, we do not consider any correlations between components $\mathbf{H}_{\mathrm{th}1}$ and $\mathbf{H}_{\mathrm{th}2}$.

In a CFL structure, the layer F_1 is influenced by STT induced by the polarizer F_0, as well as by STT due to the layer F_2. In turn, the layer F_2 is influenced by the torques from the layer F_1. Hence for the STT components one can write

$$\boldsymbol{\tau}_{\parallel_1} = I\,\hat{\boldsymbol{S}}_1 \times \left[\hat{\boldsymbol{S}}_1 \times \left(a_1^{(0)}\hat{\boldsymbol{S}}_0 + a_1^{(2)}\hat{\boldsymbol{S}}_2\right)\right]\,, \tag{11.4a}$$

$$\boldsymbol{\tau}_{\perp 1} = I\,\hat{\boldsymbol{S}}_1 \times \left(b_1^{(0)}\hat{\boldsymbol{S}}_0 + b_1^{(2)}\hat{\boldsymbol{S}}_2\right)\,, \tag{11.4b}$$

$$\boldsymbol{\tau}_{\parallel_2} = I\,a_2^{(1)}\,\hat{\boldsymbol{S}}_2 \times \left(\hat{\boldsymbol{S}}_2 \times \hat{\boldsymbol{S}}_1\right)\,, \tag{11.4c}$$

$$\boldsymbol{\tau}_{\perp 2} = I\,b_2^{(1)}\,\hat{\boldsymbol{S}}_2 \times \hat{\boldsymbol{S}}_1\,, \tag{11.4d}$$

where I is positive when electrons flow from the layer F_2 towards F_0 (see Fig. 45), while the parameters $a_i^{(j)}$ and $b_i^{(j)}$ $(i, j = 1, 2)$ are independent of current I, but generally depend on magnetic configuration.

11.2 Numerical simulations

In the numerical simulations to be presented below we have assumed a spin valve of the structure Cu-IrMn(10)/Py(8)/Cu(8)/Co(d_1)/Ru(1)/Co(d_2)-Cu. The layer Py(8) is the Permalloy polarizing layer with its magnetization fixed due to exchange coupling to IrMn. In turn, Co(d_1)/Ru(1)/Co(d_2) is the CFL ($F_1/N_2/F_2$ structure) with antiferromagnetic RKKY exchange coupling *via* the thin ruthenium layer. The coupling constant between Co layers has been assumed as $J_{\mathrm{RKKY}} \simeq -0.6\,\mathrm{mJ/m^2}$, which is close to experimentally observed values [59, 60]. Here, we shall analyze two different geometries of CFL. The first one is a SyAF structure with $d_1 = d_2 = 2\,\mathrm{nm}$, while the second one is a synthetic ferrimagnet (SyF) with $d_1 = 2d_2 = 4\,\mathrm{nm}$.

We have assumed typical values of the relevant parameters, i.e., the damping parameter has been set to $\alpha = 0.01$, while the uniaxial anisotropy field $H_{\mathrm{ani}} = 45\,\mathrm{kAm^{-1}}$ in both magnetic layers of the CFL. In turn, saturation magnetization of cobalt has been assumed as $M_{\mathrm{s}}(\mathrm{Co}) = 1.42 \times 10^6\,\mathrm{Am^{-1}}$, and for permalloy $M_{\mathrm{s}}(\mathrm{Py}) = 6.92 \times 10^5\,\mathrm{Am^{-1}}$. The demagnetization field and magnetostatic interaction of magnetic layers have been calculated for layers of elliptical cross-section, with the major and minor axes equal to 130 nm and 60 nm, respectively.

11.2.1 Synthetic antiferromagnet

Consider first the dynamics of the SyAF free layer. From symmetry we have $H_{\mathrm{RKKY1}} = H_{\mathrm{RKKY2}} \equiv H_{\mathrm{RKKY}}$, and we have set $H_{\mathrm{RKKY}} = 2\,\mathrm{kOe}$, which corresponds to $J_{\mathrm{RKKY}} \sim -0.6\,\mathrm{mJ/m^2}$. We have performed a number of independent numerical simulations modeling SyAF dynamics induced by constant current and constant in-plane external magnetic field. The latter is assumed to be smaller than the critical field for transition to spin-flop phase of SyAF. Accordingly, each simulation started from an initial state close to $\hat{\boldsymbol{S}}_1 = -\hat{\boldsymbol{S}}_2 = -\hat{\mathbf{e}}_z$. To have a non-zero initial STT for $\hat{\boldsymbol{S}}_1$, both spins of the SyAF have been tilted by 1° in the layer plane so that they remained collinear.

From numerical simulations we have constructed a map of time-averaged resistance, shown in Fig. 46(a). The resistance has been averaged in the time interval of 30 ns following initial 50 ns equilibration time of the dynamics. The diagram shows only that part of the resistance, which depends on magnetic configuration, and hence varies with CFL dynamics [61]. The constant part of resistance, due to bulk and interfacial resistances of the studied structure, has been calculated to be as large as $R_{\mathrm{sp}} = 19.74\,\mathrm{f\Omega}$. For the assumed initial configuration, magnetic dynamics has been observed only for negative current density. When the current is small, no dynamics is observed since the spin motion is damped into the closest collinear state ($\hat{\boldsymbol{S}}_1 = -\hat{\boldsymbol{S}}_2 = -\hat{\mathbf{e}}_z$, marked as $\downarrow\uparrow$) of high resistance. After exceeding a certain threshold value of current density, there is a drop in the averaged resistance, which indicates current induced dynamics of the SyAF free layer. Figures 46(b) and (f) show that this drop is associated with switching of the whole SyAF structure into an opposite state ($\hat{\boldsymbol{S}}_1 = -\hat{\boldsymbol{S}}_2 = \hat{\mathbf{e}}_z$, marked as $\uparrow\downarrow$)

Figure 46 shows that the threshold current for dynamics onset depends on the applied field and reaches maximum at a certain value of H_{ext}, $H_{\mathrm{ext}} = H_0$. Furthermore, it appears that mechanisms of the switching process for $H_{\mathrm{ext}} < H_0$ and $H_{\mathrm{ext}} > H_0$ are qualitatively different. To distinguish these two mechanisms, we present in Figs. 46(b – i) basic characteristics of switching, calculated for $I = -1.0 \times 10^8\mathrm{Acm^{-2}}$ and for fields $H_{\mathrm{ext}} = -400\,\mathrm{Oe}$, which is below H_0 [Figs. 46(b – e)], and $H_{\mathrm{ext}} = 400, \mathrm{Oe}$, which lies above H_0 [Figs. 46(f – i)]. Figs. 46(b) and (f) present time evolution of the z-components of both spins. To understand the SyAF dynamics, in Figs. 46(c) and (g) we plotted

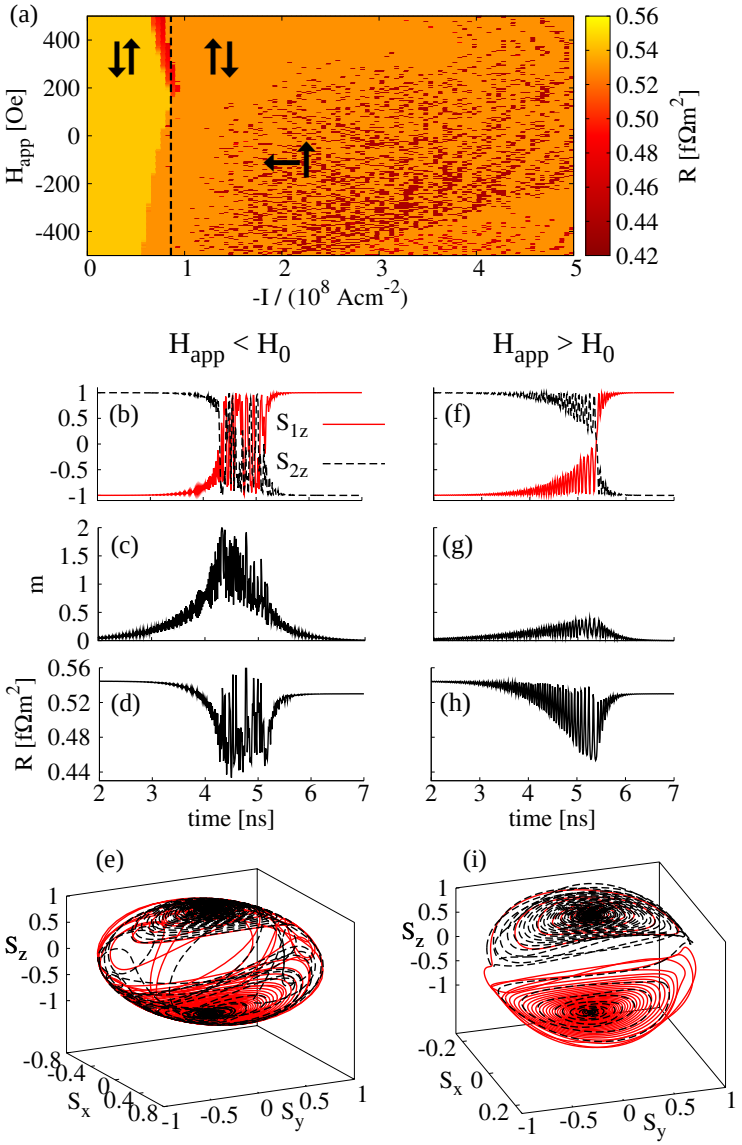

Figure 46: (a) Averaged resistance of Cu-IrMn(10)/Py(8)/Cu(8)/Co(2)/Cu(1)/Co(2)-Cu spin valve pillar with a SAF free layer as a function of current density and applied magnetic field. Examples of switching processes at $I = -1.0 \times 10^8\,\mathrm{Acm}^{-2}$ and $H_{\mathrm{ext}} = -400\,\mathrm{Oe}$ (b – e) and $H_{\mathrm{ext}} = 400\,\mathrm{Oe}$ (f – i). Figures (b) and (f) show dynamics of z-components of both spin moments, (c) and (g) present the overall magnetization of the free layer, (d) and (h) show the corresponding variation of pillar resistance, (e) and (i) show the spin trajectories of $\hat{\boldsymbol{S}}_1$ (red solid line) and $\hat{\boldsymbol{S}}_2$ (black dashed line) in the time interval

the amplitude of overall SyAF magnetization, defined as $m = |\hat{\boldsymbol{S}}_1 + \hat{\boldsymbol{S}}_2|$. This parameter vanishes for antiparallel alignment of both spins of CFL, but becomes nonzero when the configuration deviates from the antiparallel one. Furthermore, Figs. 46(d) and (h) show the corresponding time variation of the resistance, R, which might be directly extracted from experimental measurements as well. In addition, in Figs. 46(e) and (i) we show the trajectories of $\hat{\boldsymbol{S}}_1$ and $\hat{\boldsymbol{S}}_2$ in the real space taken from the time interval from $t = 0$ to 10 ns. From Figs. 46(a) follows that the point where the threshold current reaches maximum is at $H_0 \simeq H_z^{02}$, which indicates its relation to magnetostatic interaction of F_2 and fixed polarizer. This also has been confirmed by analogical simulations disregarding the magnetostatic coupling between magnetic layers, which resulted in similar diagram, but with $H_0 = 0$ (not shown).

The initial configuration above was $-\hat{\boldsymbol{S}}_1 = \hat{\boldsymbol{S}}_2 \simeq \hat{\boldsymbol{S}}_0$ with $\hat{\boldsymbol{S}}_0 = \hat{\mathbf{e}}_z$ ($\downarrow\uparrow$). When the magnitude of current density is large enough and $I < 0$, $\hat{\boldsymbol{S}}_1$ becomes unstable and starts to precess around $-\hat{\mathbf{e}}_z$. Precession of $\hat{\boldsymbol{S}}_1$ induces precession of $\hat{\boldsymbol{S}}_2$ – mainly via the RKKY coupling. Since response to the exchange field is slower than current-induced dynamics, a difference in precession phase of $\hat{\boldsymbol{S}}_2$ and $\hat{\boldsymbol{S}}_1$ appears and configuration of SyAF deviates from the initial one. This in turn enhances the STT acting on F_2, which tends to switch $\hat{\boldsymbol{S}}_2$. Its amplitude, however, is small in comparison to the strong RKKY coupling. Further scenario depends on the external magnetic field. When $H_{\text{ext}} < H_0$ [Figs. 46(b – e)] the Zeeman energy of $\hat{\boldsymbol{S}}_2$ has a maximum in the initial state and external magnetic field tends to switch $\hat{\boldsymbol{S}}_2$ to the opposite orientation. Competition between the torques acting on SyAF results in out-of-plane precessions of both spins. After several precessions $\hat{\boldsymbol{S}}_1$ reaches the opposite static state. In turn, $\hat{\boldsymbol{S}}_2$ is only slightly affected by STT, and its dynamics is damped in the external magnetic and RKKY exchange fields. In contrast, when $H_{\text{ext}} > H_0$ [Figs. 46(f – i)], Zeeman energy of F_2 has a local minimum in the initial state, which stabilizes $\hat{\boldsymbol{S}}_2$. Therefore, in a certain range of current density, SyAF does not switch but remains in self-sustained coherent in-plane precessions (red area in the upper part of Fig. 46(a)). For a sufficient current density, the SyAF becomes destabilized and the precessional angle increases until the spins pass the (x, y)-plane. Consequently, the precessional angle decreases and spins of the SyAF are stabilized in the opposite state ($\uparrow\downarrow$). Moreover, as shown in Fig. 46(c), the switching process for $H_{\text{ext}} < H_0$ is connected with high distortion of SyAF configuration, where m in a certain point reaches its maximum value (corresponding to parallel orientation). Contrary, the m remains small for $H_{\text{ext}} > H_0$ [Figs. 46(g)], and the effective magnetic moment of the free layer is smaller than magnetic moment of a single layer.

The switching mechanisms described above dominate the spin dynamics when the current density is close to the dynamics threshold. For higher current densities, the nonlinearities in SyAF dynamics become more pronounced and lead to bistable behavior of the dynamics, especially for $H_{\text{ext}} < H_0$ and $I \gtrsim 10^8 \text{Acm}^{-2}$. In that region, the number of out-of-plane precessions before SyAF switching increases with the current density. However, their precessional angle increases in time and consequently $\hat{\boldsymbol{S}}_1$ might reach an out-of-plane static point slightly tilted away from the $\hat{\mathbf{e}}_x$ direction while $\hat{\boldsymbol{S}}_2 = \hat{\mathbf{e}}_z$ remains in the layers plane. The out-of-plane static states (marked as $\leftarrow\uparrow$) have small resistance and appear as dark red spots in the diagram shown in Fig. 46(a). From the analysis of the dispersion of pillar resistance follows that except of a narrow region close to the dynamics threshold with persistent in-plane precessions, no significant steady-state dynamics of SyAF appears.

11.2.2 Synthetic ferrimagnet

Now, let us study the spin valve with SyF as a free layer, assuming $d_1 = 4\,\mathrm{nm}$ and $d_2 = 2\,\mathrm{nm}$. Accordingly, H_{RKKY2} remains 2 kOe while H_{RKKY1} is reduced to 1 kOe. As in the case of SyAF, from the averaged time-dependent part of the pillar resistance we have constructed a diagram presenting current-induced dynamics, see Fig. 47(a). The static part of resistance is now $R_{\mathrm{sp}} = 19.80\,\mathrm{f\Omega}$. The diagram has some features similar to those for SyAF. However, the maximum critical current

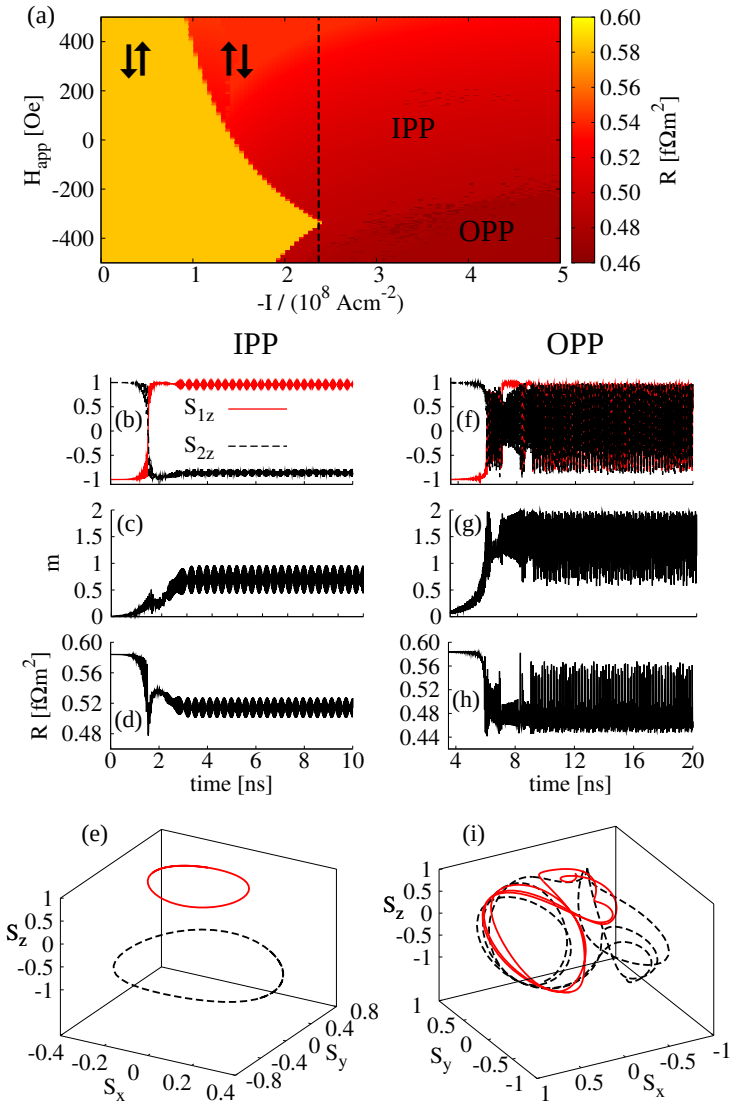

Figure 47: (a) Averaged resistance of Cu-IrMn(10)/Py(8)/Cu(8)/Co(4)/Cu(1)/Co(2)-Cu spin valve pillar with a SyF free layer, presented as a function of current density and applied magnetic field. Examples of current-induced dynamics for $I = -3 \times 10^8\,\mathrm{Am}^{-1}$ and $H_{\mathrm{ext}} = 200\,\mathrm{Oe}$ (b – e) and $H_{\mathrm{ext}} = -400\,\mathrm{Oe}$ (f – i). Panels (b) and (f) show dynamics of z-components of $\hat{\boldsymbol{S}}_1$ and $\hat{\boldsymbol{S}}_2$, (c) and (g) present the overall magnetization of the free layer, (d) and (h) show the corresponding variation of pillar resistance, (e) and (i) show spin trajectories of $\hat{\boldsymbol{S}}_1$ (red solid line) and $\hat{\boldsymbol{S}}_2$ (black dashed line) taken from a time interval as large as 30 ns after 100 ns of initial equilibration.

is shifted towards negative values of H_{ext}, even if magnetostatic interaction between magnetic layers is neglected. This asymmetry is due to the difference in exchange and demagnetization fields acting on layers F_1 and F_2.

There are now several dynamic regimes. The first one is the region of switching from ⇵ configuration to the opposite one, ⇅, which is located at largest values of H_{ext} in the diagram. Mechanism of the switching is similar to that of SyAF shown in Figs. 46(f – i), where CFL switches *via* in-plane precessional states with a weak distortion of the antiparallel alignment of $\hat{\boldsymbol{S}}_1$ and $\hat{\boldsymbol{S}}_2$. The darker area above H_0 indicates one of the possible self-sustained dynamic regimes of SyF, i.e. the in-plane precessions (IPP); see Figs. 47(b – e). This precessional regime starts directly after the SyF switching, and $\hat{\boldsymbol{S}}_1$ and $\hat{\boldsymbol{S}}_2$ precess around $\hat{\mathbf{e}}_z$ and $-\hat{\mathbf{e}}_z$, respectively. Due to different effective fields in F_1 and F_2, and energy gains due to STT, the spins precess with different precessional angles [Fig. 47(e)] and therefore different frequencies. Because of the strong interlayer coupling and spin transfer between the layers, amplitudes of their precessions are periodically modulated in time. This modulation appears also in the time dependence of pillar resistance. Conversely, below H_0 the dynamics is dominated by large angle out-of-plane precessions (OPP) of both spins, as shown in Figs. 47(f – i). This dynamic state is connected with a strong distortion of the antiparallel CFL configuration, i.e. large value of m, and large variation of the resistance. From Fig. 47(i) one can see that trajectories of $\hat{\boldsymbol{S}}_1$ and $\hat{\boldsymbol{S}}_2$ are rather complicated including both IPP and OPP regimes. Thus, self-sustained dynamics in structures with SyF free layer is much richer than that in systems with SyAF free layer.

11.2.3 Power spectral density

In this section the power spectral density (PSD) of SyAF dynamics shall be examined as a function of current density and external magnetic field. In the simulation we started from $I = 0$ and changed current density in steps $\Delta I = 10^6\,\text{Acm}^{-2}$ at a fixed applied field. As before, to protect the SyF dynamics from collapsing into collinear static state, we assumed small thermal fluctuations corresponding to $T_{\text{eff}} = 5\,\text{K}$. At each step we simulated the dynamics of coupled CFL's spins and calculated PSD. As in Ref. [124], we assumed that the input current is split between a load with resistance R_{L} and pillar with resistance $R_{\text{sp}} + R(t)$. Hence, voltage on the pillar has been calculated as $U(t) = IR(t)/[1 + R_{\text{sp}}/(R_{\text{L}}S)]$, where we assumed $R_{\text{L}} = 50\,\Omega$, and S is the cross-section of the pillar (ellipsoid with the major and minor axes equal to 130 and 60 nm, respectively). Then, at a given I we calculated voltage in the frequency domain, $U(f)$, using fast Fourier transformation over the period $t_{\text{FFT}} = 50\,\text{ns}$ following the equilibration time of $t_{\text{eq}} = 30\,\text{ns}$. The power spectral density has been defined as $\text{PSD}(f) = 2U^2(f)/(R_{\text{L}}\,\Delta f)$, where $\Delta f = 1/t_{\text{FFT}}$.

Figures 48(a) and (b) show PSD calculated at $H_{\text{ext}} = -400\,\text{Oe}$ and $200\,\text{Oe}$, respectively. The former case corresponds to that part of the diagram in Fig. 47(a), which includes OPP modes, while in the latter case we observed IPP only. Let us analyze first the situation in Fig. 48(a). When current passes through the corresponding threshold value, both spins start precessing in the layers' plane. Apart from the main peak in the PSD at $f \simeq 40\,\text{GHz}$, two additional minor peaks close to $f \simeq 20\,\text{GHz}$ are then visible. We attribute them to the oscillations of precessional amplitudes of both spins. With increasing amplitude of the current density, the precessional angles of both spins increase and their precessional frequencies slightly decrease. Moreover, with increasing current the frequencies of the minor peaks get closer, until they finally coincide. At this point the PSD becomes widely distributed along the whole range of observed frequencies, which is an evidence of noisy variation of the resistance. An example of spin dynamics in this region is shown in Figs. 48(c) and (d) which have been taken in a time window of 10 ns after the equilibration period for $H_{\text{ext}} = -400\,\text{Oe}$ and $I = -2.8 \times 10^8\,\text{Acm}^{-2}$ [within the broad feature of PSD in

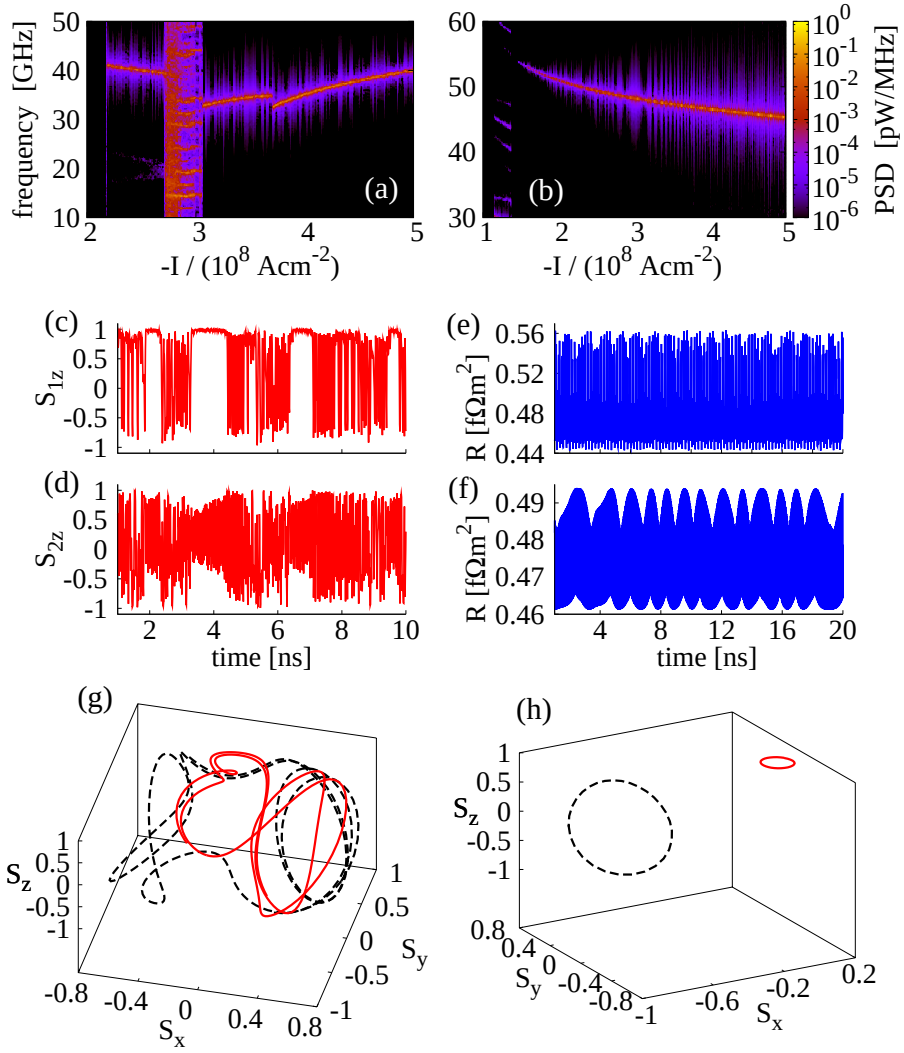

Figure 48: Power spectral density calculated for the spin valve with SyF free layer at $T_{\text{eff}} = 5\,\text{K}$ and $H_{\text{ext}} = -400\,\text{Oe}$ (a) and 200 Oe (b). (c) and (d) show steady time evolution of spins z-components in a time window of 10 ns after the equilibration at $H_{\text{ext}} = -400\,\text{Oe}$ and $I = -2.8 \times 10^8\,\text{Acm}^{-2}$. (e) and (f) show steady time evolution of the time-dependent part of spin valve resistance in a time window of 20 ns after the equilibration at $H_{\text{ext}} = -400\,\text{Oe}$ and $I = -3.6 \times 10^8\,\text{Acm}^{-2}$ (both $\hat{\boldsymbol{S}}_1$ and $\hat{\boldsymbol{S}}_2$ precess out of layer plane) and $I = -3.8 \times 10^8\,\text{Acm}^{-2}$ ($\hat{\boldsymbol{S}}_2$ performs out-of-plane precessions while $\hat{\boldsymbol{S}}_1$ precesses in the layer's plane), respectively. Panels (g) and (h) depict trajectories of $\hat{\boldsymbol{S}}_1$ (red solid line) and $\hat{\boldsymbol{S}}_2$ (black dashed line) corresponding to resistance oscillations (e) and (f), respectively.

Fig. 48(a)]. Firstly, the figures show that $\hat{\boldsymbol{S}}_2$ starts to perform out-of-plane precessions as a result of the competition between STT and RKKY coupling. Secondly, one can note thermally activated random transitions of $\hat{\boldsymbol{S}}_1$ between OPP and IPP modes. These random transitions modify OPP precessions of $\hat{\boldsymbol{S}}_2$ as well. Simultaneous dynamics of both spins causes chaotic variation of spin valve resistance and broadens the PSD.

Further increase in current density leads to stabilization of the OPP mode of $\hat{\boldsymbol{S}}_1$. Hence spin valve resistance becomes more periodic [see Fig. 48(e)] and PSD reveals a narrow peak again. Since both spins perform rather complicated dynamics including IPP but dominated by OPP regime [see Fig. 48(g)], we observe a blue-shift in PSD with current, which is connected with a decrease in the precessional angles. However, at a certain value of I there is a drop in the peak's frequency. At this current density the STT acting on the left interface of layer F_1 starts to dominate the dynamics of $\hat{\boldsymbol{S}}_1$ and enables only small angle IPPs along the $\hat{\boldsymbol{S}}_0$ direction, which modifies the trajectory of $\hat{\boldsymbol{S}}_2$. $\hat{\boldsymbol{S}}_2$ still remains in the OPP regime [see Fig. 48(h)] and hence the blue-shift with current appears. The fact that IPP of $\hat{\boldsymbol{S}}_1$ still influence the dynamics of the whole SyF is also shown in Fig. 48(f), which presents the dynamic part of the spin valve resistance at $I = -3.8 \times 10^8 \mathrm{Acm}^{-2}$ and $H_{\mathrm{ext}} = -400\,\mathrm{Oe}$. As a result of IPPs of $\hat{\boldsymbol{S}}_1$, amplitude of the resistance varies periodically. Comparison of Figs. 48(e) and (f) shows that the simultaneous OPPs of both spins lead to stronger variation of the resistance than in the case when the layers are in the IPP state.

At $H_{\mathrm{ext}} = 200\,\mathrm{Oe}$ one observes only IPP modes of both spins similar to those shown in Fig. 47(e). The in-plane precessional angle increases with current density and hence the peak frequency in PSD decreases and becomes broader. In real systems, however, one might expect the peaks narrower than those obtained in the macrospin simulations, as observed in standard spin valves with a simple free layer [125, 126].

11.3 Current-induced hysteresis

To compare switching of the SyAF and SyF free layers from the $\downarrow\uparrow$ to $\uparrow\downarrow$ configurations with the opposite one ($\uparrow\downarrow$ to $\downarrow\uparrow$), we have simulated dynamics of the corresponding CFLs assuming $H_{\mathrm{ext}} = 0$ and varying current density. The simulations have been performed in the quasistatic regime, i.e., for each value of current density the spin dynamics was first equilibrated for 50 ns and then averaged values of spin components and pillar resistance were calculated from the data taken for the next 30 ns of dynamics. Starting from $I = 0$ and going first towards negative currents we have constructed the current dependence of the averaged resistance and related z-components of both spins, as shown in Fig. 49. For both SyAF [Figs. 49(a –c)] and SyF [Figs. 49(d – f)] free layers, one finds relatively symmetric hysteresis with the current density. In both cases direct switching from $\downarrow\uparrow$ to $\uparrow\downarrow$ state occurs. In contrast, in the case of SyF free layer, the second transition ($\uparrow\downarrow$ to $\downarrow\uparrow$) does not appear directly, but through IPP precessions. The in-plane precessions are connected with a significant drop in the resistance and with a reduction of the s_z-components. The range of IPP regime is particularly large in the case of SyF. From the analysis of spins' trajectories one may conclude that the angle of IPPs increases with increasing current density, and after exceeding a certain threshold angle CFL switches to the $\downarrow\uparrow$ configuration.

An origin of the difference in switching from $\uparrow\downarrow$ to $\downarrow\uparrow$ and from $\downarrow\uparrow$ to $\uparrow\downarrow$ follows from the fact that the magnetostatic interaction of the CFL's layers with the polarizer is different in the $\downarrow\uparrow$ and $\uparrow\downarrow$ states. To prove this we have constructed analogical hysteresis loops for SyAF and SyF free layers disregarding magnetostatic interaction with the F_0 layer; see Figs. 49(g) and (h). For

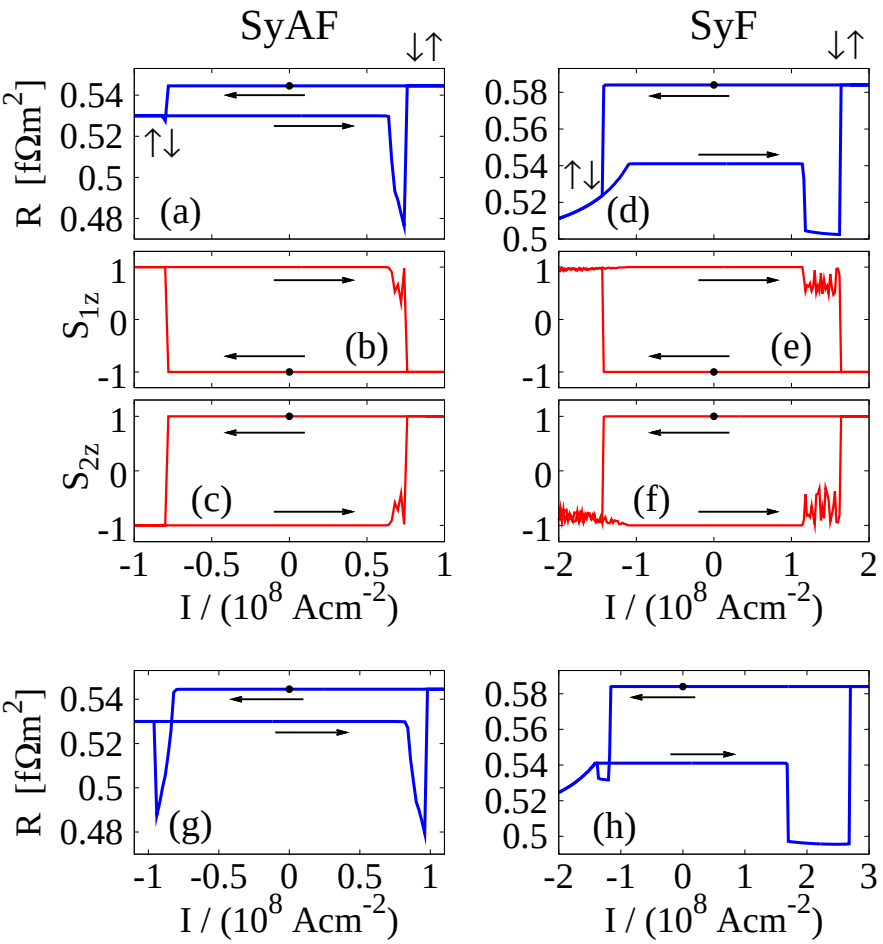

Figure 49: Hysteresis loops of the resistance for the studied pillars with SyAF (a) and SyF (d) free layers. Panel (b) and (c) depict spin dynamics of $\hat{\boldsymbol{S}}_1$ and $\hat{\boldsymbol{S}}_2$ in SyAF, respectively, corresponding to resistance loop (a). Panels (e) and (f) show dynamics of $\hat{\boldsymbol{S}}_1$ and $\hat{\boldsymbol{S}}_2$ in SyF, respectively, corresponding to resistance loop (d). The initial point of each hysteresis loop is marked with a dot. The arrows indicate direction of the current change. Figures (g) and (h) correspond to the upper parts of (a) and (d), in which however the effects due to magnetostatic field of the reference layer to the CFL spins have been omitted.

both SyAF and SyF free layers we observe now large decrease in R for both switchings. This implies that both switchings are realized *via* in-plane precessions, in contrast to the case when F_0 influences the CFL dynamics via the corresponding magnetostatic field. While the hysteresis loop for SyAF remains symmetric, the one for SyF becomes highly asymmetric. The asymmetry of SyF loop is due to a significant asymmetry of STT in $\uparrow\downarrow$ and $\downarrow\uparrow$ states, which was previously shaded by the magnetostatic coupling with the layer F_0.

12 Nonlinear magnetotransport in dual spin valves

In case of spin valves based on layered magnetic structures, spin accumulation and GMR are usually accounted for using the Valet-Fert description (for details see section 3.1), in which the spin accumulation is linear in current, while resistance and magnetoresistance are independent of current magnitude and current orientation. The description involves a number of phenomenological parameters which usually are taken from CPP-GMR experimental data. The Valet-Fert description was successfully applied not only to single spin valves, but also to double (dual) spin valves [48], which have been described in chapter 8. As mentioned there, when the magnetic configuration of the outer (fixed) layers is antiparallel, the spin accumulation in the central layer may be then several times larger than in the corresponding single spin valves [48, 52].

An interesting consequence of the enhanced spin accumulation in the central layer of a dual spin valve is the possibility of nonlinear transport effects. Recent experimental results [49] indicate that the enhanced spin accumulation may cause unusual dependence of magnetoresistance on dc current. It has been shown that when magnetizations of the outer layers are antiparallel, resistance of a DSV for one current orientation is lower when the F_C layer is magnetized along the F_R one and higher when it is aligned along magnetization of the F_L layer, while for the opposite current orientation the situation is reversed. Moreover, the difference in resistance of both collinear configurations markedly depends on the applied current. These observations strongly differ from the predictions of the Valet-Fert model [16], which gives resistance (and magnetoresistance) independent of the current density.

The Valet-Fert description is based on the assumption of constant (independent of spin accumulation and current) basic parameters of the model, like bulk/interface resistance, bulk/interface spin asymmetry, spin diffusion lengths, etc. This is justified when spin accumulation is small and/or change in the density of states on the energy scale comparable to spin accumulation is negligible in the vicinity of the Fermi level. Density of states can be then considered constant, i.e. independent of energy. Since the density of states determines electron scattering rates, one may safely assume that the transport parameters mentioned above are also constant. However, when the density of states at the Fermi level varies remarkably with energy and spin accumulation is sufficiently large, this assumption may not be valid, and the parameters mentioned above may depend on spin accumulation [49]. This, in turn, may lead to nonlinear effects [49, 50].

The spin accumulation, however, is rather small – of the order of 0.1 meV for current density of 10^8 A/cm^2. Thus, to account for the experimental observations one would need rather large gradient of the density of states with respect to energy at the Fermi level. More specifically, to account the experimental observations, the change in density of states should be of the order of 10% on the energy scale of 1 meV. Although this is physically possible, one cannot exclude other contributions to the effect. Spin accumulation can directly change effective scattering potential for electrons at the Fermi level. Moreover, spin accumulation can also indirectly influence transport parameters, for instance *via* current-induced shift of the energy bands due to charging of the layers or due to electron correlations, which are neglected in the description of the spin accumulation. Since the experimental results show that the nonlinear effects appear only in the antiparallel configuration, where spin accumulation in the central layer is large, we assume that the indirect contributions are proportional to spin accumulation (at least in the first order). Since, it is not clear which contribution is dominant, we present a phenomenological approach, which effectively includes all contributions to the observed nonlinear transport. We assume that bulk and interfacial

resistances as well as spin asymmetries vary with spin accumulation and show that such variation leads to effects comparable to experimental observations [49, 50].

12.1 Model

Electron scattering rate and its spin asymmetry become modified when the spin-dependent Fermi levels are shifted due to spin accumulation. We consider the situation when the effect originates from the bulk resistivity and bulk spin asymmetry factor β of the central layer, which are assumed to depend on spin accumulation, as well as from similar dependence of the corresponding interface parameters.

The spin-dependent bulk resistivity of a magnetic layer is usually written in the form given by (3.37)

$$\rho_{\uparrow(\downarrow)} = 2\rho^*(1 \mp \beta)\,, \tag{12.1}$$

where ρ^* is determined by the overall bulk resistivity ρ_F as $\rho^* = \rho_F/(1-\beta^2)$. When the spin accumulation is sufficiently large, one should take into account the corresponding variation of ρ^*. In the lowest approximation linear in the spin accumulation one can write

$$\rho^* = \rho_0^* + q\,\langle g\rangle\,, \tag{12.2}$$

where ρ_0^* is the corresponding *equilibrium* (zero-current limit) value, and $\langle g\rangle$ is the average value of the spin accumulation in the central layer, $\langle g\rangle = (1/d)\int_{\mathrm{F_C}} g(x)dx$. In Eq.(12.2) q is a phenomenological parameter, which depends on the band structure. This parameter effectively includes all effects leading to the modification of transport parameters. Equation (12.2) can be rewritten as

$$\rho^* = \rho_0^*\,(1 + \tilde{q}\,i\,\langle\tilde{g}\rangle)\,, \tag{12.3}$$

where $\tilde{g}$ is a dimensionless variable related to spin accumulation, $\tilde{g} = (e^2 j_0 \rho_0^* l_{\mathrm{sf}})^{-1}\,g$, with j_0 denoting the particle current density and l_{sf} being the spin-flip length. We also introduced a dimensionless current density $i = I/I_0$, with I_0 being a current density scale typical for metallic spin valves, $I_0 = 10^8\mathrm{A/cm}^2$. The parameter $\tilde{q}$ in Eq. (12.3), $\tilde{q} = (eI_0 l_{\mathrm{sf}})q$, is a dimensionless phenomenological parameter which is independent of current.

The bulk spin asymmetry parameter β becomes modified by spin accumulation as well, and this modification can be written as

$$\beta = \beta_0 + \xi\langle g\rangle\,, \tag{12.4}$$

where β_0 is the corresponding equilibrium value and ξ effectively includes all the contributions. In terms of the dimensionless spin accumulation defined above, one can rewrite Eq. (12.4) as

$$\beta = \beta_0 + \tilde{\xi}\,i\,\langle\tilde{g}\rangle\,, \tag{12.5}$$

where $\tilde{\xi} = (eI_0\rho_0^* l_{\mathrm{sf}})\xi$.

Similar equations can be written for the interfacial resistance R^* and interfacial asymmetry parameter γ, which define spin-dependent interface resistance as

$$R_{\uparrow(\downarrow)} = 2R^*(1 \mp \gamma)\,. \tag{12.6}$$

The dependence of R^* and γ on spin accumulation can be written in the form

$$R^* = R_0^* + q'\, g(x_i)\,, \tag{12.7a}$$
$$\gamma = \gamma_0 + \xi'\, g(x_i)\,, \tag{12.7b}$$

where $g(x_i)$ is spin accumulation at a given interface. The constants R_0^* and γ_0 are equilibrium interfacial resistance and asymmetry parameter, respectively. Relations (12.7) lead to the following dependence of the interfacial parameters on the current density:

$$R^* = R_0^* \left(1 + \tilde{q}'\, i\, \tilde{g}(x_i)\right), \tag{12.8a}$$
$$\gamma = \gamma_0 + \xi'\, i\, \tilde{g}(x_i)\,, \tag{12.8b}$$

where $\tilde{q}' = (eI_0\rho_0^* l_{\mathrm{sf}})\, q'$ and $\tilde{\xi}' = (eI_0\rho_0^* l_{\mathrm{sf}})\xi'$.

The parameters q, ξ, q', and ξ' introduced above describe deviation from usual behavior of the resistance (magnetoresistance) described by the Valet-Fert model.

12.2 Numerical results

To find resistance and spin accumulation for arbitrary magnetic configuration, we apply the formalism described in chapter 3 [33, 61]. This formalism, however, is modified by assuming ρ^*, β, R^* and γ to depend on current density (spin accumulation). Therefore, for a particular magnetic configuration and for certain values of i, $\tilde{q}$, $\tilde{\xi}$, $\tilde{q}'$, and $\tilde{\xi}'$, the spin accumulation has to be calculated together with ρ^*, R^*, β, and γ in a self-consistent way. In the first step, we assume equilibrium values; $\rho^* = \rho_0^*$ and $\beta = \beta_0$ ($R^* = R_0^*$ and $\gamma = \gamma_0$), and calculate the corresponding spin accumulation $g_0(x)$ in the central magnetic layer. Then, we calculate the zero approximation of the out-of-equilibrium parameters according to Eqs. (12.3), (12.5), and/or (12.8). With these new values for ρ^* and β (R^* and γ) we calculate the out-of-equilibrium spin accumulation in the central layer and *new* out-of-equilibrium values of ρ^* and β (R^* and γ). The iteration process is continued until a stable point is reached. Finally, for the obtained values of ρ^*, β, R^*, γ, and spin accumulation, we calculate the resistance R of the DSV at a given magnetic configuration.

Magnetizations of the outermost layers are assumed to be fixed and antiparallel (like in experiments [49, 50]). Current is defined as positive for electrons flowing from $\mathrm{F_R}$ towards $\mathrm{F_L}$. The equilibrium parameters have been taken from the relevant literature (see Appendix A). The above described model is applied to two different DSV structures. The first one is a symmetric DSV with $\mathrm{F_L} = \mathrm{F_R} = \mathrm{Co}(20\,\mathrm{nm})$, $\mathrm{F_C} = \mathrm{Py}(8\,\mathrm{nm})$, and with the magnetic layers separated by 10nm thick Cu spacers. The second structure is an asymmetric exchange-biased DSV similar to that used in experiment [49], namely Cu-Co(6)/Cu(4)/Py(2)/Cu(2)/Co(6)/IrMn(10)-Cu.

12.2.1 Bulk effects

Consider pure bulk effects assuming $\tilde{q}' = 0$ and $\tilde{\xi}' = 0$. We start from a symmetric DSV, and the corresponding numerical results are shown in Fig. 50. First, we analyze the case with $\tilde{q} = 0.1$ and $\tilde{\xi} = 0$. Figure 50(a) shows how ρ^* varies when magnetization of the central layer is rotated in the layer plane. This rotation is described by the angle θ between magnetizations of the $\mathrm{F_L}$ and $\mathrm{F_C}$ layers. The higher the current density, the more pronounced is the deviation of ρ^* from its equilibrium value ρ_0^*. The current-induced change in ρ_0^* reaches maxima when magnetic moment

of the central layer is collinear with magnetic moments of the outer layers. These maxima are different for the two opposite orientations of the magnetic moment of F_C layer. For $\theta = \pi/2$, however, one finds $\rho^* = \rho_0^*$. This is because spin accumulation vanishes then due to opposite contributions of both interfaces. Variation of ρ^* in Fig. 50(a) is shown only for positive current, $i > 0$. When current is negative, the change in ρ^* due to spin accumulation changes sign (not shown).

The current-induced angular dependence of ρ^* makes the resistance of the DSV dependent on the current density. As shown in Fig. 50(c), the angular dependence of the resistance becomes asymmetric, i.e. the resistances in the opposite collinear states ($\theta = 0$ and π) are different. Such an asymmetric angular dependence qualitatively differs from that obtained from the Valet-Fert description, where the resistance is symmetric. When magnetization of the central layer switches from one collinear state to the opposite one, one finds a drop (positive or negative) in the resistance, defined as $\Delta R = R(\theta = \pi) - R(\theta = 0)$. If the current direction is reversed, the corresponding drop in resistance also changes sign, as shown in Fig 50(c).

Consider now the situation where β changes with the spin accumulation (current), while ρ^* is constant, $\tilde{\xi} = 0.1$ and $\tilde{q} = 0$. General behavior of β and of the corresponding resistance with the angle θ is similar to that discussed above (see Fig 50(b,d)), although the sign of the resistance drop is now opposite to that obtained in the case discussed above, compare Figs 50(c) and (d).

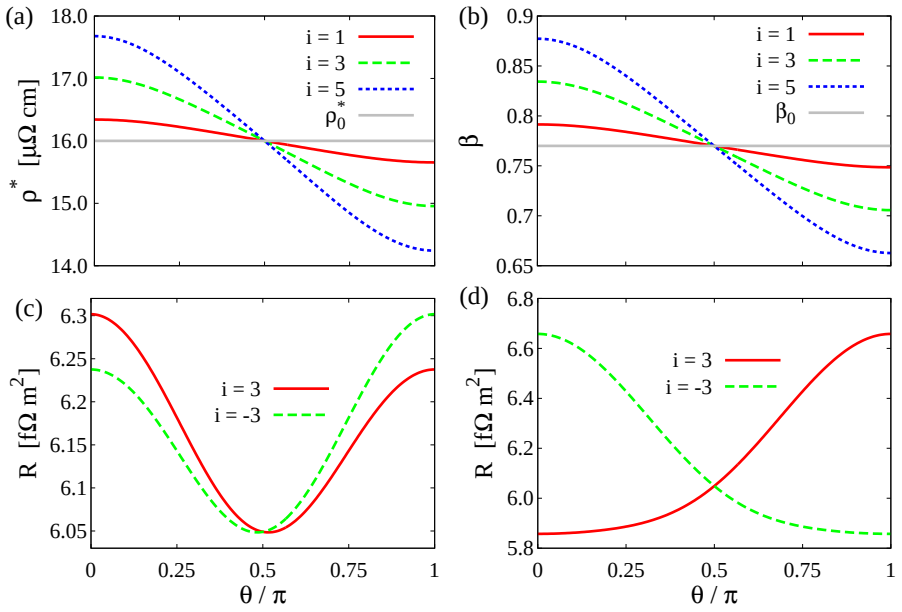

Figure 50: Symmetric dual spin valve Cu-Co(20)/Cu(10)/Py(8)/Cu(10)/Co(20)-Cu: (a) angular dependence of ρ^* for $\tilde{q} = 0.1$ and $\tilde{\xi} = 0$; (b) angular dependence of β for $\tilde{\xi} = 0.1$ and $\tilde{q} = 0$; (c) angular dependence of the resistance (per unit square) for $\tilde{q} = 0.1$ and $\tilde{\xi} = 0$; (d) angular dependence of the resistance for $\tilde{\xi} = 0.1$ and $\tilde{q} = 0$. The relative current density i as indicated.

In real structures, however, both parameters, $\tilde{\xi}$ and $\tilde{q}$, may be different from zero, and the observed behavior results from the interplay of the bulk and interface effects discussed above. To show this, we consider now an asymmetric exchange-biased DSV structure, Cu-Co(6)/Cu(4)/-Py(2)/Cu(2)/Co(6)/IrMn(10)-Cu, similar to that studied experimentally.

Figures 51(a) and (b) show the current-induced angular dependence of ρ^* and β for $\tilde{q} = \tilde{\xi} = 0.1$. In comparison to the symmetric DSV structure, the difference in the deviations of both parameters

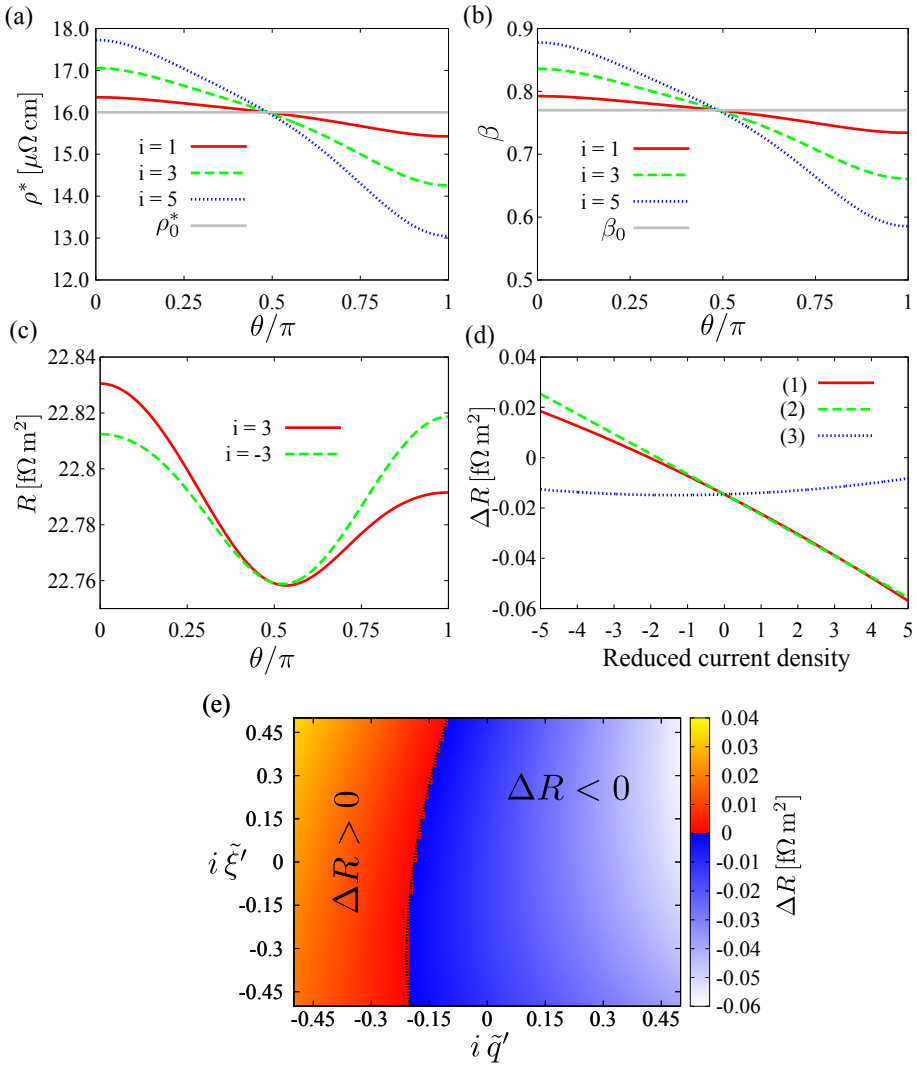

Figure 51: Asymmetric exchange-biased dual spin valve Cu-Co(6)/Cu(4)/Py(2)/Cu(2)/Co(6)/IrMn(10)-Cu: angular dependence of ρ^* (a) and β (b) for $\tilde{q} = 0.1$ and $\tilde{\xi} = 0.1$, and the angular dependence of the corresponding resistance (c); (d) dependence of the drops in resistance (per unit square) as a function of the reduced current density i for $\tilde{q} = 0.1$, $\tilde{\xi} = 0.1$ [line (1)], $\tilde{q} = 0.1$, $\tilde{\xi} = 10^{-3}$ [line (2)], and $\tilde{q} = 10^{-3}$, $\tilde{\xi} = 0.1$ [line (3)]; (e) drop in the resistance as a function of $i\tilde{q}$ and $i\xi$ (with reduced current density i); the line covers the points where $\Delta R = 0$.

from their equilibrium values for $\theta = \pi$ and $\theta = 0$ is now much more pronounced. As before, the nonequilibrium values of the parameters cross the corresponding equilibrium ones for nearly perpendicular configuration, $\theta \approx \pi/2$. The resistance shown in Fig. 51(c) reveals well defined drop between both collinear configurations, and the drop changes sign when the current is reversed.

Figure 51(d) shows the resistance drops as a function of the current density for three different sets of parameters. For $\tilde{q} = \tilde{\xi} = 0.1$ [line (1)], the absolute value of the drop increases rather linearly with increasing magnitude of current, although the growth of ΔR is faster for positive current. In the second case, $\tilde{q} = 0.1$ and $\tilde{\xi} = 10^{-3}$ [line (2)], the dependence remains nearly the same, with only a small deviation from the first case. For $\tilde{q}$, $\tilde{q} = 10^{-3}$, and $\tilde{\xi} = 0.1$ [line (3)], the dependence strongly differs from the first two cases. ΔR only slightly varies with current

and remains rather small. Such a behavior results from the interplay of the bulk and interface contributions. This interplay is presented also in Fig. 51(e), where the resistance drop is shown as a function of $i\tilde{q}$ and $i\tilde{\xi}$. Additionally, the latter figure shows that for any value of $\tilde{q}$ there is a certain value of $\tilde{\xi}$ for which $\Delta R = 0$, as presented by the line.

12.3 Interfacial effects

For both symmetric and asymmetric spin valves we assume that the parameters $\tilde{q}'$ and $\tilde{\xi}'$ are equal for both interfaces of the central layer. Consider first a symmetric DSV. The corresponding results are summarized in Fig. 52. Variation of R^*, when the central magnetization rotates in the layer plane, is shown in Fig. 52(a) for $\tilde{q}' = 0.1$ and $\tilde{\xi}' = 0$. The curves below the equilibrium value R_0^* correspond to R^* on the left interface, while these above R_0^* describe R^* on the right interface. When the central magnetization is close to the collinear orientation ($\theta = 0,\pi$), R^* on the left and right interfaces are significantly different, and this difference becomes partly reduced when θ tends to $\theta = \pi/2$. Generally, the higher current density, the more pronounced is the shift of R^* on both interfaces from their equilibrium values. The corresponding angular dependence of the DSV resistance is shown in Fig. 52(c) for the current densities $i = \pm 3$. This angular dependence results in small resistance drops of opposite signs for opposite currents. The small value of ΔR is due to a relatively large thickness of the central layer. The case when $\tilde{q}' = 0$ and γ depends on spin accumulation leads to similar conclusions, as shown in Figs. 52(b) and (d).

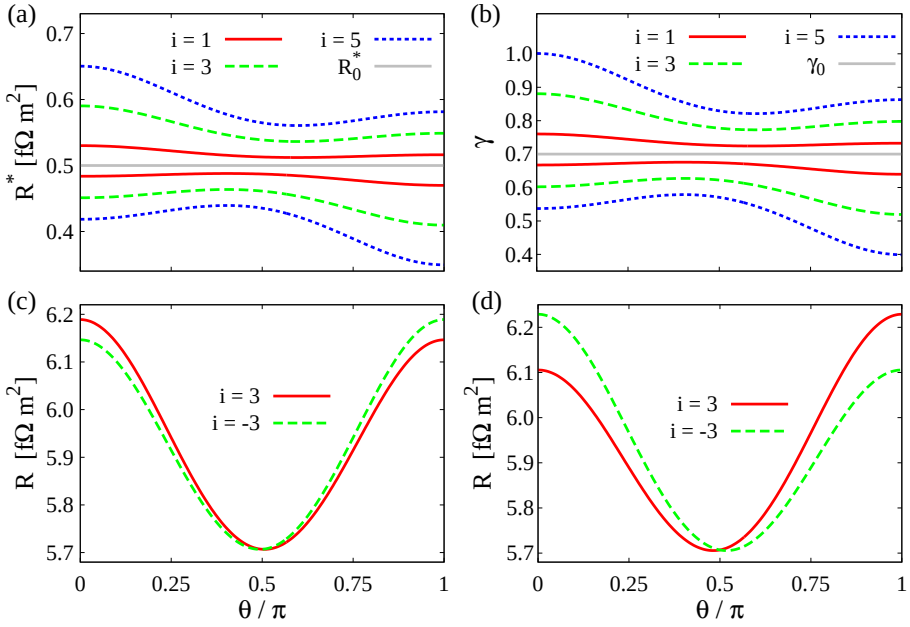

Figure 52: Symmetric dual spin valve Cu-Co(20)/Cu(10)/Py(8)/Cu(10)/Co(20)-Cu: (a) angular dependence of R^* on the left (curves below R_0^*) and right (curves above R_0^*) interfaces of the central layer for $\tilde{q}' = 0.1$ and $\tilde{\xi}' = 0$; (b) angular dependence of γ on the left (curves below γ_0) and right (curves above γ_0) interfaces of the central layer for $\tilde{\xi}' = 0.1$ and $\tilde{q}' = 0$; (c) angular dependence of the resistance (per unit square) for $\tilde{q}' = 0.1$ and $\tilde{\xi}' = 0$; (d) angular dependence of the resistance (per unit square) for $\tilde{\xi}' = 0.1$ and $\tilde{q}' = 0$

For the asymmetric DSVs, we assume that both R^* and γ depend on spin accumulation. As shown in Fig. 53(a) for $\tilde{q}' = \tilde{\xi}' = 0.1$, there is a relatively large drop in resistance. This resistance

drop ΔR increases rather linearly with the current density, as shown in Fig. 53(b). A small deviation from the linear behavior can be observed only for larger values of negative current. The slope of the curves representing the resistance drop as a function of the current density decreases as the thickness of the central layer increases, see Fig. 53(b). In other words, the dependence of resistance on current becomes less pronounced when the central layer is thicker. Such a behavior was not observed in the case of bulk contribution. Additionally, the slope of the curves presenting the resistance drop as a function of current density depends on the parameters $\tilde{q}'$ and $\tilde{\xi}'$, and can change sign for appropriate values of these parameters. This is shown in Figs. 53(c) and (d), where one of the parameters, either $\tilde{\xi}'$ (c) or $\tilde{q}'$ (d) has been reduced to 10^{-3}. Since $\tilde{q}'$ and $\tilde{\xi}'$ are of the same sign, their effects are opposite and the corresponding contributions may partly compensate each other. This is also shown in Fig. 53(e), where the resistance drop ΔR is shown as a function of $i\tilde{q}'$ and $i\tilde{\xi}'$. From this figure also follows that total compensation of the contributions to the resistance drop occurs for the points corresponding to the line in Fig. 53(e).

In addition, comparing the theoretical results with experiment, one can estimate the magnitude of some of the phenomenological parameters. The resistance drop measured experimentally at the current density of $I = 10^7\,\mathrm{Acm}^{-2}$ is about $0.04\,\mathrm{f\Omega m}^2$. To reach effects of similar magnitude within the interfacial model, as shown in Fig. 53, one needs $\tilde{\xi}' \sim 1$, i.e. $\xi \simeq 1.13\,(\mathrm{meV})^{-1}$ (when assuming the effect is due to variation of interfacial asymmetry parameter only). If direct contribution from spin accumulation would dominate, then the corresponding change in the density of states would be of the order of 10% on the energy scale of 1 meV. Note, that this slope may be much smaller in the presence of other contributions.

12.4 Magnetization dynamics

In the description presented above magnetization of the central layer was in the layer plane. However, when the magnetization switches between the two collinear orientations (due to applied magnetic field), it precesses and comes into out-of-plane orientations as well. Such a precessional motion modifies spin accumulation and DSV's resistance. Now we describe variation of the resistance, when magnetization of the central layer is switched by an external magnetic field back and forth. We assume that the magnetic field is applied along the easy axis of the central layer, similarly as in experiment and make use of the single-domain approximation.

Time evolution of the spin moment of central layer is described by the Landau-Lifshitz-Gilbert equation (5.73). Magnetic moments of the outer layers are assumed to be fixed due to much larger coercive fields of these layers. Moreover, the torque due to spin-transfer is not included.

Figure 54 shows quasistatic minor hysteresis loops of the resistance in external magnetic field, calculated for asymmetric exchange-biased DSV at $T = 70\,\mathrm{K}$. These figures are in agreement with the results obtained in the preceding section, and also in good agreement with experimental observations [49]. They also show that the drop in resistance changes sign when the direction of current is reversed. In Fig. 54 only interfacial contribution is taken into account. The minor hysteresis loops appear also in the case when the nonlinear effect is due to bulk parameters (not shown). Some differences however appear, especially in their dependence on the layer thickness. This suggests, that the experimentally observed effects are more likely due to interface contribution, which is quite reasonable as the spin accumulation is maximal just at the interfaces.

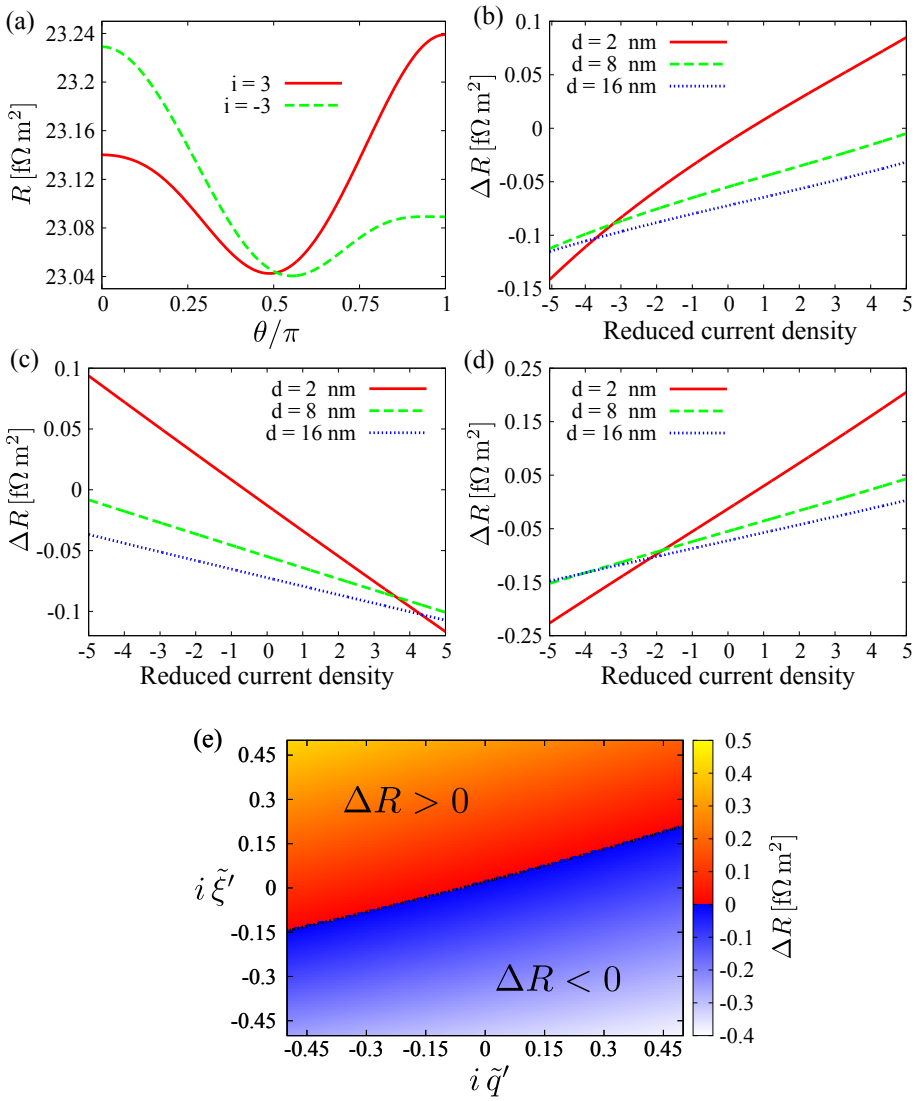

Figure 53: Asymmetric exchange-biased dual spin valve Cu-Co(6)/Cu(4)/Py(d)/Cu(2)/Co(6)/IrMn(10)-Cu: (a) angular dependence of resistance (per unit square) calculated for central layer thickness $d = 2\,\mathrm{nm}$, $\tilde{q}' = 0.1$ and $\tilde{\xi}' = 0.1$; (b) dependence of the resistance drop (per unit square) on the reduced current density i for $\tilde{q}' = 0.1$, $\tilde{\xi}' = 0.1$, and for different values of d; (c) resistance drop as a function of the reduced current density i for $\tilde{q}' = 0.1$, $\tilde{\xi}' = 10^{-3}$, and indicated values of d; (d) resistance drop *vs* current density i for $\tilde{\xi}' = 0.1$, $\tilde{q}' = 10^{-3}$, and for indicated values of d; (e) resistance drop as a function of $i\tilde{q}'$ and $i\tilde{\xi}'$, calculated for $d = 2$. The line covers the points where $\Delta R = 0$.

13 Spin transfer torque in a thick Neel domain wall

In all the previous chapters we focused on the current-induced dynamics in spin valve structures, where spin momentum is transfered between two magnetic films separated by a nonmagnetic layer. However, it has been shown that spin accumulation might appear also in case of one magnetic layer with nonhomogeneous magnetization. The most common case studied in experiments is a magnetic nanowire with domain structure, where magnetic domains are separated by domain walls

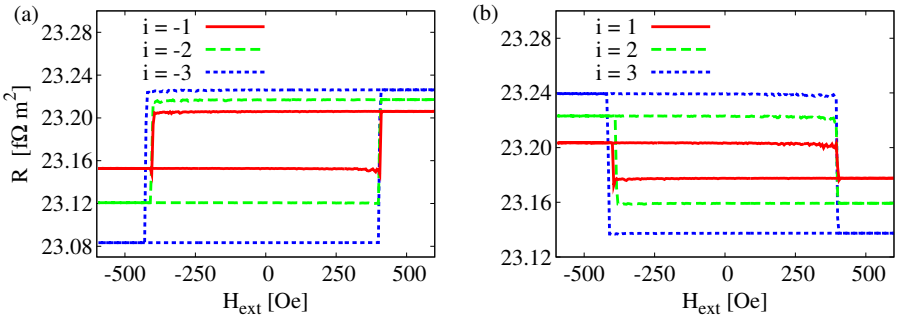

Figure 54: Asymmetric exchange-biased dual spin valve Cu-Co(6)/Cu(4)/Py(2)/Cu(2)/Co(6)/IrMn(10)-Cu: Minor hysteresis loops of resistance in external magnetic field calculated for $\tilde{q}' = 0.1$, $\tilde{\xi}' = 0.1$, and for different current densities i. Only interface contribution is considered here.

(DWs). It has been shown, that appearance of a domain wall leads to increasing in the resistance of a nanowire. On the other hand, when current passes along such a nanowire, the conduction electrons transfer the spin momentum between the localized magnetic moments and induce domain wall dynamics. This phenomenon has been observed experimentally [127, 128] and theoretically studied [129, 130, 131]. The broad interest in the current-induced dynamics of domain walls in magnetic nanostructures is stimulated by perspective applications in novel spintronic devices and modern magnetic memory elements [132, 133].

There are several types of domain walls observed experimentally. In nanowires with in-plane anisotropy along the main axis of the wire the most common domain wall structure is so called Neel domain wall, when magnetization changes in the wire's plane. When the wire has an easy plane, which is perpendicular to the axis of the wire, a Bloch domain wall appears.

Similarly, as in spin valves, the domain wall motion is usually described by a classical Landau-Lifshitz-Gilbert equation, which additionally includes the current-induced spin torque term, which appears due to the exchange interaction between conduction electrons and localized net spin moments, given by Hamiltonian

$$H_{\mathrm{int}} = -J\,\mathbf{S}\cdot\mathbf{n}(\boldsymbol{r})\,, \tag{13.1}$$

where $\mathbf{S}$ is the spin of conduction electron, $\mathbf{n}(\boldsymbol{r}) = \mathbf{M}(\boldsymbol{r})/M_{\mathrm{s}}$ describes the magnetization texture as a function of position, $\boldsymbol{r}$, and J is the exchange constant between conduction and localized electrons. From the equation of motion for the localized magnetization one finds

$$\frac{d\mathbf{n}}{dt} = -\frac{|\gamma|J}{M_{\mathrm{s}}}\,\mathbf{n}\times\mathbf{S}. \tag{13.2}$$

Thus, the torque exerted on the localized magnetization is

$$\mathbf{T} = \frac{J}{M_0}\,\mathbf{M}\times\mathbf{S}\,. \tag{13.3}$$

Furthermore, if one considers that $\mathbf{S}$ is given in the local frame of $\mathbf{M}$, i.e. quantization axis is aligned with the local magnetization, one can write the spin torque as a sum of the in-plane and out-of-plane component, $\mathbf{T} = \mathbf{T}_{\parallel} + \mathbf{T}_{\perp}$, where

$$\mathbf{T}_{\parallel} = -JS_y\,, \tag{13.4a}$$

$$\mathbf{T}_{\perp} = JS_x\,. \tag{13.4b}$$

On the other hand, one can generally define both spin torque components as [129, 94, 130]

$$\mathbf{T}_{\parallel} = \tilde{a}\,\boldsymbol{n} \times [\boldsymbol{n} \times (\boldsymbol{j} \cdot \nabla)\,\boldsymbol{n}]\,, \tag{13.5a}$$

$$\mathbf{T}_{\perp} = \tilde{b}\,\boldsymbol{n} \times (\boldsymbol{j} \cdot \nabla)\,\boldsymbol{n}\,, \tag{13.5b}$$

where $\boldsymbol{j}$ is the unit vector along the current direction, and parameters $\tilde{a}$ and $\tilde{b}$ stand for the amplitudes of the torque components. In case of simplified 1-dimensional model, where magnetization changes only in one direction (let say z) and electric current flows in the same direction, expressions (13.5) reduces to

$$\mathbf{T}_{\parallel} = \tilde{a}\,\boldsymbol{n} \times \left(\boldsymbol{n} \times \frac{\partial \boldsymbol{n}}{\partial z}\right) = -\tilde{a}\,\frac{\partial \boldsymbol{n}}{\partial z}\,, \tag{13.6a}$$

$$\mathbf{T}_{\perp} = \tilde{b}\,\boldsymbol{n} \times \frac{\partial \boldsymbol{n}}{\partial z}\,. \tag{13.6b}$$

First component , $\mathbf{T}_{\parallel}$, is aligned with direction $\boldsymbol{n}$ variation. Spin transfer torque in this direction arises due to adiabatic change of conduction electrons' spin. Thus this component is called also as *adiabatic spin torque*. Contrary, $\mathbf{T}_{\perp}$, has been identified as *nonadiabatic spin torque* [130] since it appears due to nonadiabatic spin relaxation of the conduction electrons in the exchange field of localized magnetic moments. Both parameters define so called *nonadiabaticity*, $\beta = \tilde{b}/\tilde{a}$, which is usually small ($\beta \ll 1$) since $\tilde{a} \gg \tilde{b}$. According to the analysis by Zhang and Li [130], the nonadiabaticity is given by $\beta = \tau_{\mathrm{ex}}/\tau_{\mathrm{sf}}$, where τ_{sf} is the spin-flip relaxation time and τ_{ex} is the precessional period of a spin in the exchange field. Usually this ratio is about $\beta \sim 10^{-2}$. Recently, it has been shown that in thin domain walls (i.e. when domain wall width, L, is comparable with electrons' wavelength, λ) nonadiabaticity, β, is not just a function of material parameters, but might oscillate with the domain wall width [134]. However, as the domain wall width increases, oscillation amplitude of β decreases and β becomes constant for $L \ll \lambda$. In addition, parameter $\tilde{a}$ is proportional to initial DW velocity (immediately after the current is switched on). On the other side, parameter $\tilde{b}$ dominates the terminal velocity of DW (for $t \to \infty$), which is $v_{\mathrm{T}} \propto \tilde{b}/\alpha$, where α is the Gilbert damping parameter. If $\tilde{b} = 0$ the domain wall for $t \to \infty$ is pushed just by the external magnetic field.

Both $\tilde{a}$ and $\tilde{b}$ depend on the material and can be extracted from experiments. The goal of this chapter, is to provide an effective theory for spin transfer torque in a thick Neel domain wall, i.e. to find formulas for $\tilde{a}$ and $\tilde{b}$ for a given magnetization texture. The main assumption we made is, that in a thick domain wall magnetization varies slowly. Thus we can make use the linear response theory to calculate the current-induced spin density and the spin torque exerted on the domain wall. We identify both the adiabatic (in-plane) and nonadiabatic (out-of-plane) spin torque components, and upon numerical calculations for realistic material parameters we have found that the nonadiabatic component is significantly smaller than the adiabatic one.

13.1 Model

We consider a ferromagnetic metal with nonuniform magnetization corresponding to a single domain wall described by the magnetization profile $\mathbf{M}(\mathbf{r}) = M_{\mathrm{s}}\mathbf{n}(\mathbf{r})$, where $\mathbf{n}(\mathbf{r})$ is a unit vector field corresponding to $\mathbf{M}(\mathbf{r})$.

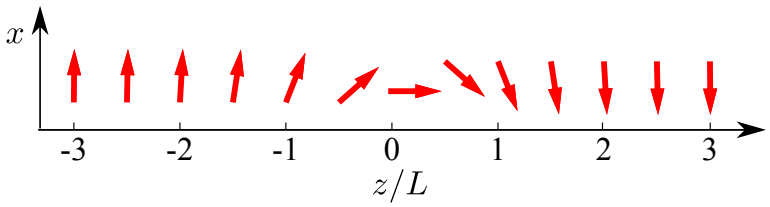

Figure 55: Schematic picture of the magnetization profile in a Neel domain wall.

The single-particle Hamiltonian describing conduction electrons which are locally exchange-coupled to the magnetization $\mathbf{M}(\mathbf{r})$ can be written in the form [135]

$$H_0 = -\frac{\hbar^2}{2m}\,\psi_\alpha^\dagger\,\frac{\partial^2}{\partial \mathbf{r}^2}\,\psi_\alpha - J\,\psi_\alpha^\dagger\,\boldsymbol{\sigma}_{\alpha\kappa}\cdot\mathbf{n}(\mathbf{r})\,\psi_\kappa\,, \tag{13.7}$$

where J is the exchange parameter, ψ_α and $\psi_\alpha^\dagger$ are the spinor field operators of electrons, and $\boldsymbol{\sigma} = (\sigma_x, \sigma_y, \sigma_z)$ represents the Pauli matrices with $\alpha, \kappa = 1, 2$ (for details see Appendix **??**).

Here, we restrict the calculations to a translationally invariant domain wall in the x-y plane, so $\mathbf{n}(\mathbf{r}) \to \mathbf{n}(z)$. Second, we consider a Neel domain wall, where $\mathbf{n}(z)$ changes in the plane normal to the wall as

$$\mathbf{n}(z) = (\,\sin\varphi(z),\ 0,\ \cos\varphi(z)\,)\ , \tag{13.8}$$

where the phase $\varphi(z)$ describes shape of the domain wall. For instance, if we assume the domain wall in the form of a kink, then

$$\varphi(z) = -\frac{\pi}{2}\,\tanh\,(z/L)\,. \tag{13.9}$$

where L is the domain wall width. The schematic magnetization profile associated with the studied domain wall is presented in Fig. 55.

It is useful to rewrite the Hamiltonian (13.7) in a local frame of magnetization, i.e. where the local quantization axis is aligned with $\mathbf{n}(\boldsymbol{r})$ vector. Hence, we make use of a unitary transformation, $\psi \to T(\mathbf{r})\,\psi$ with $T^\dagger(\mathbf{r})\,T(\mathbf{r}) = 1$, which removes the inhomogeneity of $\mathbf{n}(\boldsymbol{r})$ [136]. Transformation $T(\mathbf{r})$ transforms the second term in Eq. (13.7) as

$$T^\dagger(\mathbf{r})\,\boldsymbol{\sigma}\cdot\mathbf{n}(\mathbf{r})\,T(\mathbf{r}) = \sigma_z\,. \tag{13.10}$$

The explicit form of the transformation corresponding to the wall described by Eq.(13.8) is

$$T(z) = \frac{1}{\sqrt{2}}\left(\sqrt{1+\cos\varphi(z)} - i\sigma_y\,\frac{\sin\varphi(z)}{\sqrt{1+\cos\varphi(z)}}\right)\,. \tag{13.11}$$

The transformed Hamiltonian can be then presented in the following form [135]

$$H_0 = -\frac{\hbar^2}{2m}\,\frac{\partial^2}{\partial\mathbf{r}^2} - J\sigma_z + \hbar^2\left[\frac{m\,\kappa^2(z)}{2} + i\sigma_y\,\frac{\kappa'(z)}{2} + i\sigma_y\,\kappa(z)\frac{\partial}{\partial z}\right]\,, \tag{13.12}$$

where

$$\kappa(z) = \frac{\varphi'(z)}{2m}, \tag{13.13}$$

and $\kappa'(z) \equiv \partial\kappa(z)/\partial z$, while $\varphi'(z) \equiv \partial\varphi(z)/\partial z$. For a slowly varying smooth function $\varphi(z)$ (thick domain wall) centered at $z = 0$, the perturbation due to the domain wall is weak and localized close to the center of the wall [137], $|z| \ll L$. When the domain wall is in the form of given by equation (13.9), the parameter $\kappa(z)$ takes the form

$$\kappa(z) = -\frac{\pi}{4mL\,\cosh^2(z/L)}. \tag{13.14}$$

In the quasiclassical approximation, which is valid for thick domain walls ($L \gg \lambda$), the electron wave function has the form of plane wave $\psi_{\mathbf{k}\alpha}(\boldsymbol{r}) = V^{-1/2}\, e^{i\mathbf{k}\cdot\boldsymbol{r}}\xi_\alpha$, where ξ_α is the spinor wave function and $V \propto L^3$. Thus one can write the Hamiltonian (13.12) in the basis of semiclassical functions as [135]

$$H_0 = \frac{\hbar^2 k^2}{2m} - J\sigma_z + \hbar^2\left[\frac{m\,\kappa^2(z)}{2} + i\sigma_y\,\frac{\kappa'(z)}{2} - \sigma_y\,\kappa(z)k_z\right]. \tag{13.15}$$

The main contribution from the domain wall in the latter Hamiltonian comes from the last term, which is proportional to $\kappa(z)k_{\mathrm{F}}$ while the term proportional to κ^2 is smaller. The term including κ' is of the order of κ/L and therefore can be neglected [135].

The domain wall leads to scattering of electrons, which in turn gives rise to excess spin density within the wall. The equilibrium (in the absence of external electric field) spin density of conduction electrons in the local frame can be calculated as

$$\mathbf{S} = -i\,\mathrm{Tr}\int \frac{d\varepsilon}{2\pi}\frac{d^3k}{(2\pi)^3}\,\boldsymbol{\sigma}\,G_\varepsilon(\mathbf{k})\,, \tag{13.16}$$

where $G_\varepsilon(\mathbf{k})$ is the Green function

$$G_\varepsilon(\mathbf{k}) = \frac{\varepsilon - \varepsilon_k - J\sigma_z - \hbar^2 k_z\kappa\sigma_y + \mu}{(\varepsilon - \varepsilon_{k\uparrow} + \mu + i\delta_\uparrow\mathrm{sgn}\varepsilon)(\varepsilon - \varepsilon_{k\downarrow} + \mu + i\delta_\downarrow\mathrm{sgn}\varepsilon)}, \tag{13.17}$$

where $\varepsilon_k = \hbar^2k^2/2m$, $\varepsilon_{k\uparrow(\downarrow)} = \varepsilon_k \mp J$, μ denotes the chemical potential, and $\delta_{\uparrow(\downarrow)} = \hbar/2\tau_{\uparrow(\downarrow)}$, with $\tau_\uparrow$ and $\tau_\downarrow$ denoting the relaxation times for the majority and minority conduction electrons, respectively.

The equilibrium spin density within the domain wall was calculated and thoroughly analyzed [135]. However, here, we are interested in the current-induced part of the spin density, which is responsible for the current-induced spin transfer torque exerted on the domain wall.

13.2 Spin accumulation in the linear response regime

We assume now that the system is in an external field described by the time dependent vector potential $\mathbf{A}(t) = \mathbf{A}_\omega \exp(-i\omega t)$. The electric field is then

$$\mathbf{E}(t) = -\frac{1}{c}\frac{\partial\mathbf{A}(t)}{\partial t} = i\frac{\omega}{c}\,\mathbf{A}_\omega \exp(-i\omega t)\,, \tag{13.18}$$

or equivalently $\mathbf{E}_\omega = (i\omega/c)\mathbf{A}_\omega$. Hamiltonian of the system in the vector field $\mathbf{A}(t)$ can be obtained by replacing $-i\hbar(\partial/\partial\mathbf{r})$ in Eq. (13.12) by $-i\hbar(\partial/\partial\mathbf{r}) - (e/c)\mathbf{A}(t)$. The total Hamiltonian takes then the form

$$H = H_0 + H_A\,, \tag{13.19}$$

where H_A is the perturbation due to the external field. The linear in $\mathbf{A}(t)$ term contributing to Eq. (13.19) takes then the following form:

$$H_A(\mathbf{k},\omega) = -\frac{\hbar e \mathbf{k}\cdot\mathbf{A}_\omega}{mc} + \frac{\hbar e A^z_\omega}{c}\kappa\sigma_y\,. \tag{13.20}$$

Now, we calculate the electron spin density induced by the external field $\mathbf{A}(t)$ in the linear approximation with respect to $\mathbf{A}(t)$. Furthermore, since our considerations are based on the adiabatic approximation (valid for small values of $\kappa(z)$), we will consider only the terms linear in the parameter $\kappa(z)$, too. The field-induced spin density $\mathbf{S}$ can be calculated from the formula

$$\mathbf{S} = \mathrm{Re}\left\{(-i)\,\mathrm{Tr}\int\frac{d\varepsilon}{2\pi}\frac{d^3\mathbf{k}}{(2\pi)^3}\,\boldsymbol{\sigma}\,G_{A\varepsilon}(\mathbf{k})\right\}, \tag{13.21}$$

where the Green's function $G_{A\varepsilon}(\mathbf{k})$ should be taken in the linear approximation with respect to the perturbation given by Eq. (13.20),

$$G_{A\varepsilon}(\mathbf{k}) \to G_{\varepsilon+\hbar\omega}(\mathbf{k})\,H_A(\mathbf{k},\omega)\,G_\varepsilon(\mathbf{k})\,, \tag{13.22}$$

where G_ε is given by (13.17).

Since there are two different terms in H_A, see Eq. (13.20), we will calculate separately the corresponding contributions to the induced spin density. Moreover, we consider the electric field along the z-axis, i.e. $\mathbf{E}_\omega = (0,0,E_\omega)$.

13.2.1 First contributing term

The contribution of the first term in Eq. (13.20),

$$H^{(1)}_{\mathrm{A}} = i\,\frac{\hbar e E}{m\omega}\,k_z\,, \tag{13.23}$$

to $\mathbf{S}$ can be then written as

$$\mathbf{S}^{(1)} = \frac{\hbar e E_\omega}{m\omega}\,\mathrm{Re}\,\mathrm{Tr}\int\frac{d\varepsilon}{2\pi}\frac{d^3\mathbf{k}}{(2\pi)^3}\,k_z\,\boldsymbol{\sigma}\,G_{\varepsilon+\hbar\omega}(\mathbf{k})\,G_\varepsilon(\mathbf{k}). \tag{13.24}$$

Taking into account Eqs. (13.17) and (13.24), and calculating the trace one finds the two components of the field-induced spin density in the form

$$S^{(1)}_x = 0\,, \tag{13.25a}$$

$$S^{(1)}_y = -\frac{2e\hbar^3 E_\omega\kappa}{m\omega}\,\mathrm{Re}\int\frac{d\varepsilon}{2\pi}\frac{d^3\mathbf{k}}{(2\pi)^3}\,k_z^2\,\frac{2(\varepsilon-\varepsilon_k+\mu)+\hbar\omega}{F(\varepsilon)F(\varepsilon+\hbar\omega)}\,, \tag{13.25b}$$

where $F(\varepsilon)$ is defined as

$$F(\varepsilon) = (\varepsilon-\varepsilon_{k\uparrow}+\mu+i\delta_\uparrow\mathrm{sgn}\,\varepsilon)(\varepsilon-\varepsilon_{k\downarrow}+\mu+i\delta_\downarrow\mathrm{sgn}\,\varepsilon)\,. \tag{13.26}$$

Calculating the integrals in Eq. (13.25) one obtains

$$S^{(1)}_y = \frac{e\hbar E_\omega\kappa}{6\pi^2 J}\left(\tau_\uparrow k^3_{F\uparrow} - \tau_\downarrow k^3_{F\downarrow}\right) + \frac{e\hbar^2 E_\omega\kappa}{24J^2\pi^2\omega}\left(\frac{1}{\tau_\uparrow}-\frac{1}{\tau_\downarrow}\right)\left(k^3_{F\uparrow}-k^3_{F\downarrow}\right)\,. \tag{13.27}$$

where $k_{F\uparrow}$ and $k_{F\downarrow}$ are the Fermi wave vectors corresponding to the spin majority and spin minority electron subbands, respectively. We note that $k_{F\uparrow}$ and $k_{F\downarrow}$ are related via the formula $2J = (\hbar^2/2m)(k^2_{F\uparrow}-k^2_{F\downarrow})$.

13.2.2 Second contributing term

Now, we calculate the contribution due to the second term in Eq. (13.20), which reads

$$H_{\mathrm{A}}^{(2)} = -i\,\frac{\hbar e E_\omega}{\omega}\,\kappa\sigma_y\,. \tag{13.28}$$

Its contribution to the spin density can be written as

$$\mathbf{S}^{(2)} = -\frac{\hbar e E_\omega \kappa}{\omega}\,\mathrm{Re}\,\mathrm{Tr}\int\frac{d\varepsilon}{2\pi}\frac{d^3\mathbf{k}}{(2\pi)^3}\,\boldsymbol{\sigma}\,G_{\varepsilon+\hbar\omega}(\mathbf{k})\,\sigma_y G_\varepsilon(\mathbf{k}). \tag{13.29}$$

Since we intend to find this contribution in the linear approximation with respect to κ, and the above formula includes already a prefactor κ, we can take the Green functions in the limit of $\kappa = 0$. As a result one obtains

$$\begin{aligned} S_x^{(2)} &= -\frac{e\hbar E_\omega\kappa}{\omega}\,\mathrm{Re}\int\frac{d\varepsilon}{2\pi}\frac{d^3\mathbf{k}}{(2\pi)^3} \\ &\quad\times i\left[G^{0\downarrow}_{\varepsilon+\hbar\omega}(\mathbf{k})\,G^{0\uparrow}_{\varepsilon}(\mathbf{k}) - G^{0\uparrow}_{\varepsilon+\hbar\omega}(\mathbf{k})\,G^{0\downarrow}_{\varepsilon}(\mathbf{k})\right], \end{aligned} \tag{13.30a}$$

$$\begin{aligned} S_y^{(2)} &= -\frac{e\hbar E_\omega\kappa}{\omega}\,\mathrm{Re}\int\frac{d\varepsilon}{2\pi}\frac{d^3\mathbf{k}}{(2\pi)^3} \\ &\quad\times\left[G^{0\downarrow}_{\varepsilon+\hbar\omega}(\mathbf{k})\,G^{0\uparrow}_{\varepsilon}(\mathbf{k}) + G^{0\uparrow}_{\varepsilon+\hbar\omega}(\mathbf{k})\,G^{0\downarrow}_{\varepsilon}(\mathbf{k})\right], \end{aligned} \tag{13.30b}$$

where

$$G_\varepsilon^{0\uparrow(\downarrow)} = \frac{1}{\varepsilon - \varepsilon_{k\uparrow} + \mu + i\delta_{\uparrow(\downarrow)}\mathrm{sgn}\,\varepsilon} \tag{13.31}$$

are the elements of the Green function in the zeroth-order with respect to κ (more specifically, the Green functions for spin-up(down) electrons). Calculating the integrals one finds

$$S_x^{(2)} = -\frac{e\hbar^2 E_\omega\kappa}{12J^2\pi^2}\left(k_{F\uparrow}^3 - k_{F\downarrow}^3\right), \tag{13.32a}$$

$$S_y^{(2)} = -\frac{e\hbar E_\omega m\kappa}{8\pi^2 J^2}\,\frac{\tau_\uparrow k_{\mathrm{F}\uparrow} + \tau_\downarrow k_{\mathrm{F}\downarrow}}{\tau_\uparrow\tau_\downarrow} - \frac{e\hbar^2 E_\omega\kappa}{24\pi^2J^2\omega}\left(\frac{1}{\tau_\uparrow} - \frac{1}{\tau_\downarrow}\right)\left(k_{F\uparrow}^3 - k_{F\downarrow}^3\right). \tag{13.32b}$$

13.2.3 Total spin density

The total spin density components are $S_x = S_x^{(1)} + S_x^{(2)}$ and $S_y = S_y^{(1)} + S_y^{(2)}$. Note, that the singular terms in $S_y^{(1)}$ and $S_y^{(2)}$, proportional to ω^{-1}, cancel each other, so we can take the static limit $\omega \to 0$. Thus, the field-induced spin density is given finally by the formulas,

$$S_x = -\frac{e\hbar^2 E\kappa}{12J^2\pi^2}\left(k_{F\uparrow}^3 - k_{F\downarrow}^3\right), \tag{13.33a}$$

$$S_y = \frac{e\hbar E\kappa}{6\pi^2 J}\left(\tau_\uparrow k_{F\uparrow}^3 - \tau_\downarrow k_{F\downarrow}^3\right) - \frac{e\hbar E m\kappa}{8\pi^2J^2}\,\frac{\tau_\uparrow k_{F\uparrow} + \tau_\downarrow k_{F\downarrow}}{\tau_\uparrow\tau_\downarrow}, \tag{13.33b}$$

where E is the static electric field that drives the current. The above expressions for spin density will be now used to calculate spin torque exerted on the domain wall.

13.3 Spin torque

Let us now calculate the spin transfer torque acting on the local magnetization. To estimate parameters $\tilde{a}$ and $\tilde{b}$, defined by (13.6), we compare the expression for the torque components given by (13.6) and (13.4). Taking into account the fact that the spin components are given in the transformed coordinate frame and also that $\mathbf{S}$ is proportional to $\partial\varphi/\partial z = 2m\kappa$, one can find

$$\tilde{a} = e\hbar\, E \left[\frac{\tau_\uparrow k_{\mathrm{F}\uparrow} + \tau_\downarrow k_{\mathrm{F}\downarrow}}{16\pi^2 J \tau_\uparrow \tau_\downarrow} - \frac{\tau_\uparrow k_{F\uparrow}^3 - \tau_\downarrow k_{F\downarrow}^3}{12\pi^2 m} \right], \tag{13.34a}$$

$$\tilde{b} = -\frac{e\hbar^2}{24\pi^2 J m}\, E \left(k_{F\uparrow}^3 - k_{F\downarrow}^3 \right). \tag{13.34b}$$

The spin torque components are usually related to current density and not to electric field. Using the Drude formula for electric conductivity of two independent spin channels one finds the relation

$$E = \frac{6\pi^2 m}{e^2} \frac{1}{\tau_\uparrow k_{F\uparrow}^3 + \tau_\downarrow k_{F\downarrow}^3} I, \tag{13.35}$$

where I stands for current density. From this $\tilde{a}$ and $\tilde{b}$ can be rewritten in the form

$$\tilde{a} = \frac{\hbar}{2e}\, I \left[\frac{3m}{4J\tau_\uparrow\tau_\downarrow} \frac{\tau_\uparrow k_{\mathrm{F}\uparrow} + \tau_\downarrow k_{\mathrm{F}\downarrow}}{\tau_\uparrow k_{F\uparrow}^3 + \tau_\downarrow k_{F\downarrow}^3} - \frac{\tau_\uparrow k_{F\uparrow}^3 - \tau_\downarrow k_{F\downarrow}^3}{\tau_\uparrow k_{F\uparrow}^3 + \tau_\downarrow k_{F\downarrow}^3} \right], \tag{13.36a}$$

$$\tilde{b} = -\frac{\hbar}{2e}\, I \left[\frac{\hbar}{2J} \frac{k_{F\uparrow}^3 - k_{F\downarrow}^3}{\tau_\uparrow k_{F\uparrow}^3 + \tau_\downarrow k_{F\downarrow}^3} \right]. \tag{13.36b}$$

The spin torque components can be thus written in the form

$$\mathbf{T}_\parallel = a\, I\, \mathbf{n} \times (\mathbf{n} \times \partial\mathbf{n}/\partial z), \tag{13.37a}$$

$$\mathbf{T}_\perp = b\, I\, \mathbf{n} \times \partial\mathbf{n}/\partial z, \tag{13.37b}$$

where a and b are given as

$$a = \frac{\hbar}{2e} \left[\frac{1}{\eta} \left(\frac{\tau_{\mathrm{ex}}}{\tau_\uparrow} \right)^2 \frac{3}{4^3\pi^2} (1-x^2)(1+\eta x) - 1 + \eta x^3 \right] / (1+\eta x^3), \tag{13.38a}$$

$$b = -\frac{\hbar}{2e} \left[\frac{1}{4\pi} \left(\frac{\tau_{\mathrm{ex}}}{\tau_\uparrow} \right) \frac{1-x^3}{1+\eta x^3} \right], \tag{13.38b}$$

with $\tau_{\mathrm{ex}} = 2\pi\hbar/J$, $\eta = \tau_\downarrow/\tau_\uparrow$. The parameter x is defined as

$$x = \frac{k_{\mathrm{F}\downarrow}}{k_{\mathrm{F}\uparrow}} = \left(\frac{1 - J/\mu}{1 + J/\mu} \right)^{1/2}. \tag{13.39}$$

When deriving the above equations we have also taken into account the fact that $2J = (\hbar^2/2m)({k_{\mathrm{F}\uparrow}}^2 - {k_{\mathrm{F}\downarrow}}^2)$ (see also the previous section). The latter expressions for a and b might be rewritten using the current polarization, P, defined as

$$P = \frac{\sigma_\uparrow - \sigma_\downarrow}{\sigma_\uparrow + \sigma_\downarrow} = \frac{\tau_\uparrow k_{F\uparrow}^3 - \tau_\downarrow k_{F\downarrow}^3}{\tau_\uparrow k_{F\uparrow}^3 + \tau_\downarrow k_{F\downarrow}^3}, \tag{13.40}$$

where $\sigma_{\uparrow(\downarrow)} = (n_{\uparrow(\downarrow)} e^2 \tau_{\uparrow(\downarrow)})/m$ is the conductivity of the $\uparrow$ ($\downarrow$) spin channel with $n_{\uparrow(\downarrow)}$ being the corresponding electron density. Then, the dimensionless parameters x and η are related to the current polarization *via* the formula

$$x^3 = \frac{1}{\eta}\,\frac{1-P}{1+P} \tag{13.41}$$

In addition, one can easily find a relation between polarization and J, which reads

$$P = \frac{(1+J/\mu)^{3/2} - \eta\,(1-J/\mu)^{3/2}}{(1+J/\mu)^{3/2} + \eta\,(1-J/\mu)^{3/2}}\,. \tag{13.42}$$

The above expressions for the current-induced spin torque components constitute the final results. These formula simplify in some limiting cases. For instance, when $\tau_\uparrow = \tau_\downarrow = \tau$ one finds

$$a = \frac{\hbar}{2e}\left[\frac{3}{4^3\pi^2}\left(\frac{\tau_{\rm ex}}{\tau}\right)^2 \frac{(x-1)(x+1)^2}{1+x^3} - P\right], \tag{13.43a}$$

$$b = -\frac{\hbar}{2e}\left[\frac{1}{4\pi}\left(\frac{\tau_{\rm ex}}{\tau}\right) P\right], \tag{13.43b}$$

where the polarization reduces to

$$P = \frac{n_\uparrow - n_\downarrow}{n_\uparrow + n_\downarrow} = \frac{k_{F\uparrow}^3 - k_{F\downarrow}^3}{k_{F\uparrow}^3 + k_{F\downarrow}^3}\,. \tag{13.44}$$

13.4 Numerical results and discussion

In the corresponding numerical calculations we assumed $\mu = 10\,\text{eV}$ and $\tau_\uparrow = 10^{-14}\,\text{s}$. First, let us analyze dependences of the spin torque amplitudes on the basic parameters of the model. Figure 56 shows the dependence of the coefficients a and b on the exchange parameter J. As one could expect, a is linear in J in the relevant range of the parameter J where the approach based on the quasiclassical approximation is valid. The parameter b depends on J also almost linearly. However, its magnitude is about 2 orders of magnitude smaller than that of a. Both a and b increase with decreasing η, which reflects increase in a and b with increasing spin polarization of the current.

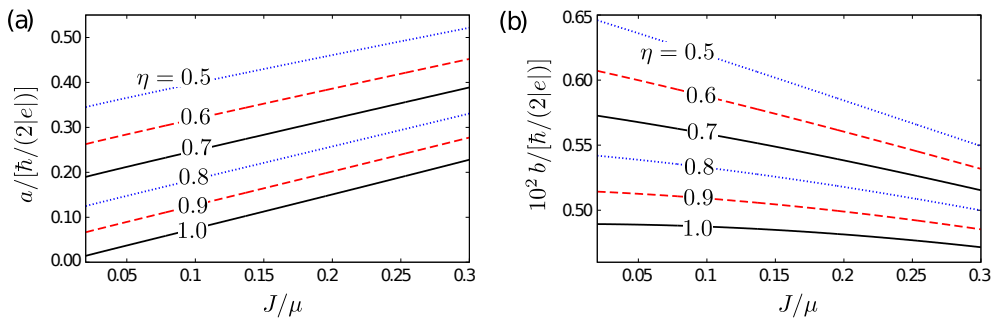

Figure 56: Dependence of the spin torque coefficients a (a) and b (b) on the exchange parameter J [see Eqs. (13.37)] for indicated values of the parameter η defined as $\eta = \tau_\downarrow/\tau_\uparrow$ (see the main text).

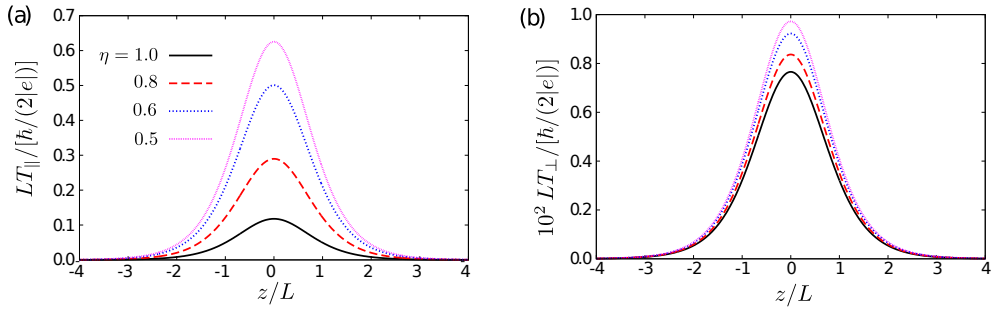

Figure 57: Variation of the amplitudes of the in-plane (a) and out-of-plane (b) spin torque components along the z-axis calculated for $J = 0.1\mu$ and indicated values of η. The center of the domain wall is located at $z = 0$.

Variation of the in-plane and out-of-plane spin torque components along the normal to the domain wall is shown in Fig. 57. Both torque components reach the corresponding maxima in the center of the wall and decay towards the wall boundaries. Similarly to the coefficients a and b, both torque components increase with decreasing η, and the out-of-plane component is about 2 orders of magnitude smaller than the in-plane one.

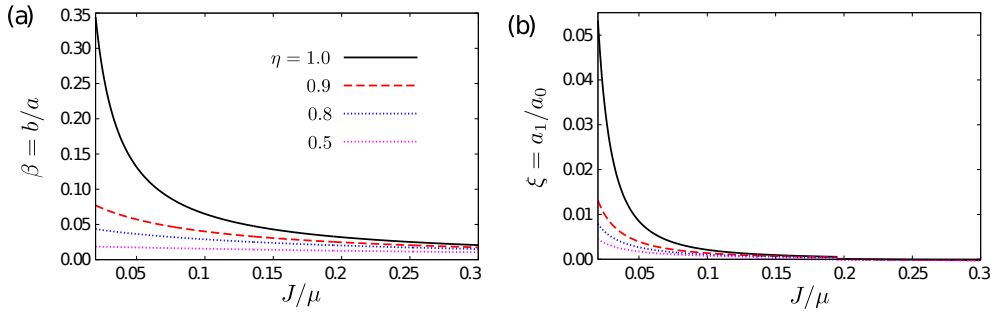

Figure 58: The nonadiabaticity parameter β (a) and the parameter ξ (b) as a function of the exchange parameter J, calculated for indicated values of η.

Following Zhang and Li [129, 130], we can define the nonadiabaticity, $\beta = b/a$, which is plotted in Fig. 58(a). Experimentally, this parameter appears to be small ($\beta \sim 10^{-2}$) [130], which corresponds to our results when η is markedly smaller than 1 and/or the exchange coupling is strong enough. Oppositely, for $\eta = 1$ and small J, one observes an increase of β. This enhancement of β is connected with a weak coupling of conduction electrons to the localized magnetic moments, which leads to misalignment of the conduction and localized spins and gives rise to the nonadiabatic spin torque component, $T_{\perp}$.

Let us consider again equation (13.38a) for the parameter a associated with the in-lane spin torque $T_{\parallel}$ and write it as $a = a_0 + a_1$, where [see equation (13.38a)]

$$a_0 = -\frac{\hbar}{2e}\,\frac{1-\eta x^3}{1+\eta x^3} = -\frac{\hbar}{2e}\,P\,, \tag{13.45}$$

and

$$a_1 = \frac{\hbar}{2e}\left(\frac{\tau_{\mathrm{ex}}}{\tau_{\uparrow}}\right)^2 \left[\frac{1}{\eta}\frac{3}{4^3\pi^2}\,(1-x^2)(1+\eta x)\right]/(1+\eta x^3)\,. \tag{13.46}$$

Models considered for the spin torque usually lead to the term similar to a_0 (proportional to P). Thus, the term a_1 may be treated as a correction to a. Fig. 58(b) shows the ratio $\xi = a_1/a_0$ for different values of η. From this figure follows that ξ decays rapidly with increasing exchange coupling and consequently $a_1 \ll a_0$. Therefore, in many situations one can use a simplified expression for the adiabatic component of the spin torque, which includes only the term linear in P. Thus, one can consider a_1 as a correction to the adiabatic spin torque which appears in the regime of enhanced nonadiabaticity.

The relaxation time $\tau_{\uparrow(\downarrow)}$ in the formulas (13.38) generally includes the spin-conserving momentum relaxation time $\tau^0_{\uparrow(\downarrow)}$ and spin-flip relaxation time $\tau^{sf}_{\uparrow(\downarrow)}$, i.e.

$$\frac{1}{\tau_\uparrow} = \frac{1}{\tau^{sf}_\uparrow} + \frac{1}{\tau^0_\uparrow}\,, \quad \text{and} \quad \frac{1}{\tau_\downarrow} = \frac{1}{\tau^{sf}_\downarrow} + \frac{1}{\tau^0_\downarrow}\,. \tag{13.47}$$

For a domain wall without structural defects, the only source of scattering is the domain wall, which generally gives rise to spin-flip scattering. Scattering on defects, on the other hand, gives rise to both momentum and spin relaxation. We write

$$\frac{1}{\tau_\uparrow} = \frac{1}{\tau^{sf}_\uparrow}\left(1 + \frac{\tau^{sf}_\uparrow}{\tau^0_\uparrow}\right)\,. \tag{13.48}$$

Then, the factor appearing in equations (13.43) reads

$$\frac{\tau_{\rm ex}}{\tau_\uparrow} = \frac{\tau_{\rm ex}}{\tau^{sf}_\uparrow}\left(1 + \frac{\tau^{sf}_\uparrow}{\tau^0_\uparrow}\right)\,. \tag{13.49}$$

This indicates that momentum scattering can enhance the torque. The reason for this effect is the fact, that when electron momentum scattering is strong, electron spends more time within the domain wall and therefore the chance for spin-flip scattering is also increased.

14 Conclusions

In this thesis, a systematic study of current-induced magnetization dynamics in metallic structures has been presented. Based on a diffusive transport approach, spin transfer torque in various spin valve types has been calculated, and its consequences on the spin dynamics have been examined using macrospin numerical simulations. The presented research ranges from single spin valves with standard and nonstandard toque angular dependence, through dual spin valves with in-plane and/or perpendicular polarizers and spin valves with composite free layer, up to magnetic nanowires with nonhomogeneous magnetization. In the case of spin valve structures, we focused mainly on the current-induced switching and on the possibility of current-induced steady magnetization precessions without need of external magnetic field.

In chapter 7, it has been shown that one of the most important elements for effective switching is optimization of the applied current pulse. The pulse optimization has to be done for each spin valve type separately because the spin torque and hence also the magnetization dynamics depend on the spin valve structure as well as on the used materials. The switching time for a standard and nonstandard spin valves has been mapped as a function of current density and pulse duration. It has been shown that a standard spin valve can be easily switched by a rectangular pulse exceeding certain current density and duration. In contrast, to achieve a fast switching in a nonstandard spin valve, the current pulse parameters have to be properly chosen in a narrow parameter range. However, the presented results show that the switching in nonstandard spin valves can be enhanced using double-pulse switching scheme making use of two following pulses of opposite current direction.

In chapter 8, dual spin valve (DSV) geometry has been considered in a general noncollinear magnetic configuration. Particularly, the current-induced dynamics in DSVs has been studied in the dependence on the angle Ω between outermost layers' magnetizations. It has been shown that in an asymmetric DSV geometry, the spin-torque angular dependece can be efficiently controlled via the angle Ω. This fact has an important effect on the current-induced magnetization dynamics in the central layer. On one hand side, one can observe self-sustained magnetization precessions for $\omega \lesssim \pi/2$, while on the other hand, a fast efficient magnetization switching processes take place for $\Omega \simeq \pi$.

Further improvement of the magnetization switching can be achieved in a dual spin valves geometry with perpendicular and in-plane polarizers, studied in chapters 9 and 10. For this type of stuctures the stationary points and their stability under the spin transfer torque and effective magnetic field have been also studied. In accord with experiment, the numerical simulations reveal a reliable switching with 100 % switching probability by subnanosecond current pulses, which however, decreases with the pulse length. In addition, the influence of in-plane polarizer's dynamics on the dynamics of the central layer has been studied. It has been shown that for a certain current densities, the polarizer's dynamics might increase the current-induced precessions of the central layer and consequently enhance the switching probability by a current-pulse.

In chapter 11 the current-induced dynamics of composite free layers with antiferromagnetic exchange coupling, ie. synthetic antiferromagnet (SyAF) and synthetic ferrimagnet (SyF), has been studied. In both cases different switching mechanisms and their dependence on the external magnetic field has been identified. As shown by numerical simulations, both SyAF and SyF are switchable back and forth without the need of external magnetic field. Moreover, a possibility of steady state out-of-plane precessions in SyF has been demonstrated.

In addition, elementary nonlinear transport properties of magnetic structures have been also studied. In chapter 12, we deal with the magnetotransport in dual spin valve with thin central layer, which shows nonlinear behaviour. We assumed that basic material parameters vary with the density of states, and therefore are modified by the spin accumulation. This model has been studied numerically and reveals features similar to experimental observations [49]. Moreover, we identify variation of interfacial parameters as a dominant contribution to the nonlinear effects. Recently, this result has been confirmed by additional measurements [50].

Finally, in chapter 13, we employed the equilibrium Green function formalism in order to find spin accumulation and spin transfer torque acting on a thick Neel domain wall. In the linear response approximation we calculated the spin torque components and evaluated the spin torque nonadiabaticity as a function of basic material parameters. Apart from this, we identify a small correction to the in-plane spin torque component.

A Material parameters

Here,the bulk and interfacial material parameters, which have been used in the calculations presented in this thesis. The parameters are obtained from relevant experiments and ab initio calculations presented in the literature [57, 138, 139, 49, 140].

material	temperature [K]	ρ^* [$\mu\Omega$cm]	β	l_{sf} [nm]
Co	300	5.1	0.51	60.0
CoFe	300	9.0	0.45	12.0
Py (NiFe)	300	16.0	0.77	5.5
IrMn	300	150.0	0.00	1.0

Table 1: Bulk parameters of magnetic materials used in the calculations

material	temperature [K]	ρ^* [$\mu\Omega$cm]	β	l_{sf} [nm]
Cu	4.2	0.5	0.00	1000.0
Cu	300	0.5	0.00	300.0
Au	300	2.0	0.00	5.5
IrMn	300	150.0	0.00	1.0

Table 2: Bulk parameters of nonmagnetic materials used in the calculations

interface	temperature [K]	R^* [fΩm^2]	γ	Re $\{G_{\uparrow\downarrow}\}$ [1/fΩm^2]	Im $\{G_{\uparrow\downarrow}\}$ [1/fΩm^2]
Co/Cu	300	0.5	0.77	0.542	0.016
CoFe/Cu	300	0.35	0.65	0.542	0.016
Py/Cu	300	0.5	0.70	0.390	0.012
Co/Au	300	0.5	0.70	0.390	0.012
Co/Ru	300	0.5	-0.20	0.260	0.008

Table 3: Interfacial parameters of N/F interfaces

B Rotation Transformation

Consider a transformation in two dimensional real space, $\mathbb{R}^2$, which rotates the coordinate system in the counterclockwise direction by an angle θ. Such a matrix reads

$$\check{R}_2(\theta) = \begin{pmatrix} \cos\theta & \sin\theta \\ -\sin\theta & \cos\theta \end{pmatrix} \tag{B.1}$$

In the three dimensional real space, $\mathbb{R}^3$, one has to specify a fixed axis around which the rotation is performed. Specifically, the rotation of the coordinate system in the counterclockwise direction when looking towards the origin around the x, y, and z axis, respectively, by an angle θ might be expressed as

$$\check{R}_x(\theta) = \begin{pmatrix} 1 & 0 & 0 \\ 0 & \cos\theta & \sin\theta \\ 0 & -\sin\theta & \cos\theta \end{pmatrix} , \tag{B.2a}$$

$$\check{R}_y(\theta) = \begin{pmatrix} \cos\theta & 0 & -\sin\theta \\ 0 & 1 & 0 \\ \sin\theta & 0 & \cos\theta \end{pmatrix} , \tag{B.2b}$$

$$\check{R}_z(\theta) = \begin{pmatrix} \cos\theta & \sin\theta & 0 \\ -\sin\theta & \cos\theta & 0 \\ 0 & 0 & 1 \end{pmatrix} . \tag{B.2c}$$

Then, the transformation described by Eqs. (3.35) might be obtained as

$$\check{R}(\theta,\phi) = \check{R}_x(-\theta)\check{R}_z(\phi-\pi/2) = \begin{pmatrix} \sin\phi & -\cos\phi & 0 \\ \cos\theta\cos\phi & \cos\theta\sin\phi & -\sin\theta \\ \cos\phi\sin\theta & \sin\theta\sin\phi & \cos\theta \end{pmatrix} . \tag{B.3}$$

Then any vector, $\boldsymbol{a}$, from the original coordinate system is expressed in the transformed coordinate system as $\boldsymbol{a}' = \check{R} \cdot \boldsymbol{a}$.

C Demagnetization tensor for array of rectagular blocks

The main idea of the general tensor formulation of the magnetostatic field, proposed by Newell et al [66], is explained in the section 4.3.1. Here, we shall apply their formalism to an array of rectangular blocks. This method allows us to calculate approximately the magnetostatic field induced by magnetized objects of various shapes with generally non-uniform magnetization.

Let us consider the magnetization to be represented by a dicrete distribution $\{\mathbf{M}_i\}$ of vectors at positions $\boldsymbol{r}_i$. The magnetostatic field at $\boldsymbol{r}_i$ is then given by

$$\mathbf{H}_i = -\sum_j \bar{\boldsymbol{N}}(\boldsymbol{r}_i - \boldsymbol{r}_j) \cdot \mathbf{M}_j \,, \tag{C.1}$$

and the total energy density is

$$\varepsilon_m = -\frac{\mu_0}{2} \sum_i \mathbf{M}_i \cdot \mathbf{H}_i = \frac{\mu_0}{2} \sum_{ij} \mathbf{M}_i \cdot \bar{\boldsymbol{N}}(\boldsymbol{r}_i - \boldsymbol{r}_j) \cdot \mathbf{M}_j \,. \tag{C.2}$$

Let us now assume that a magnetic body (or several magnetic bodies) is separated into an array of identical rectangular blocks with dimensions Δx, Δy, and Δz. The relative position of two such block with coordinates (x, y, z) and (x', y', z') is given by vector (X, Y, Z). The components of the demagnetization tensor shall be calculated from the interaction of two pairs of rectangular surfaces according to equation (4.24). For example, to calculate N_{xx} component, one needs to consider faces lying in the $y - z$ plane, because normal to other faces has no component in the x direction. Similarly, to calculate N_{xy} component one needs to consider faces in the $y - z$ plane for the first block and $x - z$ faces for the second one.

Component N_{xx}

The N_{xx} component of demagnetization tensor might be separated into four contributions

$$N_{xx}(X, Y, Z) = \frac{1}{4\pi v} \left[2F(X, Y, Z) - F(X + \Delta x, Y, Z) - F(X - \Delta x, Y, Z) \right] , \tag{C.3}$$

where $v = \Delta x \Delta y \Delta z$, and

$$F(X, Y, Z) = \int_0^{\Delta z} \mathrm{d}z \int_0^{\Delta y} \mathrm{d}y \int_0^{\Delta z} \mathrm{d}z' \int_0^{\Delta y} \mathrm{d}y' \times \frac{1}{\sqrt{X^2 + (y + Y - y')^2 + (z + Z - z')^2}} \,, \tag{C.4}$$

which can be rewritten as

$$F(X, Y, Z) = \int_Z^{Z+\Delta z} \mathrm{d}z \int_Y^{Y+\Delta y} \mathrm{d}y \int_{z-\Delta z}^{z} \mathrm{d}z' \int_{y-\Delta y}^{y} \mathrm{d}y' \, \frac{1}{\sqrt{X^2 + y'^2 + z'^2}} \,. \tag{C.5}$$

This can be split into 16 integrals of the form

$$F_2(X, Y, Z) = \int_0^{Z} \mathrm{d}z \int_0^{Y} \mathrm{d}y \int_0^{z} \mathrm{d}z' \int_0^{y} \mathrm{d}y' \, \frac{1}{\sqrt{X^2 + y'^2 + z'^2}} \,. \tag{C.6}$$

Taking into accunt that the latter integral is even in Y and Z, we can replace Y and Z by their absolute values. Then we have

$$\begin{aligned} F(X,Y,Z) = {} & F_1(X,Y+\Delta y,Z+\Delta z) - F_1(X,Y,Z+\Delta z) \\ & - F_1(X,Y+\Delta y,Z) + F_1(X,Y,Z)\,, \end{aligned} \tag{C.7}$$

where

$$\begin{aligned} F_1(X,Y,Z) = {} & F_2(X,Y,Z) - F_2(X,Y-\Delta y,Z) \\ & - F_2(X,Y,Z-\Delta z) + F_2(X,Y-\Delta y,Z-\Delta z)\,. \end{aligned} \tag{C.8}$$

Finally, function $F_2(X,Y,Z)$ can be written as [141]

$$F_2(X,Y,Z) = f(X,Y,Z) - f(X,0,Z) - f(X,Y,0) + f(X,0,0)\,, \tag{C.9}$$

where

$$\begin{aligned} f(x,y,z) = {} & (y/2)\,(z^2-x^2)\,\phi\!\left(\frac{y}{\sqrt{x^2+z^2}}\right) \\ & + (z/2)\,(y^2-x^2)\,\phi\!\left(\frac{z}{\sqrt{x^2+y^2}}\right) \\ & - xyz\,\tan^{-1}\!\left(\frac{yz}{xR}\right) + (2x^2-y^2-z^2)\,(R/6)\,, \end{aligned} \tag{C.10}$$

with $\phi(x) = \sinh^{-1}(x) = \ln(x+\sqrt{1+x^2})$, and $R = \sqrt{x^2+y^2+z^2}$

Component N_{xy}

Similarly, we can calculate N_{xy} component, which is even in Z and odd in X and Y. It can be written as

$$\begin{aligned} N_{xy}(X,Y,Z) = \frac{1}{4\pi v}\big[& G(X,Y,Z) - G(X-\Delta x,Y,Z) - \\ & G(X,Y+\Delta y,Z) + G(X-\Delta x,Y+\Delta y,Z)\big]\,, \end{aligned} \tag{C.11}$$

where

$$G(X,Y,Z) = \int_{Y-\Delta y}^{Y}\mathrm{d}y\int_{Z-\Delta z}^{Z}\mathrm{d}z\int_{z}^{z+\Delta z}\mathrm{d}z'\int_{X}^{X+\Delta x}\mathrm{d}x'\,\frac{1}{\sqrt{x'^2+y^2+z'^2}}\,. \tag{C.12}$$

$G(X,Y,Z)$ can be split as

$$\begin{aligned} G(X,Y,Z) = {} & G_1(X,Y,Z) - G_1(X,Y-\Delta y,Z) \\ & - G_1(X,Y,Z-\Delta z) + G_1(X,Y-\Delta y,Z-\Delta z)\,, \end{aligned} \tag{C.13}$$

where

$$\begin{aligned} G_1(X,Y,Z) = {} & G_2(X+\Delta x,Y,Z+\Delta z) - G_2(X+\Delta x,Y,Z) \\ & - G_2(X,Y,Z+\Delta z) + G_2(X,Y,Z)\,. \end{aligned} \tag{C.14}$$

Finally, $G_2(X,Y,Z)$ can be expressed as

$$G2(X,Y,Z) = g(X,Y,Z) - g(X,Y,0)\,, \tag{C.15}$$

where

$$
\begin{aligned}
g(x,y,z) = {} & xyz\,\sinh^{-1}\!\left(\frac{z}{\sqrt{x^2+y^2}}\right) \\
& + (y/6)\,(3x^2-y^2)\,\sinh^{-1}\!\left(\frac{x}{y^2+z^2}\right) \\
& - (x/6)\,(3z^2-x^2)\,\sinh^{-1}\!\left(\frac{x}{x^2+z^2}\right) \\
& - (z^3/6)\,\tan^{-1}\!\left(\frac{xy}{zR}\right) - (zy^2/2)\,\tan^{-1}\!\left(\frac{xz}{yR}\right) \\
& - (zx^2/2)\,\tan^{-1}\!\left(\frac{yz}{xR}\right) - xyR/3\,.
\end{aligned}
\tag{C.16}
$$

Other components

All the others components of the demagnetization tensors might be calculated in a similar way as N_{xx} and N_{yz}. They can be obtained simply by permuting X, Y, and Z and the cell dimensions Δx, Δy, and Δz. Namely,

$$N_{yy}(X,Y,Z,\Delta x,\Delta y,\Delta z) = N_{xx}(Y,X,Z,\Delta y,\Delta x,\Delta z)\,, \tag{C.17}$$

$$N_{zz}(X,Y,Z,\Delta x,\Delta y,\Delta z) = N_{xx}(Z,Y,X,\Delta z,\Delta y,\Delta x)\,, \tag{C.18}$$

$$N_{xz}(X,Y,Z,\Delta x,\Delta y,\Delta z) = N_{xy}(X,Z,Y,\Delta x,\Delta z,\Delta y)\,, \tag{C.19}$$

$$N_{yz}(X,Y,Z,\Delta x,\Delta y,\Delta z) = N_{xy}(Y,Z,X,\Delta y,\Delta z,\Delta x)\,. \tag{C.20}$$

The components below the diagonal are determined from the symmetry of demagnetization tensor: $N_{yx} = N_{xy}$, $N_{zx} = N_{xz}$, and $N_{zy} = N_{yz}$.

D Landau-Lifshitz-Gilbert equation in spherical coordinates

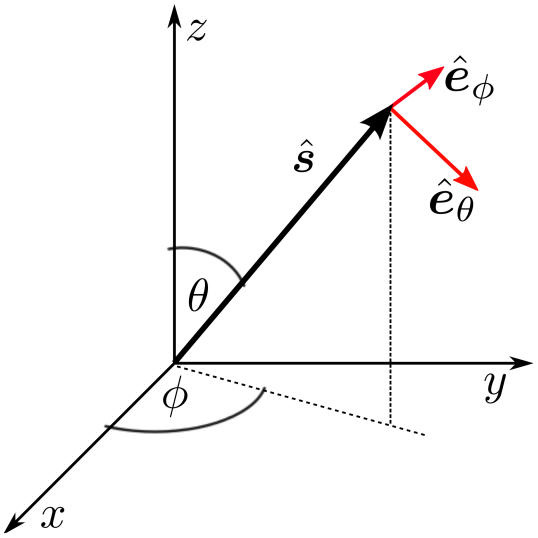

Figure 59: System of local spherical coordinates

For analytical studies of Landau-Lifshitz-Gilbert equation it is often useful to transform the equation into local spherical coordinate system connected with the spin $\hat{\boldsymbol{s}}$. We start from a general form of LLG defined by (5.73), which reads

$$\frac{\mathrm{d}\hat{\boldsymbol{s}}}{\mathrm{d}t} + \alpha\, \hat{\boldsymbol{s}} \times \frac{\mathrm{d}\hat{\boldsymbol{s}}}{\mathrm{d}t} = \boldsymbol{\Gamma}\,, \tag{D.1}$$

where in spherical coordinates $\hat{\boldsymbol{s}} = (\cos\phi \sin\theta, \sin\phi \sin\theta, \cos\theta)$. Then the local coordinate system is defined by [97]

$$\hat{\mathbf{e}}_\phi = [\hat{\mathbf{e}}_z \times \hat{\boldsymbol{s}}] \,/\, \sin\theta = (-\sin\phi, \cos\phi, 0)\,, \tag{D.2a}$$

$$\hat{\mathbf{e}}_\theta = \hat{\mathbf{e}}_\phi \times \hat{\boldsymbol{s}} = (\cos\phi\cos\theta, \sin\phi\cos\theta, -\sin\theta)\,. \tag{D.2b}$$

For the terms on the left-hand side of (D.1) we can easily find

$$\frac{\mathrm{d}\hat{\boldsymbol{s}}}{\mathrm{d}t} = \frac{\mathrm{d}\theta}{\mathrm{d}t}\,\hat{\mathbf{e}}_\theta + \sin\theta\,\frac{\mathrm{d}\phi}{\mathrm{d}t}\,\hat{\mathbf{e}}_\phi\,, \tag{D.3}$$

and

$$\hat{\boldsymbol{s}} \times \frac{\mathrm{d}\hat{\boldsymbol{s}}}{\mathrm{d}t} = \frac{\mathrm{d}\theta}{\mathrm{d}t}\,\hat{\mathbf{e}}_\phi - \sin\theta\,\frac{\mathrm{d}\phi}{\mathrm{d}t}\,\hat{\mathbf{e}}_\theta\,, \tag{D.4}$$

where we used $\hat{\boldsymbol{s}} \times \hat{\mathbf{e}}_\theta = \hat{\mathbf{e}}_\phi$ and $\hat{\boldsymbol{s}} \times \hat{\mathbf{e}}_\phi = -\hat{\mathbf{e}}_\theta$. Therefore, the left-hand side of (D.1) reads

$$\frac{\mathrm{d}\hat{\boldsymbol{s}}}{\mathrm{d}t} + \alpha\, \hat{\boldsymbol{s}} \times \frac{\mathrm{d}\hat{\boldsymbol{s}}}{\mathrm{d}t} = \left(\frac{\mathrm{d}\theta}{\mathrm{d}t} - \alpha\,\frac{\mathrm{d}\phi}{\mathrm{d}t}\,\sin\theta\right)\hat{\mathbf{e}}_\theta + \left(\frac{\mathrm{d}\phi}{\mathrm{d}t}\,\sin\theta + \alpha\,\frac{\mathrm{d}\theta}{\mathrm{d}t}\right)\hat{\mathbf{e}}_\phi\,, \tag{D.5}$$

which can be rewritten in a matrix form as

$$\begin{pmatrix}\hat{\mathbf{e}}_\theta & \hat{\mathbf{e}}_\phi\end{pmatrix}\begin{pmatrix}1 & -\alpha\sin\theta \\ \alpha & \sin\theta\end{pmatrix}\begin{pmatrix}\mathrm{d}\theta/\mathrm{d}t \\ \mathrm{d}\phi/\mathrm{d}t\end{pmatrix}\,. \tag{D.6}$$

The right hand side of (D.1) can be written in the local coordinate system as

$$\begin{pmatrix} \hat{\mathbf{e}}_\theta & \hat{\mathbf{e}}_\phi \end{pmatrix} \begin{pmatrix} v_\theta \\ v_\phi \end{pmatrix} , \tag{D.7}$$

where $v_\theta = \boldsymbol{\Gamma} \cdot \hat{\mathbf{e}}_\theta$ and $v_\phi = \boldsymbol{\Gamma} \cdot \hat{\mathbf{e}}_\phi$. Comparing (D.6) and (D.7) one obtains

$$\begin{pmatrix} 1 & -\alpha \sin\theta \\ \alpha & \sin\theta \end{pmatrix} \begin{pmatrix} \mathrm{d}\theta/\mathrm{d}t \\ \mathrm{d}\phi/\mathrm{d}t \end{pmatrix} = \begin{pmatrix} v_\theta \\ v_\phi \end{pmatrix} . \tag{D.8}$$

Inverting the 2×2 matrix one finally gets [97]

$$\frac{\mathrm{d}}{\mathrm{d}t} \begin{pmatrix} \theta \\ \phi \end{pmatrix} = \frac{1}{1+\alpha^2} \begin{pmatrix} 1 & \alpha \\ -\alpha \sin^{-1}\theta & \sin^{-1}\theta \end{pmatrix} \begin{pmatrix} v_\theta \\ v_\phi \end{pmatrix} , \tag{D.9}$$

where the parameters v_θ and v_ϕ depend on the torques acting on the net spin moment $\hat{\boldsymbol{s}}$; i.e. effective magnetic field and current-induced torques.

E Heun scheme

Heun scheme (see e.g. [107]) is a predictor-corrector type integration scheme used especially for stochastic differential equations. In general, the statistical error of the scheme can be made arbitrarily small by averaging over large number of stochastic paths.

Consider generalized stochastic Landau-Lifshitz-Gilbert equations given by (5.73) with stochastic noise (5.59). Let, in a given time t the net spin moment is $\hat{\boldsymbol{s}} = \hat{\boldsymbol{s}}(t)$. First, we generate values of $\mathbf{H}_{\mathrm{th}}$ as given by equation (5.59). The right-hand side of LLG equation reads

$$\mathrm{LLG}(\hat{\boldsymbol{s}}, t) = -\hat{\boldsymbol{s}} \times (\mathbf{H}_{\mathrm{eff}}(\hat{\boldsymbol{s}}, t) + \mathbf{H}_{\mathrm{th}}) + \alpha \hat{\boldsymbol{s}} \times [\hat{\boldsymbol{s}} \times (\mathbf{H}_{\mathrm{eff}}(\hat{\boldsymbol{s}}, t) + \mathbf{H}_{\mathrm{th}})] + \boldsymbol{\tau}(\hat{\boldsymbol{s}}, t) \tag{E.1}$$

Then we estimate spin $\bar{\boldsymbol{s}}$ with so called *predictor*, which is given by the Euler integration scheme [107]

$$\boldsymbol{s}'(t + \Delta t) = \hat{\boldsymbol{s}} + \mathrm{LLG}(\hat{\boldsymbol{s}}, t)\Delta t\,. \tag{E.2}$$

We say that $\boldsymbol{s}'$ is prediction of $\hat{\boldsymbol{s}}$ in time $t + \Delta t$. To obtain the solution in time $t + \Delta t$ we use *corrector* scheme given by

$$\boldsymbol{s}''(t + \Delta t) = \hat{\boldsymbol{s}} + \frac{1}{2}\left[\mathrm{LLG}(\boldsymbol{s}', t + \Delta t) + \mathrm{LLG}(\hat{\boldsymbol{s}}, t)\right]\Delta t\,. \tag{E.3}$$

Since the Euler integration scheme does not protect the vector length, which is protected by LLG equation, one needs to normalize the vector length after each integration step

$$\hat{\boldsymbol{s}}(t + \Delta t) = \frac{\boldsymbol{s}''}{|\boldsymbol{s}''|}\,. \tag{E.4}$$

F Computer generation of random numbers

Random number generators are one of the most important parts of computer simulations. They enable computer implementation of random process which can occur in frame of some physical models. Most of programming languages dispose with implemented random generator which generates random numbers from the interval $\langle 0, 1)$ with uniform probability density. However, in case of many physical processes (as eg. in case of thermally activated magnetization dynamics) one needs a random numbers with Gaussian distribution. To obtain such a random numbers using the implemented generator with uniform probability we employ the *Box-Müller algorithm* [142], which is based on the variable transformation, i.e. it uses the fact that if some random number X has probability density $P_X(x)$, the value of transformed variable $Y = f(x)$ has not the same probability density $P_Y(y)$ in general.

Let X is a continuous stochastic variable generated with probability density $P_X(x)$. This variable one can transform to a new one Y

$$Y = f(X)\,. \tag{F.1}$$

The goal of this part is to establish probability density $P_Y(y)$ of variable Y. Let

$$\Delta y = \frac{\mathrm{d}y}{\mathrm{d}x}\Delta x.$$

The *principle of probability flow* by variable change tells

$$P_Y(y)|\Delta y| = P_X(x)|\Delta x| \tag{F.2}$$

and in differential form $\Delta x \to 0$

$$P_Y(y) = P_X(x)\left|\frac{\mathrm{d}x}{\mathrm{d}y}\right|, \tag{F.3}$$

what is in fact desired probability density of variables Y.

In two-dimensional case we need two transformation functions

$$Y_1 = f_1(X_1, X_2)\,, \tag{F.4a}$$
$$Y_2 = f_2(X_1, X_2) \tag{F.4b}$$

obeying

$$\begin{aligned}\mathrm{d}y_1 = \mathrm{d}f_1(x_1, x_2) &= \frac{\partial f_1}{\partial x_1}\mathrm{d}x_1 + \frac{\partial f_1}{\partial x_2}\mathrm{d}x_2,\\ \mathrm{d}y_2 = \mathrm{d}f_2(x_1, x_2) &= \frac{\partial f_2}{\partial x_1}\mathrm{d}x_1 + \frac{\partial f_2}{\partial x_2}\mathrm{d}x_2.\end{aligned}$$

Eq. (F.3)take the form

$$P_Y(y_1, y_2)\mathrm{d}V_y = P_X(x_1, x_2)\mathrm{d}V_x\,, \tag{F.5}$$

where $\mathrm{d}V_x = \mathrm{d}x_1\mathrm{d}x_2$ and $\mathrm{d}V_y = \mathrm{d}y_1\mathrm{d}y_2$ are volume elements in the two-dimensional space, for which reads

$$dV_y = \left|\det\begin{pmatrix}\partial f_1/\partial x_1 & \partial f_1/\partial x_2\\ \partial f_2/\partial x_1 & \partial f_2/\partial x_2\end{pmatrix}\right|\mathrm{d}V_x\,.$$

Analogous with Eq. (F.3) we can write

$$P_Y(f_1, f_2) \equiv P_Y(y_1, y_2) = P_X(x_1, x_2)\frac{\mathrm{d}V_x}{\mathrm{d}V_y}\,.$$

Finally, we obtain

$$P_Y(y_1, y_2) = \frac{P_X(x_1, x_2)}{\left|\det\begin{pmatrix}\partial f_1/\partial x_1 & \partial f_1/\partial x_2\\ \partial f_2/\partial x_1 & \partial f_2/\partial x_2\end{pmatrix}\right|} \tag{F.6}$$

Now, let us apply this procedure to the transformation of the type

$$y_1 = \sqrt{-2\ln x_1}\cos(2\pi x_2), \tag{F.7a}$$
$$y_2 = \sqrt{-2\ln x_1}\sin(2\pi x_2), \tag{F.7b}$$

where $x_1, x_2 \in \mathcal{U}(0,1)$. Next we have to calculate the partial derivations

$$\frac{\partial y_1}{\partial x_1} = \frac{-1}{x_1\sqrt{-2\ln x_1}}\cos(2\pi x_2)\,, \qquad \frac{\partial y_1}{\partial x_2} = -2\pi\sqrt{-2\ln x_1}\sin(2\pi x_2)\,,$$
$$\frac{\partial y_2}{\partial x_1} = \frac{-1}{x_1\sqrt{-2\ln x_1}}\sin(2\pi x_2)\,, \qquad \frac{\partial y_1}{\partial x_2} = -2\pi\sqrt{-2\ln x_1}\cos(2\pi x_2)\,.$$

From transformations (F.7) we can express

$$x_1 = \exp\left(-\frac{y_1^2 + y_2^2}{2}\right)\,.$$

Using latter expressions one can calculate Jacobian

$$\left|\det\begin{pmatrix}\partial f_1/\partial x_1 & \partial f_1/\partial x_2\\ \partial f_2/\partial x_1 & \partial f_2/\partial x_2\end{pmatrix}\right| = 2\pi\exp\left(\frac{y_1^2 + y_2^2}{2}\right)\,. \tag{F.8}$$

On the basis of (F.6) we can write

$$\tilde{P_Y}(y_1, y_2) = \frac{1}{2\pi}\exp\left(-\frac{y_1^2}{2}\right)\exp\left(-\frac{y_2^2}{2}\right), \tag{F.9}$$

what expresses the Gaussian probability density function in two-dimensional space. This result confirms that random quantities y_1 a y_2 given in (F.7) have Gaussian probability density. In one dimensional case, one can use numbers y_1 a y_2 as two independent variables of Gaussian distribution [142].

Streszczenie - Abstract in Polish language

Spintronika jest nową dziedziną fizyki, która bada możliwości wykorzystania dodatkowej właściwości elektronu - *spinu*. Konwencjonalne układy elektroniczne wykorzystują elektron jako nośnik ładunku oraz energii. Natomiast jeśli do obwodu elektronicznego zostaną dołączone elementy magnetyczne, prąd elektronów zostanie spinowo spolaryzowany, co oznacza, że jeden kierunek spinu staje się dominującym. W związku z tym, prąd staje się także nośnikiem momentu pędu. Układy spintroniczne są interesujące nie tylko ze względu na nowe możliwości prowadzenia badań podstawowych dotyczących transportu elektronowego, ale także z punktu widzenia możliwych zastosowań w pamięciach komputerowych oraz w telefonii komórkowej.

Wstęp

Badania naukowe w dziedzinie spintroniki rozpoczęto pod koniec lat 80-tych dwudziestego wieku, kiedy odkryto efekt gigantycznego magnetooporu w wielowarstwowych układach metalicznych [7, 8]. W eksperymentach tych pokazano, że opór układu złożonego z warstw magnetycznych oddzielonych warstwami niemagnetycznymi zależy od konfiguracji magnetycznej układu. Zjawisko to zostało wyjaśnione teoretycznie [14, 15] w ramach modelu dwukanałowego, który zakłada, że elektrony poruszają się w układzie dwoma niezależnymi kanałmi: dla elektronów o spinie większościowym oraz dla elektronów o spinie mniejszościowym. Ponadto, zgodnie z wcześniejszymi obserwacjami Mott'a [3, 4], właściwości transportowe dla elektronów w różnych kanałach są inne, ponieważ gęstości stanów elektronów na poziomie Fermiego różnią się pomiędzy kanałami. W przypadku kiedy magnetyzacje warstw w układzie skierowane są równolegle, elektrony ze spinem w górę ($\uparrow$) rozpraszane są w całym układzie słabiej niż elektrony ze spinem w dól ($\downarrow$). Natomiast jeśli namagnesowania poszczególnych warst uporządkowane są antyrównolegle, zarówno elektrony ze spinem $\uparrow$ jak i $\downarrow$ rozpraszane są silnie w co drugiej warstwie magnetycznej. Z tego powodu opór całego układu w konfiguracji równoległej jest mniejszy niż opór w konfiguracji antyrównoległej. Różnica między tymi dwoma oporami definiuje gigantyczny magnetoopóru [równanie (2.9)]. Układy wielowarstwowe wykazujące zjawisko gigantycznego magnetooporu nazywamy też *zaworami spinowimi*.

Dynamiczny rozwój spintroniki przypada na okres od połowy lat 90-tych dwudziestetego wieku, kiedy Slonczewski [25] i Berger [26] pokazali teoretycznie, że prąd przepływający przez układ $F_1/N/F_2$ złożony z dwóch nierównych warstw magnetycznych, F_1 i F_2, oddzielonych warstwą niemagnetyczną, N, może spowodować przełączenie kierunku namagnesowania jednej z warstw. Zjawisko to jest związane z transmisją momentu pędu pomiędzy warstwami magnetycznymi za pomocą elektronów przepływających przez układ. Elektrony spolaryzowane w warstwie F_1 przepływają przez warstwę N do warstwy F_2, w której ponownie zostają spolaryzowane w kierunku namagnesowania warstwy F_2. W przypadku gdy namagnesowania warstw F_1 i F_2 są niekolinearne, zgodnie z prawem zachowania momentu pędu, powstanie moment siły, który działa na magnetyzacje w układzie. Jeśli grubość warstwy F_2 będzie mniejsza od grubości warstwy F_1, moment siły zmieni kierunek magnetyzacji warstwy F_2 jeżeli gęstość przepływającego prądu będzie wystarczająco duża i prąd będzie miał odpowiedni kierunek. W takim przypadku warstwę F_1 nazywamy *warstwą umocowaną*, natomiast warstwę F_2 oznaczamy jako *warstwę swobodną*.

Zjawisko indukowanego prądem magnetycznego przełączania jest bardzo obiecujące ze względu na możliwe zastosowania w pamięciach komputerowych o wysokiej gęstości zapisu informacji,

sterowanych wyłącznie za pomocą prądu elektrycznego, bez potrzeby przykładania pola magnetycznego. Po odkryciu powyższego zjawiska panowało przekonanie, że zawory spinowe sterowane prądem bardzo szybko wyprą i zastąpią tradycyjne zawory spinowe sterowane polem magnetycznym. Jednak szybko okazało się, że przed wykorzystaniem układów opartych na transferze spinowym w praktyce, muszą zostać rozwiązane pewne istotne kwestie. Najważniejszą z nich jest problem zmniejszenia gęstości prądu potrzebnego do magnetycznego przełączania. Ponadto, równie istotne jest zwiększenie prawdopodobieństwa przełączania zaworów spinowych oraz zwiększenie ich stabilności termicznej. Problemy te próbowano rozwiązać na kilka sposobów. Jednym z nich jest stosowanie różnych schematów przełączania magnetycznego, które korzystają z jednego lub kilku impulsów prądu i/lub pola magnetycznego [29, 30, 31, 32]. W zależności od badanego układu, odpowiedni schemat może powiększyć prawdopodobieństwo przełączania oraz zredukować energię potrzebną do przełączenia namagnesowania. Innym sposobem na poprawienie parametrów zaworów spinowych jest dobranie odpowiedniej geometrii i materiałów. W ten sposób tworzy się niestandardowe zawory spinowe [40, 35, 36], podwójne zawory spinowe [48], zawory spinowe z prostopadłym namagnesowaniem warstwy umocowanej [42], oraz zawory spinowe ze złożoną warstwą swobodną, tj. z syntetycznym antyferromagnetykiem lub ferrimagnetykiem [9].

W niniejszej rozprawie doktorskej zbadane zostały właściwości transportowe oraz dynamika spinowa we wszystkich wyżej wymienionych układach, ze szczególnym naciskiem na możliwe zastosowania praktyczne. W związku z tym, zbadane zostały różne schematy przełączania magnetycznego. Ponadto, w pracy doktorskiej poruszono także zagadnienia związane z własnościami magnetooporu w przypadku nierównowagowego transportu spinowego przez cienką warstwę magnetyczną. Wreszcie w rozprawie przeprowadzono także analizę transportu elektronowego oraz indukowanego prądem momentu siły działającego na szeroką ściankę domenową.

Dyfuzyjny transport spinowy

Jeśli elektrony są wstrzykiwane z materiału magnetycznego do materiału niemagnetycznego, w materiale niemagnetycznym tworzy się nierównowaga spinowa, tzw. *akumulacja spinowa*, która zdefiniowana jest jako różnica między potencjałami elektrochemicznymi dla spinów większościowych i mniejszościowych. Pokazano, że akumulacja spinowa maleje wykładniczo z odległością od interfejsu między materiałami w zależności od średniej drogi dyfuzji spinu w danym materiale. W materiałach niemagnetycznych, takich jak na przyklad miedź, akumulacja spinowa istnieje nawet kilka mikrometrów od interfejsu. Oznacza to, iż wstrzykiwane spiny w metalach poruszają się w sposób dyfuzyjny.

Zależność od spinu dyfuzyjnego transportu elektronów została wykorzystana w modelu Valeta-Ferta do opisu gigantycznego magnetooporu w zaworach spinowych w przypadku gdy prąd płynie prostopadle do warstw. Model ten opisuje transport elekronów przez wielowarstwy za pomocą jednowymiarowego równania Boltzmanna (3.1). Przy założeniu symetrii cylindrycznej rozkładu prędkości elektronów, równanie Boltzmanna prowadzi do równań różniczkowych pierwszego stopnia (3.5) opisujących przestrzenną zależność spinowo-zależnych potencjałów elektrochemicznych oraz prądu spinowego w układzie. Równania te mają proste rozwiązanie w postaci funkcji (3.9). Nieznane parametry A, B, C i D w tych równaniach można otrzymać z odpowiednich warunków brzegowych, które spełnione są na interfejsach. W konsekwencji, znając profil potenciału elektrochemicznego można wyznaczyć opór elektryczny wielowarstwy dla pewnej konfiguracji magnetycznej. Zmiennymi wejściowymi dla modelu Valeta-Ferta są fenomenologiczne parametry objętoś-

ciowe wykorzystanych w układzie materiałów, tj. wartości średniej drogi dyfuzji spinu, oporności objętościowe i asymetrie spinowe, oraz parametry interfejsów. Parametry te można wyznaczyć eksperymentalnie [57] z pomiarów magnetooporu. Model Valeta-Ferta jest ograniczony do kolinearnych konfiguracji magnetycznych, co uniemożliwia obliczenie całkowitej zależności magnetooporu od pola zewnętrznego.

Model dyfuzyjny transportu spinowego został później uogólniony na przypadek niekolinearnych konfiguracji magnetycznych [33]. W modelu tym, transport spinowy został opisany za pomocą równania dyfuzyjnego (3.10), które prowadzi do równań (3.12), analogicznych do równań otrzymanych w ramach modelu Valeta-Ferta. Z równań tych można otrzymać wyrażenia na potenciał elektrochemiczny, μ_0, akumulację spinową, $\boldsymbol{g}$, oraz prąd spinowy $\boldsymbol{j}$ w warstwach magnetycznych i niemagnetycznych. Podczas gdy w warstwach magnetycznych akumulacja spinowa (3.16b) i prąd spinowy (3.20) są wielkościami skalarnymi wyrażonymi w lokalnym układzie współrzędnych (w którym oś kwantyzacji jest ustawiona wzdłuż namagnesowania), w warstwach niemagnetycznych wielkości te są wektorami, wyrażonymi poprzez (3.23b) i (3.26). Nieznane parametry w tych wyrażeniach można otrzymać, analogicznie jak w modelu Valeta i Ferta, z rozwiązania warunków brzegowych danych równaniami (3.31) oraz (3.34). Piewsza para równań opisuje składowe akumulacji spinowej i prądu spinowego, które są równoległe do namagnesowania warstwy magnetycznej (tzw. składowe podłużne). Składowe te nie ulegają zmianie przy przejściu przez interfejs. Druga para równań dotyczy składowych prądu i akumulacji spinowej, które są prostopadłe do namagnesowania (tzw. składowe poprzeczne). Składowe te są w ogólności niezerowe w warstwie niemagnetycznej, natomiast znikają w warstwie magnetycznej. W równaniach tych występuje parametr $G_{\uparrow\downarrow}$ nazywany *konduktancją mieszaną*, która jest wielkością zespoloną opisującą niekolinearny transport spinowy przez iterfejs ferromagnetyk/material niemagnetyczny. Jeśli prąd i akumulacja spinowa w warstwie niemagnetycznej nie są wyrażone w lokalnym układzie współrzędnych warstwy magnetycznej, muszą one zostać przetransformowane do tego układu za pomocą odpowiedniej transformacji obrotu (3.36). Z rozwiązania układu równań na warunki brzegowe można otrzymać profil potenciału elektrochemicznego, prądu, oraz akumulacji spinowej w badanej wielowarstwie dla dowolnej konfiguracji magnetycznej. Umożliwia to obliczenie gigantycznego magnetooporu w zależności od kąta między magnetyzacjami dwóch warstw magnetycznych, lub podczas dynamiki magnetycznej [61].

Opisany wyżej formalizm można także zastosować do obliczeń indukowanego prądem momentu siły, $\boldsymbol{\tau}$, działającego na namagnesowania warstw. Wielkość ta jest zdefinowana równaniem (3.45) jako różnica składowych poprzecznych na lewej (niemagnetycznej) i prawej (magnetycznej) stronie interfejsu. Otrzymany moment siły można zapisać za pomocą składowych (3.46) oraz (3.49), których wielkości są proporcjonalne do skladowych prądu spinowego w warstwie niemagnetycznej, j_x oraz j_y. W ten sposób można oszacować moment siły działający na namagnesowania w dowolnej konfiguracji magnetycznej, co umożliwia modelowanie indukowanej prądem dynamiki magnetycznej w zaworach spinowych. Zaletą tego podejścia jest to, iż ujednolica ono opis magnetooporu oraz indukowanego prądem momentu siły. Obie te wielkości można więc wyznaczyć w ramach tego samego modelu zakładając znajomość parametrów materiałowych warstw oraz interfejsów.

Dynamika magnetyczna

W niniejszej pracy doktorskiej badano głównie wpływ transportu spinowego na dynamikę magnetyczną w układach metalicznych. W przypadku gdy prąd nie płynie przez układ, dynamika

magnetyczna może być indukowana polem magnetycznym. Równaniem ruchu namagnesowania w polu efektywnym, $\mathbf{H}_{\text{eff}}$, jest równanie Landaua-Lifshiza-Gilberta (LLG), opisane wzorem (5.25). Pierwszy człon tego równania opisuje precesję namagnesowania $\mathbf{M}$ w polu efektywnym. Drugi człon równania LLG jest związany z tzw. tłumieniem magnetycznym, które powoduje, że po pewnym czasie dynamika namagnesowania zostanie stłumiona i wektor namagnesowania ustawi się wzdłuż pola efektywnego. Siłę tłumienia opisuje parametr tłumienia, α, wprowadzony przez Gilberta [80, 81]. Jego wielkość zależy od materiału i zawiera się w zakresie od $\alpha = 10^{-3}$ do 10^{-1}.

Efektywne pole magnetyczne może zawierać, oprócz pola zewnętrznego ($\mathbf{H}_{\text{ext}}$), także anizotropię magnetokrystaliczną (H_{ani}), pole rozmagnesowania ($\mathbf{H}_{\text{dem}}$), oraz pole magnetostatyczne ($\mathbf{H}_{\text{int}}$) pochodzące od innych namagnesowanych obiektów w otoczeniu badanej cząstki lub warstwy magnetycznej. Wszystkie te składniki pola mają znaczny wpływ na charakter dynamiki magnetycznej. Ponadto, w przypadku kiedy rozważamy cząstkę magnetyczną w niezerowej temperaturze, pole $\mathbf{H}_{\text{eff}}$ także zawiera stochastyczne pole termiczne ($\mathbf{H}_{\text{th}}$), które efektywnie zastępuje odziaływanie namagnesowania z szybko zmieniającymi się stopniami swobody zależnymi od temperatury. Pole termiczne, dane równaniami (5.36), ma właściwości szumu Gaussowskiego, co oznacza, że jego wartość średnia jest zerem, natomiast jego drugi moment statystyczny zależy od temperatury. Zależność tą można otrzymać za pomocą równania Fokkera-Plancka (5.42), które prowadzi do relacji (5.58). Jeśli przez wielowarstwę metaliczną przepływa prąd elektryczny, dynamika magnetyczna warstwy swobodnej opisana jest uogólnionym równaniem LLG rozszerzonym o indukowany prądem moment siły, $\boldsymbol{\tau}$, które opisane jest równaniem (5.60).

Badane zagadnienia i wnioski

W pracy badano kilka problemów związanych z indukowaną prądem dynamiką spinową w metalicznych zaworach spinowych. Główną część badań stanowią numeryczne rozwiązania równania LLG. Zakładając jednorodne namagnesowanie warstw magnetycznych w badanych zaworach spinowych zastosowano przybliżenia makrospinu, tj. założono, iż stan magnetyczny warstwy można opisać przy pomocy jednego wektora namagnesowania, $\mathbf{M}$, lub makrospinu, $\hat{\boldsymbol{s}}$. W przypadku dynamiki indukowanej prądem, moment siły obliczony został w limicie transportu dyfuzyjnego [33].

Przełączanie magnetyczne w standardowych i niestandardowych zaworach spinowych indukowane impulsem prądu elektrycznego

W pierwszej części dysertacji badano wpływ długości oraz amplitudy impulsu prądu na przełączanie metalicznych zaworów spinowych złożonych z dwóch warstw magnetycznych oddzielonych warstwą niemagnetyczną. Badane były dwa typy zaworów spinowych: standardowe i niestandardowe. Różnica pomiędzy tymi dwoma rodzajami zaworów spinowych uwidacznia się w zależności indukowanego prądem momentu siły od kąta θ między dwoma wektorami namagnesowania. Różnica ta jest pokazana na rysunku 21. W zaworach standardowych zależność kątowa momentu siły jest podobna do funkcji sinus, moment siły jest zerowy w kolinearnych konfiguracjach magnetycznych ($\theta = 0, \pi$) i nie zmienia znaku dla $\theta \in (0, \pi)$. Taką zależność kątową można obserwować na przykład w zaworze spinowym typu Py(20)/Cu(10)/Py(8), gdzie Py oznacza warstwę permaloju ($Ni_{80}Fe_{20}$), podczas gdy liczby w nawiasach oznaczają grubości warstw w nanometrach. Natomiast w zaworach niestandardowych, moment siły jest zerowy nie tylko w konfiguracjach kolinearnych, ale także dla pewnych konfiguracji niekolinearnych. Ponadto, dla kątów $\theta \in (0, \pi)$ wartość momentu

siły zmienia znak, co powoduje, że jego zależność kątowa jest falista. Taka zależność kątowa występuje wtedy, gdy asymetrie spinowe w warstwach magnetycznych zaworu spinowego znacznie się różnią. Warunek ten jest spełniony na przykład dla struktury Co(8)/Cu(10)/Py(8), który został zbadany w niniejszej dysertacji. W przypadku standardowej zależności momentu siły od kąta, prąd płynący w jednym kierunku stabilizuje w zaworze równoległą konfigurację magnetyczną oraz destabilizuje konfigurację antyrównoległą. Jeśli prąd płynie w przeciwnym kierunku, stabilizuje on konfigurację antyrównoległą i destabilizuje konfigurację równoległą. Natomiast w przypadku zaworów niestandardowych, prąd płynący w jedną stronę stabilizuje obie kolinearne konfiguracje, podczas gdy prąd płynący w przeciwną stronę destabilizuje obie konfiguracje [36, 37, 35]. Takie zachowanie stwarza wiele możliwości aplikacyjnych, chociażby w telefonii komórkowej, skoro umożliwia ono generowanie trwałych precesji namagnesowania bez potrzeby przykładania zewnętrznego pola magnetycznego. Z drugiej strony powstanie takich precesji uniemożliwia przełączenie kierunku namagnesowania warstwy swobodnej za pomocą prądu stałego. Dlatego w dysertacji badano możliwość przełączania takiego układu za pomocą prostokątnego impulsu prądu [32, 51].

W związku z tym, za pomocą symulacji komputerowych wyznaczono czas potrzebny do przełączenia namagnesowania warstwy swobodnej w zależności od długości i natężenia impulsu prądu [rysunek 24(a)]. Wyniki te zostały porównane z analogiczną zależnością otrzymaną dla zwykłych zaworów spinowych [rysunek 22(a)]. W zaworach spinowych standardowych otrzymujemy przełączenie namagnesowania po przekroczeniu pewnej wartości krytycznej natężenia prądu i pewnej długości impulsu. Czas przełączenia maleje z natężeniem prądu. Natomiast w zaworach niestandardowych sytuacja jest bardziej skomplikowana. W dużej części badanego zakresu impulsów prądu przełączanie jest niestabilne (tj. mocno zależne od parametrów impulsu). Ponadto, czas przełączenia wydłuża się z długością zastosowanego impulsu. Dlatego do przełączenia zaworów niestandardowych zbadano inne alternatywne schematy. Pokazano, iż najkorzystniejszym z nich jest schemat przełączania za pomocą dwóch następujących po sobie impulsów prądu o przeciwnych kierunkach. Pierwszy z nich destabilizuje wektor namagnesowania z jego początkowej kolinearnej konfiguracji, natomiast drugi impuls stabilizuje namagnesowanie w jednej z konfiguracji kolinearnych. Symulacje komputerowe pokazały, że w przypadku przełączania z konfiguracji równoległej do antyrównoległej, przełączanie jest stabilniejsze i czas przełączania maleje [rysunek 26]. W przypadku skończonej temperatury schemat podwójnego impulsu prądu także zwiększa prawdopodobieństwo przełączania.

Podwójne niekolinearne zawory spinowe

W kolejnej części dysertacji badano podwójne zawory spinowe, $F_L/N_L/F_C/N_R/F_R$. Układy te złożone są z trzech warstw magnetycznych (F_L, F_C, F_R) oddzielonych warstwami niemagnetycznymi (N_L, N_R). Jak zostało pokazane przez Bergera [48], w takich układach akumulacja spinowa tworzy się na obu interfejsach warstwy środkowej. Ponadto, jeśli namagnesowania warstw zewnętrznych są unieruchomione i skierowane antyrównolegle, akumulacja spinowa indukowana prądem w warstwie środkowej jest kilkakrotnie większa niż w zwykłych zaworach spinowych z jedną warstwą umocowaną. W związku z tym, moment siły działajcy na magnetyzację warstwy środkowej jest wzmocniony, co prowadzi do redukcji prądu krytycznego indukującego dynamikę magnetyczną w warstwie swobodnej, oraz krótszych czasów przełączania namagnesowania. Wnioski te zostały także potwierdzone w ramach modelu transportu dyfuzyjnego w połączeniu z symulacjami dla modelu makrospinu (rysunki 28 i 29). Ponadto, jeśli magnetyzacje warstw zewnętrznych

w symetrycznym podwójnym zaworze spinowym skierowane są równolegle, moment siły działający na namagnesowanie warstwy środkowej znika.

W szczególności w dysertacji zbadano indukowany prądem moment siły oraz dynamikę magnetyczną w podwójnych zaworach spinowych w przypadku gdy namagnesowania warstw zewnętrznych są niekolinearne. Taką konfigurację magnetyczną można osiągnąć eksperymentalnie w strukturach asymetrycznych, w których warstwa F_R jest na antyferromagnetycznym podłożu. Jeśli taki układ zostanie podgrzany powyżej temperatury Neéla warstwy antyferromagnetycznej i następnie schłodzony w zewnętrznym polu magnetycznym, między namagnesowaniem warstwy F_R a strukturą antyferromagnetyku powstanie silne sprzężenie wymienne zgodne z kierunkiem pola zewnętrznego. Po wyłączeniu pola namagnesowanie warstwy F_R zostanie *umocowane* w tym kierunku. W ten sposób można uzyskać układ, w którym namagnesowanie warstwy F_R umocowane jest pod kątem $\Omega \in (0, \pi)$ względem łatwej osi warstwy F_L (patrz rysunek 27). Taki układ nazywamy *niekolinearnym podwójnym zaworem spinowym.*

Rysunek 30 pokazuje zależność kątową wielkości momentu siły działającego na warstwę środkową w układzie Co(20)/Cu(10)/Py(4)/Cu(4)/Co(10)/IrMn(8) w zależności od kąta Ω. Kąt θ mierzony jest względem namagnesowania warstwy F_L. Podczas gdy w przypadku $\Omega \sim \pi$ zależność kątowa ma kształt funkcji sinus, dla mniejszych kątów, $\Omega \sim 0$, zależność ta staje się falista, podobnie jak w przypadku niestandardowych zaworów spinowych. Takie zachowanie się momentu siły ma znaczny wpływ na dynamikę magnetyczną środkowej warstwy, pokazaną na rysunku 31. Dla $\Omega \gtrsim \pi/2$ otrzymujemy przełączanie magnetyczne dla prądów dodatnich. Natomiast w przypadku $\Omega \lesssim \pi/2$ dla prądów ujemnych otrzymuje się trwałą dynamikę magnetyczną, która związana jest z oscylacjami magnetooporu układu. Ponadto, za pomocą teorii stabilności równań różniczkowych [96, 97] otrzymano wzór na prąd krytyczny dla dowolnego kąta Ω, (8.10), który dobrze opisuje wyniki otrzymane przy pomocy symulacji komputerowych.

Podwójne zawory spinowe z prostopadłym polaryzatorem

Zawory spinowe z prostopadłym polaryzatorem zostały zaproponowane przez Kenta [42], który pokazał, że jeśli namagnesowanie warstwy umocowanej jest prostopadłe do płaszczyzny warstwy, prąd krytyczny potrzebny do przełączenia namagnesowania warstwy swobodnej jest mniejszy. Powodem tego jest powiększenie początkowego momentu siły działającego na namagnesowanie warstwy swobodnej, który jest maksymalny w przypadku gdy namagnesowania są do siebie prostopadłe. W rezultacie, dynamika magnetyczna układu różni się od dynamiki zwykłych zaworów spinowych z polaryzatorem namagnesowanym w płaszczyźnie warstwy. Mianowicie, wektor namagnesowania nie wykonuje początkowych precesji wokół punktu stałego, ale od razu zaczyna precesować wokół lokalnego pola rozmagnesowania. Takie zachowanie umożliwia przełączenie namagnesowania za pomocą krótkiego impulsu prądu już po jednej połowie okresu precesji.

W najprostszym przypadku, gdy zawór spinowy złożony jest tylko z jednego polaryzatora prostopadłego i jednej warswtwy swobodnej z łatwą osią w płaszczyźnie, magnetoopór w obu punktach stałych namagnesowania warstwy swobodnej jest taki sam, gdyż jego konfiguracja względem polaryzatora nie zmienia się. Dlatego należy dodać kolejną warstwę magnetyczną z namagnesowaniem umocowanym w płaszczyźnie, aby można zarejstrować zmiany w magnetooporze przy zmianie konfiguracji zaworu spinowego. W większości prac eksperymentalnych założono, że druga warstwa magnetyczna nie wpływa, poprzez indukowany prąd spinowy, na dynamikę magnetyczną w warstwie swobodnej. Z drugiej strony, w opublikowanej ostatnio pracy eksperymentalnej okazało

się, że obie umocowane warstwy mają istotny wpływ na dynamikę warstwy swobodnej [43]. Ponadto pokazano, że prawdopodobieństwo prełączenia warstwy swobodnej w zaworach spinowych podwójnych może osiągnąć nawet 100% gdy impuls prądu jest odpowiednio krótki (0.1 ns). Natomiast dla długich impulsów, prawdopodobieństwo przełączania jest mniejsze i czasy przełączania wydłużają się.

W pracy doktorskiej zbadano statyczne i dynamiczne właściwości podwójnych zaworów spinowych z jednym polaryzatorem z prostopadłym namagnesowaniem i drugim z namagnesowaniem w płaszczyźnie warstwy. Zbadano również zawór spinowy złożony tylko z polaryzatora porostopadłego i warstwy swobodnej. W jednym i drugim przypadku pokazano, że jeśli prąd płynący przez układ jest niezerowy, istnieją punkty stałe dynamiki namagnesowania warstwy swobodnej, w których wektor namagnesowania odchylony jest z płaszczyzny warstwy. Punkty te stają się stabilne jeśli natężenie prądu przekracza pewną krytyczną granicę. Natężenia krytyczne zostały obliczone w zakresie wartości pola zewnętrznego od $-400\,\mathrm{Oe}$ do $400\,\mathrm{Oe}$ za pomocą uogólnionej teorii rezonansu ferromagnetycznego [45]. Pokazano, że w zaworze spinowym posiadającym tylko polaryzator prostopadły prądy krytyczne są niezależne od pola zewnętrznego (rysunek 35), natomiast w obecności drugiego polaryzatora jeden z prądów krytycznych zależy od przyłożonego pola magnetycznego (rysunek 37). Zachowanie to związane jest ze zmianą symetrii punktów stałych, wywołaną przez drugą warstwę umocowaną (rysunek 38).

Zbadano także prawdopodobieństwo przełączania warstwy swobodnej w układzie z prostopadłym i zwykłym polaryzatorem. Symulacje makrospinowe pokazują, zgodnie z eksperymentem, że krótki impuls może prowadzić, nawet w wyższych temperaturach, do przełączania z prawdopodobieństwem 100 %. Okazuje się jednak, że prawdopodobieństwo przełączania zależy nie tylko od długości impulsu, ale także od natężenia prądu (rysunek 41). Dla dłuższych impulsów prawdopodobieństwo przełączania jest zredukowane z powodu istnienia punktów stałych poza płaszczyzną warstwy. Zbadano też wpływ dynamiki magnetycznej drugiego polaryzatora na prawdopodobieństwo przełączania warstwy swobodnej. Pokazano, że dynamika ta ma znaczenie w procesie przełączania i może zwiększyć jego prawdopodobieństwo, szczególnie w przypadku długich impulsów (rysunek 41).

Złożona warstwa swobodna ze sprzężeniem antyferromagnetycznym

Jednym z zagadnień w układach magnetycznych nanoskopowych jest zabezpieczenie stabilności termicznej warstwy swobodnej. Wielkość, która opisuje stabilność termiczną, Δ_0, zdefiniowana jest jako stosunek bariery energetycznej między konfiguracjami stałymi warstwy swobodnej i energii termicnej ($k_\mathrm{B}T$). Aby informacja zapisana w konfiguracji magnetycznej zaworu spinowego pozostała niezmieniona przez co najmniej 10 lat, spelniony musi być warunek $\Delta_0 > 40$ [116]. Stąd, próbowano stosować w zaworach spinowych złożone warstwy swobodne, które są znane z wysokiej stabilności termicznej ($\Delta_0 \sim 100$). Chodzi o układy dwóch (lub wiecej) warstw magnetycznych oddzielonych cienkimi warstwami niemagnetycznymi (najczęściej Ruthenium), które są między sobą sprzężone oddziaływaniem wymiannym RKKY. Odziaływanie to może być, w zależności od grubości warstwy niemagnetycznej, ferromagnetyczne lub antyferromagnetyczne [9, 10]. W pracy tej badano w szczególności warstwy ze sprzężeniem antyferromagnetycznym. Jeśli obie warstwy magnetyczne są identyczne, całkowity moment magnetyczny takiego układu jest zerowy i układ nazywa się *antyferromagnetykiem syntetycznym*. Natomiast jeśli warstwy magnetyczne się różnią, układ nazywamy *ferrimagnetykiem syntetycznym*.

Najpierw zbadany został moment siły działający na obie warstwy złożonej warstwy swobodnej. W teorii transportu dyfuzyjnego momenty siły zdefiniowane są wzorami (11.4). Ponieważ w tym przypadku warstwa swobodna złożona jest z dwóch warstw magnetycznych, jej dynamika opisana jest dwoma równaniami Landaua-Lifshitza-Gilberta, które są wzajemnie sprzężone poprzez pole efektywne oraz momenty siły. Równania te zostały następnie rozwiązane numerycznie przy różnych wartościach zewnętrznego pola magnetycznego, H_{ext}, oraz natężenia prądu, zarówno dla układu z antyferromagnetykiem (rysunek 46) jak i ferrimagnetykiem (rysunek 47) syntetycznym. Symulacje pokazały, że dla obu badanych układów prąd krytyczny zależy niemonotonicznie od pola zewnętrznego. Okazuje się, że dla pewnej wartości pola zewnętrznego, H_0, prąd krytyczny osiąga maksimum. Ponadto, pokazano, że mechanizm przełączania warstwy złożonej różni się dla wartości pól poniżej i powyżej wartości H_0. Dla $H_{\text{ext}} < H_0$ przełączenie następuje poprzez precesje poza płaszczyzną warstwy i konfiguracia magnetyczna warstwy swobodnej mocno odchyla się od początkowej konfiguracji antyrównoległej. Natomiast dla $H_{\text{ext}} > H_0$ warstwa swobodna przełącza sie poprzez precesje w płaszczyźnie warstwy i zachowuje konfigurację antyrównoległą.

Podczas gdy antyferromagnetyk syntetyczny nie wykazuje stałej dynamiki indukowanej prądem, ferrimagnetyk syntetyczny wykazuje dynamikę precesyjną dla wysokich natężeń prądu. W przypadku ferrimagnetyka syntetycznego pokazano, że częstość precesji magnetooporu zaworu spinowego zależy od pola zewnętrznego oraz natężenia prądu. Dla $H_{\text{ext}} < H_0$ obserwuje się skomplikowaną wzajemną dynamikę obu namagnesowań i częstotliwość zmian oporu rośnie z natężeniem prądu. Natomiast w przypadku $H_{\text{ext}} > H_0$ obserwujemy proste precesje w obu warstwach magnetycznych i zmniejszenie częstości zmian oporu z prądem.

Magnetotransport nieliniowy w podwójnych zaworach spinowych

W kolejnej części pracy rozważane są podstawowe własności transportu spinowego przez układy wielowarstwowe metaliczne oraz ich magnetoopór. Jak już wspomniano, jeśli namagnesowania warstw zewnętrznych w zaworach spinowych podwójnych skierowane są antyrównoległe, akumulacja spinowa w warstwie środkowej może być kilka razy więsza niż w zwykłych zaworach spinowych. W eksperymencie [49] pokazano, że zwiększona akumulacjia spinowa może mieć znaczący wpływ na magnetoopór układu. Okazuje się mianowicie, że jeśli prąd płynie przez zawór spinowy w pewnym kierunku i namagnesowanie warstwy środkowej zostanie odwrócone (przy pomocy pola magnetycznego), całkowity opór układu spada. Natomiast jeśli prąd płynie w kierunku przeciwnym, magnetoopor układu przy takim samym odwróceniu namagnesowania warstwy środkowej wzrasta. Ponadto pokazano, że zmiany oporu zależą od natężenia prądu. Efekt ten został zaobserwowany w przypadku, gdy warstwa środkowa była wystarczająco cienka ($\sim 1\,\text{nm}$). Wpływ indukowanego prądem momentu siły oraz grzania się układu na wyniki eksperymentalne został wykluczony [49].

Zarówno model Valeta-Ferta, jak i uogólniony model niekolinearnego transportu dyfuzyjnego nie opisują zjawiska nieliniowego magnetooporu. Oba te modele zakładają, że magnetoopór jest niezależny od kierunku oraz natężenia przepływającego prądu. Stąd, drugi ze wspopmnianych modeli został rozszerzony w niniejszej pracy o efekty magnetotransportu nieliniowego. Założono mianowicie, że akumulacja spinowa indukowana w warstwie środkowej powoduje przesunięcie poziomu Fermiego. Ponieważ w metalach przejściowych i ich stopach gęstość stanów silnie zależy od energii, nawet mała zmiana akumulacji spinowej może spowodować dużą zmianę w gęstości stanów. W konsekwencji, parametry objętościowe (ρ^* i β) warstwy środkowej, oraz parametry jej

interfejsów (R^* i γ) mogą być zależne od akumulacji spinowej, która jest proporcionalna do natężenia prądu. W przybliżeniu liniowym, dla objętościowych parametrów warstwy środkowej zależności te są podane wzorami (12.2) i (12.4), gdzie q i ξ to parametry fenomenologiczne, które mogą być oszacowane dla konkretnego układu. Podobnie można opisać zmianę parametrów interfejsowych. Dane jest to wzorami (12.7) z nowymi parametrami fenomenologicznymi, q' i ξ'.

Zaproponowany model został następnie przebadany numerycznie dla symetrycznego i niesymetrycznego zaworu spinowego, podobnego do tego, który był badany eksperymentalnie [49]. Ponieważ w stosowanym modelu transportu dyfuzyjnego akumulacja spinowa zależy od parametrów materiałowych a parametery materiałowe zależą od akumulacji spinowej, obliczenia te zostały przeprowadzone samozgodnie. Wpływ parametrów objętościowych i interfejsowych na magnetoopór zbadany został oddzielnie. Pokazano, że zmiany jednej i drugiej pary parametrów prowadzą do podobych zachowań magnetooporu, które są także zgodne z eksperymentem [49] (rysunki 51 i 53). Z drugiej strony, przy zmianie parametrów objętościowych i interfesjsowych, zmiany magnetooporu, ΔR, obserwowane przy zmianie kierunku namagnesowania warstwy środkowej, różnią się symetrią znaku. Podczas gdy w przypadku zmian parametrów interfejsowych, dla małych wartości q' i ξ', ΔR zmienia znak symetrycznie ze zmianą kierunku prądu [rysunek 53(e)], w przypadku zmian parametrów objętościowych zmiana znaku ΔR jest zawsze niesymetryczna [rysunek 51(e)]. Jeśli porównamy te wyniki z eksperymentem [49], to okazuje się, że zależność parametrów interfejsowych jest bardziej istotna dla obserwowanego efektu. Ten wniosek został potwierdzony także w kolejnym eksperymencie [50].

Indukowany prądem moment siły w szerokiej ściance domenowej Neela

Do tej pory zajmowaliśmy się obiektami, w których momenty magnetyczne były oddzielone od siebie warstwami niemagnetycznymi. Wiadomo jednak, że moment siły indukowany prądem powstaje także w układach z niejednorodnym namagnesowaniem, na przykład w niejednorodnych cienkich warstwach magnetycznych lub nanodrutach. Eksperymentalnie zaobserwowano, że jeśli prąd elekryczny płynie w płaszczyźnie warstwy, ścianka domenowa ulega przesunięciu w kierunku strumienia elektronów. Powodem tego zjawiska jest oddziaływanie wymienne między elektronami przewodnictwa i zlokalizowanymi momentami magnetycznymi. Elektrony przewodnictwa polaryzują się według lokalnego namagnesowania i składowe poprzeczne ich momentu pędu zostają zamienione na moment siły zmieniający kierunek lokalnego namagnesowania. Teoretyczny opis tego zjawiska został podany przez Lee i Zhang'a [130], którzy pokazali, że działający moment siły ma dwie składowe. Pierwsza z nich działa w kierunku płynącego prądu i nazywa się składową *adiabatyczną*. Druga z nich jest prostopadła do adiabatycznej składowej i nazywa się składową *nieadiabatyczną*, ponieważ pojawia się ona jako skutek nieadiabatycznych procesów relaksacji spinowej. Stosunek wielkości składowej adiabatycznej do wielkości składowej nieadiabatycznej oznacza się β i nazywa się *nieadiabatycznością*. Wartość ta przyjmuje wartości rzędu $\beta \sim 10^{-2}$.

W ostatnej części niniejszej pracy doktorskiej zaprezentowano podejście do obliczenia momentu siły działającego na szeroką ściankę domenową typu Neela, pokazaną schematycznie na rysunku 55. Elektrony przewodnictwa zostały opisane za pomocą jednocząstowego Hamiltonianu H_0 (13.7) zawierającego oddziaływania wymianne z momentami magnetycznymi, których kierunek dany jest przez wektor namagnesowania $\mathbf{n}$. Następnie skorzystano z transformacji unitarnej (13.11), za pomocą której otrzymano Hamiltoniam (13.15). Wpływ pola elektrycznego opisanego został za pomocą Hamiltonianu (13.20), który potraktowano jako małe zaburzenie Hamiltonianu H_0.

W ramach teorii liniowej odpowiedzi obliczono indukowaną prądem gęstość spinową (13.21), za pomocą której zdefiniowano składowe momentu siły działającego na sciankę domenową (13.37). Wielkości tych składowych są proporcjonalne do parametrów a i b (13.38), które zostały wyrażone za pomocą stałej wymiany J, wektorów falowych na poziomie Fermiego oraz czasów relaksacji spinu. Parametr a złożony jest z dwóch członów, $a = a_0 + a_1$. Człon a_0, który jest proporcionalny do polaryzacji (P), był zaproponowany już wcześniej przez Lee i Zhang'a [130]. Człon a_1 wprowadza poprawkę do momentu siły, zależną od relaksacji spinowej. Uzyskane wyrażenia analityczne zostały zobrazowane numerycznie.

Rysunek 56 pokazuje zależność parametrów a i b od stałej sprzężenia, J (w stosunku do potenciału elektrochemicznego μ). Oba parametry zmieniają się liniowo z J. Podczas gdy skladowa adiabatyczna momentu siły rośnie z parametrem J, silniejsze sprzężenie tłumi procesy nieadiabatyczne, w związku z czym parametr b maleje. Rysunek 58 pokazuje rozkład składowych momentu siły w ściance domenowej. Obie składowe osiągają maksimum w środku ścianki i maleją z odleglością od środka. Na rysunku 58 pokazano zależność parametru nieadiabatyczności, β, który maleje z rosnącą stałą J. Pokazano ponadto zależność stosunku parametru a_1 do a_0. Stosunek ten jest mniejszy od β i w zależności od J maleje szybko do zera. W końcu pokazano, że rozpraszanie momentu pędu elektronu może spowodować powiększenie działającego momentu siły. Powodem tego jest to, że w wyniku rozproszeń elektron spędza więcej czasu w ściance domenowej, co powiększa szanse przełączenia spinu elektronu.

Podsumowanie

W niniejszej pracy rozważono problematykę indukowanej prądem dynamiki magnetycznej. Zbadano wielowarstwowe układy metaliczne w przybliżeniu dyfuzyjnego transportu spinowego. Za pomocą symulacji numerycznych zbadano wpływ wzajemnych oddziaływań kilku warstw magnetycznych. Wyniki były dyskutowane także z punktu widzenia możliwych zastosowań badanych układów. Ponadto zbadano podstawowe własności transportu spinowego, w szczególności nieliniowy magnetotransport w podwójnych zaworach spinowych, oraz indukowany prądem moment siły w ściance domenowej typu Neela.

List of publications

1. P. Baláž, and J. Barnaś,
   Current-induced dynamics of composite free layer with antiferromagnetic interlayer exchange coupling,
   Physical Review B **83**, 104422 1-10 (2011)

2. P. Baláž, J. Barnaś,
   Nonlinear magnetotransport in dual spin valves,
   Physical Review B **82**, 104430 1-6 (2010)

3. E. Jaromirska, P. Baláž, L. López Díaz, J. Barnaś,
   Computational study of microwave oscillations in nonstandard spin valves in the diffusive transport limit,
   Physical Review B **81**, 014408 1-9 (2010)

4. E. Jaromirska, P. Baláž, L. López Díaz, J. Barnaś,
   Magnetization dynamics in nanopillars in the diffusive transport regime: Macrospin versus micromagnetic analysis,
   Journal of Applied Physics **106**, 113909 1-5 (2009)

5. P. Baláž, M. Gmitra, J. Barnaś,
   Current-induced dynamics in noncollinear dual spin valves,
   Physical Review B **80**, 174404 1-6 (2009)

6. P. Baláž, M. Gmitra, J. Barnaś,
   Current-pulse-induced magnetic switching in standard and nonstandard spin-valves: Theory and numerical analysis,
   Physical Review B **79**, 144301 1-7 (2009)

7. P. Baláž, M. Gmitra, J. Barnaś,
   Current-pulse-induced switching in asymmetric spin valve,
   Acta Physica Polonica A **115**, 278-280 (2009)

References

[1] Walther Gerlach and Otto Stern. Das magnetische moment des silberatoms. *Zeitschrift für Physik A Hadrons and Nuclei*, 9:353–355, 1922.

[2] G. E. Uhlenbeck and S. Goudsmit. *Naturwissenschaften*, 47:953, 1925.

[3] N. F. Mott. The electrical conductivity of transition metals. *Proc. R. Soc.*, 153:699, 1936.

[4] N. F. Mott. Electrons in transition metals. *Adv. Phys*, 13:325, 1964.

[5] A. Fert and I. A. Campbell. Electrical resistivity of ferromagnetic nickel and iron based alloys. *J. Phys. F: Metal Physics*, 6(5):849, 1976.

[6] M. Julliere. Tunneling between ferromagnetic films. *Phys. Lett. A*, 54(3):225 – 226, 1975.

[7] N. M. Baibich, J. M. Broto, A. Fert, F. Nguyen Van Dau and. F. Petroff, P. Eitenne, G. Creuzer, A. Friederich, and J. Chazelas. Giant magnetoresistance of (001)fe/(001)cr magnetic superlattices. *Phys. Rev. Lett.*, 61:2472, 1988.

[8] G. Binasch, P. Grunberg, F. Saurenbach, and W. Zinn. Enhanced magnetoresistance in layered magnetic-structures with antiferromagnetic interlayer exchange. *Phys. Rev. B*, 39:4828, 1989.

[9] S. S. P. Parkin, N. More, and K. P. Roche. Oscillations in exchange coupling and magnetoresistance in metallic superlattice structures: Co/ru, co/cr, and fe/cr. *Phys. Rev. Lett.*, 64(19):2304–2307, 1990.

[10] S. S. P. Parkin and D. Mauri. Spin engineering: Direct determination of the ruderman-kittel-kasuya-yosida far-field range function in ruthenium. *Phys. Rev. B*, 44(13):7131, 1991.

[11] J. Mathon. Phenomenological theory of giant magnetoresistance. In Michael Ziese and Martin Thornton, editors, *Spin Electronics*, volume 569 of *Lecture Notes in Physics*, pages 71–88. Springer Berlin / Heidelberg, 2001.

[12] W. P. Pratt, S.-F. Lee, J. M. Slaughter, R. Loloee, P. A. Schroeder, and J. Bass. Perpendicular giant magnetoresistances of ag/co multilayers. *Phys. Rev. Lett.*, 66(23):3060–3063, 1991.

[13] M. A. M. Gijs, S. K. J. Lenczowski, and J. B. Giesbers. Perpendicular giant magnetoresistance of microstructured fe/cr magnetic multilayers from 4.2 to 300 k. *Phys. Rev. Lett.*, 70(21):3343–3346, 1993.

[14] R. E. Camley and J. Barnaś. Theory of giant magnetoresistance effects in magnetic layered structures with antiferromagnetic coupling. *Phys. Rev. Lett.*, 63(6):664–667, 1989.

[15] J. Barnaś, A. Fuss, R. E. Camley, P. Grünberg, and W. Zinn. Novel magnetoresistance effect in layered magnetic structures: Theory and experiment. *Phys. Rev. B*, 42(13):8110–8120, 1990.

[16] T. Valet and A. Fert. *Phys. Rev. B*, 48:7099, 1993.

[17] Shufeng Zhang and Peter M. Levy. Conductivity perpendicular to the plane of multilayered structures. *J. Appl. Phys.*, 69(8):4786–4788, 1991.

[18] Peter M. Levy and Shufeng Zhang. Our current understanding of giant magnetoresistance in transition-metal multilayers. *J. Magn. Magn. Mater.*, 151(3):315 – 323, 1995.

[19] X.-G. Zhang and W. H. Butler. Conductivity of metallic films and multilayers. *Phys. Rev. B*, 51(15):10085–10103, 1995.

[20] P. Zahn, I. Mertig, M. Richter, and H. Eschrig. Ab initio calculations of the giant magnetoresistance. *Phys. Rev. Lett.*, 75(16):2996–2999, 1995.

[21] M. A. M. Gijs and G. E. W. Bauer. Perpendicular giant magnetoresistance of magnetic multilayers. *Adv. Phys.*, pages 285–445, 1997.

[22] A. G. Aronov. Spin injection in metals and polarization of nuclei. *JETP Lett.*, 24:32, 1976.

[23] Mark Johnson and R. H. Silsbee. Interfacial charge-spin coupling: Injection and detection of spin magnetization in metals. *Phys. Rev. Lett.*, 55(17):1790–1793, 1985.

[24] M. Johnson and R. H. Silsbee. Spin-injection experiment. *Phys. Rev. B*, 37:5326, 1988.

[25] J. C. Slonczewski. Current-driven excitation of magnetic multilayers. *J. Magn. Magn. Mater.*, 159:L1–L7, 1996.

[26] L. Berger. Emission of spin waves by a magnetic multilayer traversed by a current. *Phys. Rev. B*, 54:9353–9358, 1996.

[27] M. Tsoi, A. G. M. Jansen, J. Bass, W.-C. Chiang, M. Seck, V. Tsoi, and P. Wyder. Excitation of a magnetic multilayer by an electric current. 80:4281–4284, 1998.

[28] J. A. Katine, F. J. Albert, R. A. Buhrman, E. B. Myers, and D. C. Ralph. Current-driven magnetization reversal and spin-wave excitations in Co/Cu/Co pillars. *Phys. Rev. Lett.*, 84:3149–3152, 2000.

[29] S. Serrano-Guisan, K. Rott, G. Reiss, J. Langer, B. Ocker, and H. W. Schumacher. Biased quasiballistic spin torque magnetization reversal. *Phys. Rev. Lett.*, 101(8):087201, 2008.

[30] Dmitri E. Nikonov, George I. Bourianoff, Graham Rowlands, and Ilya N. Krivorotov. Strategies and tolerances of spin transfer torque switching. *J. Appl. Phys.*, 107:113910, 2010.

[31] Luqiao Liu, Takahiro Moriyama, D. C. Ralph, and R. A. Buhrman. Reduction of the spin-torque critical current by partially canceling the free layer demagnetization field. *Appl. Phys. Lett.*, 94:122508, 2009.

[32] P. Baláž, M. Gmitra, and J. Barnaś. Current-pulse-induced magnetic switching in standard and nonstandard spin-valves: Theory and numerical analysis. *Phys. Rev. B*, 79:144301, 2009.

[33] J. Barnaś, A. Fert, M. Gmitra, I. Weymann, and V. K. Dugaev. From giant magnetoresistance to current-induced switching by spin transfer. *Phys. Rev. B*, 72:024426, 2005.

[34] M. Gmitra and J. Barnaś. Spin-transfer and current-induced dynamics in spin valves: Diffusive transport regime. In Zhiming Wang, editor, *Toward Functional Nanomaterials*, pages 285 – 322. Springer, 2009.

[35] M. Gmitra and J. Barnaś. Current-induced dynamics in asymmetric spin-valves. *Appl. Phys. Lett.*, 89:223121, 2006.

[36] M. Gmitra and J. Barnaś. Current-driven destabilization of both collinear configurations in asymmetric spin valves. *Phys. Rev. Lett.*, 96:207205, 2006.

[37] M. Gmitra and J. Barnaś. Thermally assisted current-driven bistable precessional regimes in asymmetric spin valves. *Phys. Rev. Lett.*, 99:097205, 2007.

[38] E. Jaromirska, P. Baláž, L. López Díaz, and J. Barnaś. Computational study of microwave oscillations in nonstandard spin valves in the diffusive transport limit. *Phys. Rev. B*, 81(1):014408, 2010.

[39] E. Jaromirska, P. Baláž, L. López Díaz, and J. Barnaś. Magnetization dynamics in nanopillars in the diffusive transport regime: Macrospin versus micromagnetic analysis. *J. Appl. Phys.*, 106(11):113909, 2009.

[40] O. Boulle, V. Cros, J. Grollier, L. G. Pereira, C. Deranlot, F. Petroff, G. Faini, J. Barnaś, and A. Fert. Shaped angular dependence of the spin-transfer torque and microwave generation without magnetic field. *Nature Phys.*, 3:492–497, 2007.

[41] O. Boulle, V. Cros, J. Grollier, L. G. Pereira, C. Deranlot, F. Petroff, G. Faini, J. Barnaś, and A. Fert. Microwave excitations associated with a wavy angular dependence of the spin transfer torque: Model and experiments. *Phys. Rev. B*, 77:174403, 2008.

[42] A. D. Kent, B. Özyilmaz, and E. del Barco. Spin-transfer-induced precessional magnetization reversal. *Appl. Phys. Lett.*, 84(19):3897–3899, 2004.

[43] O. J. Lee, V. S. Pribiag, P. M. Braganca, P. G. Gowtham, D. C. Ralph, and R. A. Buhrman. Ultrafast switching of a nanomagnet by a combined out-of-plane and in-plane polarized spin current pulse. *Appl. Phys. Lett.*, 95(1):012506, 2009.

[44] D. Houssameddine, U. Ebels, B. Delaët, B. Rodmacq, I. Firastrau, F. Ponthenier, M. Brunet, C. Thirion, J.-P. Michel, L. Prejbeanu-Buda, M.-C. Cyrille, O. Redon, and B. Dieny. Spin-torque oscillator using a perpendicular polarizer and a planar free layer. *Nature Mater.*, pages 447 – 453, 2007.

[45] U. Ebels, D. Houssameddine, I. Firastrau, D. Gusakova, C. Thirion, B. Dieny, and L. D. Buda-Prejbeanu. Macrospin description of the perpendicular polarize-planar free layer spin-torque oscillator. *Phys. Rev. B*, 78:024436, 2008.

[46] K. J. Lee, O. Redon, and B. Dieny. Analytical investigation of spin-transfer dynamics using a perpendicular-to-plane polarizer. *Appl. Phys. Lett.*, 86(2):022505, 2005.

[47] P.-B. He, R.-X. Wang, Z.-D. Li, Q.-H. Liu, A.-L. Pan, Y.-G. Wang, and B.-S. Zou. Current-driven magnetization dynamics in magnetic trilayers with a tilted spin polarizer. *Eur. Phys. J. B*, 73(3):417–421, 2010.

[48] L. Berger. Multilayer configuration for experiments of spin precession induced by a dc current. *J. Appl. Phys.*, 93:7693, 2003.

[49] A. Aziz, O. P. Wessely, M. Ali, D. M. Edwards, C. H. Marrows, B. J. Hickey, and M. G. Blamire. Nonlinear giant magnetoresistance in dual spin valves. *Phys. Rev. Lett.*, 103:237203, 2009.

[50] N. Banerjee, A. Aziz, M. Ali, J. W. A. Robinson, B. J. Hickey, and M. G. Blamire. Thickness dependence and the role of spin transfer torque in nonlinear giant magnetoresistance of permalloy dual spin valves. *Phys. Rev. B*, 82(22):224402, 2010.

[51] P. Baláž, M. Gmitra, and J. Barnaś. Current-pulse-induced switching in asymmetric spin valve. *Acta Physica Polonica*, A115(1):278, 2009.

[52] P. Baláž, M. Gmitra, and J. Barnaś. Current-induced dynamics in non-collinear dual spin-valves. *Phys. Rev. B*, 80:174404, 2009.

[53] P. Baláž and J. Barnaś. Current-induced dynamics of composite free layer with antiferromagnetic interlayer exchange coupling. *Phys. Rev. B*, 83(10):104422, 2011.

[54] P. Baláž and J. Barnaś. Nonlinear magnetotransport in dual spin valves. *Phys. Rev. B*, 82(10):104430, 2010.

[55] A. Brataas, Yu.V. Nazarov, and G.E.W. Bauer. Spin-transport in multi-terminal normal metal-ferromagnet systems with non-collinear magnetizations. *Eur. Phys. J. B*, 22:99–110, 2001.

[56] K. Xia, P. J. Kelly, G. E. W. Bauer, A. Brataas, and I. Turek. Spin torques in ferromagnetic/normal-metal structures. *Phys. Rev. B*, 65(220401), 2002.

[57] J Bass and W P Pratt Jr. Spin-diffusion lengths in metals and alloys, and spin-flipping at metal/metal interfaces: an experimentalist's critical review. *J. Phys.: Cond. Matt.*, 19(18):183201, 2007.

[58] Sergei Urazhdin. Dynamical coupling between ferromagnets due to spin transfer torque: Analytical calculations and numerical simulations. *Phys. Rev. B*, 78(6):060405(R), Aug 2008.

[59] D. Gusakova, D. Houssameddine, U. Ebels, B. Dieny, L. Buda-Prejbeanu, M. C. Cyrille, and B. Delaët. Spin-polarized current-induced excitations in a coupled magnetic layer system. *Phys. Rev. B*, 79(10):104406, 2009.

[60] D. Houssameddine, J. F. Sierra, D. Gusakova, B. Delaet, U. Ebels, L. D. Buda-Prejbeanu, M.-C. Cyrille, B. Dieny, B. Ocker, J. Langer, and W. Maas. Spin torque driven excitations in a synthetic antiferromagnet. *Appl. Phys. Lett.*, 96(7):072511, 2010.

[61] M. Gmitra and J. Barnaś. Correlation of the angular dependence of spin-transfer torque and giant magnetoresistance in the limit of diffusive transport in spin valves. *Phys. Rev. B*, 79:012403, 2009.

[62] A. Aharoni. *Introduction to the Theory of Ferromagnetism.* Oxford Science, Oxford, 1996.

[63] B. D. Cullity and C. D. Graham. *Introduction to magnetic materials.* Willey-IEEE, 2005.

[64] K. H. J. Buschow and Frank R. Boer. *Physics of magnetism and magnetic materials.* Springer, 2003.

[65] W. F. Brown. *Magnetostatic principles in ferromagnetism.* Wiley-Interscience, 1962.

[66] A. J. Newell, W. Williams, and D. J. Dunlop. A generalization of the demagnetization tensor for nonuniform magnetization. *J. Geophys. Res.*, 98:9551, 1993.

[67] J. D. Jackson. *Classical Electrodynamics.* Wiley, 1999.

[68] P. Grünberg, R. Schreiber, Y. Pang, M. B. Brodsky, and H. Sowers. Layered magnetic structures: Evidence for antiferromagnetic coupling of fe layers across cr interlayers. *Phys. Rev. Lett.*, 57(19):2442–2445, 1986.

[69] P. Bruno. Theory of interlayer magnetic coupling. *Phys. Rev. B*, 52(1):411–439, 1995.

[70] M. A. Ruderman and C. Kittel. Indirect exchange coupling of nuclear magnetic moments by conduction electrons. *Phys. Rev.*, 96(1):99, 1954.

[71] T. Kasuya. *Prog. Theor. Phys.*, 16:45, 1956.

[72] Kei Yosida. Magnetic properties of cu-mn alloys. *Phys. Rev.*, 106(5):893–898, 1957.

[73] Y. Yafet. Ruderman-kittel-kasuya-yosida range function of a one-dimensional free-electron gas. *Phys. Rev. B*, 36(7):3948–3949, 1987.

[74] P. Bruno and C. Chappert. Oscillatory coupling between ferromagnetic layers separated by a nonmagnetic metal spacer. *Phys. Rev. Lett.*, 67(12):1602–1605, 1991.

[75] W. H. Meiklejohn and C. P. Bean. New magnetic anisotropy. *Phys. Rev.*, 105(3):904–913, 1957.

[76] A. E. Berkowitz and K. Takano. Exchange anisotropy: a review. *J. Magn. Magn. Mater.*, 200:553, 1999.

[77] P. A. M. Dirac. *The Principles of Quantum Mechanics.* Oxford University Press, London, 1958.

[78] M. d'Aquino. *Nonlinear Magnetization Dynamics in Thin-films and Nanoparticles.* PhD thesis, Università degli studi di Napoli, Facoltà di Ingegneria, 2004.

[79] L. D. Landau and L. M. Lifshitz. On the theory of the dispersion of magnetic permeability in ferromagnetic bodies. *Physik. Zeits. Sowjetunion*, 8:153, 1935.

[80] T. L. Gilbert. A lagrangian formulation of the gyromagnetic equation of the magnetization field. *Phys. Rev.*, 100:1243, 1955.

[81] T. L. Gilbert. A phenomenological theory of damping in ferromagnetic materials. *IEEE Trans. Magn.*, 40:3443, 2004.

[82] P. Podio-Guidugli. On dissipation mechanisms in micromagnetics. *Eur. Phys. J. B*, 19(3):417–424, 2001.

[83] R. Kikuchi. On the minimum of magnetization reversal time. *J. Appl. Phys.*, 23:1352, 1956.

[84] J. Mallinson. On damped gyromagnetic precession. *IEEE Trans. Magn.*, 23:2003, 1987.

[85] M. D. Stiles, W. M. Saslow, M. J. Donahue, and A. Zangwill. Adiabatic domain wall motion and landau-lifshitz damping. *Phys. Rev. B*, 75(21):214423, 2007.

[86] T. Schrefl W. Scholz and J. Fidler. Micromagnetic simulation of thermally activated switching in fine particles. *J. Magn. Magn. Mater.*, 233:296, 2001.

[87] W. Scholz. Micromagnetic simulation of thermally activated switching in fine particles. Master's thesis, Institut für Angewandte und Technische Physik der Technischen Universität Wien, 1999.

[88] W. F. Brown. Thermal fluctuations of a single-domain particle. *Phys. Rev.*, 130:1677, 1963.

[89] H. Risken. *The Fokker-Planck Equation. Methods of Solution and Applications.* Springer, 1989.

[90] J. Z. Sun and D. C. Ralph. Magnetoresistance and spin-transfer torque in magnetic tunnel junction. *J. Magn. Magn. Mater.*, 320:1227, 2008.

[91] P. Ogrodnik, M. Wilczyński, R. Świrkowicz, and J. Barnaś. Spin transfer torque and magnetic dynamics in tunnel junctions. *Phys. Rev. B*, 82:134412, 2010.

[92] J. Xiao, A. Zangwill, and M. D. Stiles. Macrospin models of spin transfer dynamics. *Phys. Rev. B*, 72:014446, 2005.

[93] M. D. Stiles and A. Zangwill. Anatomy of spin-transfer torque. *Phys. Rev. B*, 66:014407, 2002.

[94] Z. Li and S. Zhang. Thermally assisted magnetization reversal in the presence of a spin-transfer torque. *Phys. Rev. B*, 69:134416, 2004.

[95] E. C. Stoner and E. P. Wohlfarth. A mechanism of magnetic hysteresis in heterogeneous alloys. *Phil. Trans. R. Soc. A*, 240:599–642, 1948.

[96] S. Wiggins. *Introduction to Applied Nonlinear dynamical Systems and Chaos.* Springer-Verlag, 1990.

[97] Ya. B. Bazaliy, B. A. Jones, and S.-Ch. Zhang. Current-induced magnetization switching in small domains of different anisotropies. *Phys. Rev. B*, 69:094421, 2004.

[98] Inti Sodemann and Ya. B. Bazaliy. Two scenarios of spin-transfer switching and criteria for the corresponding threshold currents. *Phys. Rev. B*, 84:064422, 2011.

[99] L. Baselgia, M. Warden, F. Waldner, Stuart L. Hutton, John E. Drumheller, Y. Q. He, P. E. Wigen, and M. Maryško. Derivation of the resonance frequency from the free energy of ferromagnets. *Phys. Rev. B*, 38(4):2237–2242, 1988.

[100] R. H. Koch, J. A. Katine, and J. Z. Sun. Time-resolved reversal of spin-transfer switching in a nanomagnet. *Phys. Rev. Lett.*, 92:088302, 2004.

[101] J.Z. Sun. Spin-current interaction with a monodomain magnetic body: A model study. *Phys. Rev. B*, 62(570), 2000.

[102] Tomohiro Taniguchi and Hiroshi Imamura. Thermally assisted spin transfer torque switching in synthetic free layers. *Phys. Rev. B*, 83:054432, 2011.

[103] E. B. Myers, D. C. Ralph, J. A. Katine, R. N. Louie, and R. A. Buhrman. Current-induced switching of domains in magnetic multilayer devices. *Science*, 285:867–870, 1999.

[104] S. I. Kiselev, J. C. Sankey, I. N. Krivorotov, N. C. Emley, R. J. Schoelkopf, R. A. Buhrman, and D. C. Ralph. Microwave oscillations of a nanomagnet driven by a spin-polarized current. *Nature*, 425:380–383, 2003.

[105] A. A. Kovalev, A. Brataas, and G. E. W. Bauer. Spin transfer in diffusive ferromagnet–normal metal systems with spin-flip scattering. *Phys. Rev. B*, 66:224424, 2002.

[106] J. L. Gargía-Palacios and F. J. Lázaro. Langevin-dynamics study of the dynamical properties of small magnetic particles. *Phys. Rev. B*, 58:14937, 1998.

[107] P. E. Kloeden and E. Platen. *Numerical Solution of Stochastic Differential Equations*. Springer-Verlag, 1992.

[108] S. W. Roberts. Control chart tests based on geometric moving averages. *Technometrics*, 42:97–101, 2000.

[109] G. E. W. Bauer, Y. Tserkovnyak, D. Huertas-Hernando, and A. Brataas. Universal angular magnetoresistance and spin torque in ferromagnetic/normal metal hybrids. *Phys. Rev. B*, 67:094421, 2003.

[110] S. Urazhdin, R. Loloee, and Jr. W. P. Pratt. *Phys. Rev. B*, 71:104430, 2005.

[111] M. Bauer, B. Fassbender, J. andl Hillebrands, and R. L. Stamps. Switching behavior of a stoner particle beyond the relaxation time limit. *Phys. Rev. B*, 61:3410, 2000.

[112] S. Kaka and S. E. Russek. Precessional switching of submicrometer spin valves. *Appl. Phys. Lett.*, 80:2958, 2002.

[113] B. Szymanski, F. Stobiecki, and M. Urbaniak. Gmr spin valve with alternating in-plane and out-of-plane magnetic anisotropy. *J. Alloys and Compounds*, 423:236 – 239, 2006.

[114] B. Szymanski, P. Mazalski, M. Urbaniak, F. Stobiecki, A. Maziewski, S. Pizzini, and F. MacCherozzi. Domain structure in (nife/au/co/au)10 multilayers with perpendicular anisotropy of co layers. *IEEE Trans. Magn.*, 46:231–234, 2010.

[115] Sining Mao, Anthony Mack, Eric Singleton, Jian Chen, Song S. Xue, Hong Wang, Zheng Gao, Jin Li, and Ed Murdock. Thermally stable spin valve films with synthetic antiferromagnet pinned by nimn for recording heads beyond 20 gbit/in.[sup 2]. *J. Appl. Phys.*, 87:5720, 2000.

[116] Tomohiro Taniguchi and Hiroshi Imamura. Thermally assisted spin transfer torque switching in synthetic free layers. *Phys. Rev. B*, 83(5):054432, 2011.

[117] J. Hayakawa, S. Ikeda, K. Miura, M. Yamanouchi, Y. M. Lee, R. Sasaki, M. Ichimura, K. Ito, T. Kawahara, R. Takemura, T. Meguro, F. Matsukura, H. Takahashi, H. Matsuoka, and H. Ohno. Current-induced magnetization switching in mgo barrier magnetic tunnel junctions with cofeb-based synthetic ferrimagnetic free layers. *IEEE Trans. Magn.*, 44:1962, 2008.

[118] Satoshi Yakata, Hitoshi Kubota, Toru Sugano, Takayuki Seki, Kay Yakushiji, Akio Fukushima, Shinji Yuasa, and Koji Ando. Thermal stability and spin-transfer switchings in mgo-based magnetic tunnel junctions with ferromagnetically and antiferromagnetically coupled synthetic free layers. *Appl. Phys. Lett.*, 95(24):242504, 2009.

[119] S. Yakata, H. Kubota, T. Seki, K. Yakushiji, A. Fukushima, S. Yuasa, and K. Ando. Enhancement of thermal stability using ferromagnetically coupled synthetic free layers in mgo-based magnetic tunnel junctions. *IEEE Trans. Magn.*, 46:2232, 2010.

[120] Joo-Von Kim, T. Devolder, C. Chappert, C. Maufront, and R. Fournel. Precession-dominated switching of synthetic antiferromagnets. *Appl. Phys. Lett.*, 85:4094, 2004.

[121] T. Ochiai, Y. Jiang, A. Hirohata, N. Tezuka, S. Sugimoto, and K. Inomata. Distinctive current-induced magnetization switching in a current-perpendicular-to-plane giant-magnetoresistance nanopillar with a synthetic antiferromagnet free layer. *Appl. Phys. Lett.*, 86(24):242506, 2005.

[122] Cheng-Tyng Yen, Wei-Chuan Chen, Ding-Yeong Wang, Yuan-Jen Lee, Chih-Ta Shen, Shan-Yi Yang, Ching-Hsiang Tsai, Chien-Chung Hung, Kuei-Hung Shen, Ming-Jinn Tsai, and Ming-Jer Kao. Reduction in critical current density for spin torque transfer switching with composite free layer. *Appl. Phys. Lett.*, 93:092504, 2008.

[123] Chun-Yeol You. The critical current density in composite free layer structures for spin transfer torque switching. *J. Appl. Phys.*, 107(7):073911, 2010.

[124] Sergei Urazhdin, Weng Lee Lim, and Andrew Higgins. Effect of polarizer dynamics on current-induced behaviors in magnetic nanopillars. *Phys. Rev. B*, 80(14):144411, 2009.

[125] J. C. Sankey, I. N. Krivorotov, S. I. Kiselev, P. M. Braganca, N. C. Emley, R. A. Buhrman, and D. C. Ralph. Mechanisms limiting the coherence time of spontaneous magnetic oscillations driven by dc spin-polarized currents. *Phys. Rev. B*, 72(22):224427, 2005.

[126] Joo-Von Kim. Stochastic theory of spin-transfer oscillator linewidths. *Phys. Rev. B*, 73(17):174412, 2006.

[127] A. Yamaguchi, T. Ono, S. Nasu, K. Miyake, K. Mibu, and T. Shinjo. Real-space observation of current-driven domain wall motion in submicron magnetic wires. *Phys. Rev. Lett.*, 92:077205, 2004.

[128] M. Kläui, C. A. F. Vaz, J. A. C. Bland, W. Wernsdorfer, G. Faini, E. Cambril, L. J. Heyderman, F. Nolting, and U. Rüdiger. Controlled and reproducible domain wall displacement by current pulses injected into ferromagnetic ring structures. *Phys. Rev. Lett.*, 94:106601, 2005.

[129] Z. Li and S. Zhang. Domain-wall dynamics and spin-wave excitations with spin-transfer torques. *Phys. Rev. Lett.*, 92:207203, 2004.

[130] S. Zhang and Z. Li. Roles of nonequilibrium conduction electrons on the magnetization dynamics of ferromagnets. *Phys. Rev. Lett.*, 93:127204, 2004.

[131] A. Thiaville, Y. Nakatani, J. Miltat, and Y. Suzuki. Micromagnetic understanding of current-driven domain wall motion in patterned nanowires. *Europhys. Lett.*, 69:990 – 996, 2005.

[132] S. S. P. Parkin, M. Hayashi, and L. Thomas. Magnetic domain-wall racetrack memory. *Science*, 320:190 – 194, 2008.

[133] M. Hayashi, L. Thomas, R. Moriya, Ch. Rettner, and S. S. P. Parkin. Current-controlled magnetic domain-wall nanowire shift register. *Science*, 320:209 – 211, 2008.

[134] Stellan Bohlens and Daniela Pfannkuche. Width dependence of the nonadiabatic spin-transfer torque in narrow domain walls. *Phys. Rev. Lett.*, 105:177201, 2010.

[135] V. K. Dugaev, J. Barnaś, A. Łusakowski, and Ł. A. Turski. Electrons in a ferromagnetic metal with a domain wall. *Phys. Rev. B*, 65:224419, 2002.

[136] Gen Tatara and Hidetoshi Fukuyama. Resistivity due to a domain wall in ferromagnetic metal. *Phys. Rev. Lett.*, 78:3773–3776, 1997.

[137] Arne Brataas, Gen Tatara, and Gerrit E. W. Bauer. Ballistic and diffuse transport through a ferromagnetic domain wall. *Phys. Rev. B*, 60:3406–3413, 1999.

[138] A. C. Reilly, W. Park, R. Slater, B. Ouaglal, R. Loloee, W. P. PrattJr., and J. Bass. Perpendicular giant magnetoresistance of co91fe9/cu exchange-biased spin-valves: further evidence for a unified picture. *J. Magn. Magn. Mater.*, 195(2):269 – 274, 1999.

[139] S. D. Steenwyk, S. Y. Hsu, R. Loloee, J. Bass, and W. P. Pratt. Perpendicular-current exchange-biased spin-valve evidence for a short spin-diffusion lenght in permalloy. *J. Magn. Magn. Mater.*, 170(1-2):L1 – L6, 1997.

[140] W. Park, R. Loloee, J. A. Caballero, Jr. W. P. Pratt, P. A. Schroeder, J. Bass, A. Fert, and C. Vouille. Test of unified picture of spin-dependent transport in perpendicular (cpp) giant magnetoresistance and bulk alloys. *J. Appl. Phys.*, 85(8):4542–4544, 1999.

[141] G. Rowlands P. Rhodes. Demagnetizaing energies of uniformly magnetized rectangular blocks. *Philos. Lit. Soc. Sci. Sect.*, 6:191–210, 1954.

[142] G. E. P Box and M. E Müller. A note on the generation of random normal deviates. *Ann. Math. Statist.*, 29:610 – 611, 1958.

Oświadczenie

Ja, niżej podpisany Pavel Baláž, doktorant Wydziału Fizyki Uniwersytetu im. Adama Mickiewicza w Poznaniu oświadczam, że przedkładaną rozprawę doktorską pt. *Current-induced dynamics in magnetic nanopillars* napisałem samodzielnie. Oznacza to, że przy pisaniu pracy, poza niezbędnymi konsultacjami, nie korzystałem z pomocy innych osób, a w szczególności nie zlecałem opracowania rozprawy lub jej istotnych części innym osobom, ani nie odpisywałem tej rozprawy lub jej istotnych części od innych osób.

Równocześnie wyrażam zgodę na to, że gdyby powyższe oświadczenie okazało się nieprawdziwe, decyzja o nadaniu mi stopnia naukowego doktora zostanie cofnięta.

Pavel Baláž

W Poznaniu 15 października 2011